

FERROELECTRIC MEMORY BASED ON PARTIAL POLARIZATION FOR
ANALOG WEIGHT STORAGE

A Dissertation

Submitted to the Graduate School
of the University of Notre Dame
in Partial Fulfillment of the Requirements
for the Degree of

Doctor of Philosophy

by

Pratyush Pandey

Alan C. Seabaugh, Director

Graduate Program in Electrical Engineering

Notre Dame, Indiana

April 2021

© Copyright by
Pratyush Pandey
2021
CC-BY-4.0

FERROELECTRIC MEMORY BASED ON PARTIAL POLARIZATION FOR ANALOG WEIGHT STORAGE

Abstract

by

Pratyush Pandey

The dynamics of reading and writing the partial polarization state in ferroelectric (FE) capacitors have been explored for use in nonvolatile analog memory for application in training neural networks. New pulse measurement protocols that minimize spurious interface charging effects have been developed to more precisely measure polarization, polarization reversal, and current-voltage characteristics. Analytic methods to interpret these measurements have also been developed.

A strictly symmetric pulse protocol, where the integral of the measurement waveform over a measurement cycle is zero, was developed to measure dynamic effects in FE capacitors. In this way, the effects of biasing were balanced equally to minimize charging of the interfaces. Unsaturated polarization reversal was observed in TiN/HZO/TiN capacitors with asymmetric measurements; the unsaturation was substantially eliminated using the strictly symmetric protocol.

Using the strictly symmetric measurement protocol, partial polarization in metal-FE-metal capacitors was shown to be stable up to 250 ms. A surprising dependence of partial polarization on the delay between reset and write pulses, and the reset conditions, was discovered, with the partial polarization changing by 50% of the FE remanent polarization. This delay-before-write dependence was qualitatively attributed to the dynamics of subcritical nuclei that exist up to 1 s in HZO, and whose

size is estimated to be less than 4x4x4 HZO unit cells.

A strictly symmetric pulsed protocol was designed for current-voltage-time (I-V-t) measurements on Pd/HZO/p⁺ Si capacitors. The I-V-t measurements showed the capacitor current direction to be opposite to the applied bias polarity for voltages lower in magnitude than certain characteristic zero crossing voltages. The current magnitudes increased when the applied bias magnitudes were decreased further. A quantitative analysis showed these observations to be consistent with the assumption that the HZO electric field controls the capacitor current direction, and that a flat band condition exists in HZO at the zero crossing voltages.

A spectroscopic photoresponse measurement system was constructed, capable of measuring electrical responses to photons ranging in energy from 0.6 - 7 eV, to measure polarization dependent band offsets of metal-FE-semiconductor capacitors by internal photoemission (IPE). The bandgap of HZO was extracted as 6.2 ± 0.2 eV from Pd/HZO IPE transitions.

CONTENTS

Figures	v
Tables	viii
Chapter 1: Introduction	1
1.1 Context and trends in analog memory	1
1.2 Ferroelectric memory	4
1.2.1 Ferroelectric partial polarization	6
1.2.2 State-of-the-art ferroelectric memory	8
1.2.3 Limitations	10
1.3 Objectives and approach	11
1.4 Accomplishments	12
1.5 Organization of the thesis	13
Chapter 2: Theoretical background	14
2.1 Nucleation-limited switching in polycrystalline ferroelectrics	15
2.2 Depolarization field in ferroelectrics	18
Chapter 3: Ferroelectric partial polarization	24
3.1 Metrology of polarization and partial polarization	24
3.1.1 Triangular wave polarization-field (P-E) measurements	24
3.1.2 Pulsed measurement protocol for polarization reversal measurement	26
3.2 Polarization reversal in hafnium zirconate (HZO)	31
3.2.1 Polarization reversal in W/HZO/W and TiN/HZO/TiN capacitors	31
3.3 Asymmetric versus symmetric pulsing	38
3.4 Polarization reversal in HZO versus lead-zirconium-titanate (PZT)	40
Chapter 4: Dynamics in setting of partial polarization	44
4.1 Dynamics of delay-before-read	44
4.2 Dynamics of delay-before-write	48
4.3 Dynamics of subcritical nuclei	50
4.4 Implications for analog weight storage	54

Chapter 5: Internal photoemission measurement system	56
5.1 Measurement principle and theory	56
5.2 Instrumentation	59
5.2.1 Components and optical path	60
5.2.2 Control and data acquisition	62
5.3 Calibration and stability	66
5.4 Flux density vs NIST	68
Chapter 6: Internal photoemission measurements on HZO capacitors	70
6.1 Current in Si/HZO/Pd capacitors	70
6.1.1 Band diagrams of Pd/HZO/p ⁺ Si capacitors	71
6.1.2 Polarization reversal in Pd/HZO/p ⁺ Si capacitors	74
6.1.3 Pulsed measurement protocol for current transients	77
6.1.4 Measurement and interpretation of pulsed current-voltage	79
6.1.5 Analysis of flat band voltages	85
6.2 Band Alignment in Pd/HZO/p ⁺ Si capacitors	89
6.2.1 IPE measurement protocol for FE capacitors	92
6.2.2 Analysis of IPE measurements	97
6.2.3 Band alignment in Pd/HZO/p ⁺ Si capacitors	100
6.2.4 Polarization dependent IPE transitions in Pd/HZO/p ⁺ Si capacitors	102
6.2.5 Improving measurement signal-to-noise	106
Chapter 7: Conclusions	108
Appendix A: Partial switching of ferroelectrics for synaptic weight storage	113
Appendix B: Switching dynamics of ferroelectric Zr-doped HfO ₂	116
Appendix C: Experimentally validated, predictive monte carlo modeling of ferroelectric dynamics and variability	121
Appendix D: Monte Carlo simulation of switching dynamics in polycrystalline ferroelectric capacitors	126
Appendix E: Process dependent switching dynamics of ferroelectric hafnium zirconate	135
Appendix F: Programming-pulse dependence of ferroelectric partial polarization: Insights from a comparative study of PZT and HZO capacitors	138
Appendix G: Traveler with fabrication details of W/HZO/W and TiN/HZO/TiN capacitors	145

Appendix H: Specifications of components in internal photoemission setup . . .	152
Appendix I: Traveler with fabrication details of Pd/HZO/p ⁺ Si capacitors . . .	178
Appendix J: Codes developed to control instruments in internal photoemission	
setup	186
J.1 Monochromator	186
J.1.1 setmono4	186
J.1.2 monoshutteron	189
J.1.3 monoshutteroff	192
J.2 Filter wheel	195
J.2.1 setfilterV4	195
J.3 Power meter	198
J.3.1 setpower_v2	198
J.4 Keithley Sourcemeter	201
J.4.1 openKeithley_Eth	201
J.4.2 VoltageListSweep	203
J.4.3 VoltagePulseSweepCycle	206
J.5 Combined codes	208
J.5.1 Calibration	208
J.5.2 TER_Meas	212
J.5.3 IPE_Pol	218
J.5.4 IPE_Pol_fun_debugfull_chop	222
References	231

FIGURES

1.1	Single step matrix multiplication by a resistive crossbar array	2
1.2	Ferroelectric lattice	5
1.3	Physical gate length scaling of FeFETs	6
1.4	Partial polarization of a polycrystalline FE	8
1.5	Characteristics of FeFET used for DNN acceleration	9
2.1	Comparison of polarization reversal in single crystal and polycrystalline FEs	16
2.2	Equivalent circuit showing origin of depolarization in FEs	19
2.3	Band diagrams of metal/HZO/p ⁺ Si capacitors	22
3.1	Ideal PE measurement	26
3.2	Measurement protocol for polarization reversal characterization	29
3.3	Cross section of fabricated HZO MFM capacitors	32
3.4	Measurement protocol for polarization reversal characterization of W/HZO and TiN/HZO capacitors	33
3.5	Measured polarization reversal characteristics of W/HZO/W capacitors grown via PE-ALD in the Oxford FlexAL ALD	34
3.6	Extracted activation voltage distribution of W/HZO annealed at 500 °C	35
3.7	Unsaturation in TiN/HZO/TiN polarization reversal	37
3.8	Polarization reversal in TiN/HZO capacitors with symmetric and asymmetric pulsing	39
3.9	Comparison of polarization reversal in W/HZO and PZT FE capacitors	42
4.1	Pulse protocol for delay-before-read and delay-before-write measurements	45
4.2	FE partial polarization dependence on delay-before-read in HZO and PZT capacitors	47
4.3	FE partial polarization dependence on delay-before-write in HZO and PZT capacitors	49
4.4	Schematic showing dynamics of subcritical nuclei	52
5.1	Physical mechanism underlying the IPE measurement	57
5.2	Block diagram of IPE setup configured at Notre Dame	59
5.3	Optical power vs wavelength at device location measured over six months	67
5.4	Calibration of monochromator output using a handheld spectrometer	68

5.5	Comparison of photon flux vs photon energy between the IPE setup at Notre Dame and NIST, Gaithersburg	69
6.1	Band diagrams of metal/HZO/p ⁺ Si capacitors	72
6.2	Schematic of fabricated Pd/HZO/p ⁺ Si capacitors	74
6.3	Measured polarization reversal characteristics of Pd/HZO/p ⁺ Si capacitors	75
6.4	Measurement protocol for current transients in MFS capacitors	78
6.5	Measured current transients in Pd/HZO/p ⁺ Si capacitors	80
6.6	First and last current data points from I-V-t measurements on Pd/HZO/p ⁺ Si capacitors	82
6.7	Extracted flat band voltages for Pd/HZO/p ⁺ Si capacitors	84
6.8	Equivalent circuit to analyze flat band in MFIS capacitors	86
6.9	Band diagrams of Pd/HZO/p ⁺ Si capacitors with possible IPE transitions	91
6.10	IPE measurement protocol for Metal-FE-Semiconductor capacitors	93
6.11	Measured current transients in Pd/HZO/p ⁺ Si capacitors in the IPE setup	95
6.12	Extracted zero crossing voltages in the IPE setup for Pd/HZO/p ⁺ Si capacitors	96
6.13	IPE yield measurements and fits for Pd/HZO/p ⁺ Si capacitors	98
6.14	Barrier heights extracted from fitting IPE Yields	100
6.15	Flat band offsets in Pd/HZO/p ⁺ Si capacitors	102
6.16	Band alignment in Pd/HZO/p ⁺ Si capacitors with + <i>P</i> polarization orientation	103
6.17	Band alignment in Pd/HZO/p ⁺ Si capacitors with - <i>P</i> polarization orientation	105
H.1	IPE light source specifications, Part 1	152
H.2	IPE light source specifications, Part 2	153
H.3	Monochromator specifications	154
H.4	Monochromator grating specifications	155
H.5	Monochromator filter wheel specifications	156
H.6	Monochromator filter specifications	157
H.7	Monochromator filter 2 spectral response	158
H.8	Monochromator filter 3 spectral response	159
H.9	Monochromator filter 4 spectral response	160
H.10	Newport collimator specifications, Part 1	161
H.11	Newport collimator specifications, Part 2	162
H.12	Newport collimator specifications, Part 2	163
H.13	Thorlabs fiber coupler specifications, Part 1	164
H.14	Thorlabs fiber coupler specifications, Part 2	165
H.15	Thorlabs optic fiber spectral attenuation	166
H.16	Cascade fiber optic probe specifications	167
H.17	Cascade probe positioner specifications	168

H.18 Thorlabs power meter specifications	169
H.19 Thorlabs power meter response	170
H.20 Thorlabs power meter drawings	171
H.21 Thorlabs USB power meter interface specifications	172
H.22 Keithley sourcemeter specifications, Part 1	173
H.23 Keithley sourcemeter specifications, Part 2	174
H.24 Keithley sourcemeter specifications, Part 3	175
H.25 GPIB to Ethernet connector specifications, Part 1	176
H.26 GPIB to Ethernet connector specifications, Part 2	177

TABLES

1.1	Comparison of presently available nonvolatile analog memory technologies	3
3.1	Extracted NLS parameters	36
3.2	Summary of physical parameters and reset voltages of tested HZO and PZT capacitors	41
4.1	Summary of physical parameters and reset voltages of tested HZO and PZT capacitors	46
6.1	Summary of measured and extracted physical parameters of Pd/HZO/p ⁺ Si capacitors	89
6.2	Expected FE polarization during IPE measurements	97
6.3	Comparison of extracted HZO/p ⁺ Si band offsets with HfO ₂ /Si and ZrO ₂ /Si band offsets	101
6.4	Predicted polarization dependent IPE transitions in Pd/HZO/p ⁺ Si capacitors	106

CHAPTER 1

INTRODUCTION

1.1 Context and trends in analog memory

The currently prevalent von Neumann model of computing envisions memory and processing to be physically separate [1], thereby limiting computation by the data transfer bandwidth and memory speed [2, 3]. For a large class of computing problems that utilize matrix multiplication as a computational primitive, in-memory computing using resistive arrays provides a solution to this von Neumann bottleneck [4, 5]. Figure 1.1 shows such a crossbar array, where a vector whose elements are encoded as voltages, is multiplied with a matrix whose elements are encoded as conductances, in a single, parallel step yielding a vector whose elements are encoded as currents. In this example, analog memory devices form the conductances in the array, with any single device capable of exhibiting multiple values of conductance. Current graphical processing units (GPUs), on the other hand, perform matrix multiplication by transferring the individual matrix elements from an external memory to the GPU, performing the matrix multiplication element-wise in the GPU, and then transferring the resulting matrix element from the GPU to the external memory [4, 6].

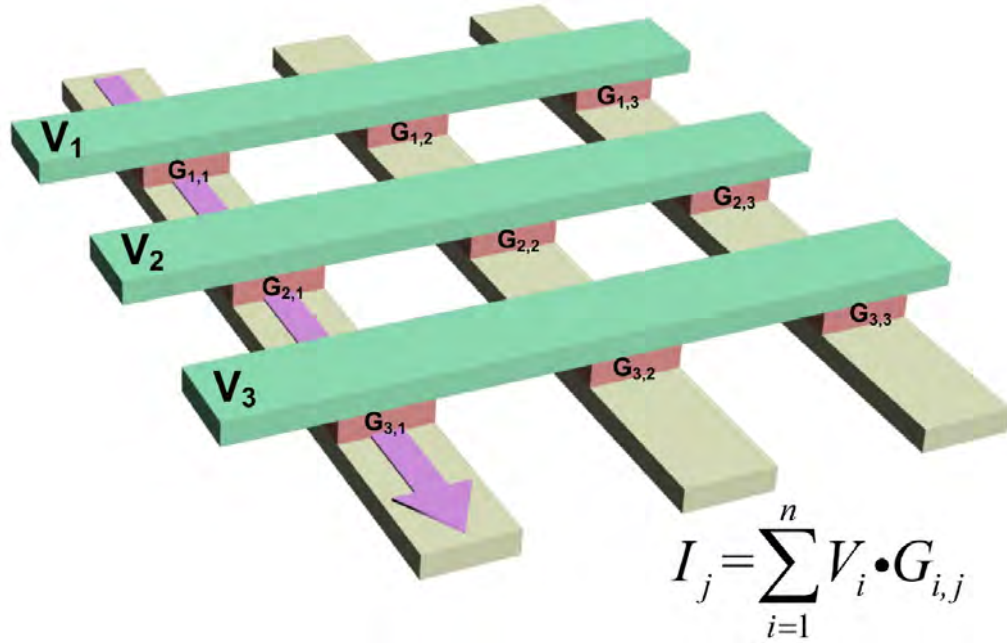


Figure 1.1. A crossbar array of resistors multiplies a vector, with elements V_i encoded as voltages, and a matrix, with elements encoded as conductances $G_{i,j}$, in a single step to yield a vector with elements encoded as currents I_j . Ohm's Law provides the multiplication, and Ampere's Law the addition. Figure from Xi 2020 [2].

Analog functionality can be implemented in many emerging nonvolatile memories (NVMs), such as phase change memory (PCM), resistive random access memory (RRAM), charge trap memory, redox transistors, and ferroelectric (FE) field effect transistors (FeFETs) [7]. Comparative analyses of the different physical implementations for analog memory have been carried out from both device [5, 6, 8] and architecture [2, 9] centric points of view. Table 1.1, reproduced from Xiao 2020 [9], summarizes the relative advantages and disadvantages of the emerging NVMs. It can be seen from the table that compared to RRAMs and PCMs, FeFETs have a higher device resistance, lower stochasticity, and lower write current, while main-

taining similar write speeds and device areas. FeFETs allow for faster write speed and lower device area than charge trap memories and redox transistors, although at the expense of update stochasticity. Therefore, FeFETs are competitive candidates among emerging NVMs for analog memory.

	RRAM	PCM	Charge Trap Mem- ory	Redox Tran- sistor	FeFET
Maximum Resistance	$\sim 1 \text{ M}\Omega$	$\sim 1 \text{ M}\Omega$	$\sim 1 \text{ G}\Omega$	$\sim 10 \text{ M}\Omega$	$\sim 1 \text{ G}\Omega$
Device Area	4F^2	4F^2	$4\text{-}10\text{F}^2$	Large	4F^2
Endurance	10^{12} cycles	10^{12} cycles	10^5 cycles	$>10^9$ cycles	10^9 cycles
Write current	$1 \mu\text{A}$	$100 \mu\text{A}$	1 pA	10 nA	...
Write speed	ns	ns	ms	ms, μs	ns
Update stochasticity	High	High	Low	Low	Moder- ate
Update linearity	Poor	Poor	Moder- ate	Good	Poor
Symmetric update	No	No	Variable	Yes	No

TABLE 1.1

A COMPARISON OF PRESENTLY AVAILABLE NONVOLATILE
ANALOG MEMORY TECHNOLOGIES AS GIVEN BY XIAO 2020 [9].

1.2 Ferroelectric memory

Ferroelectric materials are dielectrics having a noncentrosymmetric lattice unit cell, as shown in Fig 1.2, leading to a permanent dipole moment that can be switched when an external electric field is applied. The difference in polarization between the two antiparallel crystal states of an FE is referred to as its remanent polarization, $2P_R$, and is measured in $\mu\text{C}/\text{cm}^2$.

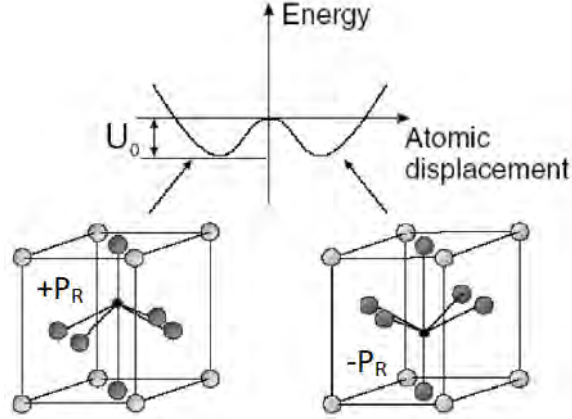


Figure 1.2. FE lattice unit cell illustrating the noncentrosymmetric structure, leading to a permanent dipole polarization that can be changed by an electric field. Figure from Kalinin 2010 [10].

Ferroelectrics have long been proposed for analog weight storage, e.g. in Ishawara 1993 [11]. More recent studies have focused on perovskite FEs such as lead zirconium titanate (PZT) [12], barium titanium oxide (BTO) [13], and bismuth iron oxide (BFO) [14]. These perovskite FEs suffer from a reduction in their remanent polarization for thicknesses below 50 nm, or require epitaxial growth on single crystal substrates, not compatible with conventional complementary metal oxide semiconductor (CMOS) processes to avoid a reduction in their saturation polarization in sub-10-nm layers [15]. These materials also do not have any established atomic layer deposition (ALD) growth processes [15, 16], which would allow fabrication of compact, high-aspect ratio structures and enable a reduction in device footprint for a given capacitance.

The discovery in 2011 of ferroelectricity in the CMOS-compatible ALD HfO_2 [17] sparked an interest in FE-based memory. In 2017, the first measurements of analog weight storage appeared [18–20] and interest has continued [21, 22]. The scaling

advantage of HfO_2 based FEs is made clear in Fig. 1.3, which shows the “scaling gap” between reported FeFET gate lengths and eNVM ITRS guidelines, before and after the discovery of ferroelectricity in ALD HfO_2 . The demonstration of HZO-based FeFETs in 22 nm fully-depleted Si-on-insulator (22FDSOI) [23] closed this “scaling gap”, underscoring the applicability of HfO_2 -based FeFETs in advanced CMOS technology nodes.

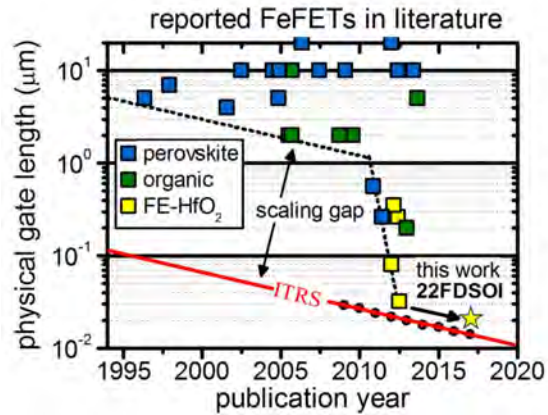


Figure 1.3. Physical gate length of reported FeFETs classified by material system and compared with ITRS guidelines for emerging nonvolatile memories (eNVMs). Figure from Dunkel 2017 [23]

1.2.1 Ferroelectric partial polarization

In a polycrystalline FE like HZO, the individual polycrystalline grains can switch independently between two polarization directions. When the polarization directions of all the grains are aligned, the FE can be said to be fully polarized. The FE is said to be partially polarized when the grains are in a mixed state of alignment and anti-alignment. This is illustrated in Fig. 1.4 showing the two fully polarized states

as well as the intermediate states of partial polarization.

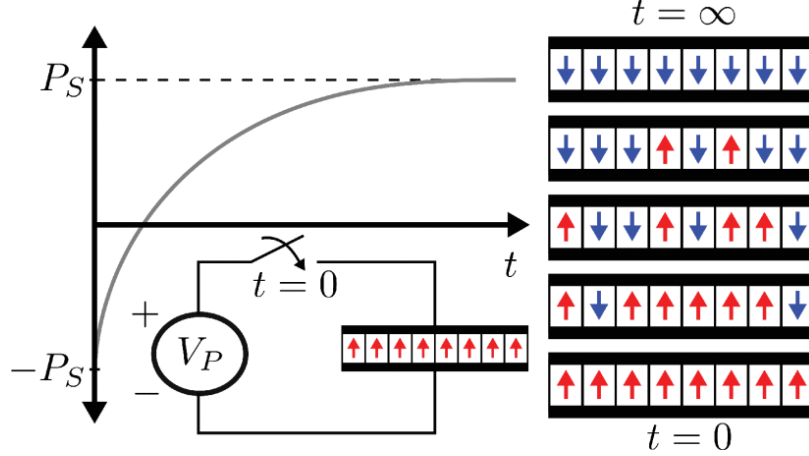


Figure 1.4. Polycrystalline FE switches from one fully polarized state ($-P_S$) to the other ($+P_S$) by application of a voltage pulse, and schematic illustration of partial polarization due to independently switching FE grains. Figure from Alessandri and Pandey 2018 [24].

1.2.2 State-of-the-art ferroelectric memory

Ferroelectric memory devices utilize the FE polarization as the state variable but differ in the read-out mechanism. Ferroelectric memory devices can be broadly classified into three categories - FE random access memories (FeRAMs), FeFETs, and FTJs [25]. This section briefly summarizes the state-of-the-art in these categories.

A common FeRAM memory cell consists of an FE capacitor and a select transistor, in what is known as the 1 transistor 1 capacitor (1T1C) configuration [26]. The 1T1C configuration of FeRAM is similar to the 1T1C memory cell in dynamic RAM (DRAM), which consists of a non-FE capacitor and a select transistor. The FeRAM is a nonvolatile alternative to DRAM, with both featuring a destructive readout scheme [27]. Texas Instruments currently produces the most scaled commercially available FE memory, a PZT-based FeRAM with a 65 nm FE PZT layer at the 130 nm technology node [26–30].

Ferroelectric FETs transduce FE polarization to the FET conductance. This has been done in HfO₂-based FeFETs [23, 31], which are MOSFETs with an FE gate dielectric. This configuration also allows for analog memory, as shown in Fig. 1.5; the partially polarized states of the FE control the threshold voltage, and hence the conductance of the transistor. Results showcasing the suitability of HZO FeFETs for analog memory are reported, based on simulations of FeFET arrays calibrated to measurements on single transistors and capacitors [18, 31]. The simulations revealed a 10³ to 10⁶ reduction in time taken for online learning when benchmarked using 1 million images from the Modified National Institute of Standards and Technology (MNIST) database compared to RRAM implementations, while maintaining >90% accuracy [18].

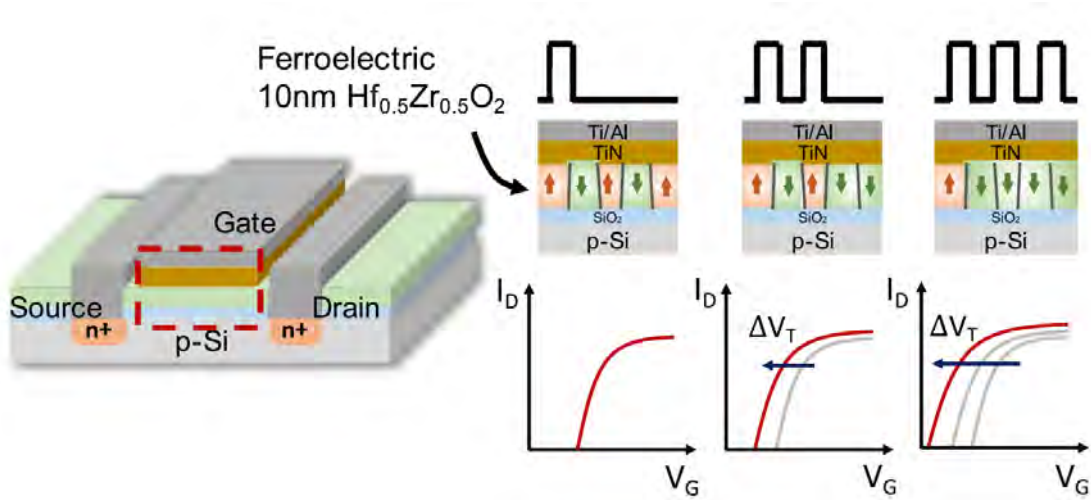


Figure 1.5. (a) Schematic diagram illustrating operation of an FeFET. Grains in a polycrystalline FE switch independently, leading to partial polarization states that shift the transistor threshold voltage V_T . Figure from Jerry 2018 [31].

The FTJ consists of two electrodes separated by a quantum-mechanically-thin insulating FE [32]. The resistance presented by the FE to current flow between the two electrodes depends on the direction of FE polarization. Crossbar arrays of FTJs [22] fabricated in a CMOS process have been demonstrated with 4 nm Si-doped HfO₂ as the FE, where each FTJ exhibited 16 distinct conductance levels in its I-V characteristics. Similar to the reports on FeFETs, the FTJs pulsing response was measured, and these measurements were used to calibrate models describing the pulsing response of FTJs. Simulations based on these models were reported, which indicate a 3x improvement in computational efficiency (measured in Tera operations per second per watt, or TOPS) over PCM devices in training a fully connected neural network to classify images of fashion items in the standardized Fashion-MNIST (F-MNIST) data set, while operating at less than 10% power [22].

1.2.3 Limitations

Projections of HfO₂-based FE memory show the feasibility of their use as a non-volatile technology in a variety of applications [18, 22, 31]. However, a fundamental understanding of the dynamics of FE partial polarization is lacking [33]. While pulse programming protocols to set the FE partial polarization are reported for both FeFETs [31] and FTJs [22], it has been found during this dissertation research that there are unreported dynamic dependencies of FE capacitors that result from changes in reset conditions, timing parameters, applied voltages, and pulsing history. Write and read disturbs in large arrays of FE-based analog memory devices may be effected by these dynamics [34]. It appears that the understanding based on the findings in this thesis can be used to develop read/write protocols for FE-based device arrays implementing neural network acceleration algorithms like that utilizing stochastic pulsing [35].

The reports on FTJs highlight the variation of measured capacitor current with

FE polarization [22, 36], but do not report the evolution of the capacitor current with time for a given readout protocol. The research carried out in this dissertation has found the FTJ capacitor current to be dependent on the delay after the FE partial polarization has been set. It is important to incorporate the time dependence of FTJ currents to design FTJ read protocols. Furthermore, in these devices [22, 36], tunneling is not clearly established as the transport mechanism leading to the measured current. In Berdan 2020 [22], an exponential current-voltage dependence is considered indicative of tunneling. In Kobayashi 2019 [36], the band offsets of HfO_2 are used to fit tunneling models to the measured current. The known band offsets of HfO_2 and ZrO_2 can be used to calculate tunneling currents in HZO-based FTJs. However, since the FTJ current has an exponential dependence on the band offsets [37], a direct measurement of HZO band offsets is expected to aid in calculating tunneling currents in HZO FTJs with greater accuracy.

1.3 Objectives and approach

The objective of this thesis has been to develop a quantitative physical understanding of FE capacitors, and thereby investigate their potential for analog weight storage and acceleration of training in deep neural networks (DNNs) [35, 38]. Since the analog weight in an FE corresponds to its partial polarization, this thesis aims to develop a careful experimental understanding of factors influencing the setting of FE partial polarization [39, 40]. An internal photoemission (IPE) system has been configured at Notre Dame to make the first direct measurements of various band offsets in the Si-HZO material system. By utilizing these capabilities, this thesis aims to develop an understanding of the dynamics of FE partial polarization, as well as transport in FE capacitors, both of which are essential towards leveraging FEs for analog weight storage.

1.4 Accomplishments

The thesis of this research is that the partial polarization of FE HZO can be used to store analog weights. This was proposed by Kinder, Alessandri, Pandey, et al. in 2017 [19]. Measurements of FE partial polarization [24] established the early measurement protocol for characterization of polarization reversal in HZO capacitors, with the HZO deposited by ALD. This paper [24] also established a theory in agreement with measurements over different programming pulse amplitudes, and durations over 5 orders of magnitude in time. The model was extended [39, 41] to show predictions for arbitrary pulse protocols. Continuing experiments to optimize the FE properties for analog weight storage revealed that for certain experimental growth and electrode conditions, the FE partial polarization did not saturate [42]. This led to the discovery that symmetry of the pulse protocol affects the FE partial polarization, and this can be reduced with a symmetric pulse protocol [40]. The programming pulse dependence of FE partial polarization was further explored, and a surprising dependence was found on the reset duration and the delay-before-write durations. This dependence was reported [40] and a qualitative description was proposed to explain these observations. An IPE measurement system was configured and set up at Notre Dame to investigate the band offsets in Si/HZO/Metal capacitors. While performing the IPE measurements, the measured current in p⁺-Si/HZO/Pd capacitors was found to depend on time; this dependence was carefully characterized and quantitatively modeled. An FE-specific IPE measurement protocol was then developed based on the analysis of measured current transients and used to extract the band offsets in p⁺-Si/HZO/Pd capacitors.

1.5 Organization of the thesis

With this introduction the thesis is organized as follows. Chapter 2 describes the theoretical framework - a physics-based predictive model describing polarization reversal in polycrystalline FEs is presented, and the depolarization field in FE-based capacitors is discussed. Chapter 3 describes the measurement protocol for characterizing polarization reversal and partial polarization in FE capacitors, and compares the measured polarization reversal in HZO and PZT capacitors. Chapter 4 highlights new findings relating to the dependence of FE partial polarization on various timing parameters in the measurement protocol. Chapter 6 describes the IPE setup developed at Notre Dame, along with the theory behind IPE measurements. The characterization of current transients in p^+ -Si/HZO/Pd capacitors fabricated for IPE measurements is described in Chapter 6. Observations from analysis of these measurements led to the design of a new IPE measurement protocol to extract the flat band offsets in the Si/HZO/Pd material system. Finally, Chapter 7 summarizes the accomplishments, and gives some perspective on the use of FEs for analog weight storage. The papers published during the course of this research are attached as appendices, with Kinder 2017 [19] in Appendix A, Alessandri 2018 [24] in Appendix B, Alessandri and Pandey 2018 [41] in Appendix C, Alessandri and Pandey 2019 [39] in Appendix D, Pandey 2019 [42] in Appendix E, and Pandey 2020 [40] in Appendix F.

CHAPTER 2

THEORETICAL BACKGROUND

The aim of this chapter is to provide the theoretical background necessary to analyze polarization reversal in metal-FE-metal (MFM) capacitors and metal-FE-semiconductor (MFS) capacitors. Early models of polarization reversal assumed an infinite single crystal FE [43]; these theories had to be modified to a nucleation-limited-switching (NLS) theory to account for the polycrystalline nature of modern thin-film (< 100 nm in thickness) FEs [44]. The NLS theory provides a physics-based predictive framework to describe the dependence of switching dynamics on the applied electric field duration and magnitude. The agreement of this model with measurements of FE HZO is well established [24].

In an ideal MFM capacitor, the entire FE polarization is screened by the metallic electrodes, since the ideal metal electrodes have an infinite capacitance. However, if there is a finite capacitance in series with the FE capacitor in a capacitive stack, the FE polarization is not completely screened [45]. The finite capacitance can be an interfacial oxide between the metal and FE layers of an MFM capacitor, or the semiconducting layer in an MFS capacitor. Due to the incomplete screening of FE polarization, the field in the FE layer of an MFS capacitor differs significantly from that in an ideal MFM capacitor [45]. Thus, understanding the effect a finite series capacitance has on the electric field in an FE capacitor is crucial to extend the understanding of FE behavior from an ideal MFM capacitor to practical metal-FE-insulator-metal (MFIM) and MFS capacitors.

2.1 Nucleation-limited switching in polycrystalline ferroelectrics

One of the early physics-based models for polarization reversal in an FE was the Kolmogorov-Avrami-Ishibashi (KAI) model [43], applicable to an infinite single crystal. In this model, reversal of the polarization is considered to occur by nucleation of domains having an opposing polarization relative to the extant FE polarization. Subsequent expansion of the domain can be described in terms of the motion of domain walls. The expression for the polarization as a function of time $P(t)$, when switching from a $-P_S$ to a $+P_S$ state, is given by [46]

$$P(t) = -P_S + 2P_S(1 - e^{-A(t)}), \quad (2.1)$$

where $A(t)$ refers to Avrami's extended volume [43] and t is time. For a constant nucleation rate and domain wall velocity,

$$A(t) = (t/\tau(E))^n. \quad (2.2)$$

Here, $\tau(E)$ is an electric field dependent characteristic switching time, E is the electric field, and n is the Avrami exponent which is dependent on whether the domain wall growth is 1, 2, or 3 dimensional in nature, leading to $n = 1, 2, \text{ or } 3$ respectively [43]. Experiments show that the measured exponent often has noninteger values [47].

The assumption of an infinite single crystal FE that the KAI model is based upon requires modification for polycrystalline FEs [44]. Polycrystalline FEs contain multiple crystalline grains separated by grain boundaries that arrest domain wall expansion. The difference between polarization reversal in single crystal and polycrystalline FEs is schematically shown in Fig. 2.1. As can be seen from Fig. 2.1, once a particular grain is fully switched, it cannot affect the neighboring grains by domain wall expansion, and nucleation in another grain is necessary for the polarization reversal to continue. For the case of nanoscale polycrystalline FEs, the grain sizes are

comparable to the film thickness, and once a domain of the opposite polarization is nucleated within a grain, it expands to switch the entire grain in a time short with respect to domain nucleation. As a consequence, domain wall expansion can be ignored in such films, and the polarization reversal is considered nucleation-limited.

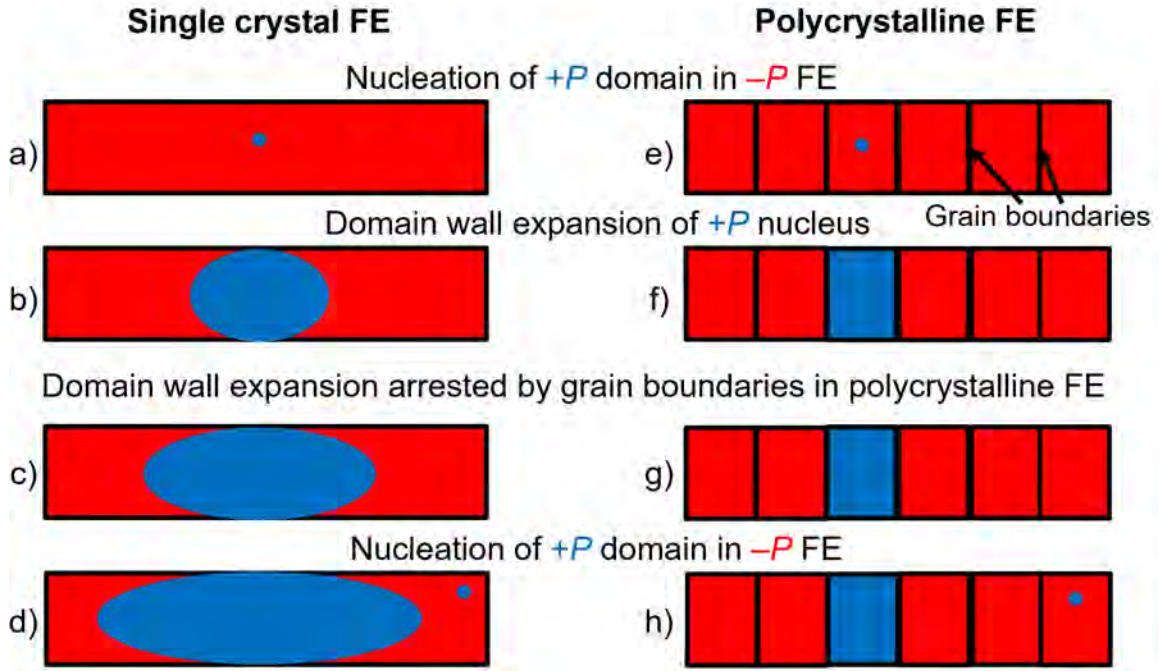


Figure 2.1. Polarization reversal from $-P$ to $+P$ compared between (a-d) a single crystal and (e-h) a polycrystalline FE. Polarization reversal starts with (a,e) the nucleation of a domain having opposite polarization, which then (b,f) expands its volume. The domain in (c) continues to grow in a single crystal FE, however its growth is terminated by the grain boundaries in a polycrystalline FE as indicated in (g). While in (d) polarization reversal continues in the single crystal FE, (h) nucleation of another domain in a different grain is necessary for continuation of polarization reversal in the polycrystalline FE.

Based on this picture, the NLS model was proposed to account for polarization re-

versal in nanoscale polycrystalline FEs [44, 46]. Mathematically, this model considers the FE to be an ensemble of independently switching grains, each having a separate, field dependent, characteristic time constant $\tau(E)$, belonging to a probability density function $f(\tau(E))$. Since the limiting process is nucleation, the characteristic time constant corresponds to the waiting time for a nucleation event, and $\tau(E)$ can be referred to as the electric field-dependent nucleation time constant. The polarization as a function of time is then written as the expectation value of Eq. 2.1 as [39, 46]

$$P(t) = -P_S + 2P_S \int_0^\infty (1 - e^{-A(t, \tau(E))}) f(\tau(E)) d\tau. \quad (2.3)$$

In this model, the extended volume $A(t, \tau(E))$ obeys the power law given in Eq. 2.2. The field dependence of the nucleation time constant $\tau(E)$ was developed [48] as

$$\tau(E) = \tau_\infty e^{(E_a/E)^\alpha}, \quad (2.4)$$

where τ_∞ is the minimum nucleation time constant (i.e. the nucleation time constant observed when an infinite field is applied), E_a is an activation electric field, E is the external applied electric field, and α is an empirical parameter.

This approach allows for rewriting the distribution of switching times as a distribution of activation fields $f(E_a)$, allowing the NLS model to be written in a field dependent form,

$$P(t) = -P_S + 2P_S \int_0^\infty \left(1 - e^{-\left(\frac{t}{\tau(E)}\right)^n}\right) f(E_a) dE_a. \quad (2.5)$$

The distribution of activation fields $f(E_a)$ is the generalized beta distribution of type 2 [39],

$$f(E_a) = \frac{aE_a^{(ap-1)}}{b^{ap}B(p, q)(1 + (E_a/b)^a)^{p+q}}, \quad (2.6)$$

with distribution parameters a , b , p , and q , and $B(p, q)$ is the beta function .

Therefore, in the NLS model, the switching behavior of the FE film is described by 4 parameters relating to the FE switching dynamics, P_S, τ_∞, n , and α , and the 4 parameters, a, b, p , and q , that describe the distribution function $f(E_a)$. For polycrystalline FEs, a polarization between $-P_S$ and $+P_S$, i.e. a partially polarized state, occurs when a fraction of the grains switch.

2.2 Depolarization field in ferroelectrics

Ma and Han have argued that the gate stack of an FeFET can be simply modeled as the series connection of an FE capacitor and a semiconductor capacitance [45]. As will be shown below, when a finite capacitance is connected in series with an FE capacitor, the FE polarization charge is not fully compensated at the FE/semiconductor interface, leading to a depolarization field in the FE [45]. The depolarization field is oriented in a direction that promotes depolarization of the extant FE polarization. This picture also applies to an MFM capacitor which is in series with a dielectric.

A capacitive stack consisting of an FE capacitor, C_F , in series with a semiconductor, C_{IS} , is shown in Fig. 2.2. The FE capacitor is assumed to have a polarization charge P ; charges Q_F and Q_{IS} represent free charges on the FE and semiconductor capacitors, respectively. By charge neutrality,

$$Q_{IS} = Q_F. \tag{2.7}$$

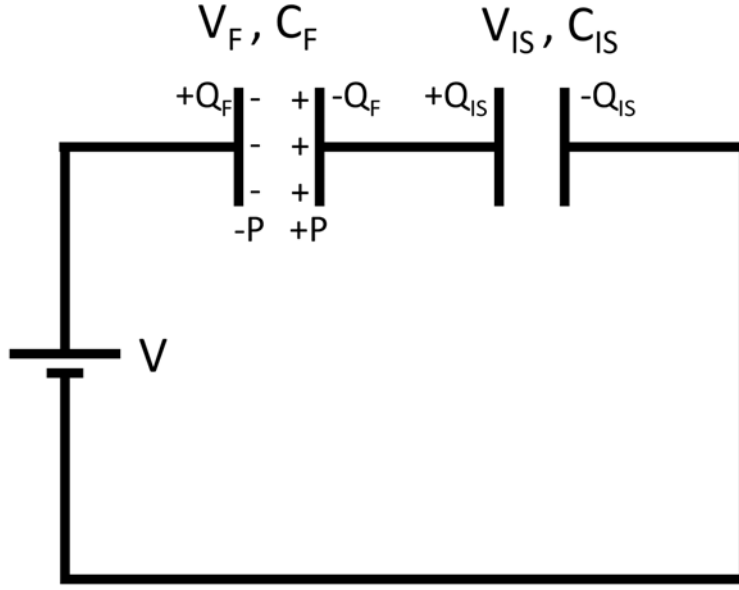


Figure 2.2. Equivalent circuit showing origin of depolarization in FEs. The FE capacitor C_F is in series with the semiconductor capacitance C_{IS} , and the capacitors are connected to a voltage source V . An FE polarization charge $\pm P$ exists on the FE capacitor, and current flows through the circuit leading to a charge Q_F on the FE capacitor, and Q_{IS} on the semiconductor capacitor. Figure modified from Ma and Han 2002 [45].

The charge on the FE capacitor plate Q_F is a combination of the geometrical capacitance $C_F V_F$ and FE polarization P ,

$$Q_F = C_F V_F + P. \quad (2.8)$$

An external voltage V is applied across the stack, which is divided between the FE (V_F) and the semiconductor (V_{IS}), such that

$$V = V_F + V_{IS}. \quad (2.9)$$

where

$$V_{IS} = \frac{Q_{IS}}{C_{IS}}. \quad (2.10)$$

Rearranging Eqs. 2.8, 2.10, 2.9, and 2.7 yields a relation for the voltage across the FE

$$V_F = \frac{C_{IS}V - P}{C_F + C_{IS}}. \quad (2.11)$$

If no external voltage is applied, $V = 0$, a nonzero voltage exists across the FE capacitor in an orientation opposite to the FE polarization, which is termed the depolarization voltage, V_{DEP} ,

$$V_{DEP} = \frac{-P}{C_F + C_{IS}}. \quad (2.12)$$

The depolarization voltage can be converted to a depolarization field upon division by the FE thickness

$$E_{DEP} = \frac{-V_{DEP}}{t_{FE}} = \frac{P}{t_{FE}(C_F + C_{IS})}. \quad (2.13)$$

Therefore, an MFS capacitor with FE polarization P will experience a depolarization field E_{DEP} when zero external voltage is applied.

It follows from the NLS model, Eq. 2.4, that a polycrystalline FE will undergo polarization reversal in the presence of a depolarization field with a depolarization time constant approximately given as

$$t_{DEP} = \tau_{\infty} e^{(\langle E_a \rangle / E_{DEP})^{\alpha}}. \quad (2.14)$$

where $\langle E_a \rangle$ is the FE mean activation field. As the FE polarization reverses under the influence of E_{DEP} , the FE polarization P would also decrease, in turn

decreasing the depolarization field (Eq. 2.13) and increasing the depolarization time constant (Eq. 2.14). Therefore, the depolarization is expected to progressively slow as the depolarization progresses. It can be seen from Eq. 2.14 that depolarization of the FE would occur with a higher time constant if the FE mean activation field is increased. Therefore, a higher mean activation field is conducive to longer retention in FE memory at the expense of write voltage.

The depolarization field in MFS capacitors can be visualized using band diagrams in Fig. 2.3. The band diagrams are computed using 1D Poisson Solver software developed by Snider [49].

The flat band diagram for a metal/HfO₂/p⁺ Si capacitor with zero FE polarization is shown in Fig. 2.3(a). A +15 $\mu\text{C}/\text{cm}^2$ FE polarization is simulated in Fig. 2.3 by introducing a delta-function charge at the HfO₂ surfaces to mimic FE HZO. For the charge polarity in Fig. 2.3(b), an electron inversion layer is induced in the p⁺ Si. Placing a $-15 \mu\text{C}/\text{cm}^2$ sheet charge at the Si/HZO interface results in the band diagram Fig. 2.3(c). The negative FE polarization at the Si/HZO interface in Fig. 2.3(a) causes accumulation of holes in the p⁺ Si. In both cases, the net charge in the Si layer is not equal to the FE polarization, leading to the depolarization field E_{HZO} in the HZO layer.

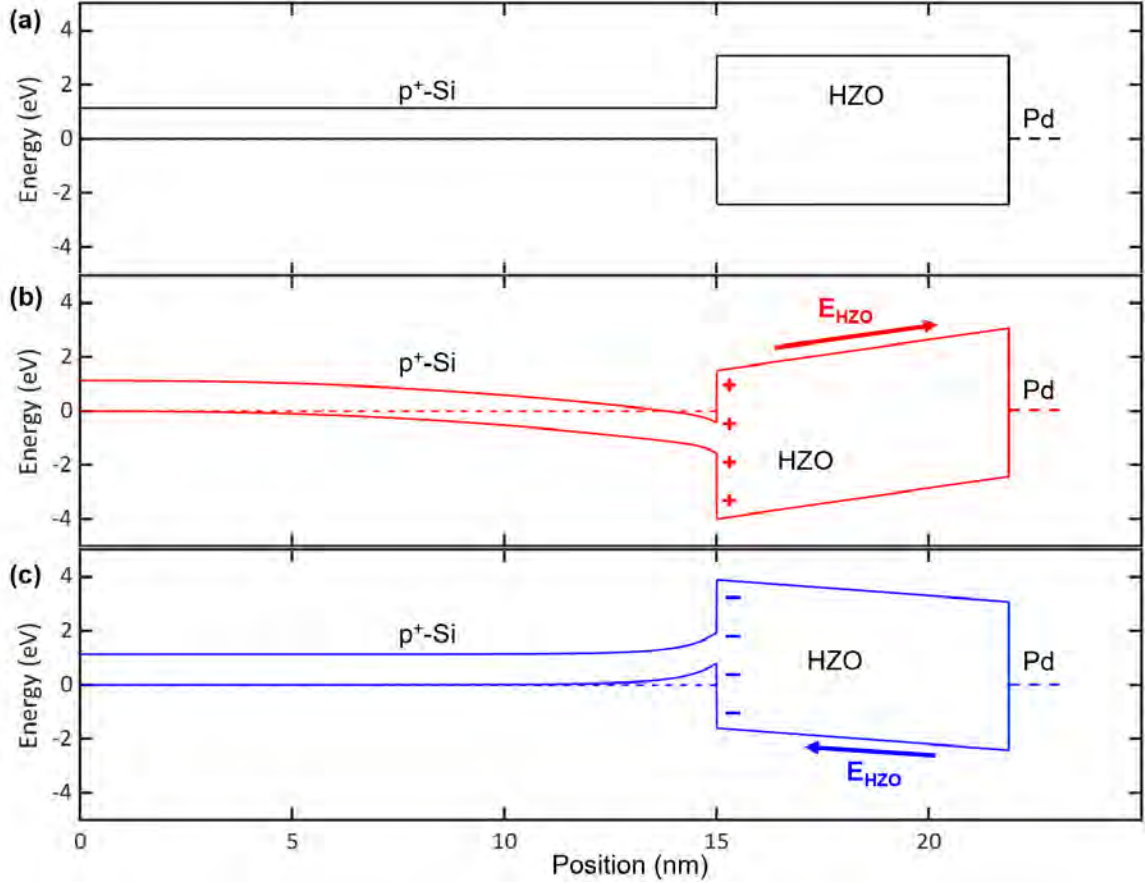


Figure 2.3. Band diagrams of metal/HZO/ p^+ Si capacitors with zero capacitor bias, plotted using 1D Poisson Solver [49] with (a) zero FE polarization at the Si/HZO interface, (b) $+15 \mu\text{C}/\text{cm}^2$ FE polarization at the Si/HZO interface, and (c) $-15 \mu\text{C}/\text{cm}^2$ FE polarization at the Si/HZO interface. The direction of electric field in the HZO layer E_{HZO} is indicated, and the FE polarization charges are also shown. HZO thickness is 7 nm, Si doping is taken to be 10^{19}cm^{-3} , HZO relative permittivity of 25 is assumed, and Si/HfO₂ band offsets [50] are used for Si/HZO. The metal workfunction is considered to be the same as the Si workfunction for this example.

The depolarization field E_{HZO} in Figs. 2.3(b) and (c) can be seen to have a direction promoting neutralization of the FE polarization. Furthermore, since the inversion capacitance of Si is lower than its accumulation capacitance, the depolar-

ization field in Fig. 2.3(c) is higher than in Fig. 2.3(a). Due to this, a positive FE polarization at the Si/HZO interface would have a higher retention than a negative FE polarization at the Si/HZO interface for a p⁺-Si substrate. The depolarization fields in Fig. 2.3(b) and (c) were ~ 1 and 2 MV/cm, respectively. Substituting these depolarization field values in Eq. 2.14 along with $\tau_\infty = 164$ ns, $\langle E_a \rangle = 1.87$ MV/cm, and $\alpha = 3.39$ [42], a depolarization time constant $t_{DEP} = 683$ μ s and 360 ns can be calculated for Si in accumulation and inversion, respectively.

The NLS theory of polarization reversal described in this chapter will be used to analyze polarization reversal in HZO capacitors in Chapter 3. The NLS model parameters, particularly the minimum nucleation time constant τ_∞ and the activation field distribution $f(E_a)$ provide useful metrics to quantify the switching dynamics of FE capacitors. The discussion regarding depolarization fields in MFS capacitors will be used to interpret current transients in fabricated Pd/HZO/p⁺ Si capacitors.

CHAPTER 3

FERROELECTRIC PARTIAL POLARIZATION

A polycrystalline FE is said to be in a partially polarized state when the FE grains are in a mixture of aligned and anti-aligned orientations. The first characterization of the partial polarization switching dynamics of HZO capacitors was presented as part of the research in this thesis [19]. Furthermore, in course of this research, the pulsing protocol itself was found to affect the FE partial polarization [40]. The metrology developed to investigate these findings, and their results, will be discussed in this chapter.

3.1 Metrology of polarization and partial polarization

3.1.1 Triangular wave polarization-field (P-E) measurements

A method to measure the polarization in FE capacitors is to measure the capacitor current in response to a triangular voltage waveform [51]. Integration of the current with respect to time yields the polarization charge. A schematic of this measurement is shown in Fig. 3.1, with the applied triangular voltage waveform written here as electric field, obtained by dividing the applied voltage by FE thickness. Figure 3.1(a) shows the FE current response to the applied waveform. The current at the point labeled 1 corresponds to the displacement current CdV/dt in the FE capacitor, while the current peak at point 2 corresponds to the charge flow when the FE polarization changes from the remanent polarization $-P_R$ to $+P_R$ (P_r in the figure). The remanent polarization is the surface charge density that exists after the applied bias is removed,

i.e. at zero bias. The remanent polarization P_R may be lower than the saturation polarization P_S if the polarizations of all the FE grains are not oriented in the same direction when the applied voltage bias is removed. An ideal, single crystal FE is expected to fully switch at a given field, known as the coercive field E_C , corresponding to the solid line in the curve. An FE like HZO has many different grains that have a distribution of coercive fields, leading to the dashed, distributed peak shown in Fig. 3.1(a). When the FE current $I(t)$ is integrated with respect to time, and plotted against applied voltage (here, field $E(t)$), the polarization-field (P-E) characteristics in Fig. 3.1(b) are generated,

$$P(E(t)) = \frac{1}{A} \int_0^t I(t') dt' \quad (3.1)$$

where A is the area.

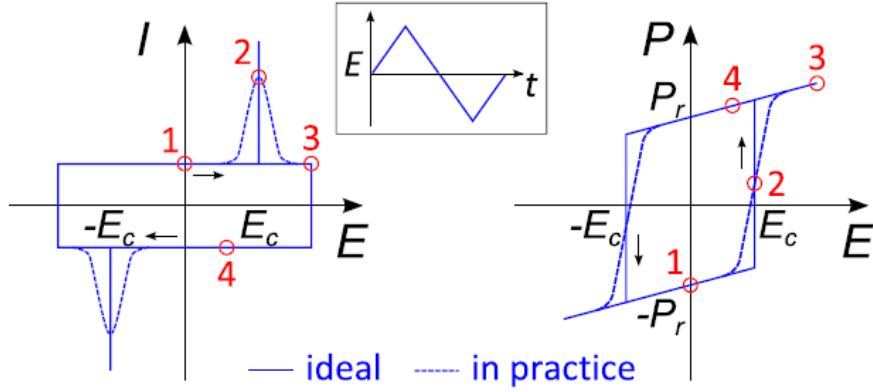


Figure 3.1. A triangular electric field waveform (inset) is applied across an FE capacitor to obtain the polarization-field characteristics of the FE. (a) The current peaks in the current-electric field (I-E) curve correspond to the FE switching, while the the current at zero bias corresponds to the displacement current. (b) Polarization-field (P-E) curve obtained by integrating the current in (a) with respect to time and plotting against the applied field, with the numbers indicating the corresponding points in (a). Response of an ideal, single domain FE is shown as solid lines, while that of a multidomain FE having a distribution of coercive fields is shown with dashed lines. Figure from Schenk 2014 [51].

Polarization-voltage measurements provide a useful characterization of the FE properties - remanent polarization and coercive field. However, these values depend on the amplitude and slew rate of the voltage waveform. A pulsed measurement protocol was proposed [24] which allows the FE partial polarization to be characterized as a function of pulse voltage amplitude and duration.

3.1.2 Pulsed measurement protocol for polarization reversal measurement

Polarization reversal refers to the measurement of the FE polarization state between the two fully saturated polarization states $\pm P_S$. These partially polarization states in a polycrystalline FE are set by first resetting the FE to its remanent po-

larization, and subsequently applying a voltage pulse, the amplitude and duration of which is systematically varied. The pulsed measurements are used to measure the polarization reversal characteristics of FE capacitors. Fitting of these measurements to the NLS model (Sec. 2.1) yields the minimum nucleation time constant, distribution of activation fields, and saturation polarization.

The measurements were performed using a Keithley 4200 parameter analyzer with a 4225-PMU pulse measurement unit and two 4225-RPM remote preamplifiers. The combined resistance of the 50 Ω output resistance of the RPM and the series resistance of the probes was measured to be 54 Ω [52]. The voltage waveforms were applied to the capacitor electrode having a larger area, corresponding to a higher parasitic geometrical capacitance; the smaller area electrode was kept at zero volts. For the HZO capacitors, this corresponds to applying the voltage waveforms to the chuck while keeping the lithographically patterned top electrode at zero volts. The current flowing through the smaller area electrode, corresponding to a lower parasitic geometrical capacitance, is then recorded [52].

Prior to measuring the polarization reversal in an FE capacitor, the FE is cycled by applying triangular waveforms with V_R amplitude and 4 ms period [52]. When the FE polarization monotonically increases with cycling this is commonly termed wake-up and is observed in the first cycling of the FE film after fabrication [53–57]. Wake-up is usually attributed to either the stabilization and coordination of the FE phase mediated by electric field [53, 58] or redistribution of defects such as oxygen vacancies in the FE layer [54–57]. For the FE capacitors measured in this thesis, the wake-up protocol consists of applying 3000 triangular waveforms with V_R amplitude and 4 ms period [52]. The wake-up voltage V_R is determined by applying triangular waveforms of increasing amplitude and observing the measured current response of the FE in real time, similar to a polarization-voltage measurement. The wake-up voltage V_R is chosen such that applying triangular waveforms with voltage

amplitudes $> V_R$ does not lead to an increased FE switching current, corresponding to point 2 in Fig. 3.1(a), in the capacitor. The wake-up voltage V_R is used as the read and reset voltage in the polarization reversal measurement protocol as well. During wake-up, the capacitor response to an applied voltage waveform is dependent on the prior voltage waveforms applied to the capacitor. This dependence of FE partial polarization on its cycling history is referred to as history dependence. Fatigue is another form of history dependence observed in FEs, where the remanent polarization decreases with cycling [53, 55]. Fatigue in FEs is usually attributed to the generation of defects such as oxygen vacancies in the FE layer [53, 55]. Apart from wake-up and fatigue, additional sources of history dependence can exist in setting the FE partial polarization, as reported in Pandey 2020 [40].

The polarization reversal measurement utilizes a sequence of pulses designed to measure the change in polarization of an FE as a function of write pulse amplitude and duration. This polarization change is measured with respect to the fully polarized state. Fig. 3.2 shows the measurement protocol developed in this proposal and which will be later shown to substantially suppress history dependence. The upper (lower) waveform in Fig. 3.2 is utilized to measure the polarization reversal characteristics of an FE capacitor from $-P_R$ to $+P_R$ ($+P_R$ to $-P_R$) by applying write pulses with $V_P > 0$ ($V_P < 0$).

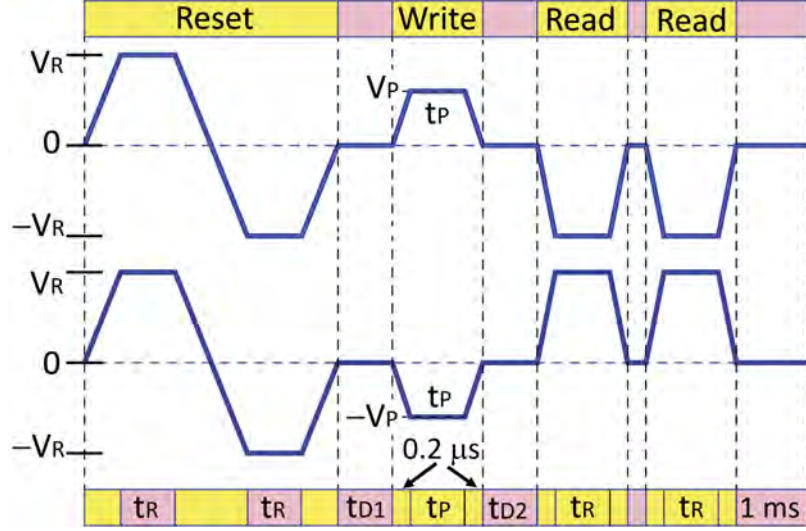


Figure 3.2. Measurement protocols for polarization reversal characterization of FE capacitors. The upper waveform corresponds to FE switching from $-P$ to $+P$ under influence of a $+V_P, t_P$ write pulse, and the lower waveform corresponds to switching from $+P$ to $-P$ due to a $-V_P, t_P$ write pulse. The times labeled at the bottom of the figure are variables in the protocols. The slew rates and hold times are fixed in a given measurement protocol, and listed along with the particular measurements.

The waveform starts with a bipolar trapezoidal reset pulse having a sufficient amplitude, V_R and $-V_R$ to ensure the FE completely switches between P_R and $-P_R$ state by the end of the pulse. The write pulse of magnitude V_P and duration t_P is then applied after a delay-before-write interval t_{D1} , which causes the FE to switch from the state of $-P_R$ to $P(V_P, t_P)$, and is followed by a delay-before-read interval t_{D2} . Delays are introduced after every slew interval to allow PMUs to settle. After the delay-before-read t_{D2} , the write pulse is followed by a unipolar double trapezoidal readout waveform having the same amplitude as the reset pulse.

The first trapezoidal readout pulse switches the FE back to the $-P_R$ state. The net areal charge moved during this pulse is the sum of the FE charge $P(V_P, t_P) - P_R$,

the integrated displacement current density $\int CdV/dt$, and the integrated leakage current density. The charge moved by the second trapezoid corresponds only to the latter two phenomenon; subtracting the charge moved in the two pulses gives the net FE charge switched by the (V_P, t_P) write pulse. Data is recorded only during the two readout pulses, with a sampling rate chosen to ensure >1000 data points in each readout pulse. The measured currents in both the readout pulses are multiplied by the timestamp differences reported by the Keithley PMU and added to yield the charge moved in each readout pulse. The charge moved in the second readout pulse is then subtracted from the charge moved in the first readout pulse to give the net FE charge switched by the (V_P, t_P) write pulse. Both the pulse widths and amplitudes are varied to generate the polarization reversal characteristics. The maximum applied pulse voltage is taken to be V_R , and the reset duration t_R is chosen for a particular sample so that a (V_R, t_R) pulse substantially switches the FE from $-P_R$ to $+P_R$. The write pulse amplitudes and durations $V_P < V_R$ and t_P are then chosen to explore a wide range of partial polarizations from small to substantially switched states. Typically, pulse widths are varied by 5 orders of magnitude and V_P is varied linearly from 0 to $\pm V_R$. The entire measurement is repeated three times to characterize any run-to-run variations.

In the measurement protocol of Fig. 3.2, if the upper waveform is immediately followed by the lower waveform, the integral of the upper and lower voltage waveforms is zero. We call this a strictly symmetric waveform, and it assures there is no waveform-induced polarization bias per cycle. This strictly symmetric measurement protocol applies complementary positive and negative waveforms in every cycle so that no preference is given to one polarization direction. This is then repeated for different V_P, t_P write pulses to obtain the polarization reversal characteristics. In contrast, it is possible to make this same polarization reversal measurement by simply repeating the upper waveform in Fig. 3.2(a) to obtain all of the positive V_P, t_P

characteristics, and then the lower waveform for all the negative V_P, t_P polarity pulses to characterize the partial polarization. The asymmetric measurement protocol was used in published measurements of polarization reversal in HZO capacitors in early work of this thesis [19, 24, 41, 42], before the impact of using the strictly symmetric measurement protocol [40] was demonstrated.

3.2 Polarization reversal in hafnium zirconate (HZO)

3.2.1 Polarization reversal in W/HZO/W and TiN/HZO/TiN capacitors

Alessandri and Pandey [24] showed the first extraction of NLS parameters from polarization reversal characteristics of HZO capacitors. The NLS fitting and parameter extraction was carried out by fitting Eq. 2.5 to the measurements using a least squares fitting procedure. The accuracy of the NLS fits confirmed polarization reversal in HZO capacitors to be nucleation-limited by a minimum nucleation time constant of ~ 100 ns under applied electric fields < 2.5 MV/cm. Subsequent research by Alessandri and Pandey [39, 41] used the extracted NLS parameters to develop the first FE switching model that could accurately predict the FE response to an arbitrary applied waveform without needing additional fitting parameters, further highlighting the applicability of the NLS theory to polarization reversal in HZO. In these publications, the same set of NLS parameters accurately captured the FE polarization reversal from $-P_R$ to $+P_R$ and from $+P_R$ to $-P_R$. However, HZO capacitors fabricated for a subsequent study exhibited asymmetric polarization reversal from $-P_R$ to $+P_R$ and from $+P_R$ to $-P_R$, as is described in this section.

Measurements were made on FE HZO capacitors fabricated in an Oxford FlexAL ALD via Plasma Enhanced ALD (PE-ALD) at 300 °C and annealed at 500 °C, with both W and TiN as top and bottom electrodes, and an FE thickness of 10 nm, the cross section of which is shown in Fig. 3.3. The traveler describing the capacitors'

fabrication is attached in Appendix G.

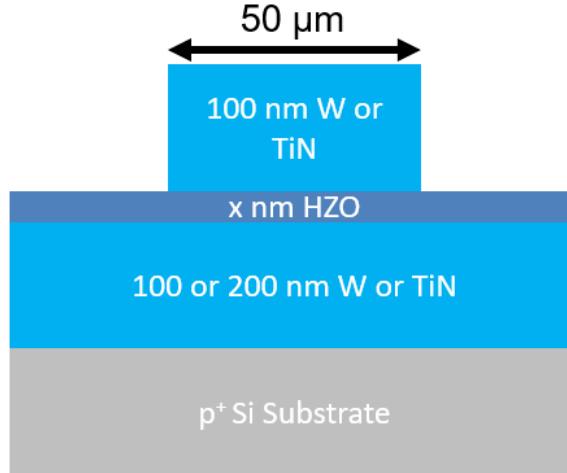


Figure 3.3. Cross section of the measured HZO MFM capacitors.

The asymmetric pulsed measurement protocol with timing parameters in Fig. 3.4 was applied to HZO MFM capacitors to obtain their polarization reversal characteristics. For these measurements, the reset, write, and read waveforms were set up as separate waveforms in the Keithley PMU; the delay-before-read and delay-before-write therefore corresponds to the time taken by the Keithley PMU to switch from one waveform to another, and are not fixed in these measurements. During this measurement, the pulse duration t_P was stepped logarithmically from 200 ns to 1 ms for a given pulse amplitude V_P , after which the pulse amplitude V_P was stepped in 0.1 V increments from 0.1 V to 2 V for the W/HZO capacitors, and from 0.1 V to 2.5 V for the TiN/HZO capacitors.

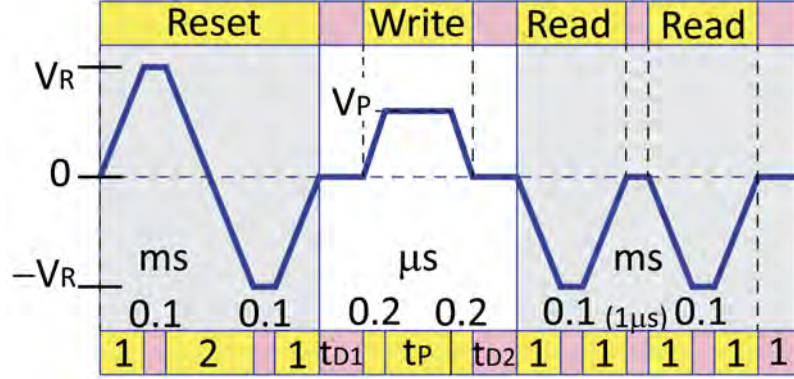


Figure 3.4. Measurement protocol used to characterize polarization reversal in W/HZO and TiN/HZO capacitors, with timing parameters. The pulse amplitude and duration V_P , t_P are varied; the delays t_{D1} and t_{D2} are introduced by the Keithley PMU and are not fixed for this measurement.

The measured polarization reversal characteristics of the W/HZO/W capacitor for write pulses with positive and negative polarity are shown with circular markers in Fig. 3.5(a) and (b), respectively. The polarization reversal measurements themselves indicate that the HZO shows stable, repeatable characteristics over the 3 runs, where each of the runs involves ~ 1000 cycles. However, the polarization reversal characteristics for positive and negative write pulse polarities could not be fitted to a single set of NLS parameters. The two different sets of extracted NLS parameters for positive and negative write polarities are listed in Table 3.1. Note that in Alessandri and Pandey 2018 [24], a single set of NLS parameters were able to capture the polarization reversal for both positive and negative write pulse polarities in W/HZO/W capacitors; these parameters are also listed in Table 3.1. Fitting the polarization reversal characteristics separately yielded the fits shown as solid lines in Fig. 3.5. General agreement of the fitted NLS model over 4 orders of magnitude of pulse width is apparent.

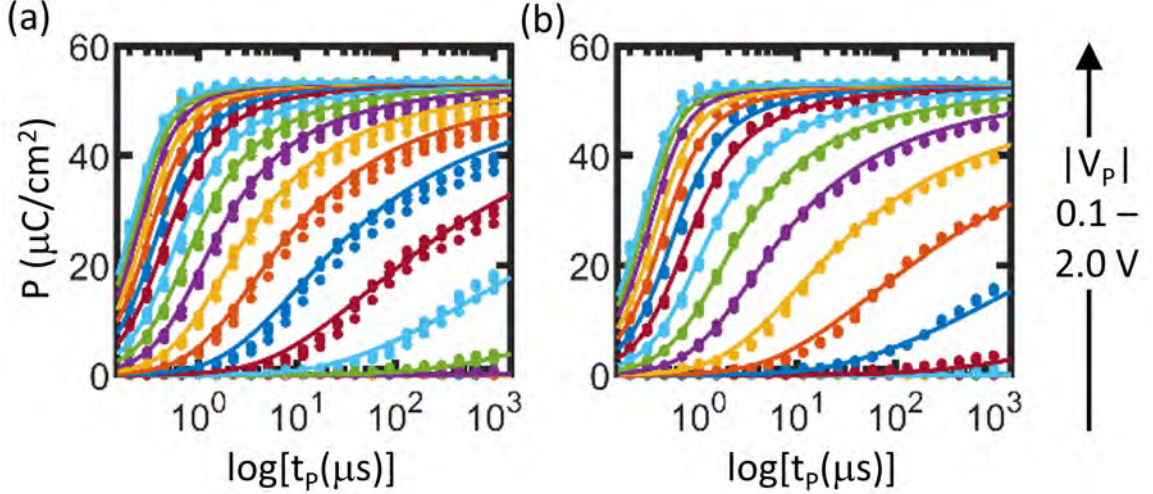


Figure 3.5. Measured polarization reversal characteristics (3 runs) and NLS fits for W/HZO/W capacitor grown via PE-ALD in the Oxford FlexAL ALD and annealed at 500 °C from (a) $-P_R$ to $+P_R$, and (b) $+P_R$ to $-P_R$.

The extracted minimum nucleation time constant for positive and negative polarization reversal characteristics in Fig. 3.5 were 112 and 164 ns, respectively. The extracted distributions of activation voltages are plotted in Fig. 3.6, with the solid and dashed lines corresponding to positive and negative write pulse polarities, respectively. Figure 3.6 also shows the activation field distribution of W/HZO/W capacitors studied in Alessandri and Pandey 2018 [24]. The mean (standard deviation) of the activation field distribution was found to be 1.87 V (0.51 V) and 1.72 V (0.33 V) for positive and negative pulse polarities, respectively. The observed difference in the NLS parameters for positive and negative polarization reversal characteristics can plausibly be attributed to structural differences in the top and bottom W/HZO interfaces. Differences in surface roughness between the two W/HZO interfaces can lead to a differences in the internal field experienced in the HZO layer for the same applied external field, thereby modifying the nucleation dynamics and introducing

asymmetry in the polarization reversal characteristics. Alternately, if nucleation is stabilized by defects or mobile ions, a difference in defect or ionic density at the two W/HZO interfaces can also affect the nucleation dynamics and lead to asymmetric polarization reversal characteristics.

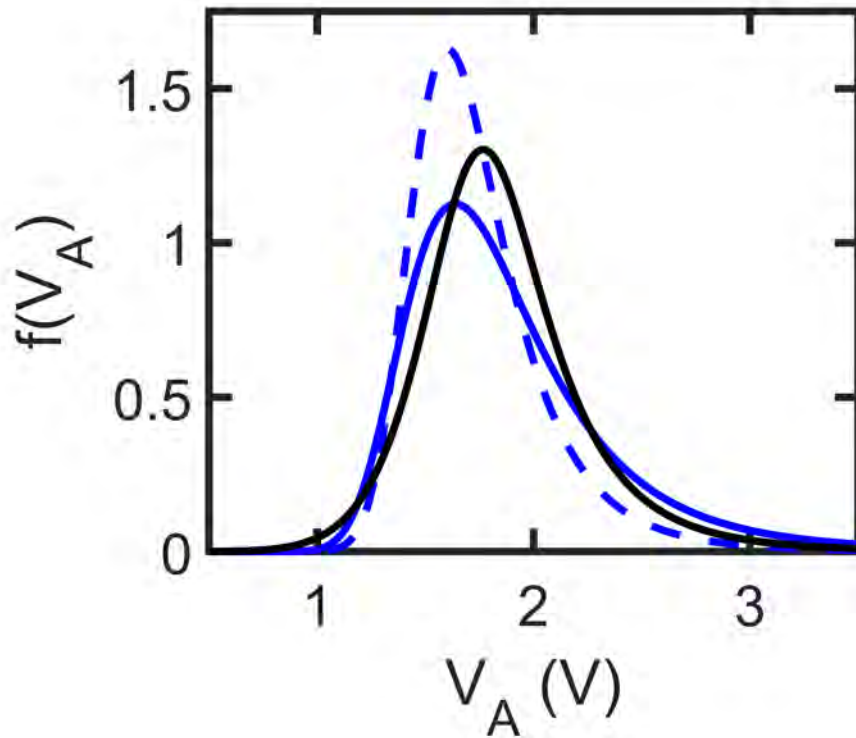


Figure 3.6. Extracted activation voltage distribution from NLS fits for W/HZO/W capacitors studied in Pandey 2019 [42] with 10 nm HZO grown via PE-ALD, annealed at 500°C, for $-P_R$ to $+P_R$ (solid blue line), and $+P_R$ to $-P_R$ (dashed blue line). The activation voltage distribution from NLS fits for W/HZO/W capacitors studied in Alessandri and Pandey 2018 [24] for both polarities of polarization reversal (solid black line).

Parameter	W/HZO [41], $\pm P_R$ to $\mp P_R$	W/HZO [42], $-P_R$ to $+P_R$	W/HZO [42], $+P_R$ to $-P_R$
P_R ($\mu\text{C}/\text{cm}^2$)	22.9	26.6	26.5
τ_∞ (ns)	387	112	164
α	4.11	2.36	3.39
β	2.07	1.83	1.74
a	12.1	4.78	7.96
b	1.79	1.17	1.38
p	0.691	7.73	3.88
q	0.633	1.29	1.03

TABLE 3.1

EXTRACTED NLS PARAMETERS OF W/HZO/W CAPACITORS
STUDIED IN ALESSANDRI AND PANDEY 2018 [41] AND PANDEY
2019 [42].

The remanent polarization and threshold voltage of HZO capacitors have previously been shown to depend on the electrode materials [16, 59]. Using a sputtered W top and bottom electrode instead of a sputtered TiN top and bottom electrode was shown to increase the P_R of ALD HZO from 5 to 10 $\mu\text{C}/\text{cm}^2$ in Karbasian 2017 [59]. Therefore, TiN/HZO/TiN capacitors were also fabricated via PE-ALD along with W/HZO/W capacitors to investigate the effects of electrode material on polarization reversal characteristics. The TiN/HZO/TiN capacitors exhibited more asymmetry than the W/HZO/W capacitors in polarization reversal behavior between

positive and negative write polarities. Figure 3.7 shows the measured polarization reversal characteristics, which do not reach a saturated polarization as the pulse duration is increased. The TiN/HZO/TiN capacitors were measured with a higher V_R than the W/HZO/W capacitors to investigate whether the unsaturation was due to the reset voltage being insufficient to substantially switch the FE. The extent of unsaturation as well as the maximum measured FE polarization are different for positive and negative write pulse polarities, plotted in Fig. 3.7(a) and (b), respectively. Due to the observed unsaturation, NLS fitting was not carried out on the measured TiN/HZO/TiN polarization reversal characteristics. Further investigation, reported in Pandey 2020 [40], revealed that the observed unsaturation can also arise due to the population and depopulation of interfacial traps, or motion of mobile ionic charges.

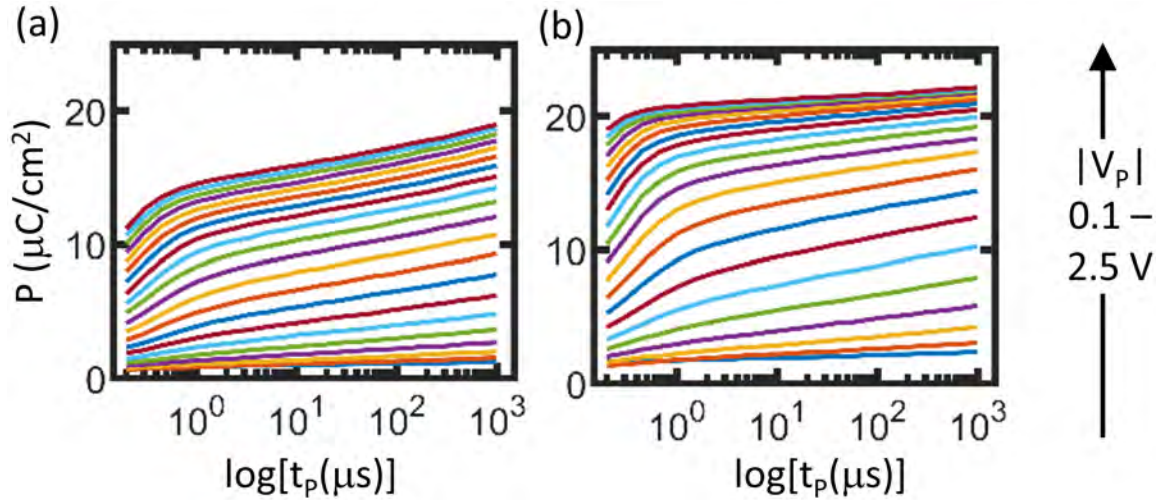


Figure 3.7. Measured polarization reversal characteristics of TiN/HZO/TiN capacitors grown via PE-ALD in the Oxford FlexAL ALD and annealed at 500 °C from (a) $-P_R$ to $+P_R$, and (b) $+P_R$ to $-P_R$.

3.3 Asymmetric versus symmetric pulsing

In addition to the wake-up effect, additional history dependence in FE polarization reversal was reported to be introduced by the measurement protocol itself in Pandey 2020 [40]. To investigate the cause behind the unsaturated polarization reversal characteristics in TiN/HZO/TiN capacitors shown in Fig. 3.7, polarization reversal in TiN/HZO/TiN capacitors was measured using both a strictly symmetric and an asymmetric measurement protocol with timing parameters shown in Fig. 3.8. If the reset were effective in always returning the FE to the same state, then the results of the symmetric and asymmetric protocols would be the same. However, polarization reversal measurements on TiN/HZO/TiN capacitors, shown in Figs. 3.8(b) and (c) show significant differences in the polarization reversal characteristics. Both measurements used a reset voltage of ± 3.5 V and write pulse amplitudes were stepped from 0.1 V to ± 3.5 V with a step of 0.2 V. Under the asymmetric pulse protocol, Fig. 3.8(b), the polarization did not saturate for positive write voltages, but showed saturation for negative write voltages; while using the symmetric pulsing protocol, Fig. 3.8(c), improved saturation was exhibited for both write polarities. These results were not related to wake-up or fatigue in the FE, since all the three repeats plotted in Fig. 3.8 exhibited a reduction in unsaturation when measured using a strictly symmetric vs an asymmetric protocol.

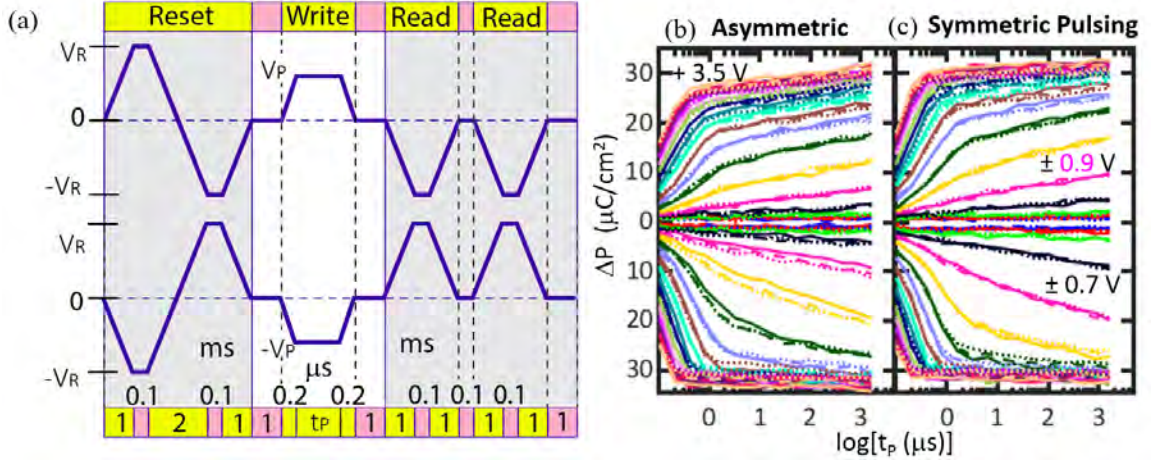


Figure 3.8. (a) Measurement protocol for polarization reversal characterization of FE capacitors, along with timing parameters used. Measured polarization reversal ΔP vs. pulse width t_P and pulse amplitude V_P in TiN/HZO capacitors, with each measurement repeated thrice; the first, second, and third runs are plotted with solid, dashed, and dotted lines, respectively. (b) TiN/HZO capacitor tested using an asymmetric pulse protocol and (c) using a strictly symmetric protocol.

An accumulation of ionic or trap charges at the metal/HZO interfaces can account for the observed unsaturation under asymmetric pulsing, and its reduction under symmetric pulsing. As the positive write voltages are incremented in sequence, the FE capacitor experiences negative voltages for a longer duration than positive voltages (due to the double pulse read). This causes charge, ionic or electronic, to accumulate at the electrodes. This charge is of opposite sign to the FE polarization charge switched by the write pulse. This can have two effects. First, this interfacial charge modifies the internal field of the HZO, thereby affecting the activation field. Secondly, the accumulated charge has its own time dependence and does not necessarily return to the same initial condition during the reset. This accumulated charge introduces a history dependence in the polarization switching, causing more charge

to be switched by the write pulse in the asymmetric protocol, leading to unsaturated polarization reversal characteristics. The asymmetry in the polarization saturation between different write pulse polarities shown in Fig. 3.8(b) suggests differences in the accumulated charge density at the two electrodes due to differences in the electronic properties of these two interfaces.

It is not a general property of HZO polarization reversal characteristics to exhibit a dependence on asymmetric vs. symmetric programming. To show this, the W/HZO/W capacitor was tested using the asymmetric pulse protocol, Fig. 3.5, as well as with the symmetric pulse protocol, Fig. 3.9(a). The symmetric and asymmetric measurements were carried out on different devices, precluding a direct comparison; however, no significant differences in saturation of the polarization reversal characteristics were observed between the two test methods. This is plausibly explained by the lower density of ionic/trap charges in W/HZO/W as compared to TiN/HZO/TiN capacitors. The observed electrode dependence is consistent with Karbasian [59], who reported a higher concentration of charged oxygen vacancies in the sputtered TiN/ALD HZO system compared to sputtered W/ALD HZO, attributed to the diffusion of N atoms into the HZO.

3.4 Polarization reversal in HZO versus lead-zirconium-titanate (PZT)

Polarization reversal characteristics of PZT FEs supplied by Texas Instruments. The aim of this comparison, carried out in collaboration with Texas Instruments, was to analyze whether the fundamental switching behavior, including the observed history dependence, remains the same in both FEs.

The strictly symmetric measurement protocol was used with timing parameters shown in Fig. 3.8(a). The PZT capacitors with thicknesses of 65, 59, and 52 nm (PZT1, PZT2, and PZT3) were deposited by metal organic chemical vapor deposition (MOCVD) in Texas Instrument's production, five-level Cu metallization 130

nm FRAM process [27] with Ir/IrOx electrode thicknesses of 60 nm. The total capacitor area was $400 \mu\text{m}^2$ consisting of four $10 \times 10 \mu\text{m}^2$ capacitors in parallel using Cu metallization in a standard production test structure. In this process, switched polarization density was previously shown to be independent of capacitor area in the range from 0.1 to $100 \mu\text{m}^2$ [29]. For the measurements in this section, the pulse duration t_P was stepped logarithmically from 200 ns to 2.5 ms, after which the pulse amplitude V_P was stepped from 0.2 V for the W/HZO and PZT1, and 0.1 V for PZT2 and PZT3, to the reset voltage V_R in 0.2 V increments. Measurements for both were initiated after a wake-up of 3000 cycles of 250 Hz triangular waves. The capacitor physical parameters and reset voltages are summarized in Table 3.2.

Wafer	Stack	t_{FE} (nm)	Area (μm^2)	V_R (V)
HZO1	W/HZO/W	10	1964	2
PZT1	Ir/PZT/Ir	65	400	2
PZT2	Ir/PZT/Ir	59	400	1.5
PZT3	Ir/PZT/Ir	52	400	1.3

TABLE 3.2

DESCRIPTION OF TESTED FE CAPACITORS, WITH FE LAYER THICKNESS t_R AND RESET VOLTAGE V_R . TABLE FROM PANDEY

2020 [40]

Figure 3.9(a) shows the measured polarization reversal in W/HZO, and Figs. 3.9(b-d) showing PZT with thicknesses 65, 59, and 52 nm, respectively. For the W/HZO sample, the minimum nucleation time constant was extracted in Pandey 2019 [42] as 112 and 183 ns for positive and negative write pulse polarities, respectively.

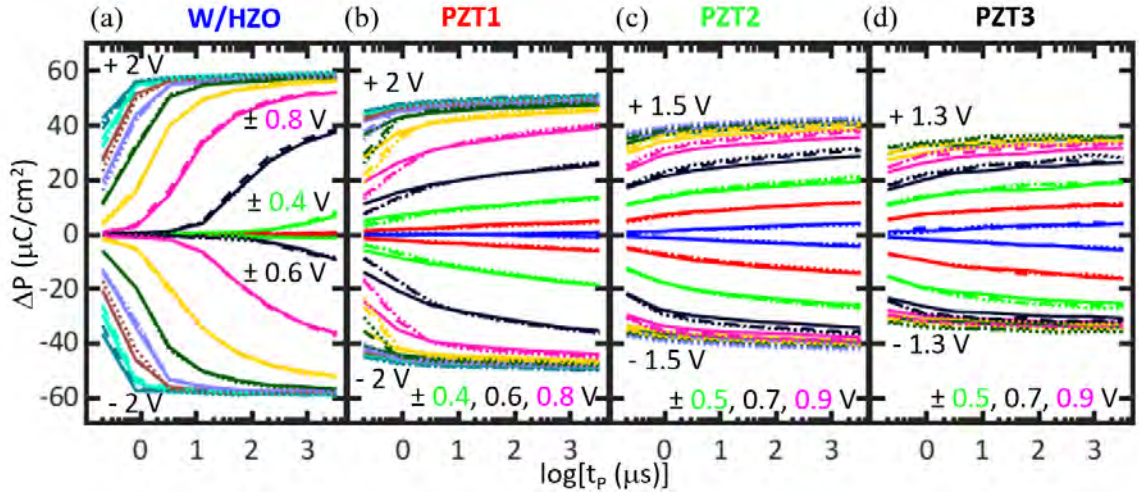


Figure 3.9. Measured polarization reversal ΔP vs. pulse width t_P and pulse amplitude V_P in HZO and PZT capacitors, with each measurement repeated thrice; the first, second, and third runs are plotted with solid, dashed, and dotted lines, respectively. (a) Measured ΔP - V_P , t_P characteristics of W/HZO capacitor and (b-d) PZT capacitors, measured using the symmetric protocol.

When PZT and HZO polarization reversal characteristics in Fig. 3.9 are compared for the same pulse amplitude and duration, the PZT partial polarization is a greater percentage of its remanent polarization than the HZO, indicating that PZT is clearly faster than the HZO. PZT-based FRAM have been demonstrated having access/cycle times of 30-35 ns, with PZT switching in less than 5 ns [60]. This difference in

the switching speeds of HZO and PZT is not related to RC instrumentation delay; the capacitance of the PZT capacitors is only $\sim 3x$ lower than the HZO capacitors, whereas the PZT switches $>50x$ faster than the HZO when switched at the same voltage. The difference in speed is reasonably associated with the lower coercive field in PZT as compared to HZO. There was insufficient data to fit the PZT polarization reversal characteristics to the NLS model since substantial switching occurred in the PZT capacitors even for the smallest applied write pulse duration of 200 ns.

The net charge switched is greater in HZO1 than in PZT1 which is not out of the ordinary: for HZO1 $P_R = 29 \mu\text{C}/\text{cm}^2$ and for PZT1 with a thickness of 65 nm, $24 \mu\text{C}/\text{cm}^2$. The HZO1 film, Fig. 3.9(a), shows significantly more switched-polarization asymmetry at sub-saturation voltages than PZT, Figs. 3.9(b-d). In HZO, this is again likely due to structural asymmetry in the metal-FE electrodes arising from differences in FE-on-metal and metal-on-FE deposition during the capacitor fabrication. The better symmetry of the PZT capacitor may be related to the maturity of the process and not any intrinsic difference in PZT vs. HZO.

CHAPTER 4

DYNAMICS IN SETTING OF PARTIAL POLARIZATION

Previous reports characterizing the partial polarization dynamics of FE capacitors explore a range of write pulse voltages and durations [18, 31, 61]. However, in Pandey 2020 [40], a surprising dependence of the FE partial polarization on the reset conditions and delay-before-write was reported. These measurements, made using strictly symmetric pulsing protocols, revealed an additional source of history dependence unrelated to the ionic/trap charging leading to unsaturated polarization reversal under asymmetric pulsing. This history dependence was quantified for the first time, and a qualitative explanation was provided, attributing the observed effects to the dynamics of subcritical nuclei in the NLS model of polarization reversal. This chapter discusses the observed dependencies of FE partial polarization on the different delays in the programming pulse; the paper [40] is attached as Appendix F.

4.1 Dynamics of delay-before-read

As discussed in Sec. 2.2, an FE having a finite capacitance in series, such as a semiconductor capacitance, experiences a depolarization field [45]. When the depolarization field is substituted for the applied field in the NLS model, the depolarization field causes the FE partial polarization to eventually ($t \rightarrow \infty$) decay to a state of zero net polarization with a time constant given by t_{EDep} in Eq. 2.14. From Eq. 2.13, it can be seen that the depolarization field in an FE capacitor is reduced if the electrode capacitance C_S is much higher than the FE geometric capacitance C_F , leading to a higher t_{EDep} and greater retention. The electrode capacitance may be due to

an interfacial oxide at the metal/FE interface of MFM capacitors, or a semiconductor or a dielectric in series with the FE. The dependence of the FE polarization on the delay-before-read is used to quantify the retention of partially polarized states in MFM capacitors. This measurement protocol designed to study retention in FE capacitors, is also applicable to FeFETs.

The objective of this measurement is to quantify the relaxation of the FE partial polarization set by a V_P, t_P write pulse. The double trapezoidal readout waveform in Fig. 4.1 measures the FE polarization at the end of the delay-before-read t_{D2} . Therefore, if the FE partial polarization decreases after being set by the write pulse, the extent of the decrease can be quantified by observing the change in the polarization measured by the readout waveform as the delay-before-read t_{D2} is increased.

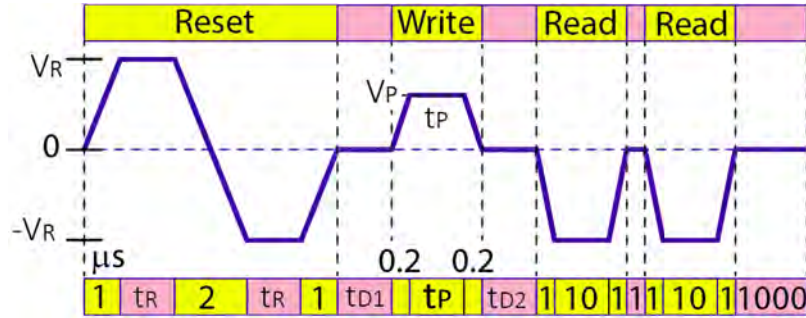


Figure 4.1. Symmetric pulse protocol (positive branch) with timing parameters, which is immediately followed by its negative, used to measure the dependence of FE polarization on delay-before-write and delay-before-read. Figure from Pandey 2020 [40].

The symmetric measurement protocol used to measure the effects of delay-before-read t_{D2} , along with all the timing parameters used, is shown in Fig. 4.1, and the

delay-before-write t_{D1} is kept fixed at $1 \mu\text{s}$. In this measurement, all the timing parameters are fixed and the delay-before-read t_{D2} is stepped in 4x increments from $1 \mu\text{s}$ to 262.144 ms . The measurements are made on the HZO and PZT capacitors discussed in Sections 3.2.1 and 3.4, respectively. A summary of the tested FE capacitors, with FE thickness and reset voltage, is shown in Table 4.1.

Wafer	Stack	t_{FE} (nm)	Area (μm^2)	V_R (V)
HZO1	W/HZO/W	10	1964	2
PZT1	Ir/PZT/Ir	65	400	2
PZT2	Ir/PZT/Ir	59	400	1.5
PZT3	Ir/PZT/Ir	52	400	1.3

TABLE 4.1

DESCRIPTION OF TESTED FE CAPACITORS, WITH FE LAYER THICKNESS t_{FE} AND RESET VOLTAGE V_R

The FE polarization set by a $1 \mu\text{s}$ (HZO) and $10 \mu\text{s}$ (PZT) write pulse is plotted with respect to the delay-before-read t_{D2} in Fig. 4.2(a) for HZO and in Fig. 4.2(b) for PZT1 for three repeats. The different applied write pulse duration for HZO and PZT was due to an error in setting up the measurement; however this does not affect the conclusion. As can be seen in Figs. 4.2(a) and (b), the FE polarization is independent of delay-before-read for all write amplitudes.

The PZT measurements show an apparently greater fluctuation in the polarization charge density with delay-before-read, Fig. 4.2(b) compared to the HZO in Fig. 4.2(a). This is a consequence of the fact that the capacitor areas tested for PZT are 5x smaller than the HZO capacitor so that fluctuations in the polarization charge are amplified by 5x when the polarization charge is divided by the area to give the polarization charge density.

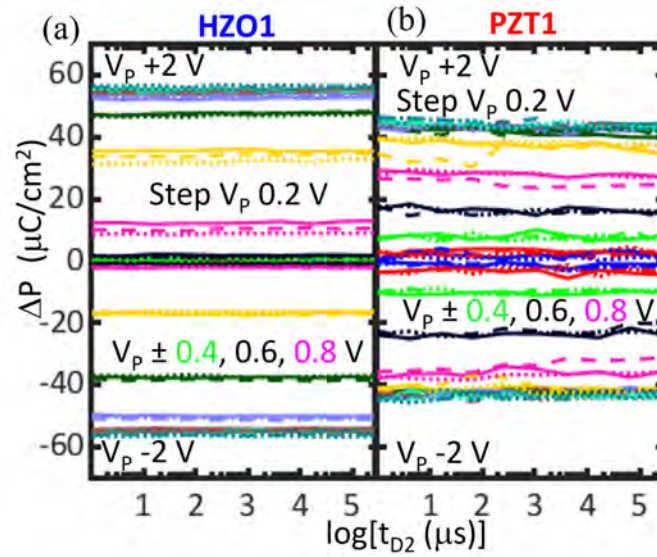


Figure 4.2. (a) Measured polarization reversal in HZO1 vs. delay-before-read at $t_P = 1 \mu\text{s}$, $t_R = 10 \mu\text{s}$, and $t_{D1} = 1 \mu\text{s}$. (b) Measured polarization reversal in PZT1 vs. delay-before-read at $t_P = 10 \mu\text{s}$, $t_R = 10 \mu\text{s}$, and $t_{D1} = 1 \mu\text{s}$. Figure from Pandey 2020 [40].

An upper bound on the stability of the FE partial polarization can be estimated from the current measurement resolution of the measurement. Based on the specifications for the Keithley 4225-PMU, the current resolution is 0.5%; since the charge is obtained by subtracting currents in the readout pulses, the charge resolution is

approximately 1% of the remanent polarization. Therefore, once set, the partially polarized states in both HZO and PZT are stable in that they decay less than 1% of their full remanent polarization for delays t_{D2} up to 262 ms.

4.2 Dynamics of delay-before-write

After it was established that the FE partial polarization does not decay as the delay-before-read is increased, the dependence of the polarization set by the write pulse on the delay-before-write was studied. This ensured that any observed variations in FE polarization due to delay-before-write were not due to change of the FE polarization between the reset waveform and the write pulse.

A symmetric measurement protocol was once again utilized to analyze the dependence of the polarization on the delay-before-write t_{D1} . The measurement waveform and timing parameters are in Fig. 4.1, and the delay-before-read t_{D2} was kept fixed at 1 μ s.

Polarization switched by a 10 μ s write pulse as a function of delay-before-write t_{D1} is shown for three different t_{RS} in Figs. 4.3(a-c) for HZO, and for $t_R = 10 \mu$ s for PZT1 in Fig. 4.3(d). Three measurement repeats are plotted in Figs. 4.3.

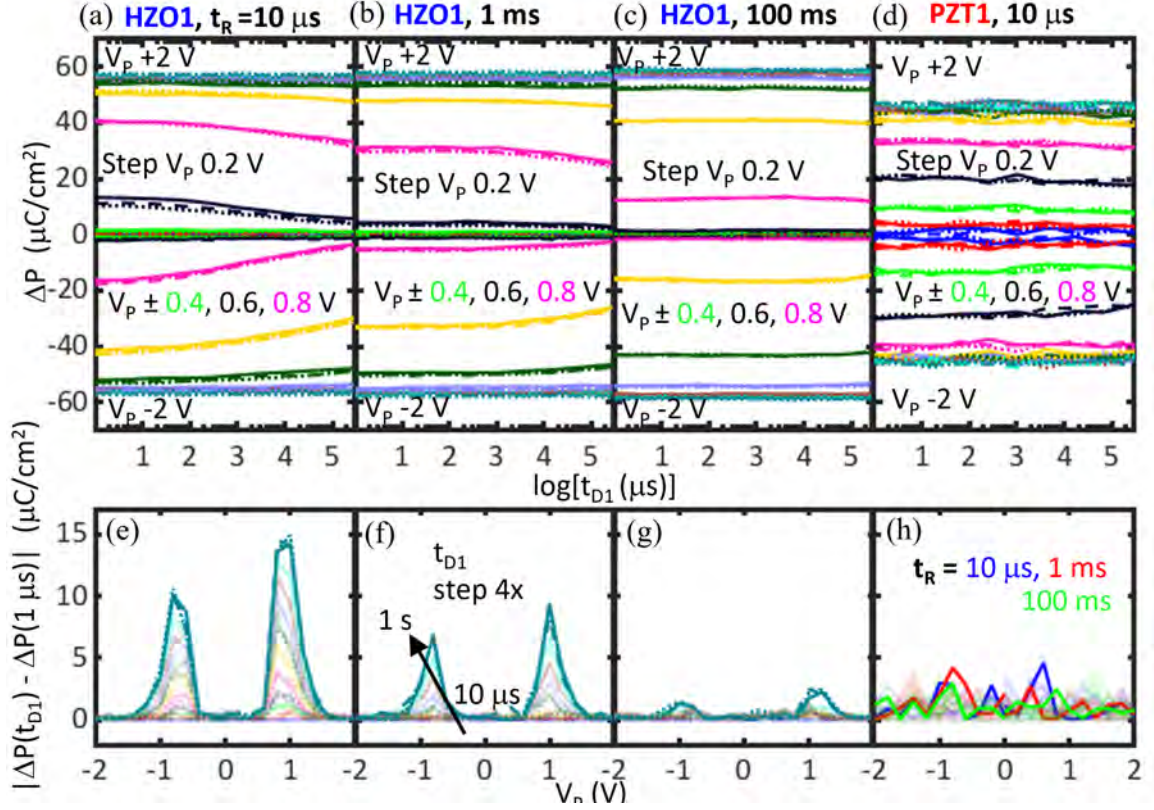


Figure 4.3. Measured polarization reversal vs. delay-before-write at $t_{D2} = 1\ \mu\text{s}$ and $t_P = 10\ \mu\text{s}$. In HZO, the measured partial polarization depends also on the reset time t_R , (a) $10\ \mu\text{s}$, (b) $1\ \text{ms}$, (c) $100\ \text{ms}$, while in (d) PZT1, $10\ \mu\text{s}$, there is no clear dependence on reset time. $|\Delta P(t_{D1}) - \Delta P(1\ \mu\text{s})|$ plotted vs. V_P in (e-g) corresponding to the measurements in (a-c). (h) For PZT, the results for all three $t_{R\text{s}}$ are summarized. Figure from Pandey 2020 [40].

The switched polarization in the vicinity of the coercive voltage decreases as the delay-before-write is increased from $1\ \mu\text{s}$ to $1.048576\ \text{s}$ in 4x increments, whereas the polarization is relatively constant for the FE in either of the two ($\pm P_R$) fully polarized states. The partial polarization change is indicative of a phenomenon inhibitory to FE switching that increases with time spent at zero bias, for write amplitudes V_P in the vicinity of the coercive voltage. This is more pronounced for HZO than PZT.

HZO ΔP vs t_{D1} is also found to depend on reset time as t_R is stepped from 10 μs to 1 ms to 100 ms, Fig. 4.3(a), (b), and (c), respectively. In these figures it is apparent that the switched polarization ΔP for the same write amplitude and delay-before-write decreases as the reset time is increased, again in the vicinity of the coercive voltage. As the duration of this reset pulse is increased, less FE polarization is switched. Therefore, the inhibitory mechanism that increases with time spent at zero bias (i.e. during t_{D1}) also increases with time spent at a bias of opposite polarity (i.e. during the t_R just preceding the write pulse). The repeatability of the measurements highlights that if the reset time, write delay, pulse amplitude, and pulse duration are fixed, the FE partial polarization can be set with precision.

To accentuate the delay-before-write dependence of the partial polarization on write pulse amplitude, we plot the difference in $|\Delta P(t_{D1}) - \Delta P(1 \mu\text{s})|$ vs. V_P and as t_{D1} is incremented in 4x steps from 1 μs to 1.048576 s, in Figs. 4.3(e-h). These plots show clearly that the strongest delay-before-write dependence occurs in the vicinity of the coercive voltage, or when the FE is partially polarized. The largest variation in HZO polarization due to delay-before-write can be seen to be 15 $\mu\text{C}/\text{cm}^2$, corresponding to $\sim 25\%$ of the $2P_R$. Furthermore, as the reset pulse width is increased from 10 μs in Fig. 4.3(e) to 100 ms in (g), the amplitude of the partial polarization difference decreases. For PZT all of the measurements can be summarized in a single plot, Fig. 4.3(h). While the largest variations are near the coercive voltages, there is no clear dependence on reset pulse width.

4.3 Dynamics of subcritical nuclei

The observed delay dependencies in partial polarization can be understood from the nucleation-limited-switching model described in Sec. 2.1 [39, 44]. Once a nucleus of the opposite orientation reaches a critical volume, it expands to switch the entire grain in a time short with respect to the nucleation time. Before reaching critical size,

a nucleus of subcritical size expands or contracts under the influence of an electric field, depending on the relative orientation of the field with respect to the nucleus. If the field is removed, a subcritical nucleus decays due to strain at its boundary, however these decaying nuclei can revert to a state of expansion by a subsequent write pulse [62, 63]. When the FE is pulsed, an FE grain having larger residual subcritical nuclei will switch with a higher probability than a grain with smaller subcritical nuclei. The expansion of a subcritical nucleus occurs slowly for a low electric field, while it occurs quickly for a high electric field. Therefore, it is for intermediate values of electric field, close to the mean FE activation field, that the influence of subcritical nuclei on partial polarization is most prominent.

A simple picture is provided in Fig. 4.4 to explain the dependence of delay-before-write and delay-before-read on partial polarization switching. This picture is a simple extension of the dynamics governing the formation of critical nuclei in an NLS framework, as discussed by Mulaosmanovic [62, 63]. Following the completion of a negative reset pulse at time 1 the polarization is substantially set to the $-P$ state (red), but there may exist a few unflipped $+P$ grains (blue). In each of the grains some subcritical nuclei are shown. These nuclei grow or decay with time depending on the electric field magnitude and polarity. When no voltage is applied, as between times 1 and 2 (delay-before-write) and times 3 and 4 (delay-before-read), the subcritical nuclei decrease in volume over time independent of their polarity. On the other hand when a positive voltage is applied, as during the write pulse, the $+P$ nuclei expand and $-P$ nuclei contract, and during the negative read pulses the opposite occurs.

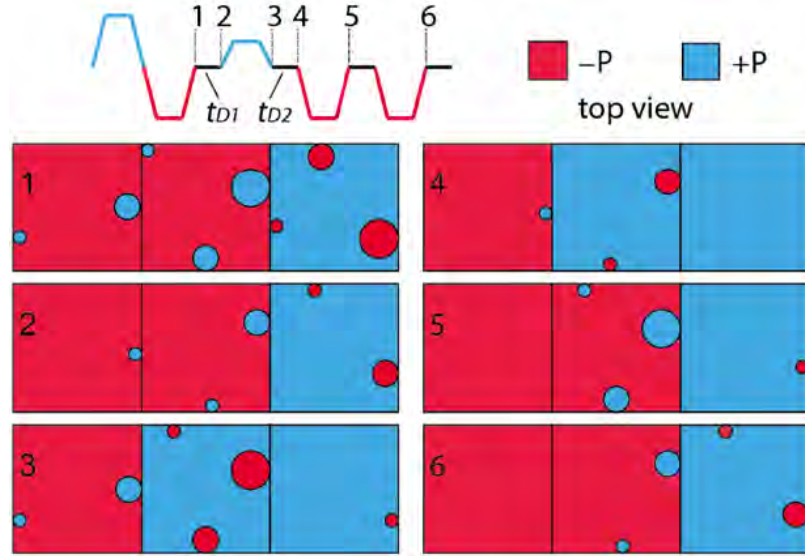


Figure 4.4. Partial-polarization measurement waveform and time evolution of the subcritical nuclei within the FE grains. Three grains are shown at each time point to schematically illustrate how the nuclei grow and decay with time. The left and middle grains represent the majority of the polycrystalline film after the negative reset pulse, while the right grain accounts for the fact that for a given reset pulse some small number of grains may remain unswitched. These minority grains still develop subcritical nuclei during the pulse sequence and evolve with an opposing polarity over time. Figure from Pandey 2020 [40].

The decrease in switched polarization with increasing delay-before-write can be understood by considering the time interval between 1 and 2 in Fig. 4.4. Each of the grains contain subcritical nuclei with opposing polarity; these nuclei reduce in size with increasing time spent at zero bias, i.e. during the delay-before-write t_{D1} . As a result, the switched polarization caused by longer delay-before-write in the range of the coercive voltage is reduced because there are fewer near-critical nuclei to enable the switching process.

For a fixed delay-before-write and write pulse amplitude, a lower FE polarization

is switched as the reset time t_R is increased. This can be explained by the reduction in volume of the subcritical nuclei as the reset pulse time is increased. Therefore, a longer reset time leads to smaller subcritical nuclei at time 1 itself, leading to smaller subcritical nuclei at time 2 before the write pulse, causing less grains to be switched. These effects are most prominent for write pulses with amplitudes close to the mean activation field.

As the measurements of Figs. 4.3(a-c) show, subcritical nuclei remain active for a remarkably long time, extending up to 1 s. Their effect on the switched FE grains (i.e. $\Delta P(t_{D1})$) decreases approximately as the logarithm of the delay-before-write time. This suggests the presence of processes opposing the decay of subcritical nuclei in the absence of any field; such processes may be due to interactions of the nuclei with interfaces or defect complexes, as well as thermal excitations. Comparing HZO and PZT, the latter does not show a significant delay-before-write dependence. This may simply be due to the PZT switching faster than the HZO, and therefore the delay-before-write in PZT being significant only for t_{D1} smaller than 1 μ s. More delay-before-write dependence might be expected in PZT if testing were to be conducted with shorter reset times; however, to fully saturate PZT, a reset time greater than 1 μ s is needed for the conditions evaluated in this study. The larger grain size and lower activation field (as opposed to activation voltage) in PZT may play a role in the quick decay of subcritical nuclei. In case the long decay time in HZO is primarily related to defects, this may indicate a lower defect density in PZT, since it is FE as-deposited via MOCVD, whereas the HZO requires a post-deposition recrystallisation anneal, which can then introduce defects.

The independence of switched polarization on delay-before-read can also be understood from Fig. 4.4. Since in this measurement the delay-before-write time is fixed, the condition at time interval 2 is fixed. As the delay-before-read is increased between interval 3 and 4, the sizes of the subcritical nuclei decrease. The negative

read pulse has an amplitude $-V_R$, which resets the grains switched during the write pulse, shown by the switching of the middle grain at time 5. This switching is independent of the size of the remaining nuclei which is consistent with the experimental observation.

The dependence of switched polarization on delay-before-write indicates that subcritical nuclei are generated, and that these nuclei enhance the charge switched in a subsequent write pulse. For short (10 μs), low voltage (0.1 V) write pulses, the subcritical nucleus volume is large, and yet no polarization change is detected in the delay-before-read measurements, Fig. 4.2(a). This fact can be used to infer a maximum size of the subcritical nuclei, whose volume must represent a charge which should be measurable unless it is below the system measurement limits. Based on the specifications for the Keithley 4225-PMU (pulse measurement unit), the current resolution is 0.5%, which means the charge resolution is approximately 1%. From this we can infer that the subcritical volume is less than 1% of the grain volume. For a cubic HZO grain with sides commensurate with the thickness of the film, the volume is 1000 nm^3 . This suggests a subcritical grain volume of approximately 10 nm^3 , or a 4x4x4 array of HZO unit cells. This volume represents approximately 0.29 $\mu\text{C}/\text{cm}^2$ of polarization charge when summed over all the FE grains in the 50 μm diameter capacitor. Remarkably, this small subcritical charge gives rise to measured polarization enhancement as large as $\sim 15 \mu\text{C}/\text{cm}^2$, Fig. 4.3(e), and represents a polarization gain of ~ 50 .

4.4 Implications for analog weight storage

The delay-before-read measurements establish that partially polarized states in an FE decay less than 1% of the FE P_R up to 250 ms. A lower bound on the time constant of FE decay can be estimated as $\tau = 24.9 \text{ s}$ by solving $e^{-0.25/\tau} = 0.99$. These results are for a symmetric MFM capacitor; as the conductivity of the materials surrounding

the FE reduces, the depolarization field in the FE would increase, Eq. 2.13, causing a reduction in retention as compared to the MFM capacitor. The delay-before-read measurement can be used to quantify the retention in such devices.

The observed dependence of the FE polarization set by a fixed V_P, t_P write pulse on both the delay-before-read and reset time has implications on pulsing protocols for setting the partial polarization, as well as limiting the number of partially polarized states that can be used for a given pulsing protocol. The quantitative limits on the number of states depend on the write pulse duration, amplitude, reset conditions, and delays between subsequent write pulses. In applications where the delays and reset times are fixed, the FE partial polarization can be repeatably set. However, for application in neural network training, especially using stochastic write pulses [35], the FE is not reset prior to setting the partially polarized state, and the delays between consecutive write pulses is not fixed. In this case the delay dependencies will need evaluation for the cycle times of the proposed system, and would limit the number of partially polarized states that can be used. These limits can be obtained by performing delay-before-write measurements with the delay-before-write being stepped from the minimum to the maximum expected delays in the stochastic pulsed schemes. The maximum observed variation in partial polarization with respect to the delay-before-write would then set the minimum spacing in partial polarization corresponding to one analog memory level.

In summary, since the programming pulse dependencies in setting the FE partial polarization can lead to a variation up to $\sim 25\%$ of the $2P_R$, the inclusion of these effects is crucial in design of analog memory, and for simulations evaluating the suitability of FE devices for analog memory and neural network acceleration.

CHAPTER 5

INTERNAL PHOTOEMISSION MEASUREMENT SYSTEM

IPE is a measurement method to obtain the relative band alignments of semiconductors/metals and dielectrics. The increased number of new materials being explored in the electronic devices community has led to the use of this method to obtain band alignments of high- κ dielectrics such as Al_2O_3 , HfO_2 , and ZrO_2 on Si [64], and 2D materials on SiO_2 [65]. An IPE system was configured at Notre Dame as part of this thesis to investigate the band alignments of HZO capacitors. This chapter introduces the principle and theory of the IPE measurement, and describes the components, optical path, and validation of the measurement system.

5.1 Measurement principle and theory

A comprehensive treatment of IPE physics is provided in the textbook by Afanas'ev [66]; the relevant details are summarized in this section. Internal photoemission is a spectroscopic photocurrent measurement applied to MOS structures. As shown in the inset of Fig. 5.1, in an IPE measurement, an electrode-insulator-electrode structure having a semi-transparent top electrode is illuminated with photons of a particular energy, and the resultant photocurrent is measured as a function of photon energy. The photocurrent is generated by the optical excitation of charge carriers within a source material, their transport to the interface due to an electric field, and their transport over this energy barrier to a conducting electrode where the current is measured, as shown in Fig. 5.1. The source material may be semi-transparent top electrode or the bottom semiconducting electrode.

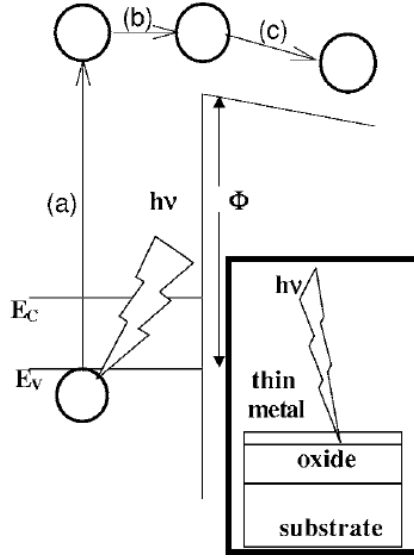


Figure 5.1. IPE measurements are performed by irradiating an electrode/dielectric/electrode structure having a semi-transparent top electrode with photons having a particular frequency, as shown in the inset. The resultant current occurs due to a combination of three processes - (a) optical excitation of a charge carrier within a material, (b) transport of the charge carrier to the potential barrier at the relevant interface due to an electric field, and (c) transport of the excited carrier over the interface.

Figure from Afanas'ev and Stesmans 2007 [64].

If the energy $h\nu$ of the incident photon is greater than the barrier height Φ , the quantum yield $Y(h\nu)$ of the entire process is modeled as [50, 64]

$$Y(h\nu) = A(h\nu - \Phi)^p, \quad (5.1)$$

where the coefficient p depends on the energy distribution of electrons $N_i(E)$ at a particular energy E in the energy band from which photoexcited carriers are generated. If $N_i(E)$ has the functional form of an impulse function, physically corresponding to photoemission from a very narrow filled band, then $p = 1$ [67]. If $N_i(E)$ has the func-

tional form of a step function, $p = 2$; this is a first approximation for photoemission from a metal at 0 K, with the step corresponding to the Fermi energy [67]. If $N_i(E)$ has a linear functional form, $p = 3$; experimental observations of vacuum photoemission from semiconductors indicate the electron energy distribution is approximately linear [67]. Experimentally, the quantum yield is determined by first measuring the photon energy dependent IPE current I_{IPE} as the difference of the current with and without irradiation, I_{TOT} and I_{DARK} , which is typically obtained by mechanically blocking the light source,

$$I_{IPE}(h\nu) = I_{TOT}(h\nu) - I_{DARK}. \quad (5.2)$$

The quantum yield is then defined as the ratio of the IPE current to the incident photon flux density $N_{PH}(h\nu)$, having the units of number of photons/cm²s,

$$Y(h\nu) = \frac{I_{IPE}(h\nu)}{N_{PH}(h\nu)}. \quad (5.3)$$

The photon flux density can in turn be calculated using the measured optical power $P(h\nu)$ and the beam diameter d as

$$N_{PH}(h\nu) = \frac{P(h\nu)/h\nu}{\pi d^2}. \quad (5.4)$$

Carrier transport occurs in the capacitor due to electric field, which may be due to a superposition of internal electric fields and electric fields due to an externally applied bias [64]. The measured IPE current is taken to be proportional to the quantum yield, and the barrier height Φ can then be obtained by fitting Eq. 5.1 to the measured yield.

5.2 Instrumentation

The essential elements of an IPE setup include a high intensity photon source, a monochromator to select photons with variable frequency/energy, an optical path allowing photons to irradiate the device under test (DUT), a voltage source, a current measurement instrument, and a calibrated photodetector. The complete block diagram of the setup is shown in Fig. 5.2. The manufacturer specifications of all the components are compiled in Appendix H.

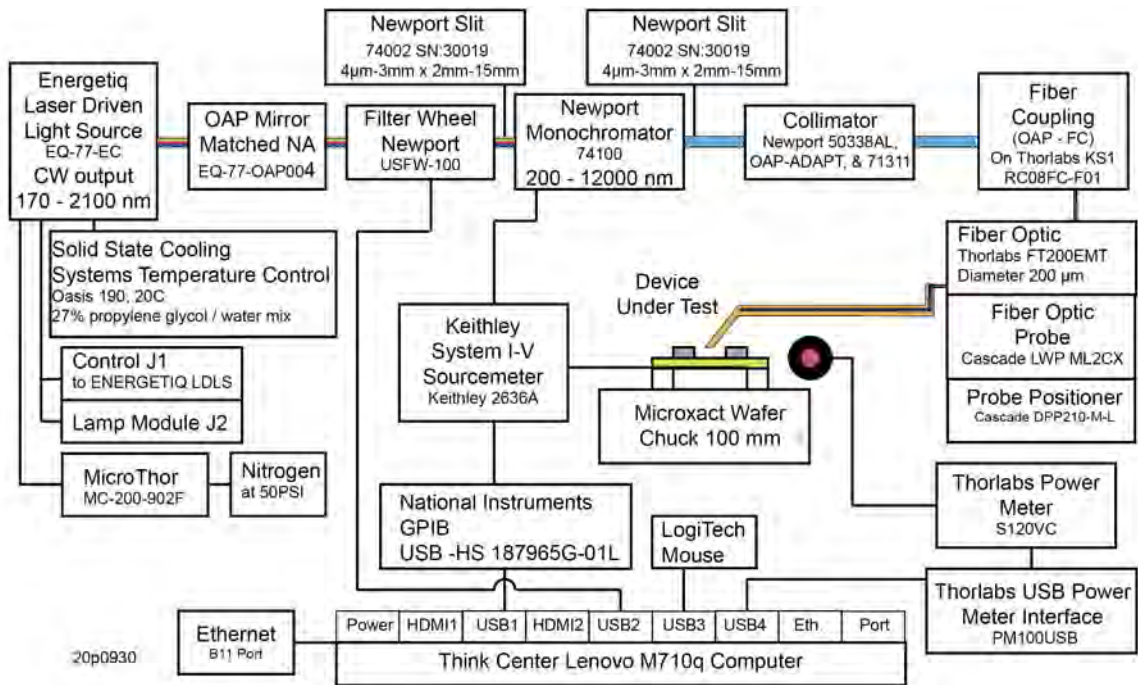


Figure 5.2. Block diagram of IPE setup configured at Notre Dame

5.2.1 Components and optical path

A high power laser driven light source (LDLS) from Energetiq, EQ-77-EC, having a broadband and stable output spectrum from 170 - 2100 nm (0.6 - 7 eV), and a spectral radiance of 100 mW/mm²/sr.nm at 400 nm, is used as the photon source. The broadband optical output is emitted by a confined (<150 μ m diameter) plasma that is optically excited by a 974 nm laser. Cooling water at 21 °C is circulated through the LDLS by a chiller; ultra-high purity (> 99.9999% purity) nitrogen, obtained by connecting an inline purifier to the house nitrogen supply, is circulated in the system to prevent the formation of ozone that is harmful to humans and can oxidize equipment. The wavelength dependent refractive indices of lenses cause deviations in alignment as the wavelength is varied. To avoid re-alignment for every wavelength, mirrors are used instead of lenses as optical components. Using geometry and the laws of reflection, it can be shown that spherical mirrors do not focus parallel rays to a single focal point; this is known as spherical aberration. Based on geometrical arguments, parabolic mirrors form the only shape that can focus a parallel beam of light to a single point, and are therefore used instead of spherical mirrors to minimize spherical aberrations [68].

The LDLS is coupled to the monochromator by imaging the confined plasma source at the input slit of the monochromator. This is accomplished by inserting a set of off-axis parabolic (OAP) mirrors having an effective focal length (EFL) of 4 inches, supplied by Energetiq, between the LDLS output and the monochromator input. The EFL is also referred to as the reflected focal length (RFL), and its relation to the actual, or parent focal length, of a parabolic mirror is depicted in the specifications attached in Appendix H. The EFL is chosen to maximize power throughput by ensuring that the LDLS output exactly fills the acceptance cone of the monochromator, a procedure known as Numerical Aperture (NA) matching [69].

The Newport 74100 monochromator utilizes diffraction gratings to cause disper-

sion in the broadband optical input. The monochromator contains three gratings, operating in the wavelength ranges 200-1400 nm, 875-2200 nm, and 2500-10000 nm. Only a specified wavelength band from the dispersed output is incident on the output slit of the monochromator, thereby yielding an output with a narrow wavelength linewidth. The output wavelength can be set by rotating the diffraction grating, thereby changing the wavelength that is incident at the output slit. The output slit of the monochromator has a reciprocal dispersion of 3 nm/mm, i.e. the output linewidth increases by 3 nm for every 1 mm that the output slit is opened, allowing a tradeoff between output power and linewidth.

In the dispersed output of the diffraction gratings, the 1st maxima of a given wavelength λ is coincident with the 2nd maxima of wavelength $\lambda/2$, and the n^{th} maxima of wavelength λ/n . Therefore, a filter wheel with three different long pass filters (in the wavelength domain) is placed between the OAP mirrors and the input of the monochromator to suppress higher order harmonics at the monochromator output by ensuring that when a beam of wavelength λ is required, there is insignificant input power with wavelength less than or equal to $\lambda/2$. Spectral responses of the 3 filters used for IPE measurements are attached in Appendix H.

The diverging optical beam exiting the monochromator is collimated using another OAP mirror with an Al(MgF₂) coating, having an EFL of 4 inches. The Al(MgF₂) coating minimizes optical power losses in the UV-region with respect to the uncoated aluminum surface of the mirror. The collimated beam is then coupled to an FC-terminated optic fiber using another parabolic mirror with a proprietary UV-enhanced aluminum coating. A high hydroxyl ion concentration (high-OH) multimode optic fiber with 200 μm diameter and 50 cm length is chosen to minimize optical losses in the UV region. The attenuation of the fiber with respect to wavelength is attached in Appendix H. The optic fiber is then passed through a Cascade light wave probe (LWP) mounted on a probe positioner with X, Y, and Z-axis mi-

cromanipulators. The X and Y axis micromanipulators are used to align the beam to the DUT. The Z axis micromanipulator is used to position the fiber tip in vertical proximity of the DUT. The fiber tip is flat-cut, and the LWP is angled at 9° , leading to a 9° angle of incidence on the DUT. The beam size is estimated by eye to be $\sim 500 \mu\text{m}$ at the DUT location.

The DUT is biased using the wafer chuck as one contact, and a probe connected to the top electrode as the other. The top probe is mounted on another probe positioner, and both the probe and the wafer chuck are connected to a Keithley Model 2636A sourcemeter to provide a voltage bias and measure the current. The DUT is placed on a MicroXact wafer chuck with 3-axis control, and all the probes are mounted on a stainless-steel platform.

The incident optical power is measured by replacing the DUT by a Thorlabs S120VC calibrated Si photodiode based optical power meter; in this way the spectral response of the system is determined. The power meter is individually calibrated with a NIST- or PTB-traceable certificate of calibration, and its calibration curve is attached in Appendix H. The power meter is recommended by ThorLabs to be annually recalibrated.

5.2.2 Control and data acquisition

For the IPE measurements, it is necessary to control the Newport monochromator, Newport filter wheel, Keithley sourcemeter, and Thorlabs power meter. The monochromator and sourcemeter are connected via a general purpose interface bus to universal serial bus (GPIB-to-USB) converter to the control computer, while the power meter and filter wheel are connected to the computer via USB ports. All the instruments are recognized by the computer by National Instruments (NI) drivers. Codes to write to and read from each individual instrument were written using the Instrument Control Toolbox of the MATLAB [70] computational software. These

control codes are attached in Appendix J.

The codes developed to set the monochromator wavelength require the desired wavelength and grating to be specified and can be implemented with the input shutter of the monochromator either open or closed. The monochromator may take up to 10 s for setting the wavelength; if the shutter is open during this period, the DUT is irradiated with light of wavelengths different from the desired wavelength while the grating is rotating to the desired setpoint. Therefore, in the IPE measurement code, the wavelength of the monochromator is first set with the shutter closed, after which the shutter is opened. The code includes a 10 s delay to account for the wavelength change and queries the monochromator regarding its set wavelength to confirm that the specified wavelength has been set before proceeding with the measurement.

The wavelength dependent responsivity of the Thorlabs optical power meter is stored in the Thorlabs USB Power Meter Interface connecting the power meter to the computer. Therefore, the codes developed to read the power detected by the power meter specify the incident wavelength. The wavelength returned upon querying the monochromator is input to the power meter as the incident wavelength.

The filter wheel can hold up to 6 filters; position 1 in the filter wheel is left empty to allow characterization of the system throughput without any filter. The wavelengths at which the filter wheel switches the filters is determined so that higher order harmonics are suppressed while minimizing discontinuities in the power vs wavelength spectrum. Therefore, filter 1 (i.e. no filter) is used for wavelengths 0-311 nm, filter 2 for wavelengths 311-600 nm, filter 3 for 600-1100 nm, and filter 4 for wavelengths greater than 1100nm.

Codes to interface with the Keithley sourcemeter are developed for two terminal measurements that apply a voltage and measure the current. The voltages can be specified as a linear sweep or as a list of voltages to be applied in a sequence. The former is used to measure the I-V characteristics of the DUT, whereas the latter

can be used to configure a pulse sequence as needed for setting and testing an FE capacitor.

Before performing an IPE measurement, the optical power at the DUT location is measured using the following steps.

1. Place Thorlabs power meter at DUT location.
2. Specify the start, end, step, and repeats of photon energy sweep.
3. Convert the photon energy sweep to a wavelength sweep.
4. Darken the room.
5. Set the monochromator to output the specified wavelength, with input shutter closed.
6. Query the monochromator to verify specified wavelength has been set.
7. Set the appropriate filter in the filter wheel for the set wavelength.
8. Open the monochromator input shutter.
9. Specify the incident wavelength to the power meter.
10. Read the optical power measured by the power meter.
11. Close the monochromator input shutter.
12. Step the monochromator wavelength.
13. Repeat steps 5-10 until complete.

The IPE measurement is obtained according to the following protocol.

1. Place the DUT on chuck and make electrical connections.

2. Set the monochromator wavelength to green (532 nm) with input shutter open.
3. Position LWP so that green colored fiber output is incident on DUT.
4. Close monochromator input shutter.
5. Darken the room.
6. Specify the start, end, step, and repeats of the photon energy sweep.
7. Convert the photon energy sweep to a wavelength sweep.
8. Set the monochromator to output the specified wavelength, with input shutter closed.
9. Query the monochromator to verify specified wavelength has been set.
10. Set the appropriate filter in the filter wheel for the set wavelength.
11. Apply a voltage bias or voltage pulse sequence to the DUT.
12. Measure the current in the DUT, I_{DARK} .
13. Remove voltage bias from the DUT.
14. Open the monochromator input shutter to illuminate the DUT.
15. Apply the same voltage bias or voltage pulse sequence to the DUT as step 11.
16. Measure the current in the DUT, I_{TOT} .
17. Remove voltage bias from the DUT.
18. Close the monochromator input shutter.

19. Step the monochromator wavelength.

20. Repeat steps 8-19 until complete.

In addition to the above procedure, every measurement is preceded by a calibration whereby the DUT is replaced by a calibrated optical power meter, measuring the spectral response at the device location.

5.3 Calibration and stability

Optical power at the location of the DUT in Fig. 5.2 was measured using the Thorlabs power meter over a period of 6 months, corresponding to calibrations preceding various measurements. A total of five measurements are plotted, the first in March 2020, the following three taken over a 5 day period in June, and the final measurement in September, 2020. The measurements of power with respect to wavelength are plotted in Fig. 5.3, from which a maximum deviation of 10% in optical power is observed over 6 months, and a maximum deviation of 5% in optical power is observed in the measurements taken over a 5 day period in June. This establishes the stability of the power output of the source.

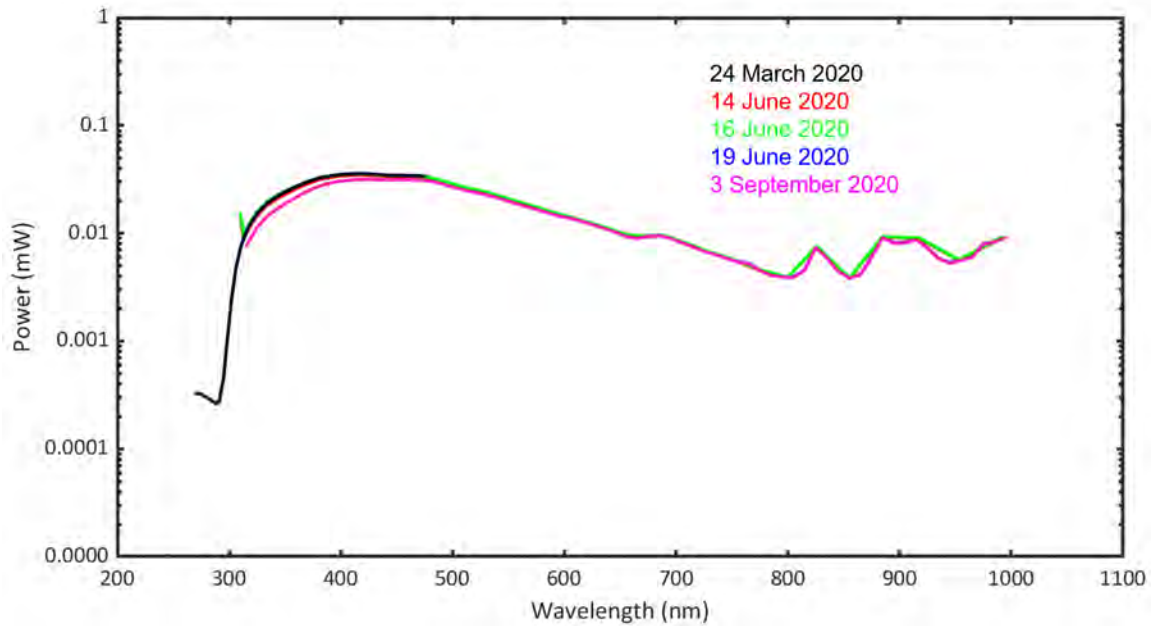


Figure 5.3. Five measurements, with dates listed, of optical power vs wavelength at the DUT location. Measurements were made over a period of six months using a calibrated Thorlabs power meter.

To verify the wavelength calibration, the beam exiting the monochromator was coupled to a Thorlabs CCS200 handheld spectrometer having an accuracy of <2 nm FWHM at 633 nm, with a wavelength range from 200 - 1000 nm. The spectral output of the monochromator was measured at different wavelengths, and the recorded spectra are plotted in Fig. 5.4. The spectral output is shifted by an additional 5 nm as compared to the specified wavelength throughout the tested spectral range. The reason for the non-Gaussian nature of the peaks is not known.

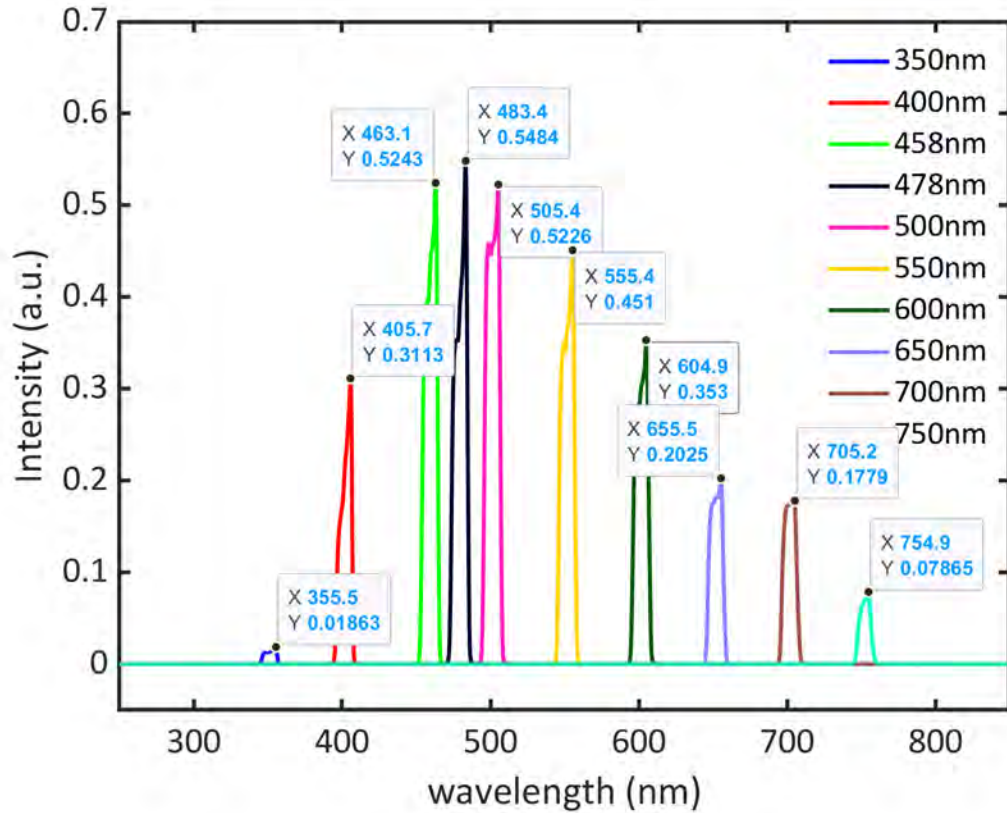


Figure 5.4. Output spectrum of the monochromator measured using a handheld spectrometer (Thorlabs CCS200) is plotted with the monochromator set at different wavelengths.

5.4 Flux density vs NIST

From Eq. 5.3, it can be seen that the IPE current in a given device increases if the photon flux density $N_{PH}(h\nu)$ is increased, if the yield is constant. Since the yield is dependent on the device, an experimental setup with a higher photon flux density would lead to a greater current, and hence an improved detection of photocurrent. Due to this, the photon flux density is an important metric quantifying the capability of an IPE setup. The measured photon flux densities of the IPE setup at Notre Dame

and at NIST, Gaithersburg [71] are compared in Fig. 5.5, which shows the IPE setup at Notre Dame having 800-1800x greater photon flux density.

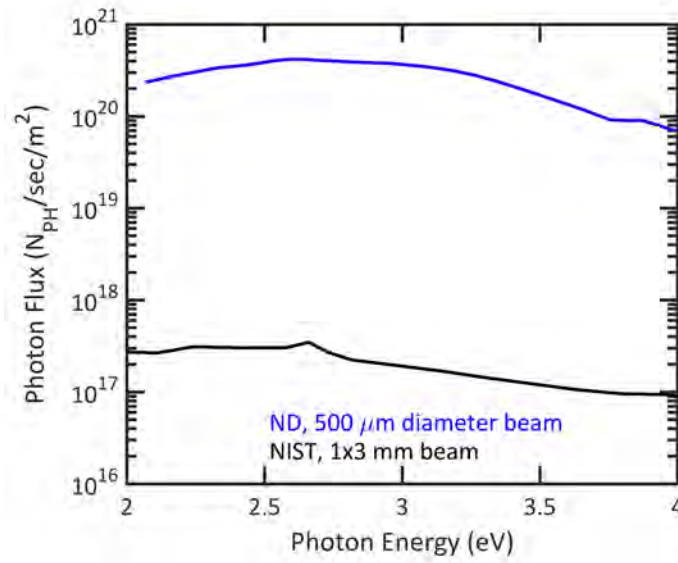


Figure 5.5. Photon flux vs photon energy of the IPE setup at Notre Dame and the IPE setup at NIST, Gaithersburg [71].

CHAPTER 6

INTERNAL PHOTOEMISSION MEASUREMENTS ON HZO CAPACITORS

Despite the recent advances in FE HZO based devices, there have been no measurements reporting the band offsets in HZO capacitors. Knowledge regarding HZO band offsets is expected to aid in the calculation of tunneling currents in HZO capacitors. Since FTJs transduce FE partial polarization into tunneling currents in an FE-based capacitor, the ability to quantify tunneling currents enables compact modeling of the behavior of FTJs. Knowledge about the band offsets in the MFS gate stack of an FeFET also aids in estimating oxide leakage in FeFETs. In this chapter the band offsets in Pd/HZO/p⁺ Si capacitors are extracted from measurements of IPE.

6.1 Current in Si/HZO/Pd capacitors

Characterization of the time dependence of currents in MFS capacitors has been found to be lacking in recent reports on HfO₂-based FTJs. Chen 2018 [72] reported the polarization dependent current in TiN/HZO/TiN capacitors at the end of 0.1 V, 100 μ s read pulses. Kobayashi 2019 [36] measured the I-V of Al/HZO/Si FTJs using DC sweeps and in response to 1 kHz triangular voltage waveforms. Tian 2017 [73] showed DC I-V characteristics of Ag/Y:HfO₂/Si FTJs. Berdan 2020 [22] showed the dependence of current at the end of a 50 ms read pulse on FE partial polarization in TiN/HfSiO/TiN FTJs FTJs. In an analog memory application, characterization of the voltage and time dependence of read currents is essential to set the read pulse voltage and duration. A careful characterization and analysis of polarization

dependent current transients in MFS capacitors is also expected to aid in analyzing IPE measurements of MFS capacitors.

6.1.1 Band diagrams of Pd/HZO/p⁺ Si capacitors

Currents in an MFS capacitor are influenced by the electric fields in the various constituent layers. Band diagrams enable visualization of the effects of FE polarization and applied bias on the electric field direction in the constituent layers of an MFS capacitor. The band diagrams are therefore a natural starting point for analyzing current flow direction in response to bias changes and polarization reversal.

The band diagrams of metal/HZO/p⁺ Si capacitors having a 0.9 nm SiO₂ interlayer between the Si and HZO and 6.9 nm HZO having 5 $\mu\text{C}/\text{cm}^2$ P_R are simulated using 1D Poisson Solver software developed by Snider [49]. The interlayer thickness, HZO thickness, and HZO polarization are chosen to represent fabricated Pd/HZO/p⁺ Si capacitors during IPE measurements. Doping in the Si layer is taken to be 10^{19} cm^{-3} , HZO is assumed to have a relative permittivity of 25 and the same band offset values as Si/HfO₂ [50]. The metal workfunction is considered to be the same as the Si work function. The band diagrams of metal/HZO/p⁺ Si capacitors with different biases and FE polarization orientations are plotted in Fig. 6.1. Band diagrams corresponding to $-P$ ($+P$) polarization at the Si/SiO₂/HZO interface are plotted in blue (red), and this polarization orientation is referred to as $-P$ HZO ($+P$ HZO) in the following discussion for brevity.

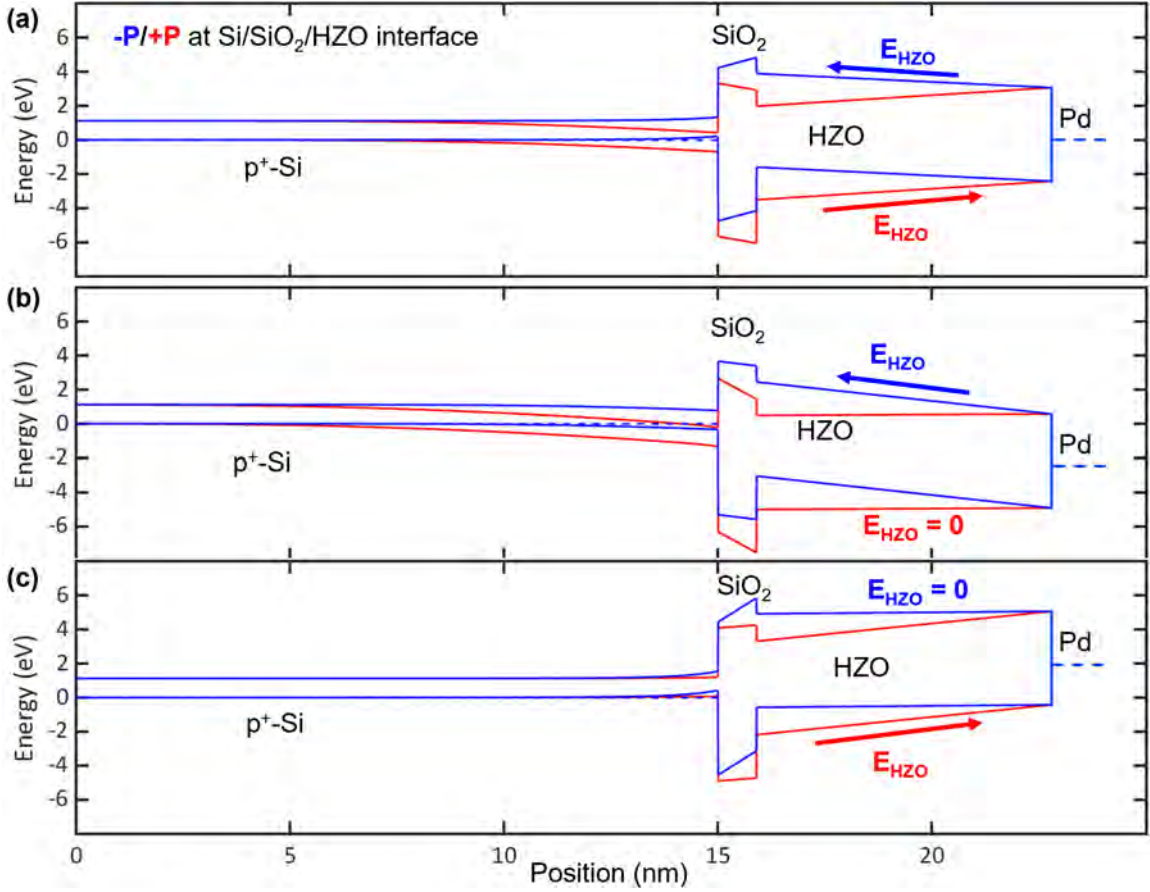


Figure 6.1. Band diagrams of metal/HZO/SiO₂/p⁺ Si capacitors plotted with $-P$ polarization at the Si/SiO₂/HZO interface in blue, and $+P$ polarization at the Si/SiO₂/HZO interface in red. The direction of electric field in the HZO layer, E_{HZO} are indicated with arrows. (a) Zero bias across capacitor. (b) Flatband in HZO layer with $+P$ polarization at the Si/SiO₂/HZO interface. (c) Flatband in HZO layer with $-P$ polarization at the Si/SiO₂/HZO interface.

When zero voltage is applied across the capacitor, Fig. 6.1(a), the depolarization field in the HZO layer is oriented opposite to the electric field in the Si layer for both $\pm P$ HZO. The metal/HZO barrier height is the lowest in the system, due to which it is reasonable to assume that the direction of electric field in the HZO

layer, E_{HZO} controls the direction of capacitor current. Under influence of E_{HZO} , the depolarization field in Fig. 6.1(a) is expected to cause a depolarizing current to flow across the HZO in a direction that would accumulate charge to reduce the net charge at the FE surface. This is true for both polarization orientations. The depolarizing current can arise from a variety of mechanisms including ionic motion, trap charging/discharging, and FE polarization reversal. The depolarizing current reduces the net charge at the FE interface, leading to a reduction in the depolarization field in the HZO layer, which in turn reduces the depolarizing current. Therefore, the depolarizing current in Fig. 6.1(a) is transient in nature, and asymptotically reduces to zero as the field in the HZO diminishes due to reduction in the net charge at the HZO interface.

A flat band condition can also occur in HZO (i.e. $E_{HZO} = 0$) by applying an external voltage of appropriate magnitude and polarity across the MFS capacitor to exactly counteract the depolarization field. For the $+P$ HZO, $E_{HZO} = 0$ when a positive voltage V_{FB}^+ , hereon referred to as the positive flat band voltage, is applied to the Si terminal as shown in Fig. 6.1(b). Therefore, if a bias $V > V_{FB}^+$ is applied to the Si terminal, current is expected to flow in the direction of the applied bias polarity for $+P$ HZO. On the other hand, an applied positive bias $V < V_{FB}^+$ will be unable to counteract the depolarization field. Therefore, if a bias $0 < V < V_{FB}^+$ is applied to the Si terminal, current is expected to flow in a direction opposite to the polarity of the bias. Based on this discussion, the capacitor current is expected to reverse polarity at $V = V_{FB}^+$.

Similarly, for $-P$ HZO, a negative voltage V_{FB}^- must be applied to the Si terminal of the MFS capacitor to exactly counteract the depolarization field and achieve a flat band condition in the HZO layer, as shown in Fig. 6.1(c). In this case, when a negative bias V lower in magnitude than the flatband voltage $V_{FB}^- < V < 0$ is applied to the Si terminal, current can be expected to flow in the opposite direction as the bias polarity

for $-P$ HZO. As the negative bias magnitude is increased, current is expected to flow in the direction of the bias polarity for $V < V_{FB}^-$.

6.1.2 Polarization reversal in Pd/HZO/p⁺ Si capacitors

Pd/HZO/p⁺ Si capacitors with the top view shown in Fig. 6.2(a) and the cross section depicted in Fig. 6.2(b) were fabricated. The HZO thickness $t_{FE} = 4.8, 5.6,$ and 6.9 nm. The Pd thickness was 11 nm for the semi-transparent layer and 150 nm for the contact layer; a back contact of 225 nm Au was evaporated on the back of the wafer. The radius of tested capacitors was $55.5 \mu\text{m}$, corresponding to a capacitor area of $9677 \mu\text{m}^2$. A detailed traveler describing the fabrication is attached as Appendix I.

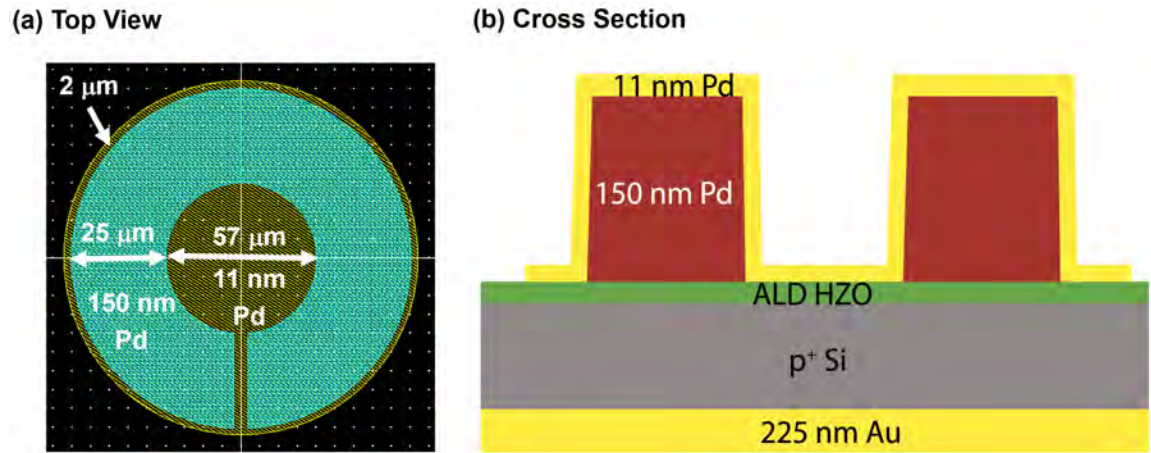


Figure 6.2. (a) Top view of fabricated Pd/HZO/p⁺ Si capacitors. (b) Cross section of the fabricated Pd/HZO/p⁺ Si capacitors with radius of $55.5 \mu\text{m}$.

Polarization reversal measurements using the strictly symmetric protocol discussed in Section 3.2.1 were made on the Pd/HZO/p⁺ Si capacitors are shown in

Fig. 6.3(a), (b), and (c) for capacitors with $t_{FE} = 4.8, 5.6,$ and 6.9 nm, respectively. For the MFS capacitors, 10000 cycles of 250 Hz triangular waves having amplitude V_R were required to fully wake-up the FEs.

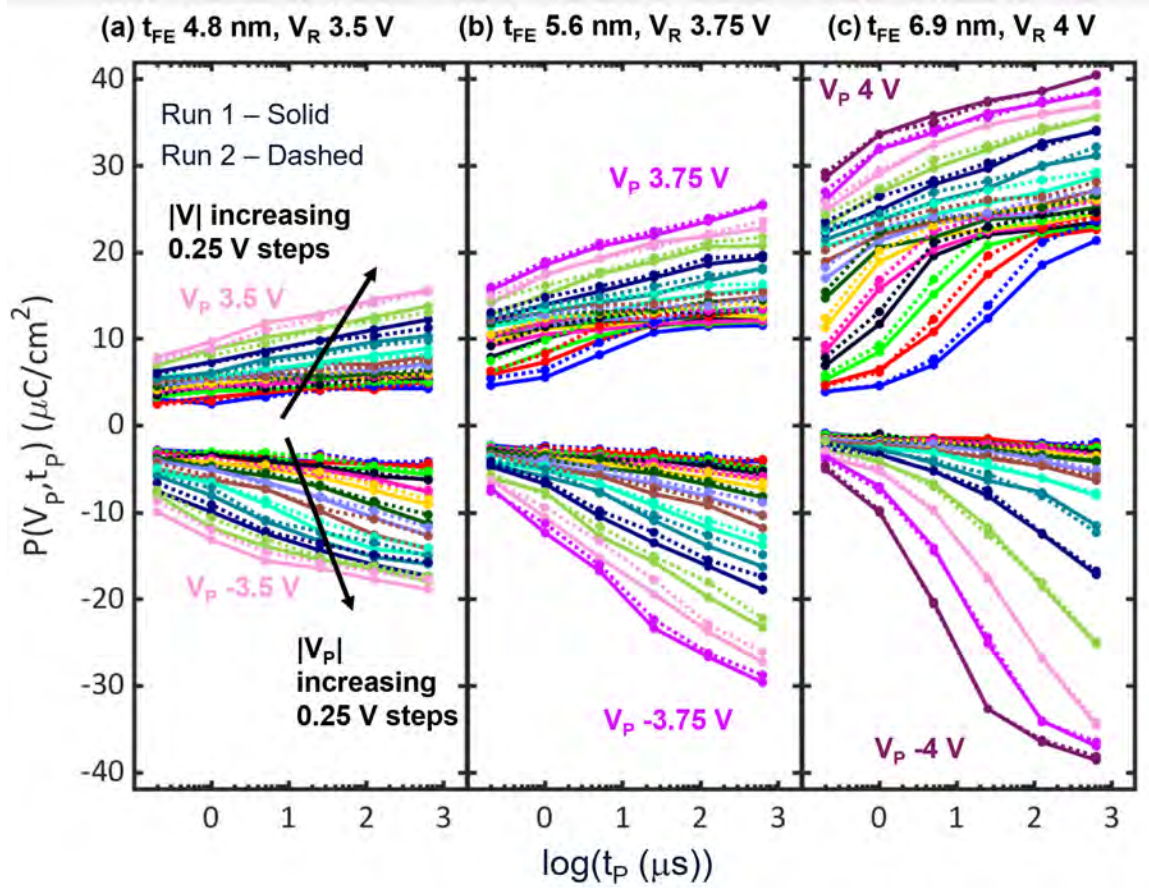


Figure 6.3. Polarization reversal characteristics of Pd/HZO/ p^+ Si capacitors. Two repeats are plotted.

The polarization reversal curves do not saturate for the applied reset voltages $V_R = 3.5, 3.75,$ and 4 V for capacitors with $t_{FE} = 4.8, 5.6,$ and 6.9 nm, respectively. Using higher reset voltages caused device breakdown before the test was complete. Signif-

icant differences in the nature of polarization reversal characteristics were observed in Pd/HZO/p⁺ Si vs W/HZO/W capacitors; these have not been analyzed, and the differences likely occur due to ALD on different substrates (Si-O-H terminated Si vs W) leading to different interfacial characteristics, as well as higher depolarization fields in MFS vs MFM capacitors. From these measurements, $2P_R$ values of 14.5, 24.0, and 37.1 $\mu\text{C}/\text{cm}^2$ were obtained for the (V_R , 1 ms) write pulses.

The higher depolarization field in Pd/HZO/p⁺ Si compared to W/HZO/W capacitors is expected to cause differences in their polarization reversal characteristics. At the end of the reset pulse of a polarization reversal measurement waveform, the FE is set to a $\pm P_R$ polarization, after which a ($\mp V_P, t_P$) write pulse sets the FE polarization to $P = \pm P_R \mp \Delta P(\mp V_P, t_P)$; the polarization difference $\Delta P(\mp V_P, t_P)$ is then measured. During polarization reversal from $-P_R$ to $+P_R$, when $P < 0$ the depolarization field orientation promotes a reduction in the FE polarization magnitude, and therefore assists in polarization reversal by the ($+V_P, t_P$) write pulse. As the partial polarization increases and $P > 0$, the depolarization field opposes an increase in the FE polarization magnitude, and therefore opposes polarization reversal by the (V_P, t_P) pulse. This can plausibly account for the observed kinks in the polarization reversal characteristics for intermediate values of partial polarization in Fig. 6.3. Furthermore, as P changes during polarization reversal, so does the depolarization field. This causes the internal field in the HZO to be dependent on the partial polarization for the same (V_P, t_P) write pulse. Finally, the Si layer is in inversion for $+|P|$ polarization and in accumulation for $+P$, leading to a higher depolarization in the first case than the second. While this explanation qualitatively accounts for some of the differences in polarization reversal characteristics between Pd/HZO/p⁺ Si capacitors, Fig. 6.3, and W/HZO/W capacitors, Fig. 3.5, performing Monte-Carlo based simulations including effects of the depolarization field would aid in investigating the veracity of this hypothesis.

6.1.3 Pulsed measurement protocol for current transients

Based on the effect of asymmetric vs. strictly symmetric polarization reversal measurements, it can be assumed that asymmetric current measurement protocols would cause charging of MFS capacitors due to ionic motion and trap charging/discharging. A DC characterization of the I-V in MFS capacitors is expected to reflect the effects of FE polarization as well as these charging effects. Significant charging effects can also be expected in unipolar pulsed I-V measurements, where the capacitor currents for different voltages of one polarity are measured at once, after which the capacitor currents for different voltages of the opposite polarity are measured. Therefore, a strictly symmetric pulsed protocol was developed to measure the transient polarization dependent currents in Pd/HZO/p⁺ Si capacitors while minimizing the effects of ionic motion and traps over multiple measurement cycles. The measurement protocol, along with the timing parameters used, is shown in Fig. 6.4. The voltage waveform in Fig. 6.4 is applied to the p⁺ Si substrate with Pd terminal set to zero volts, and current was measured at the Pd terminal. The sign of the measured current was then inverted during data analysis and plotting, so that a positive voltage would be expected to lead to a positive current if the MFS capacitor were replaced by a resistor. Measurements were performed using the Keithley 4200 parameter analyzer with 4225-PMUs, and open circuit standby conditions were set.

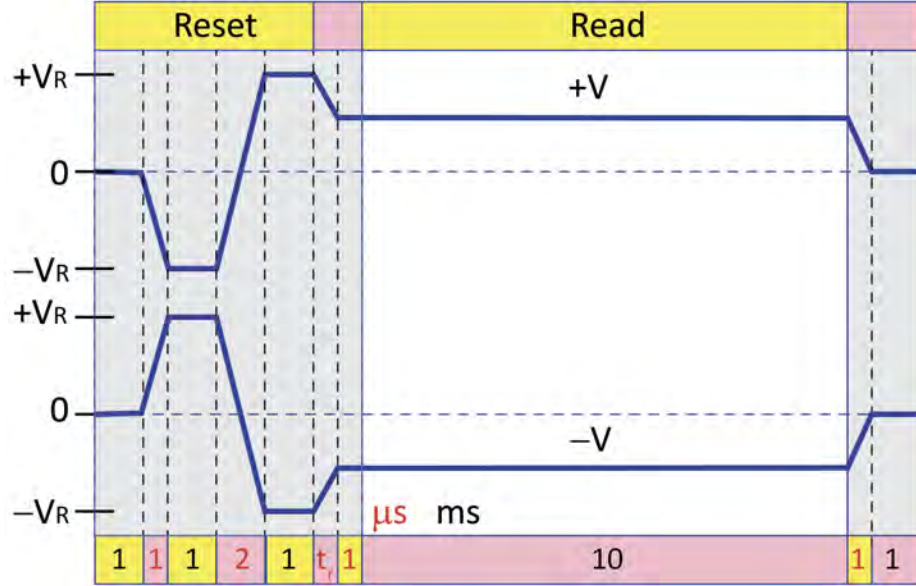


Figure 6.4. Strictly symmetric pulsing protocol for pulsed I-V-t measurements on Pd/HZO/p⁺ Si capacitors. The upper waveform is immediately followed by the lower waveform. The time response is measured only during the read interval. The timing parameters in red (black) font have units of μs (ms).

The measurement starts with a hold time of 1 ms, during which time 0 V is applied across the capacitor. The FE is then set in a $+P$ state by a bipolar trapezoidal reset pulse that ends with a $+V_R$ reset pulse, the magnitude of which was chosen based on polarization reversal measurements shown in Fig. 6.3. The voltage magnitude then ramps from $+V_R$ in the second half of the reset pulse to the measurement voltage $+V$ with a constant slew rate of $1 \text{ V}/\mu\text{s}$. The ramp time t_r is therefore set at $t_r = (V_R - V)\mu\text{s}$. This constant slew rate ensures that instrumentation RC-related transients arising from the displacement current CdV/dt ($\sim 10 \text{ A}/\text{cm}^2$) at the start of the measurement pulse is the same for different values of V . No measurements are taken during a $1 \mu\text{s}$ settling time in the V pulse. When using the 4225-PMUs,

only a single current range can be specified for the entire measurement. The settling time allows for the capacitor current to decay, allowing for a lower current range to be used for the 10 ms read duration for more accuracy. The sampling interval is 100 μs . The read pulse is followed by a 1 ms hold where 0 V is applied across the capacitor. The $(+V_R, +V)$ measurement corresponding to the upper waveform in Fig. 6.4 is immediately followed by $(-V_R, -V)$ measurement corresponding to the lower waveform in Fig. 6.4. The magnitude of V is then stepped in 0.1 V increments to a maximum value of $V = V_R - 0.1$ V. If $V = V_R$ is used, the code written to perform the measurements sets $t_r = 0$ s, which is less than the 5 ns minimum time step that can be specified in the PMUs.

6.1.4 Measurement and interpretation of pulsed current-voltage

Current-voltage and time (I-V-t) measurements made on the Pd/HZO/p⁺ Si capacitors are shown in Fig. 6.5. The measurements were made on the same capacitors as shown in Fig. 6.3. A single measurement set started with the polarization reversal measurement, followed immediately by the I-V-t measurement; two measurement sets were successively performed to characterize run-to-run variations. The upper plots in Fig. 6.5 correspond to $(+V_R, +V)$ measurements, and the lower plots correspond to $(-V_R, -V)$ measurements.

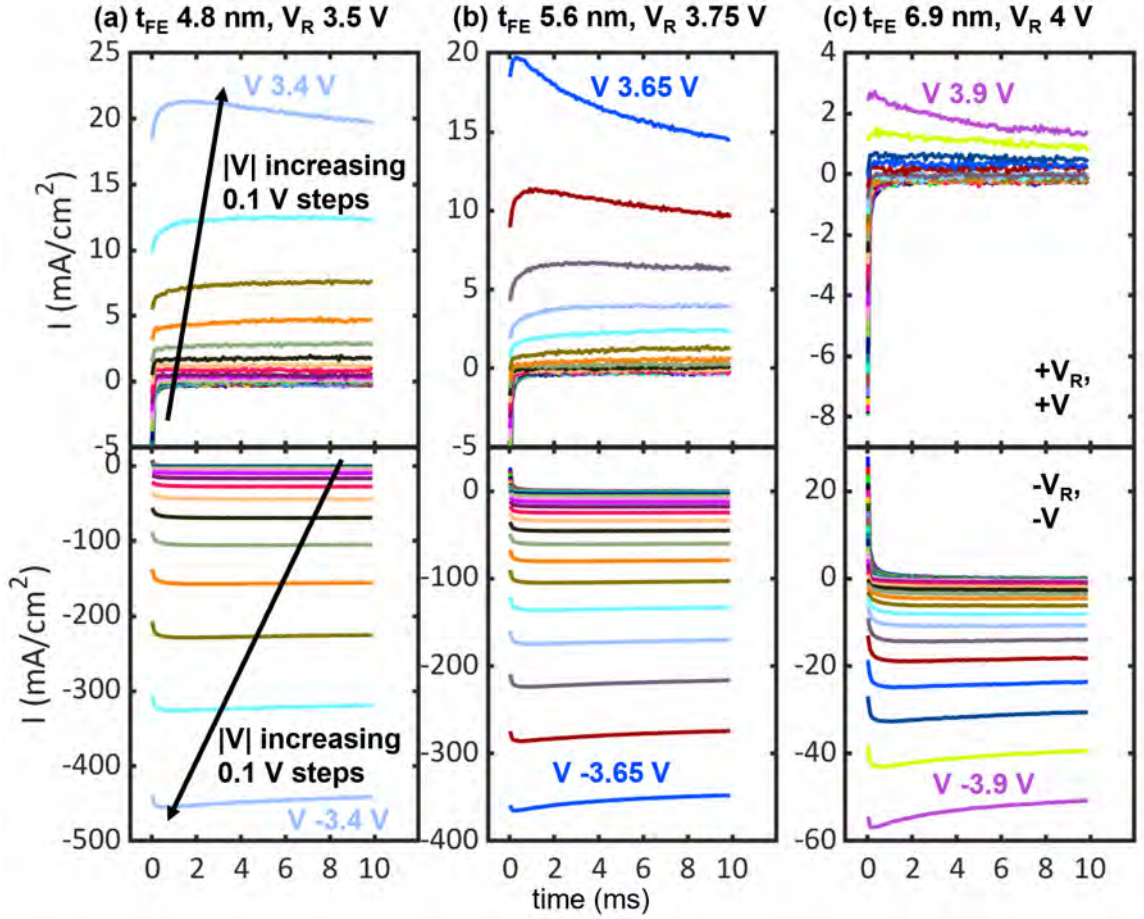


Figure 6.5. Current transients plotted with respect to measurement time in Pd/HZO/ p^+ Si capacitors. The upper and lower curves correspond to $(+V_R, +V)$ and $(-V_R, -V)$ measurements, respectively. Voltages are applied to Si.

The settled value of current is $\sim 15x$ greater for negative vs positive voltages. This can be ascribed to the p^+ Si being in inversion when the FE is set with $-V$ and in accumulation when set with $+V_R$. The peaks in absolute current, $t \sim 0.2$ ms are likely related to instrument delay. Higher electric field magnitudes exist in the constituent layers of the MFS capacitors when Si is in inversion, thereby causing larger currents

to flow.

The time dependence of the current is further highlighted by plotting the I-V using the first and last currents in the read interval, $t = 0$ and 10 ms, vs. V in Fig. 6.6. The current in Fig. 6.6 changes direction for the same bias polarity as the bias magnitude is decreased. The voltage bias at which the current changes direction are defined as the zero crossing voltages V_{ZC}^{\pm} for capacitors reset by $\pm V_R$. Currents in the opposite direction as the applied bias polarity decay from $t = 0$ to $t = 10$ ms, while currents in the same direction as the applied bias polarity follow the same curve for both the times.

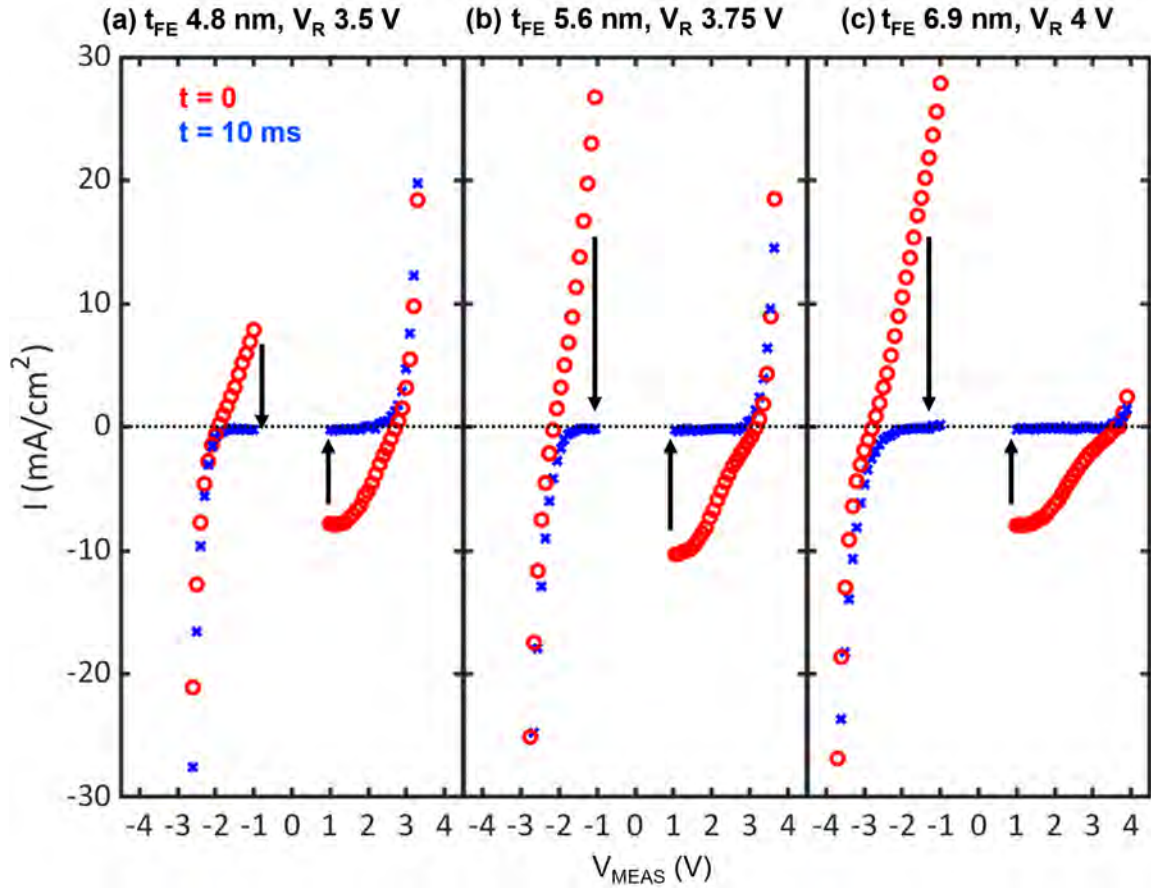


Figure 6.6. Pulsed I-V-t measurement on Pd/HZO/p⁺ Si capacitors with current measured at $t = 0$ (red) and $t = 10$ ms (blue) in the read interval.

The behavior of I-V-t curves can be qualitatively explained if the HZO electric field is assumed to control the direction of current flow. The zero crossing voltages can be expected to depend on the read interval at which the I-V curves are analyzed, and there may not be a zero crossing voltage associated with every read interval. For $|V| < |V_{ZC}^{\pm}|$, current flows in the opposite direction with respect to the applied voltage polarity. This direction of current flow tends to neutralize the FE polarization. The decreased charge density at the FE interface decreases the depolarizing field in the

HZO, which in turn leads to a reduction in the capacitor current. These differences are visible in quadrants 2 and 4 of Fig. 6.6. In comparison, currents in the 1st and 3th quadrants of Fig. 6.6 trace the same curve, and trend monotonically with voltage.

The origins of the current responses and their relaxation can be explained from the band diagrams in Fig. 6.1, assuming the zero crossing voltages arise from reversal of the electric field direction in the HZO layer. With this assumption, the zero crossing voltages should equal the flat band voltages, i.e. $V_{ZC}^{\pm} = V_{FB}^{\pm}$. The current transients are then qualitatively consistent with the assumption of the HZO electric field controlling the current direction, since $|I_{MEAS}|$ decreases with increasing $|V|$ for $|V| < |V_{ZC}^{\pm}|$, and $|I_{MEAS}|$ increases with increasing $|V|$ for $|V| > |V_{ZC}^{\pm}|$; I_{MEAS} reverses direction at $|V| = |V_{ZC}^{\pm}| = |V_{FB}^{\pm}|$.

Next, the zero crossing voltages are extracted from the current transients in Fig. 6.5. The applied voltages $+V = V_{ZC}^+$ and $V = V_{ZC}^-$ at which the current changes direction are plotted with respect to the measurement time in Fig. 6.7. $|V_{ZC}^{\pm}|$ is found to decrease with FE thickness for the same measurement time, and with measurement time for the same FE thickness. Furthermore, there is a greater decrease in $|V_{ZC}^+|$ with time than for $|V_{ZC}^-|$. Note that zero crossing voltages lower than 1 V cannot be extracted, since 1 V is the lowest $|V|$ used in the I-V-t measurements. For this reason, no $|V_{ZC}^-|$ were obtained for $t_{FE} = 4.8$ nm after $t = 1.5$ ms.

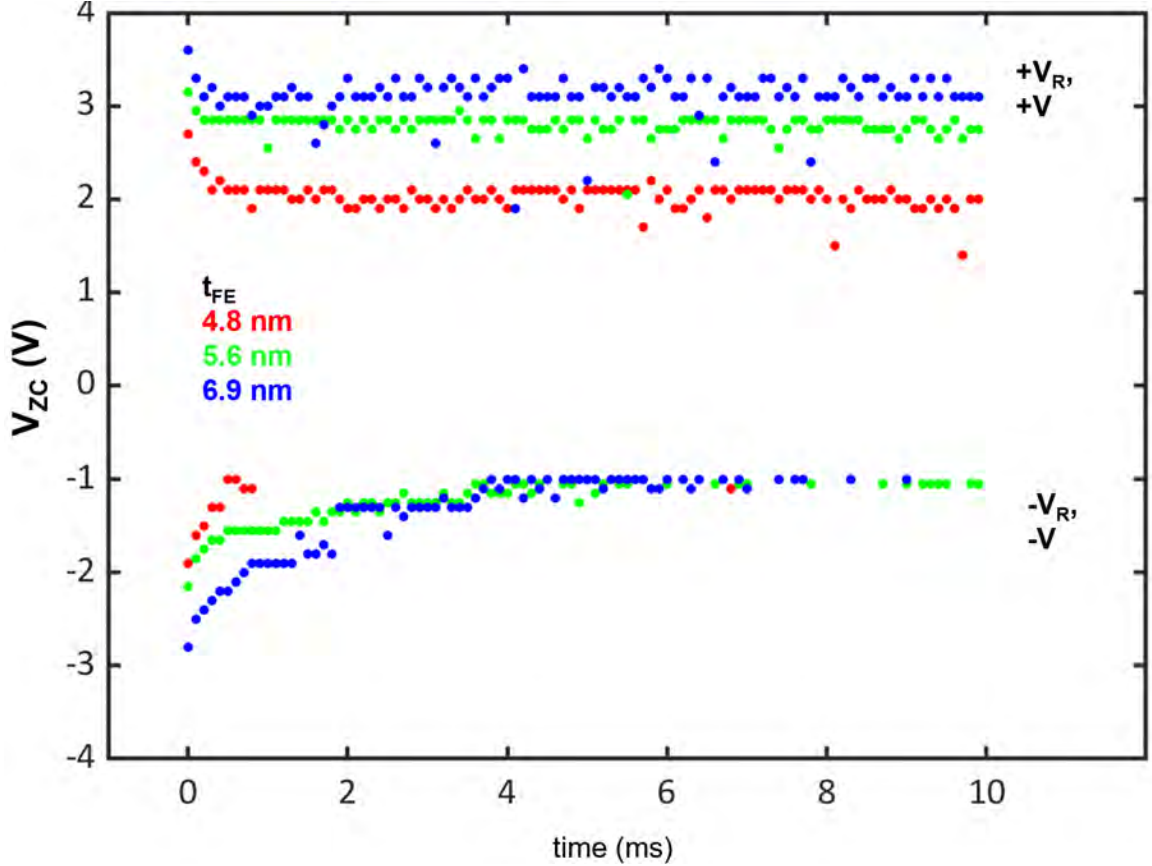


Figure 6.7. Positive and negative zero crossing voltages extracted from current transients in Pd/HZO/p⁺ Si capacitors, plotted with respect to time.

These measurements are qualitatively consistent with the assumption that HZO electric field controls the current direction, and that $V_{ZC}^{\pm} = V_{FB}^{\pm}$. The zero crossing voltage magnitudes decrease with decreasing HZO thickness. This can be explained by a reduction in HZO P_R with HZO thickness: as the P_R decreases, so does the electric field in HZO, thereby reducing the $|V_{FB}^{\pm}|$. The zero crossing voltages also depend on the measurement time, with $|V_{ZC}^{\pm}|$ decreasing as the measurement progresses. The depolarizing currents decrease the net charge at the FE interface as the

measurement time increases, thereby reducing the depolarizing field and the $|V_{FB}^\pm|$. The decrease in $|V_{ZC}^\pm|$ is more pronounced for negative than positive voltages, since p^+ Si is in inversion when the FE is reset by $-V_R$, leading to a higher depolarization field, a greater depolarizing current, and faster decay of the net charge at the FE interface.

6.1.5 Analysis of flat band voltages

The zero crossing voltages have been qualitatively ascribed to occur when there is zero electric field in the HZO layer. A quantitative analysis is presented in this section to examine this hypothesis. This quantitative analysis is based on the description of depolarization in FEs presented in Sec. 2.2, and extends the treatment by Ma and Han [45].

The circuit diagram for this analysis is shown in Fig. 6.8, where the HZO is represented by $C_F = (Q_F - P)/V_F$ with a net charge P at the FE interface. The single series capacitance considered by Ma and Han [45] is separated into two capacitors in series: an interlayer (IL) capacitance $C_I = Q_I/V_I$ and a voltage-dependent semiconductor capacitance $C_S(V_S) = Q_S/V_S$. The voltage-dependence of the semiconductor capacitance $C_S(V_S)$ is rewritten as a charge-dependence $C_S(Q_S)$ for use later. An external voltage $V = V_F + V_I + V_S + \Phi_{MS}$ is applied to the entire capacitive stack, where Φ_{MS} is the work function difference between the semiconductor and the metal. Charge $Q_F = Q_I = Q_S$ is dictated by charge neutrality. The analysis by Ma and Han provides an expression for V_{DEP} , which corresponds to the voltage across the FE layer when the zero external bias is applied. The following analysis provides an expression for V_{FB} , which corresponds to the external bias for which the voltage across the FE layer is zero.

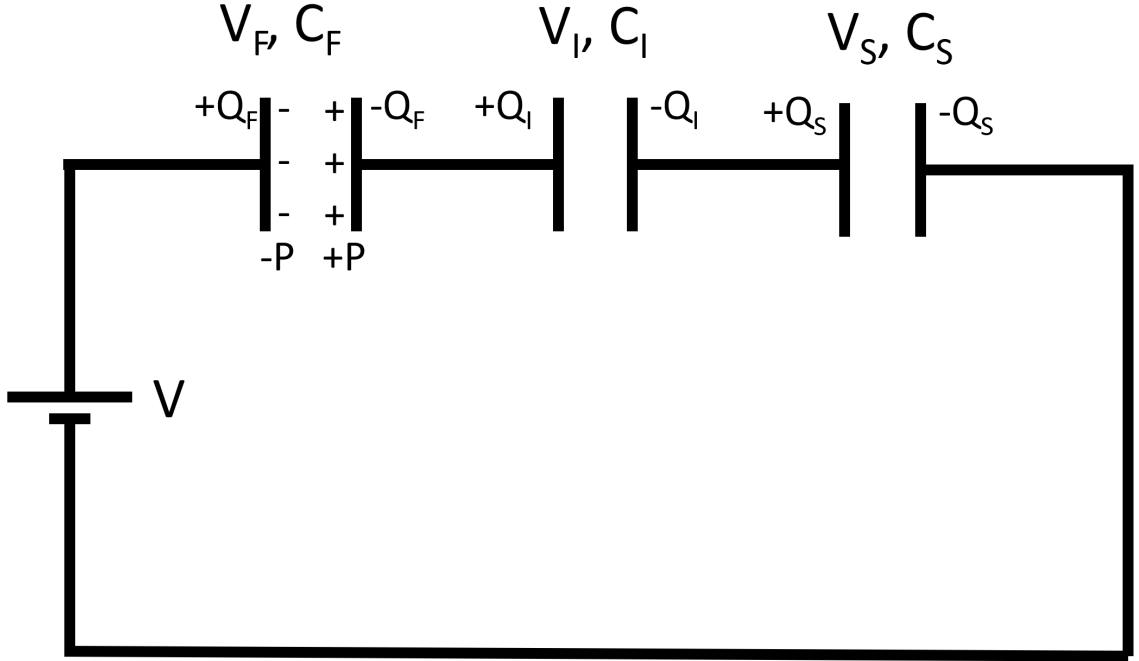


Figure 6.8. Equivalent circuit to establish the flat band in MFIS capacitors. The FE capacitor C_F is in series with an insulating interlayer C_I and a semiconductor C_S . An external voltage V is applied to the entire capacitive stack.

A zero electric field condition in the FE layer exists when $V_F = 0$, i.e. when $Q_F = P$. The external voltage when $V_F = 0$ is

$$V = V_{FB}^{\pm} = V_I + V_S + \Phi_{MS}. \quad (6.1)$$

Equation 6.1 describes the flat band voltage condition corresponding to two polarization conditions, $\pm P$. The voltage across the IL and semiconductor can in turn be

written as

$$\begin{aligned} V_I &= \frac{Q_F}{C_I} = \frac{P}{C_I} \\ V_S &= \frac{Q_F}{C_S(Q_S)} = \frac{P}{C_S(P)}. \end{aligned} \quad (6.2)$$

Therefore, the flat band voltages can be written as

$$V_{FB}^+ = \frac{+P}{C_I} + V_S(Q_S = +P) + \Phi_{MS} \quad (6.3)$$

$$V_{FB}^- = \frac{-P}{C_I} + V_S(Q_S = -P) + \Phi_{MS} \quad (6.4)$$

where $V_S(Q_S = \pm P)$ is the band bending in the semiconductor that leads to a total charge $\pm P$ in the semiconducting layer. For a given Q_S , the corresponding $V_S(Q_S)$ is calculated by numerically solving the transcendental equations [74]

$$Q_S(V_S) = -\epsilon_S E_S = \frac{\sqrt{2}\epsilon_S kT}{qL_D} F(V_S) \quad (6.5)$$

where ϵ_S is the permittivity of the semiconductor, E_S is the electric field at the semiconductor surface, k is the Boltzmann's constant, T is the temperature, and q is the electron charge. L_D is the Debye length in the semiconductor,

$$L_D = \sqrt{\frac{\epsilon_S}{qp_{p0}\beta}} \quad (6.6)$$

where $p_{p0} = n_i^2/N_A$, with n_i being the intrinsic carrier concentration in the semiconductor, N_A the density of acceptor dopants, $\beta = q/kT$, and $F(V_S)$ is from

$$F(V_S) = \sqrt{[\exp(-\beta V_S) + \beta V_S - 1] + \frac{n_{p0}}{p_{p0}} [\exp(\beta V_S) - \beta V_S - 1]} \quad (6.7)$$

Adding and subtracting V_{FB}^+ and V_{FB}^- from Eqs. 6.3 and 6.4, respectively, gives

$$\begin{aligned}\Sigma V_{FB} &= V_{FB}^+ + V_{FB}^- = V_S(Q_S = +P) + V_S(Q_S = -P) + 2\Phi_{MS} \\ \Delta V_{FB} &= V_{FB}^+ - V_{FB}^- = \frac{+P}{C_I} + V_S(Q_S = +P) - V_S(Q_S = -P)\end{aligned}\quad (6.8)$$

Therefore, ΣV_{FB} can be used to determine Φ_{MS} without needing information regarding the IL capacitance, while ΔV_{FB} can be used to determine the IL capacitance with no knowledge about the metal-semiconductor band offsets. The voltages ΣV_{FB} and ΔV_{FB} are calculated by setting $V_{FE}^\pm = V_{ZC}^\pm$ for $t = 0$ from Fig. 6.7. The $t = 0$ measurement occurs after a 1 μ s settling time, comparable to the 1 μ s delay-before-read used in the polarization reversal measurements shown in Fig. 6.3. Therefore, the zero crossing voltages for $t = 0$ are assumed to correspond to the maximum polarizations in Fig. 6.3.

The IL thicknesses corresponding to the SiO₂ relative permittivity $\epsilon_I = 3.9$, and the p⁺-Si/Pd work function differences Φ_{MS} are calculated using the model described above. The physical parameters chosen for the calculation are: $T = 300$ K, $N_A(\text{Si}) = 10^{19}$ cm⁻³, and $\epsilon_{Si} = 11.9$. Results of the calculation are summarized in Table 6.1.

t_{FE} (nm)	$2P_R$ (μ C/cm ²)	ΔV_{ZC} (V)	ΣV_{ZC} (V)	t_I (nm)	Φ_{MS} (eV)
4.8	14.5	4.6	0.8	1.1	-0.13
5.6	24.0	5.3	1.0	0.9	-0.03
6.9	37.1	6.4	0.8	0.8	-0.12

TABLE 6.1

SUMMARY OF MEASURED AND EXTRACTED PHYSICAL
PARAMETERS OF PD/HZO/P⁺ SI CAPACITORS.

Both the calculated IL thickness and the p⁺-Si/Pd work function differences are consistent across the three FE samples to within ± 0.2 nm and ± 0.1 eV, respectively. The extracted Si/Pd work function difference corresponds to a Pd workfunction of 5.06 ± 0.05 eV, close to the previously reported thermionic and photoelectric workfunctions of Pd, 4.99 and 4.97 eV, respectively [75]. Therefore, assuming the electric field in the FE layer controls the direction of capacitor current is quantitatively consistent with measurements.

6.2 Band Alignment in Pd/HZO/p⁺ Si capacitors

An IPE measurement yields band offsets by the spectroscopic measurement of photocurrent arising from photoemission over internal electronic barriers [66]. As compared to IPE on non-FE dielectrics, IPE on FE dielectrics poses unique challenges. In an IPE measurement, the kinetic energy of photoexcited carriers is lost via inelastic electron-electron scattering, and quasi-elastic electron-phonon scattering

events [76]. The probability of a photoexcited carrier generated in the semiconductor to reach the semiconductor/dielectric interface and then cross the dielectric is enhanced by electric fields in these layers [77]. Therefore, to increase the IPE current in an FE-based capacitor, a voltage greater in magnitude than the corresponding flat band voltage is applied to ensure the electric fields in all the constituent layers of the MFS capacitors are oriented in the same direction. The discussion in Sec. 6.1.5 showed that the zero crossing voltage from I-V-t measurements could consistently be equated to the flat band voltage. Therefore, for an FE capacitor set by a positive $+V_R$, the IPE measurement voltage is chosen so that $V_{IPE} > V_{ZC}^+$. Similarly, for an FE capacitor set by a negative $-V_R$, the IPE measurement voltage is chosen so that $V_{IPE} < V_{ZC}^-$.

The band diagrams of metal/HZO/p⁺ Si capacitors corresponding to the $+P$ and $-P$ polarization orientations are shown in Fig. 6.9(a) and (b), respectively, to identify the possible IPE transitions that may be observed. The possible transitions for the $+P$ polarization orientation, Fig. 6.9(a), are - (1) excitation of electrons from Pd to the HZO conduction band (CB) and their subsequent collection in Si, (2) excitation of holes from the Si valence band (VB) to the HZO VB and their subsequent collection in Pd, and (3) excitation of holes from the Si CB to the HZO VB and their subsequent collection in Pd. The possible transitions for the $-P$ orientation, Fig. 6.9(b), are - (1) excitation of holes from Pd to the HZO VB and their subsequent collection in Si, (2) excitation of electrons from the Si VB to the HZO CB and their subsequent collection in Pd, and (3) excitation of electrons from the Si CB to the HZO CB and their subsequent collection in Pd. The expected transitions are shown in Fig. 6.9, where $\Phi_{MS} = 0$ is assumed for simplicity. The band offset values of Si/HfO₂ [64] are used to estimate transition cutoff energies.

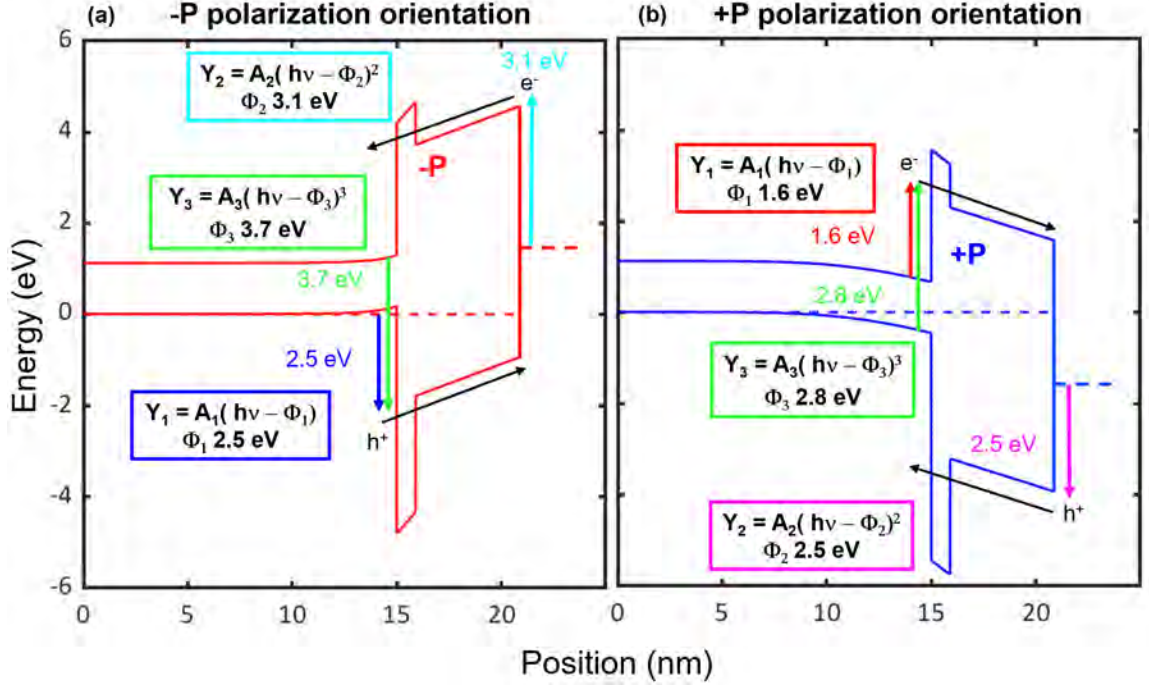


Figure 6.9. Band diagrams of Metal/HZO/p⁺ Si capacitors plotted for (a) -P, and (b) +P FE polarization orientations. Possible IPE transitions are shown with energies and yield dependences on photon energy.

The IPE transitions can also be classified based on density of states with respect to energy in the material where the photoexcited carriers are generated. For electrons (holes) being excited from the Pd layer to the HZO CB (VB), all the states below (above) the Fermi level of Pd are occupied. The IPE yield for these transitions depends on the photon energy as $Y_2 = A_2(h\nu - \Phi_2)^2$. The excitation of electrons from the Si CB to the HZO CB for $+V_R, +V_{IPE}$ occurs from the electrons occupying the triangular well between the Si CB edge and the Si Fermi level, as shown in Fig. 6.9(b). Similarly, in the $-V_R, -V_{IPE}$ measurements, holes occupying the triangular well between the Si VB edge and the Si Fermi level are excited to the HZO VB, as shown in Fig. 6.9(a). In both these cases, the IPE yield depends on the photon energy as

$Y_1 = A_1(h\nu - \Phi_1)$. Finally, electrons (holes) excited from the fully occupied VB (CB) of Si into the HZO CB (VB) lead to an IPE yield dependence on photon energy of the form $Y_3 = A_3(h\nu - \Phi_3)^3$.

6.2.1 IPE measurement protocol for FE capacitors

The protocol used for the IPE measurements involves the following steps:

1. Place the DUT on chuck and make electrical connections.
2. Set the monochromator wavelength to green (532 nm) with input shutter open.
3. Position LWP so that green colored fiber output is incident on DUT.
4. Close monochromator input shutter.
5. Darken the room.
6. Specify the start, end, step, and repeats of the IPE photon energy sweep.
7. Specify the reset voltage, IPE voltages, IPE repeats, and number of wake-up cycles.
8. Convert the photon energy sweep to a wavelength sweep.
9. Set the monochromator to output the specified wavelength, with input shutter closed.
10. Query the monochromator to verify specified wavelength has been set.
11. Set the appropriate filter in the filter wheel for the set wavelength.
12. Apply the voltage waveform in Fig. 6.10 to the DUT.
13. Measure the current in the DUT, I_{DARK} .

14. Remove voltage bias from the DUT.
15. Open the monochromator input shutter to illuminate the DUT.
16. Apply the same voltage waveform as step 11 to the DUT.
17. Measure the current in the DUT, I_{TOT} .
18. Remove voltage bias from the DUT.
19. Close the monochromator input shutter.
20. Step the monochromator wavelength.
21. Repeat steps 8-19 until complete.

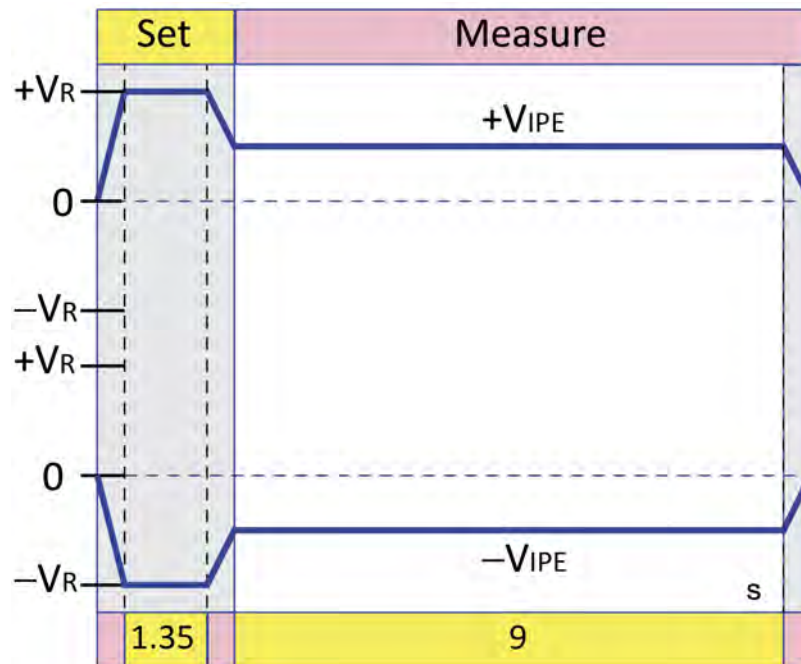


Figure 6.10. Voltage sweep along with timing parameters applied to Pd electrode of Pd/HZO/p⁺ Si capacitors for IPE measurements. The unlabeled slew times are not controlled in this measurement.

The measurement voltage waveform applied to the MFS capacitors, Fig. 6.10, is limited by the timing resolution of the Keithley 2636A sourcemeter. The IPE measurements utilize the lowest current range of the instrument (100 pA), leading to a default sampling interval of 450 ms for every voltage point. The FE capacitor is set by 3 sampling points at $\pm V_R$, corresponding to a total time of 1.35 s; the 20 data points are measured during the $\pm V_{IPE}$ measurement pulse applies, corresponding to a total time of 9 s. The capacitor current decays during the $\pm V_{IPE}$ pulse, while the current photomodulation remains constant during the measurement interval. The duration of the measurement pulse is chosen such that the measured dark current at the end of the $\pm V_{IPE}$ pulse decays to a value less than or equal to the current photomodulation by 3.5 eV (350 nm) photons. Photons with 3.5 eV energy are chosen for this test since they are higher in energy than two of the expected cutoff energies for each FE polarization orientation in Fig. 6.9, and are therefore expected to cause photomodulation. Higher energy photons were not chosen since the photon flux density reduces significantly with energy after ~ 3.5 eV. As the measurement time increases, the net charge at the FE interface is reduced by depolarization currents, leading to a reduction in the flat band voltages. The flat band voltages for the IPE measurement setup, corresponding to a total measurement time of 9 s, are obtained by measuring the current transients during the V_{IPE} pulse in Fig. 6.10.

The current transients are measured using the waveform for different V_{IPE} , and are plotted with respect to measurement time in Fig. 6.11. The current magnitudes measured using the Keithley 2636A sourcemeter in the IPE setup, Fig. 6.11, are $\sim 10^{-2}$ lower than those measured using the Keithley 4225 PMUs, Fig. 6.5. This can be expected since the current transients decay with time and the Keithley 4225 PMUs measured the currents up to $t = 10$ ms, whereas the Keithley 2636A sourcemeter measured the currents for $t > 1$ s.

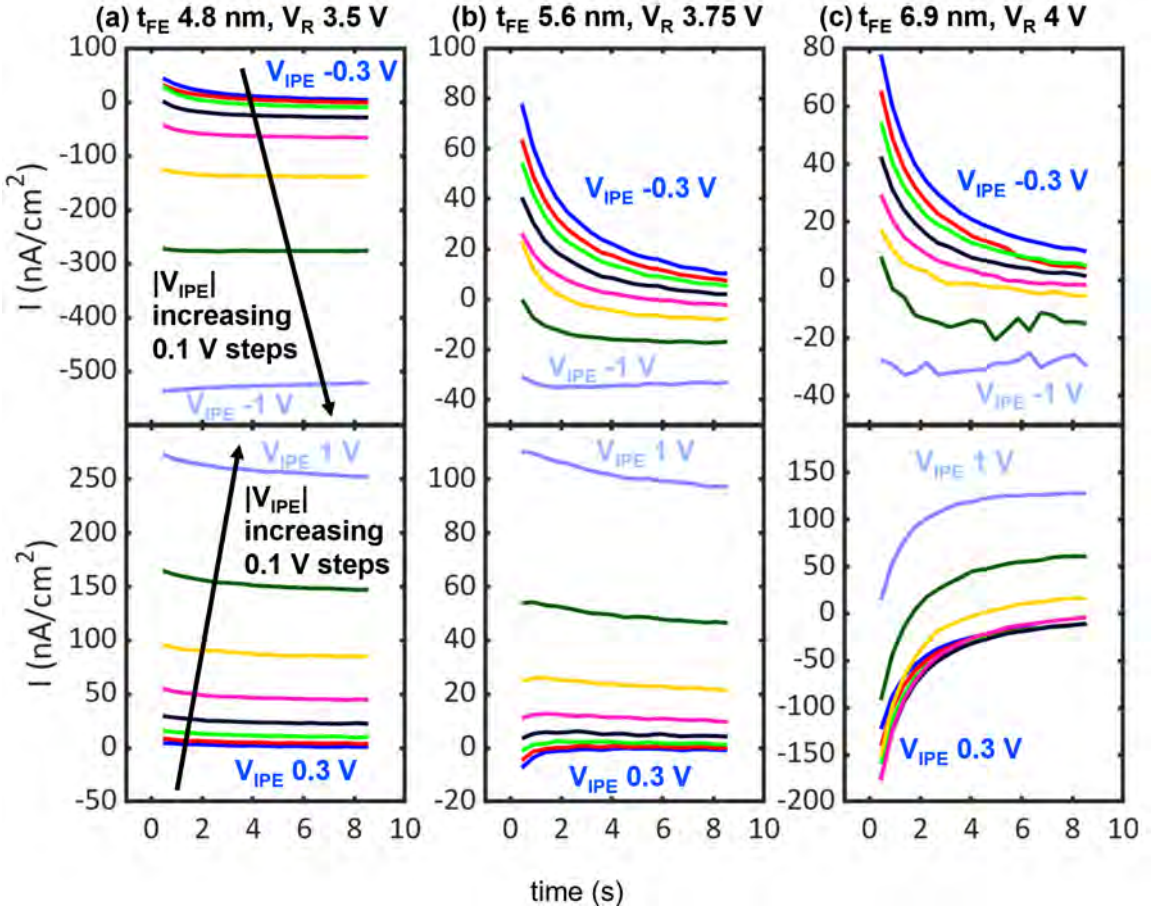


Figure 6.11. Current transients measured in the IPE setup plotted with respect to measurement time in Pd/HZO/p⁺ Si capacitors. The upper and lower plots correspond to ($-V_R, -V$) and ($+V_R, +V$) measurements, respectively. Voltages are applied to Pd.

The zero crossing voltages extracted from the current transients in Fig. 6.11 are also plotted with respect to measurement time in Fig. 6.12. As can be expected from extrapolating the dependence of V_{ZC}^{\pm} with measurement time in Fig. 6.7, the magnitudes of flat band voltages in the IPE system are lower than those observed using the Keithley PMU. The reduction in $|V_{ZC}^{\pm}|$ can be attributed to a reduction in the net charge at the FE interface by the transient depolarizing currents.

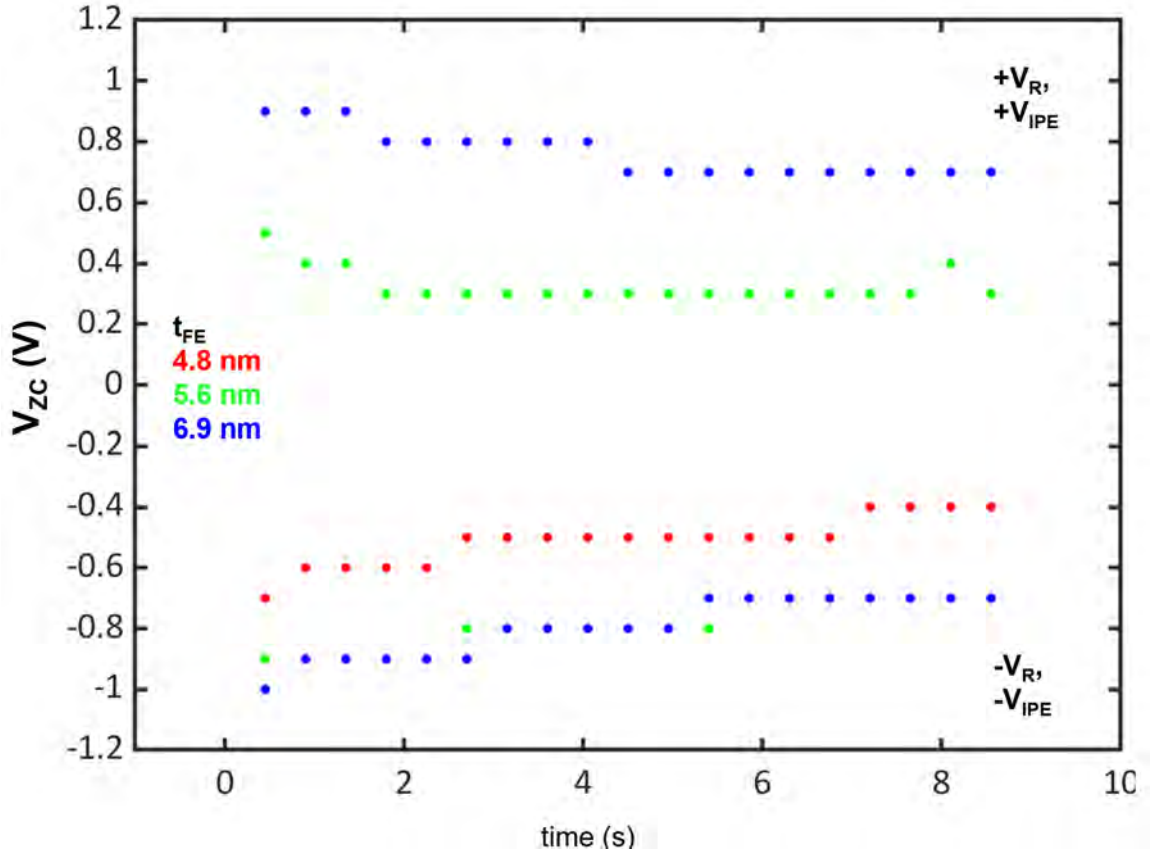


Figure 6.12. Positive and negative zero crossing voltages extracted from current transients in Pd/HZO/p⁺ Si capacitors measured using the IPE setup, plotted with respect to time.

Since the IPE measurement corresponds to $t = 9$ s in the current transients in Fig. 6.11, flat band voltages from Fig. 6.12 at $t = 9$ s are used to calculate the expected net charge P_{IPE} at the Si/HZO interface during the IPE measurement. Equations 6.4 and 6.3 are used to calculate $\pm P_{IPE}$, using the interlayer capacitance and Si-Pd work function difference from Table 6.1. The V_{ZC}^{\pm} corresponding to $t = 9$ s in Fig. 6.12, and the calculated P_{IPE} s are listed in Table 6.2. A significant reduction can be observed in P_{IPE} as compared to P_R due to the transient depolarizing currents

in the 9 s IPE measurement pulse.

t_{FE} (nm)	V_{FB}^+ (V)	V_{FB}^- (V)	$+P_{IPE}$ ($\mu\text{C}/\text{cm}^2$)	$-P_{IPE}$ ($\mu\text{C}/\text{cm}^2$)
4.8	N/A	-0.4	N/A	0.7
5.6	0.3	-0.7	1.9	1.2
6.9	0.7	-0.7	4.9	1.2

TABLE 6.2

EXTRACTED VALUES FLAT BAND VOLTAGES V_{FB}^\pm AT $T = 9$ S IN THE IPE SETUP, AND THE CORRESPONDING CALCULATED VALUES OF FE POLARIZATION P_{IPE} EXPECTED DURING THE IPE MEASUREMENT.

6.2.2 Analysis of IPE measurements

The IPE measurement protocol is applied to the Pd/HZO/p⁺ Si capacitors with $V_{IPE} = 0.7, 0.8, \text{ and } 0.9$ V used for $t_{FE} = 4.8$ nm are 0.7, 0.8, and 0.9 V; $V_{IPE} = 0.9, 1.0, \text{ and } 1.1$ V for $t_{FE} = 5.6$ nm; $V_{IPE} = 1.0, 1.1, 1.2$ V for $t_{FE} = 6.9$ nm. Note that higher magnitudes of V_{IPE} lead to a larger IPE current, but also cause capacitor breakdown in fewer measurement cycles. Therefore, intermediate values of V_{IPE} are chosen while ensuring that $|V_{IPE}| > |V_{ZC}^\pm|$. Measured yield curves of the Pd/HZO/p⁺ Si capacitors are plotted with respect to photon energy as the dotted data points in

Fig. 6.13. The curves are individually fitted to the equation

$$Y_{TOT}(h\nu) = A_1(h\nu - \Phi_1) + A_2(h\nu - \Phi_2)^2 + A_3(h\nu - \Phi_3)^3 \quad (6.9)$$

using a least square fitting procedure, with the additional constraint that $A_n = 0$ for $h\nu < \Phi_n$. The yield fits are superimposed with the measured yields in Fig. 6.13, where the fits are plotted as solid lines.

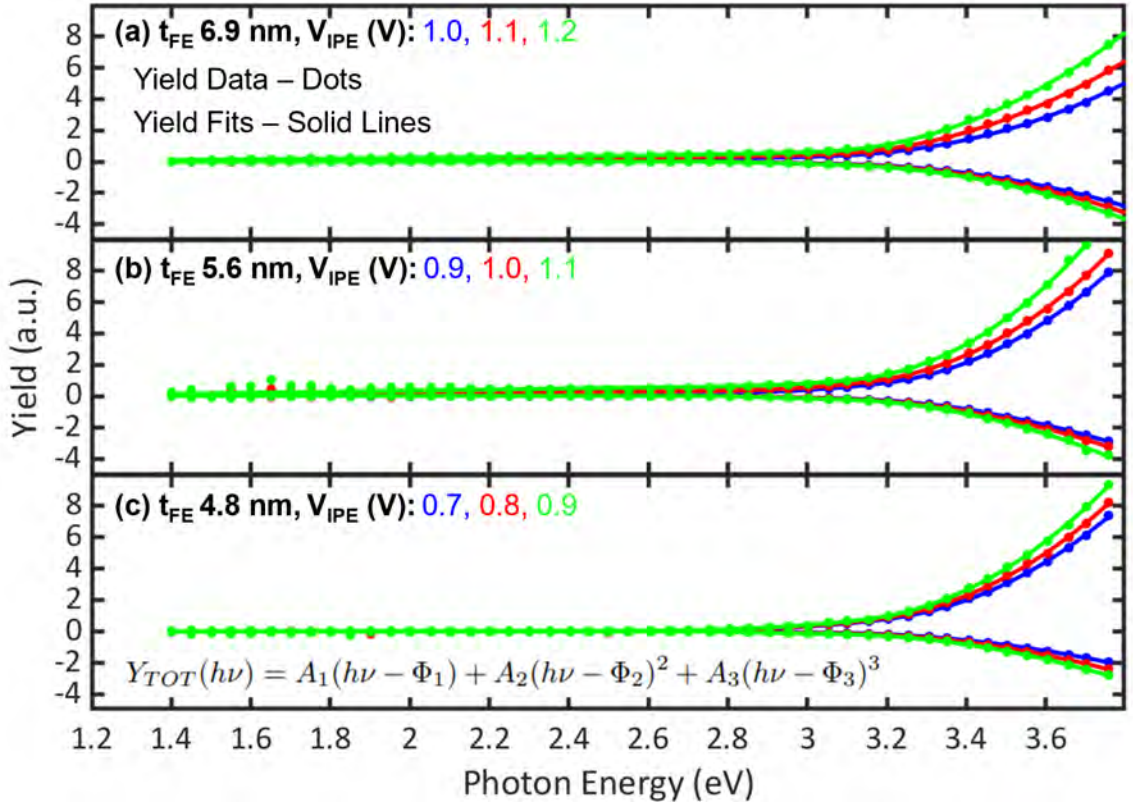


Figure 6.13. Measured (dots) and fitted (solid lines) yield curves in Pd/HZO/p⁺ Si capacitors. Both (+ V_R , + V_{IPE}) and (- V_R , - V_{IPE}) measurements are shown, for three different V_{IPE} s for each capacitor.

When the initial guess in the least square fitting procedure is modified, the extracted values of Φ_1 and Φ_3 , corresponding to Si/HZO transitions, vary up to 2 eV, while the values for Φ_2 , corresponding to Pd/HZO transitions, remain consistent within 0.1 eV. The Pd forms the top layer and has a higher density of states than Si due to its metallic nature, which should lead to the strongest transition in the measured yield curves. Only a single transition is clearly visible in the yield curves, Fig. 6.13; Φ_1 and Φ_3 correspond to weak Si/HZO transitions, and therefore could not be reliably extracted. The extracted barrier heights Φ_n are plotted with respect to the applied field $E_{IPE} = V_{IPE}/t_{FE}$ in Fig. 6.14. The Pd/HZO transitions are highlighted and used to extract the material band offsets. It should be noted that setting Φ_1 and Φ_3 to values that are consistent with the extracted Φ_2 values does not affect the goodness of fits, or the extracted Φ_2 values.

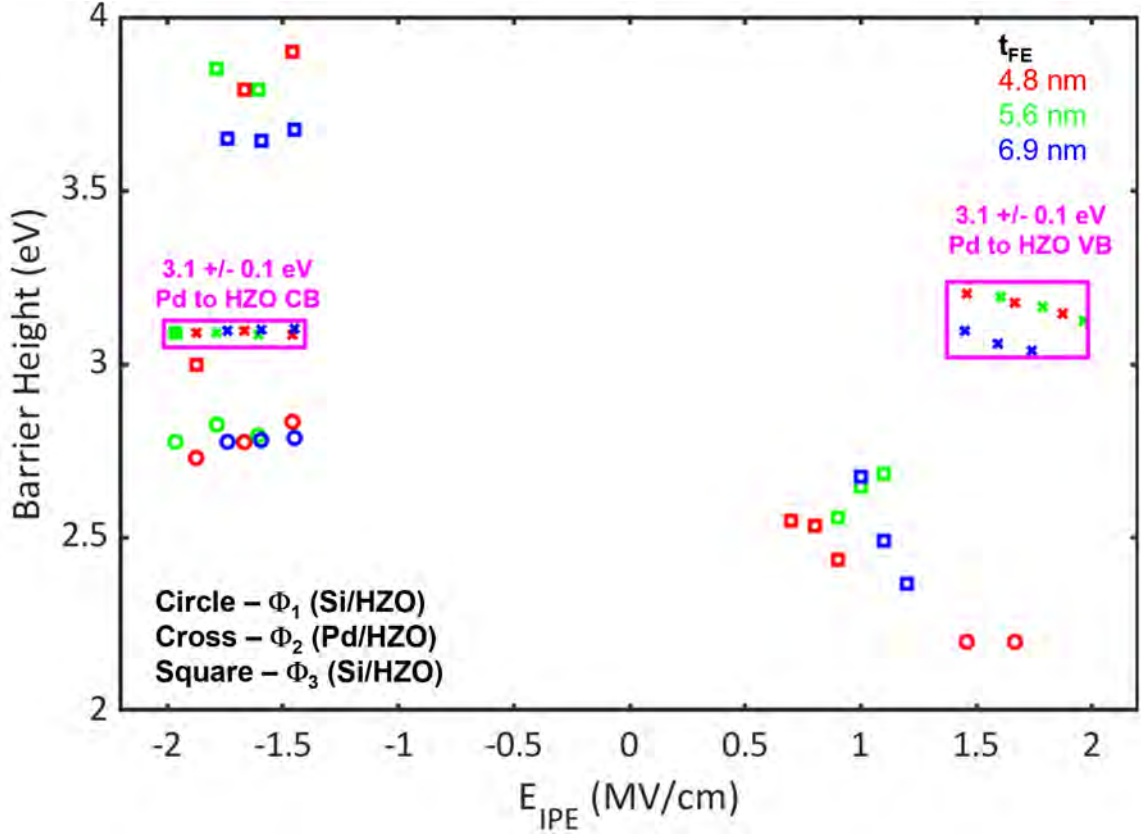


Figure 6.14. Extracted barrier heights Φ_n plotted with respect to applied electric field E_{IPE} .

6.2.3 Band alignment in Pd/HZO/p⁺ Si capacitors

The flat band offsets in Pd/HZO/p⁺ Si capacitors are obtained using the Pd/HZO barrier heights extracted from IPE yield fitting in Fig. 6.13 and the Si/Pd work function difference calculated in Sec. 6.1.5. The extracted Pd/HZO band offsets are added to yield an HZO bandgap of 6.2 ± 0.2 eV, close to the reported HfO₂ and ZrO₂ bandgaps of 5.6 ± 0.1 eV and 5.5 ± 0.1 eV, respectively [50, 78]. This suggests bowing in the Vegard's Law curve governing the material band gaps. It should be noted that the ZrO₂ and HfO₂ bandgaps have been shown to vary by up to 0.4 eV

depending on the post-deposition anneals [50, 78]. The p⁺ Si/HZO $\Phi_{MS} = 0.06 \pm 0.05$ eV extracted using flat band analysis in Sec. 6.1.5, combined with the known Si bandgap of 1.1 eV and extracted Pd/HZO VB and Pd/HZO CB band offsets provide the Si VB to HZO VB band offset $\Delta VB_{Si-HZO} = 3.2 \pm 0.2$ eV, and the Si CB to HZO CB band offset $\Delta CB_{Si-HZO} = 1.9 \pm 0.2$ eV. A comparison of these values with the corresponding values for HfO₂ and ZrO₂, Table 6.3, also suggests bowing in the corresponding Vegard's Law curves. The flat-band Pd/HZO/p⁺ Si band alignments are shown in Fig. 6.15.

Material	E_G (eV)	ΔVB (eV)	ΔCB (eV)
HZO (this work)	6.2 ± 0.2	3.2 ± 0.2	1.9 ± 0.2
HfO ₂ [50]	5.6 ± 0.1	2.5 ± 0.1	2.0 ± 0.1
ZrO ₂ [78]	5.5 ± 0.1	2.0 ± 0.1	2.4 ± 0.1

TABLE 6.3

COMPARISON OF EXTRACTED HZO/P⁺ SI BAND OFFSETS WITH HFO₂/SI AND ZRO₂/SI BAND OFFSETS EXTRACTED BY AFANASEV [50, 78].

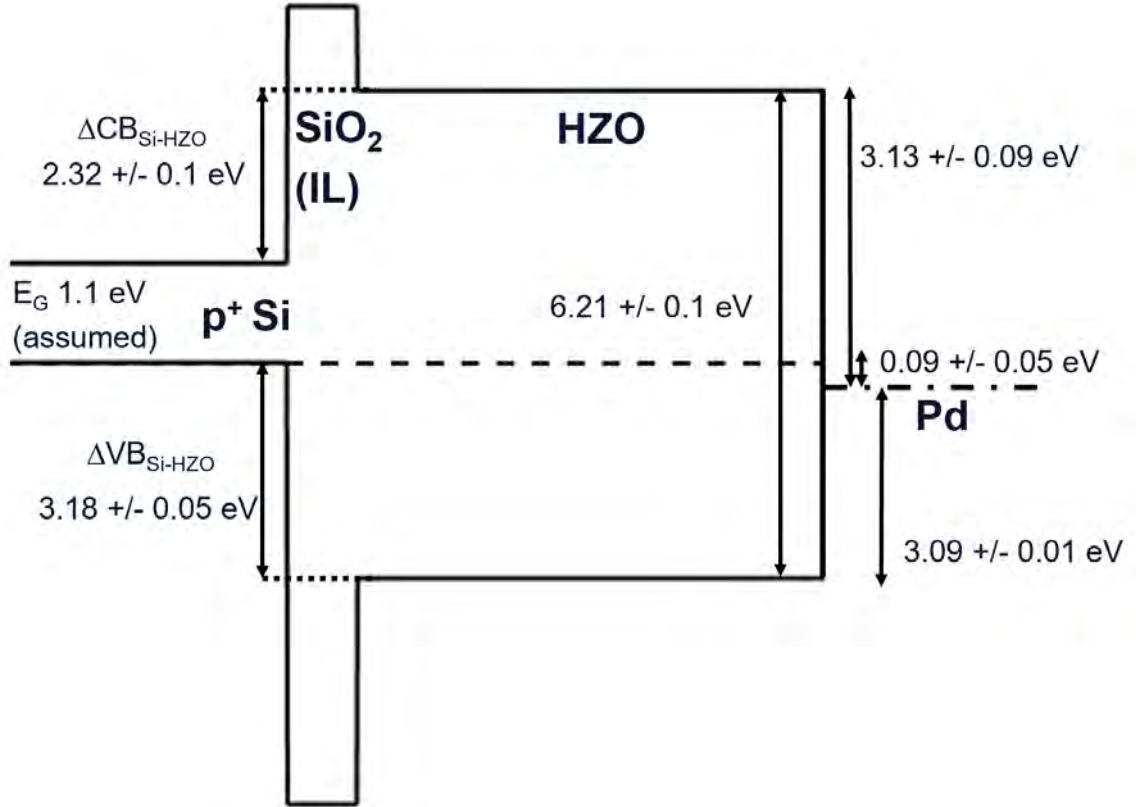


Figure 6.15. Extracted flat band alignment, considering zero FE polarization, for Pd/HZO/p⁺ Si capacitors.

6.2.4 Polarization dependent IPE transitions in Pd/HZO/p⁺ Si capacitors

The Si/HZO transitions in Fig. 6.13 were not sufficiently strong to directly extract polarization dependent Si/HZO band offsets. In this section, the band offsets ΔVB_{Si-HZO} and ΔCB_{Si-HZO} (hereon referred as ΔVB and ΔCB for brevity) are used to estimate the polarization dependent Si/HZO IPE transition cutoff energies Φ_1 and Φ_3 for both $\pm P$ orientations.

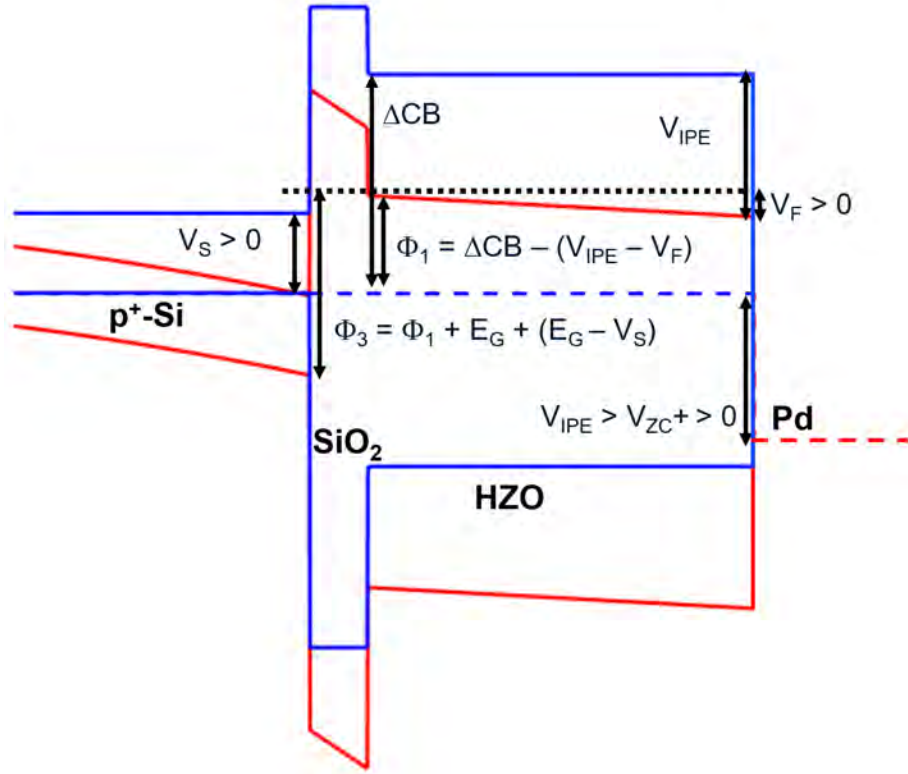


Figure 6.16. Band diagrams of a Pd/HZO/SiO₂/p⁺ Si capacitor. The blue band diagram corresponds to a flat band condition with zero voltage across the capacitor and zero FE polarization. The red band diagram corresponds to a +*P* polarization orientation.

First, the case of +*P* polarization orientation is considered. Figure 6.16 shows the band diagrams of the Pd/HZO/SiO₂/p⁺ Si structure assuming zero FE polarization and zero capacitor bias, and a band diagram corresponding to a +*P* polarization orientation. From Fig. 6.16, for a +*P* FE polarization at the Si/HZO interface, it can be seen that

$$\Phi_1 = \Delta CB - (V_{IPE} - V_F) = \Delta CB - (V_S + V_I). \quad (6.10)$$

$$\Phi_3 = \Phi_1 + E_G + (E_G - V_S). \quad (6.11)$$

Equation 6.10 signifies that the difference between the Si CB to HZO CB barrier heights in the flat band vs. the $+P$ polarization is due to band bending in the Si and the SiO₂ interlayer. The formalism developed in Sec. 6.1.5 can be used to estimate Φ_1 and Φ_3 for $+V_R, +V_{IPE}$ measurements, using the calculated P_{IPE} in Table 6.2, the calculated IL capacitance in Table 6.1, the band offsets in Fig. 6.15, and the HZO relative permittivity $\epsilon_F = 37$ measured by Alessandri and Pandey [41]. Setting $V = V_{IPE} = V_S + V_I + V_F + \Phi_{MS}$ in Fig. 6.8, the band bending in the Si and IL can be calculated by numerically solving the transcendental equation

$$V_S(Q_S) + \frac{Q_S}{C_I} + \frac{Q_S - P_{IPE}}{C_F} + \Phi_{MS} = V_{IPE}. \quad (6.12)$$

for Q_S . Here, the FE capacitance is given as $C_F = \epsilon_F/t_{FE}$.

A similar analysis can be carried out for the $-P$ polarization orientation. Figure 6.17 shows the band diagrams of the Pd/HZO/SiO₂/p⁺ Si structure assuming zero FE polarization and zero capacitor bias (i.e. a flat band diagram) and a band diagram corresponding to a $-P$ polarization orientation. From Fig. 6.17, for a $-P_{IPE}$ FE polarization at the Si/HZO interface, it can be seen that

$$\Phi_1 = \Delta VB + (V_{IPE} - V_F) = \Delta VB + (V_S + V_I). \quad (6.13)$$

$$\Phi_3 = \Phi_1 + E_G - V_S. \quad (6.14)$$

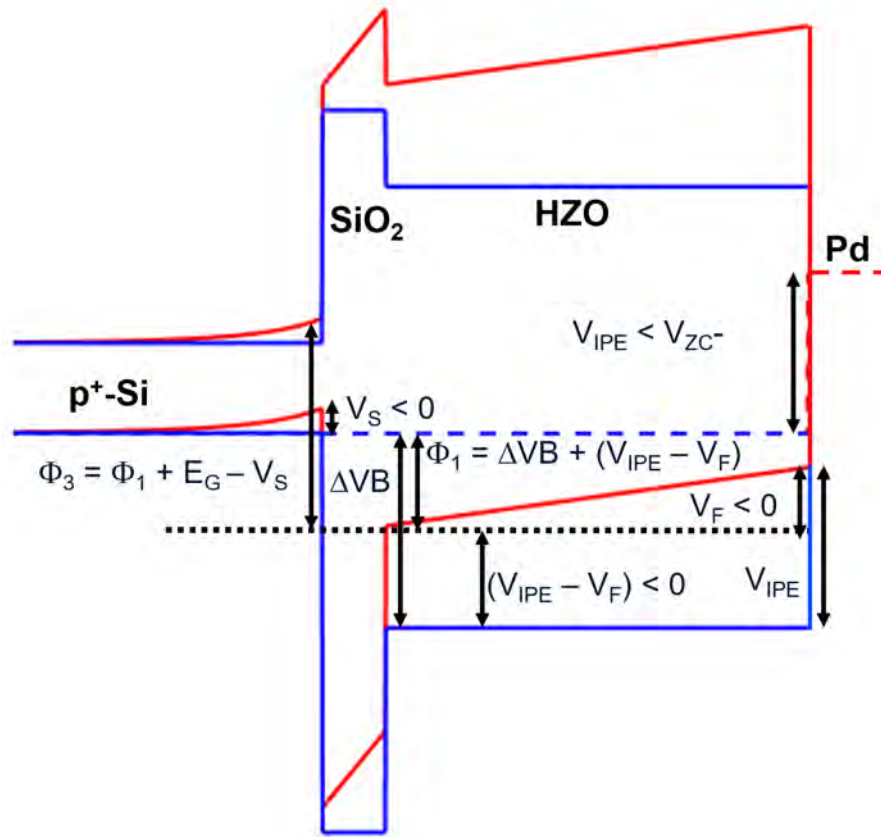


Figure 6.17. Band diagrams of a Pd/HZO/SiO₂/p⁺ Si capacitor. The blue band diagram corresponds to a flat band condition with zero voltage across the capacitor and zero FE polarization. The red band diagram corresponds to a $-P$ polarization orientation.

Once again, Eq. 6.13 signifies that the difference between the Si VB to HZO VB barrier heights in the flat band vs. the $-P$ polarized condition is due to the band bending in the Si and the SiO₂ interlayer. The polarization dependent barrier heights are calculated from Eq. 6.12 and listed in Table 6.4.

t_{FE} (nm)	$ V_{IPE} $ (V)	$-P$		$+P$	
		Φ_1 (eV)	Φ_3 (eV)	Φ_1 (eV)	Φ_3 (eV)
		VB→VB	CB→VB	CB→CB	VB→VB
4.8	0.8	2.66	3.87	N/A	N/A
5.6	1	2.59	3.82	1.26	2.73
6.9	1.1	2.65	3.88	0.74	1.80

TABLE 6.4

PREDICTED POLARIZATION DEPENDENT IPE TRANSITIONS IN
PD/HZO/P⁺ SI CAPACITORS.

6.2.5 Improving measurement signal-to-noise

The measured yield curves in Fig. 6.13 show signs of multiple transitions, but the transitions are not distinctly separated. This causes fitting errors in the weaker Si/HZO transitions. Fabricating Pd/HZO/p⁺ Si samples with different thicknesses of the semi-transparent Pd electrode is expected to improve in identifying the different IPE transitions. A thinner semi-transparent Pd electrode would allow more photons to be transmitted to the Si layer, increasing the yield of Si/HZO transitions and a reducing the yield of Pd/HZO transitions. Therefore, correlating different parts of the observed yield spectra with Pd thickness would increase the accuracy of identifying different transitions, thereby improving the goodness of fits.

Optical chopping can also be used to improve detection of the weak Si/HZO transitions. This is made challenging since the FE depolarization transient currents

decay over a 10 ms - 10 s timescale, which is comparable to the recommended optical chopping frequency of ~ 10 Hz for IPE measurements [79]. Incorporating optical chopping into the FE-specific IPE measurement protocol would therefore necessitate a detailed analysis of transients relating to photoexcited carriers in MFIS capacitors.

A larger step size between the IPE voltages can be used to extrapolate the field dependent barrier heights in Fig. 6.14 to a zero electric field value. Finally, inclusion of Pd/HZO/ n^+ Si capacitors would provide additional Si/HZO transitions, obviating the need to use the Si bandgap value to determine the Si/HZO band offsets.

CHAPTER 7

CONCLUSIONS

This thesis has explored the dynamics of reading and writing the partial polarization state in ferroelectric (FE) capacitors. In particular, new pulse measurement protocols that minimize spurious interface charging effects have been developed to more precisely measure polarization, polarization reversal, and current-voltage characteristics. Analytic methods to interpret these measurements have also been developed.

The first study of partial polarization in HZO was carried out as part of this research, and published by Kinder in 2017 [19]. In this paper the partial polarization of HZO capacitors was measured for a single write pulse amplitude and write pulse durations from 200 ns to 10 μ s. This work was extended by Alessandri and Pandey [24] to show that the switching speed of the polarization reversal is limited by the nucleation of FE domains within the grains of the polycrystalline FE thin film. The nucleation limited switching (NLS) model was then used to extract the distribution of nucleation time constants and activation fields in the FE and extrapolate to quantify the effects of scaling [39, 41], confirming the accuracy of the NLS model in predicting the switching dynamics of polycrystalline HZO capacitors. These results established the mechanisms by which the partial polarization is set in polycrystalline FEs to store analog weights, and a characterization and fitting procedure to extract the FE properties.

In an ideal MFM capacitor with symmetric electrodes, the NLS model predicts symmetric polarization reversal characteristics when the FE polarization changes

from $+P_R$ to $-P_R$ and from $-P_R$ to $+P_R$, but this is not always found to be true in practice. For the W/HZO/W capacitors studied by Alessandri and Pandey in 2019 [39], the same set of NLS parameters were able to accurately capture the polarization reversal from $+P_R$ to $-P_R$ and from $-P_R$ to $+P_R$, and predict the capacitors' response to arbitrary waveforms. However, structural differences in the metal/FE interface as well as interfacial layers can readily lead to asymmetry in FE capacitors. In Pandey 2019 [42], the polarization reversal characteristics of W/HZO/W capacitors were found to require separate NLS parameters to describe polarization reversal from $+P_R$ to $-P_R$ and from $-P_R$ to $+P_R$, indicating an asymmetry in the two W/HZO interfaces. Even greater asymmetry was found in the polarization reversal characteristics of TiN/HZO/TiN capacitors, which did not yield saturated polarization reversal curves, and exhibited markedly different degrees of unsaturation and switched polarization densities for polarization reversal from $+P_R$ to $-P_R$ and from $-P_R$ to $+P_R$. These findings led to discovering the impact of the measurement protocol itself on the FE partial polarization which was reported in Pandey 2020 [40]. The reason for the unsaturated polarization reversal characteristics in TiN/HZO/TiN was later found to be due to asymmetry in the pulse measurement protocol, and the unsaturation was reduced when a strictly symmetric measurement protocol was used.

A strictly symmetric pulse protocol is defined as the condition that the integral of the pulse measurement waveform voltage over a measurement cycle is zero. In this way, the effects of biasing are balanced equally to minimize charging of the interfaces. The observed unsaturation in the asymmetric measurements on TiN/HZO/TiN capacitors was substantially eliminated using the strictly symmetric protocol. This is ascribed to the removal of history dependent electronic charging and discharging of traps as well as ionic accumulation and depletion at the metal/FE interfaces. These results highlighted the NLS model can still be applicable in FEs if the strictly symmetric measurement protocol is applied in polarization reversal measurements.

Since device applications based on multilevel memory do not in general utilize a strictly symmetric pulsing protocol [38, 80], these measurement methods provide a procedure to distinguish polarization switching from interface charging for analog storage. If insignificant difference is observed in the FE polarization reversal characteristics measured with a strictly symmetric vs. an asymmetric protocol, it is an indication of low density of trap/ionic charges relative to the FE polarization charge density.

After discovering the impact of the measurement protocol on FE partial polarization, the impact of varying the reset time, delay-before-read, and delay-before-write was studied. The partial polarization in W/HZO/W capacitors was shown to be stable up to 250 ms delay-before-read, leading to an estimated lower bound on the decay time constant to be 24.9 s. The delay-before-read in these measurements was stepped to 250 ms; however, the same protocol can be used for longer delay-before-read times to quantify retention of partial polarization in FTJs and FeFETs.

Another surprise in the characterization of FE partial polarization is that there exists a time dependence in the partial polarization on pulse intervals where no dependence was expected. The partial polarization was found to decay with increasing delay-before-write, as well as for increasing reset times. The observed behavior was found to be qualitatively explained by the dynamics of subcritical nuclei within an FE grain. The subcritical nuclei were shown to exist for times as long as 1 s. The subcritical nuclei were estimated to be less than 10 nm^3 ($4 \times 4 \times 4$ unit cells) in size, but their dynamics were shown to affect partial polarization up to 25% of the FE remanent polarization.

The strictly symmetric pulse measurement protocol was also found to be useful in the measurement of current-voltage-time characteristics. Here, the strictly symmetric protocol was again utilized to minimize effects of ionic motion and trap charging/discharging over multiple measurement cycles. In the I-V-t measurements

on Pd/HZO/p⁺ Si capacitors, a decrease in the capacitor current was observed with respect to measurement time if the applied capacitor bias was lower in magnitude than the HZO flat band voltage. For these applied biases, the current direction was found to be opposite to the applied bias polarity, and the current magnitude increased when the applied bias magnitude was further decreased. A quantitative modeling was carried out to show that these observations were consistent with the assumption that the HZO electric field controlled the capacitor current. These results highlighted the necessity of characterizing the time dependence of MFS capacitor currents to identify read voltages and read times appropriate for analog memory applications.

A spectroscopic photoresponse measurement system was constructed, capable of measuring electrical responses to photons ranging in energy from 0.6 - 7 eV, to measure polarization dependent band offsets of MFS capacitors by internal photoemission (IPE) measurements. The measurement system was shown to have a 800-1800x greater photon flux density than the corresponding setup at NIST, Gaithersburg. Internal photoemission measurements were made on Pd/HZO/p⁺ Si capacitors using the configured system. In the IPE measurements, only Pd/HZO IPE transitions were sufficiently strong to extract band offsets, and the Si/HZO band offsets could not be directly extracted from IPE measurements. Based on the Pd/HZO band offsets, the first IPE-based bandgap of HZO was extracted as 6.2 ± 0.2 eV. The model developed to analyze I-V-t measurements was used to indirectly extract the band offsets between the Si CB/HZO CB and Si VB/HZO VB using the Pd/HZO band offsets extracted from IPE measurements. The extracted band offsets parameters were indicative of a bowing in the HfO₂-ZrO₂ Vegard's Law curve. Experimental modifications were suggested to improve the measurement accuracy and directly measure polarization dependent Si/HZO band offsets.

In conclusion, this thesis utilized pulsed measurements to uncover new effects relating to the dynamics of polarization and current in HZO MFM and MFS capac-

itors. The partial polarization in W/HZO/W capacitors was found to be sensitive to pulsing history. The current in Pd/HZO/p⁺ Si capacitors was found to be time dependent, and the time dependence was consistent with the current being controlled by the HZO electric field. These results highlighted the dynamic aspects of ferroelectric HZO, and the importance of a careful, application-specific characterization of these dynamic behaviors.

APPENDIX A

PARTIAL SWITCHING OF FERROELECTRICS FOR SYNAPTIC WEIGHT
STORAGE

Partial Switching of Ferroelectrics for Synaptic Weight Storage

Erich W. Kinder¹, Cristobal Alessandri¹, Pratyush Pandey¹, Golnaz Karbasian²,
Sayeef Salahuddin², and Alan Seabaugh¹

¹Dept. of Electrical Engineering, U. of Notre Dame, Notre Dame, IN, USA

²Dept. of Electrical Engineering and Computer Sciences, Univ. of California, Berkeley, CA, USA

Email: seabaugh.1@nd.edu / Phone: (574) 631-4473

Introduction. Gokmen and Vlasov proposed that the training of deep neural networks would be dramatically accelerated by the realization of resistive processing units that can store analog weights to minimize data movement during training [1]. Here we measure and evaluate the partial switching of the ferroelectric (FE) PbZrTiO₃ (PZT) and, for the first time, Hf_{0.8}Zr_{0.2}O₂ (HZO), formed by atomic layer deposition, for use as a nonvolatile analog memory element. The spontaneous polarization P of a FE can be switched by applying a voltage that exceeds the coercive voltage for switching of the FE. This polarization, when fully switched, can have a value of $+P$ or $-P$ (C/cm²), depending on the polarity of the applied voltage. Ferroelectric memory is typically operated in fully switched $+P$ or $-P$ polarizations, however with short (< 10 μ s) pulsed voltages, the FE can be partially switched, i.e. only a fraction of the domains are switched during the pulse duration as shown by Tokumitsu in PZT [2] and indicated in Fig. 1.

Experiment. In this work, PZT and HZO were partially switched by using < 10 μ s voltage pulses. The FEs were incorporated into a parallel plate capacitor structure, Fig. 2. To measure partial polarization, the FE was first set to the $-P$ polarization by the application of a 2-ms, negative triangular voltage waveform with amplitude exceeding the coercive voltage of the FE. The FE was then partially switched by application of either a varying number of pulses or by varying width of the pulses. The partial polarization is read out *via* the same triangular voltage waveform used to initially polarize the FE. By measuring the current as the voltage is ramped to read out and reset the device, the polarization current from the FE domain switching can be detected. By integrating this current, a polarization vs. applied voltage plot is created, where the hysteresis results from the FE partial switching.

Device Measurements. First a commercial PZT capacitor was characterized (Radiant Technologies, Type AB, 400 μ m², shown Fig. 2a). The full switching characteristic was measured by applying a triangular waveform and measuring the current as the capacitor is polarized to $+P$ and back to $-P$, Fig. 3. The polarization-voltage (P - V) curve in Fig. 4 was obtained by integrating the current. The hysteresis in this plot gives a measurement of the full polarization of the FE. By comparing the data from the P - V curve taken following partial switching (switching current shown Fig. 5, P - V in Fig. 6) to the full polarization switching P - V , Fig. 4, the partial polarization state can be identified as a function of the number of pulses, Fig. 7. With the information from the PZT capacitor to be used as a comparison, a 1000 μ m² parallel plate capacitor with HZO as a dielectric was fabricated, Fig. 2b. This was then subjected to the partial switching regimen to determine HZO's partial switching capabilities, with the switching current, P - V showing partial polarization and change in polarization for varying pulse width plotted as Figs. 8, 9 and 10 respectively.

Discussion. In a synaptic weight storage element that senses a voltage pulse and produces a current, the parameter of interest is the conductance. By gating a semiconducting channel with partially switched HZO, we can estimate $\Delta n_{\text{channel}}$ as $\Delta P/q$. Therefore, the change in conductivity is roughly $\Delta\sigma = \mu_n \Delta P$. For the HZO capacitor, the total measured polarization change was $\Delta P_{\text{total}} = 1.045$ μ C/cm², whereas the smallest polarization change was $\Delta P_{\text{min}} = 0.029$ μ C/cm², which gives at least 36 distinct levels. These measurements were limited by the minimum pulse width of 100 ns that could be used to program the HZO due to its large capacitance, so a smaller ΔP_{min} could be achieved by using a smaller area device. The number of levels will be ultimately limited by the domain density and the device area. These first measurements show that HZO can be used for a multilevel weight storage element. To explore this possibility, further study of device scaling, state retention and endurance is required.

This work was supported in part by the Center for Low Energy Systems Technology (LEAST), one of six centers of STARnet, a Semiconductor Research Corporation program sponsored by MARCO and DARPA, by the National Science Foundations under ECCS/GOALI-1408425, and by CONICYT-PCHA/Doctorado Nacional/2014-2114059.

References

[1] T. Gokmen and Y. Vlasov *Front. Neurosci.* 10, 333, (2016). [2] E. Tokumitsu et al. *Jpn. J. Appl. Phys.* 33, 5201 (1994).

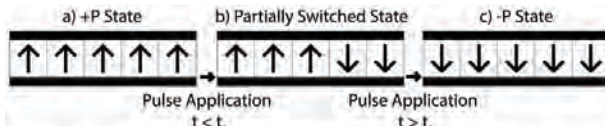


Figure 1: Schematic showing the polarization of individual domains in (a) +P, (b) partially switched (*i.e.* between +P and -P), and (c) -P



Figure 2: Cross-sectional diagram of (a) the PZT and (b) HZO ferroelectric capacitor

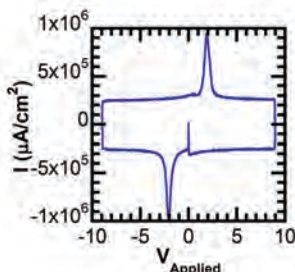


Figure 3: I-V of a PZT-dielectric capacitor showing the increase in current as the FE switches

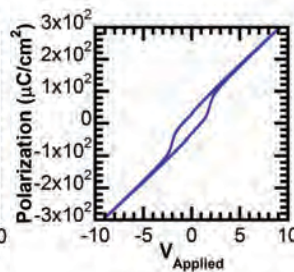


Figure 4: P-V of PZT dielectric capacitor, taken from integrating data in figure 3

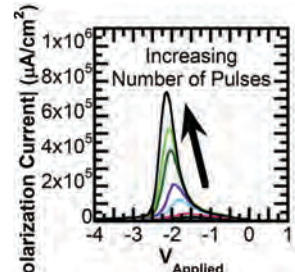


Figure 5: P-V of the PZT capacitor vs. number of 5V, 50 ns pulses, showing partial switching

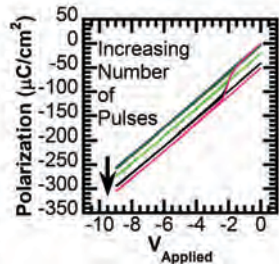


Figure 6: P-V of the PZT capacitor after pulsing, showing switching from partial polarization back to the -P state

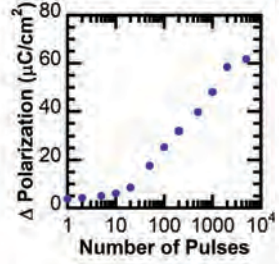


Figure 7: Change in polarization of the PZT capacitor for varying number of pulses

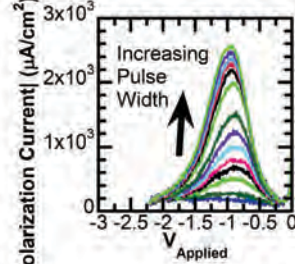


Figure 8: P-V of the HZO dielectric capacitor

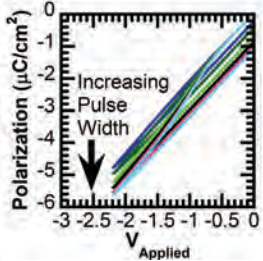


Figure 9: P-V of the HZO capacitor after pulsing showing switching from partial polarization back to the -P state

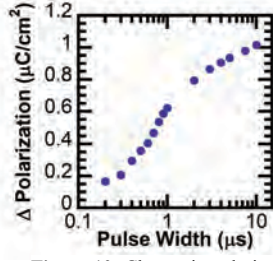


Figure 10: Change in polarization of the HZO capacitor for varying pulse width

APPENDIX B

SWITCHING DYNAMICS OF FERROELECTRIC ZR-DOPED HFO₂

Switching Dynamics of Ferroelectric Zr-Doped HfO₂

Cristobal Alessandri¹, Student Member, IEEE, Pratyush Pandey, Angel Abusleme², Member, IEEE, and Alan Seabaugh¹, Fellow, IEEE

Abstract—Ferroelectric Zr-doped HfO₂ (HZO) is a promising candidate for steep slope transistors and memory technology. For these applications, it is essential to understand and optimize the switching dynamics of the ferroelectric film. In this letter, we characterize the polarization reversal of an 8 nm-thick HZO film deposited by the atomic layer deposition with voltage pulses varying in amplitude (0.8–2 V) and duration (200 ns–7.6 ms). We show that the measurements are well described by a nucleation limited switching model, which enables extraction of the minimum switching time and the probability distribution of local electric field variations in the polycrystalline film. The close model fit spanning 5 orders of magnitude in pulse duration indicates the applicability of this model to HZO. This characterization framework can be used to quantify, compare, and optimize the switching dynamics of ferroelectric HZO.

Index Terms—Ferroelectric devices, analytical models, hafnium compounds.

I. INTRODUCTION

THE discovery of ferroelectricity in the CMOS-compatible HfO₂ material system [1] has led to a variety of applications including memory [2]–[4], steep slope transistors [5], [6], and neuromorphic computing [7], [8]. Several studies have analyzed the effect of growth and annealing conditions on the FE properties of Zr-doped HfO₂ (HZO), such as the Zr concentration [9], [10], electrode material [11], [12] and annealing temperature [13], [14]. These studies usually focus on properties that can be directly measured from the polarization-voltage (P - V) loops, such as the remanent polarization and endurance, but provide limited insight into the FE dynamics or speed limitations, a subject that is widely

Manuscript received September 12, 2018; revised September 19, 2018; accepted September 21, 2018. Date of publication September 26, 2018; date of current version October 23, 2018. This work was supported in part by the Center for Low Energy Systems Technology (LEAST), one of six centers of STARnet, through the Semiconductor Research Corporation Program sponsored by MARCO and DARPA, and in part by the National Science Foundations under Grant ECCS/GOALI-1408425. The review of this letter was arranged by Editor G. Han. (Corresponding author: Alan Seabaugh.)

C. Alessandri is with the Department of Electrical Engineering, University of Notre Dame, Notre Dame, IN 46556 USA, and also with the Department of Electrical Engineering, Pontificia Universidad Catolica de Chile, Santiago 7820436, Chile.

P. Pandey and A. Seabaugh are with the Department of Electrical Engineering, University of Notre Dame, Notre Dame, IN 46556 USA (e-mail: seabaugh.1@nd.edu).

A. Abusleme is with the Department of Electrical Engineering, Pontificia Universidad Catolica de Chile, Santiago 7820436, Chile.

Color versions of one or more of the figures in this letter are available online at <http://ieeexplore.ieee.org>.

Digital Object Identifier 10.1109/LED.2018.2872124

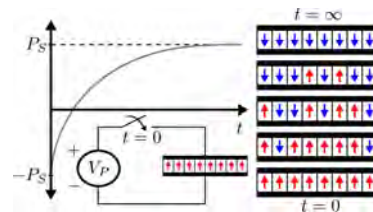


Fig. 1. Polarization reversal of a polycrystalline FE film. Starting from a fully polarized state $-P_S$, a positive voltage is applied at $t = 0$. The FE grains switch and increasingly align until the FE reaches the fully polarized state $+P_S$.

debated [15], [16]. On the other hand, nucleation limited switching (NLS) models for polarization reversal provide an accurate description of the switching transient of FE thin films, and have been experimentally validated in other material systems [17]–[19]. Although it has been shown that the polarization reversal of ferroelectric HfO₂ occurs in the nucleation limited regime [20]–[22], only one prior study reports parameter extraction by applying an NLS model to Al-doped HfO₂ [23].

In this work, we show that the NLS model [17] provides a good description of the polarization reversal of HZO films, under the assumption of a distribution of switching times that originate from variations in the local electric field [19]. We extract the probability distribution that characterizes the electric field variations and the parameters that govern the polarization dynamics. This characterization framework can be used to guide the optimization of the HZO material system.

II. MODEL FOR POLARIZATION REVERSAL IN THIN-FILM FERROELECTRICS

Figure 1 depicts the polarization reversal of a polycrystalline FE thin film, which is composed of many grains with fixed grain walls. When all the grains are polarized in the same direction, a saturation polarization P_S is obtained (C/m^2). Starting from the $-P_S$ state, if a positive voltage is applied at $t = 0$, the FE grains will start to switch polarization until the whole FE reaches the $+P_S$ state. A stable partially polarized state is obtained by pulsing the applied voltage for a time t short enough so only a fraction of the FE grains are able to switch. The NLS model was proposed to account for multigrain polarization by characterizing the thin film as an ensemble of elementary regions that switch independently with a distribution of switching times [17]. This distribution of switching times was later attributed to

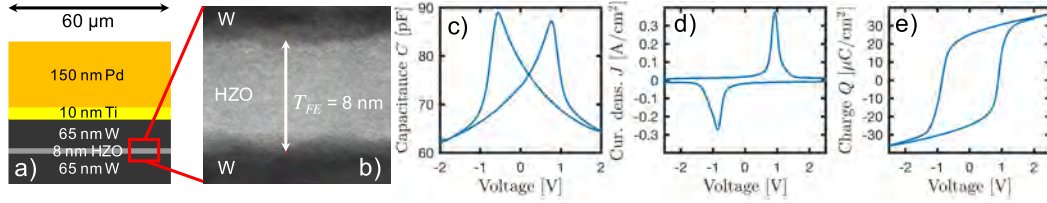


Fig. 2. a) Cross section and b) TEM of 8 nm thick $\text{Hf}_{0.5}\text{Zr}_{0.5}\text{O}_2$ FE capacitor with 60 μm -diameter top electrode. c) Capacitance-Voltage measurements with 1 V/s sweep rate and 30 mV, 100 kHz AC signal. d) Current-voltage characteristic of $\text{Hf}_{0.5}\text{Zr}_{0.5}\text{O}_2$, measured with a 2.5 V triangular waveform with 4 ms period. e) P - V loop obtained by integrating the current-voltage characteristic.

variations in the local electric field when a uniform external field is applied, due to impurities or crystal defects [18], or the intrinsic inhomogeneity of the FE film [19]. The field-dependent NLS model can be summarized as follows: The switching of a single elementary region is described by a stretched exponential with parameter β [18], [19]

$$p(t, \tau) = 1 - \exp\left[-\left(\frac{t}{\tau}\right)^\beta\right]. \quad (1)$$

The characteristic switching time τ is a function of the local field E and an activation field E_a , expressed by the empirical relation [19], [24]

$$\tau(E_a, E) = \tau_\infty \exp\left[\left(\frac{E_a}{E}\right)^\alpha\right], \quad (2)$$

where τ_∞ is the time constant obtained for an infinite applied field, and α is an empirical parameter. Assuming an inhomogeneous and field-independent dielectric permittivity, the local electric field value is expressed as $E = \eta E_{ext}$, where E_{ext} is the constant applied field and η is a random variable with probability density function (PDF) $f(\eta)$ and unity mean, defined in the $[0, \infty)$ interval [19]. As a result, the polarization reversal from $-P_S$ to $+P_S$ is computed as

$$P(E_{ext}, t) = -P_S + 2P_S \int_0^\infty p(t, \tau(E_a, \eta E_{ext})) f(\eta) d\eta \quad (3)$$

With this mathematical formulation, the FE film is characterized by the parameters P_S , E_a , β , α , τ_∞ and the probability density function $f(\eta)$.

III. EXPERIMENTAL RESULTS AND PARAMETER EXTRACTION

The cross section and transmission electron microscopy (TEM) of an 8 nm FE W/HZO/W capacitor are shown in Fig. 2a) and b). The device fabrication started by sputtering 65 nm W on a Si wafer. The HZO was deposited by atomic layer deposition at 300 °C with tetrakis(ethylmethylamino)hafnium and tetrakis(ethylmethylamino)zirconium precursors, and water vapor as the oxidant. The HZO was then capped with 65 nm of sputtered W and annealed at 500 °C for 30 s in N_2 . Then, 60 μm -diameter dots were deposited by shadow mask evaporation of Ti/Pd. Finally, the top W and HZO were etched using the Ti/Pd electrodes as a hard mask. A Hf:Zr ratio of 1:1 was verified with energy dispersive X-ray line scans.

Electrical measurements were performed with a Keithley 4200 parameter analyzer with a 4225-PMU pulse measurement

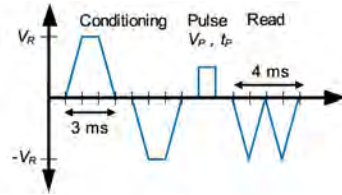


Fig. 3. Measurement protocol for polarization reversal. Conditioning pulses of amplitude $V_R = 2.5$ V are applied to reset the FE. A programming pulse of varying width and amplitude is applied, and the polarization is measured by two pulses of amplitude $V_R = 2.5$ V.

unit and two 4225-RPM remote preamplifiers. The experimental setup and the capacitor diameter were designed so that the partial polarization measurements are not limited by RC delays. The combined resistance of the 50 Ω output resistance of the remote amplifier and the series resistance of the probes was measured to be 54 Ω , which with the measured capacitance (Fig. 2c) results in a time constant in the order of 5 ns. A 2.5 V triangular waveform with 4 ms period was applied for 500 cycles for wake up. The current-voltage and P - V characteristics are shown in Fig. 2d) and e), measured after wake up. The measurement sequence performed to characterize the polarization reversal is depicted in Fig. 3. Conditioning pulses of amplitude $V_R = 2.5$ V are applied to reset the FE. The programming pulse width (t_P) was stepped from 200 ns to 7.6 ms in increments of 1.5 \times , then the amplitude (V_P) was stepped from 0.8 V to 2 V in increments of 100 mV. The polarization is measured by two consecutive negative pulses of amplitude $V_R = 2.5$ V and 1 ms rise time. The first pulse polarizes the capacitor back to the $-P_S$ state, and produces a current due to the linear capacitance and the polarization current of the switched domains. The displacement current due to the linear capacitance alone is measured by the second pulse, where there is no polarization current. The current difference is integrated to calculate the partial polarization. The pulse amplitude V_P is translated to field E_{ext} by dividing by the film thickness (T_{FE}). Figure 4 shows the polarization reversal measurements (dots) and the fitted model (solid lines) as a function of pulse width and pulse amplitude. In addition, polarization measurements with 2.5 V pulses (diamonds) are shown to verify that the conditioning and read pulses produce a saturated polarization.

The distribution of local field variations $f(\eta)$ was extracted from measurements with the method presented in [19]. The logarithmic derivative of the polarization with respect to the

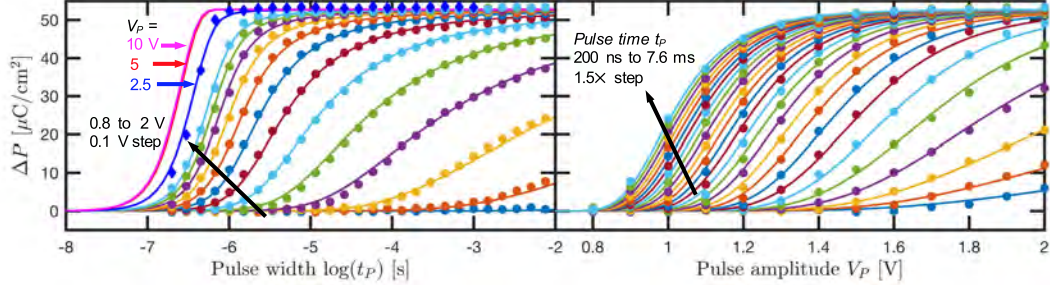


Fig. 4. Measured partial polarization (dots) vs. pulse width (left) and pulse amplitude (right) show close agreement with model (solid line) over 5 decades of pulse times. Extracted parameters are $P_S = 26.4 \mu\text{C}/\text{cm}^2$, $\tau_\infty = 236 \text{ ns}$, $E_a = 2.42 \text{ MV}/\text{cm}$, $\alpha = 3.73$ and $\beta = 2.06$. Measurements with 2.5 V pulse amplitude (diamonds) were not used for parameter extraction, which demonstrates the predictive capability of the model.

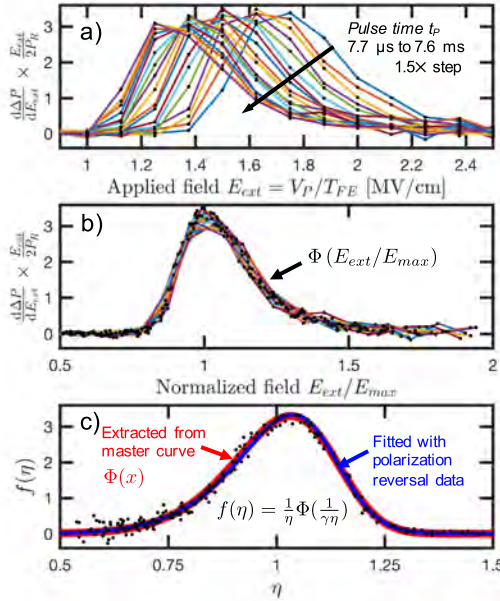


Fig. 5. Extraction of the distribution of local field variations $f(\eta)$ [19]. a) Derivatives of the polarization with respect to applied field. b) The derivatives overlap into a master curve $\Phi(x)$ when the x-axis is normalized by the field at which the derivatives are peaked. c) Distribution of local fields obtained from $\Phi(x)$ (red), with the proportionality constant γ derived from condition of unity mean. The same distribution was obtained by fitting the distribution parameters directly from the polarization reversal data (blue).

applied field exhibits a maximum at a certain field E_{max} that depends on the pulse time t_P , as shown in Fig. 5a). When the x-axis is normalized by E_{max} for each pulse time t_P , the derivatives overlap into a master curve $\Phi(x)$ (Fig. 5b)). The distribution $f(\eta)$ is obtained from the master curve as

$$f(\eta) = \frac{1}{\eta} \Phi\left(\frac{1}{\gamma\eta}\right), \quad (4)$$

where γ is a proportionality constant derived from the condition of unity mean [19]. As shown in Fig. 5c), the data is well described by a generalized beta distribution of type 2,

whose PDF is

$$GB2(\eta|a, b, p, q) = \frac{\frac{|a|}{b} \left(\frac{\eta}{b}\right)^{ap-1}}{B(p, q) \left(1 + \left(\frac{\eta}{b}\right)^a\right)^{p+q}}, \quad (5)$$

where $B(p, q)$ is the beta function. The distribution parameters are $a = 9.0986$, $b = 1.3935$, $p = 1.1101$ and $q = 15.197$. The parameters P_S , E_a , β , α and τ_∞ were then extracted by performing a least square fit of Eq. (3) with the polarization reversal data. Alternatively, once the analytic form of the distribution is known, its parameters can be extracted with the least square fit directly from the polarization reversal data. The resulting distribution is not sensitive to the extraction method, as shown in Fig. 5c), and the fitted parameters vary by less than 1%, which underscores the physicality of the model. Furthermore, the fitted model is able to predict the measured polarization reversal with 2.5 V pulses, which was not used for parameter extraction.

According to Eq. (2), as the applied field increases, τ asymptotically reaches its minimum value $\tau_\infty = 236 \text{ ns}$, which imposes a hard limit on the switching speed. This limitation is shown in Fig. 4 by extrapolating the pulse amplitude to 2.5, 5 and 10 V. The relative speed at which the FE grains switch is determined by the spread of the distribution of local field variations: grains at the higher end of the distribution have a smaller time constant and will switch sooner than those with η closer to zero. Therefore, a large variance in the local field distribution favors partial polarization, but is not desirable for fast transitions between saturated states ($\pm P_S$). Furthermore, a narrow distribution is needed for memory writing schemes that leverage the nonlinearity of the FE response to applied field [4].

IV. CONCLUSION

We modeled and characterized the polarization reversal of HZO. We show that the field-dependent NLS model provides a comprehensive description of the polarization reversal of HZO films for varying pulse amplitudes and pulse width spanning over 5 decades. We extracted the probability distribution that characterizes the local electric field variations in the FE film, and the parameters that govern the polarization dynamics. This characterization framework provides the tools to quantify, compare and optimize the switching dynamics and the nonlinear response to applied field of HZO films.

REFERENCES

- [1] T. S. Böscke, J. Müller, D. Bräuhäus, U. Schröder, and U. Böttger, "Ferroelectricity in hafnium oxide: CMOS compatible ferroelectric field effect transistors," in *IEDM Tech. Dig.*, Dec. 2011, pp. 24.5.1–24.5.4., doi: [10.1109/IEDM.2011.6131606](https://doi.org/10.1109/IEDM.2011.6131606).
- [2] X. Li, S. George, K. Ma, W. Y. Tsai, A. Aziz, J. Sampson, S. K. Gupta, M. F. Chang, Y. Liu, S. Datta, and V. Narayanan, "Advancing nonvolatile computing with nonvolatile NCFET latches and flip-flops," *IEEE Trans. Circuits Syst. I, Reg. Papers*, vol. 64, no. 11, pp. 2907–2919, Nov. 2017, doi: [10.1109/TCSI.2017.2702741](https://doi.org/10.1109/TCSI.2017.2702741).
- [3] Y. Li, R. Liang, J. Wang, Y. Zhang, H. Tian, H. Liu, S. Li, W. Mao, Y. Pang, Y. Li, Y. Yang, and T. Ren, "A ferroelectric thin film transistor based on annealing-free HfZrO film," *IEEE J. Electron Devices Soc.*, vol. 5, no. 5, pp. 378–383, Sep. 2017, doi: [10.1109/JEDS.2017.2732166](https://doi.org/10.1109/JEDS.2017.2732166).
- [4] A. Sharma and K. Roy, "1T non-volatile memory design using sub-10 nm ferroelectric FETs," *IEEE Electron Device Lett.*, vol. 39, no. 3, pp. 359–362, Mar. 2018, doi: [10.1109/LED.2018.2797887](https://doi.org/10.1109/LED.2018.2797887).
- [5] D. Kwon, K. Chatterjee, A. J. Tan, A. K. Yadav, H. Zhou, A. B. Sachid, R. dos Reis, C. Hu, and S. Salahuddin, "Improved subthreshold swing and short channel effect in FDSOI n-channel negative capacitance field effect transistors," *IEEE Electron Device Lett.*, vol. 39, no. 2, pp. 300–303, Feb. 2017, doi: [10.1109/LED.2017.2787063](https://doi.org/10.1109/LED.2017.2787063).
- [6] A. Aziz, E. T. Breyer, A. Chen, X. Chen, S. Datta, S. K. Gupta, M. Hoffmann, X. S. Hu, A. Ionescu, M. Jerry, T. Mikolajick, H. Mulaosmanovic, K. Ni, M. Niemier, I. O'Connor, A. Saha, S. Slesazek, S. K. Thirumala, and X. Yin, "Computing with ferroelectric FETs: Devices, models, systems, and applications," in *Proc. Design, Automat. Test Eur. Conf. Exhib. (DATE)*, Mar. 2018, pp. 1289–1298, doi: [10.23919/DATE.2018.8342213](https://doi.org/10.23919/DATE.2018.8342213).
- [7] E. W. Kinder, C. Alessandri, P. Pandey, G. Karbasian, S. Salahuddin, and A. Seabaugh, "Partial switching of ferroelectrics for synaptic weight storage," in *Proc. Device Res. Conf. (DRC)*, Jun. 2017, pp. 1–2, doi: [10.1109/DRC.2017.7999427](https://doi.org/10.1109/DRC.2017.7999427).
- [8] S. Oh, T. Kim, M. Kwak, J. Song, J. Woo, S. Jeon, I. K. Yoo, and H. Hwang, "HfZrO_x-based ferroelectric synapse device with 32 levels of conductance states for neuromorphic applications," *IEEE Electron Device Lett.*, vol. 38, no. 6, pp. 732–735, Jun. 2017, doi: [10.1109/LED.2017.2698083](https://doi.org/10.1109/LED.2017.2698083).
- [9] M. H. Park, H. J. Kim, Y. J. Kim, Y. H. Lee, T. Moon, K. D. Kim, S. D. Hyun, F. Fengler, U. Schroeder, and C. S. Hwang, "Effect of Zr content on the wake-up effect in Hf_{1-x}Zr_xO₂ Films," *ACS Appl. Mater. Interfaces*, vol. 8, no. 24, pp. 15466–15475, 2016, doi: [10.1021/acami.6b03586](https://doi.org/10.1021/acami.6b03586).
- [10] G. Karbasian, A. Tan, A. Yadav, E. M. H. Sorensen, C. R. Serrao, A. I. Khan, K. Chatterjee, S. Kim, C. Hu, and S. Salahuddin, "Ferroelectricity in HfO₂ thin films as a function of Zr doping," in *Proc. Int. Symp. VLSI Technol., Syst. Appl. (VLSI-TSA)*, Apr. 2017, pp. 1–2, doi: [10.1109/VLSI-TSA.2017.7942488](https://doi.org/10.1109/VLSI-TSA.2017.7942488).
- [11] G. Karbasian, R. dos Reis, A. K. Yadav, A. J. Tan, C. Hu, and S. Salahuddin, "Stabilization of ferroelectric phase in tungsten capped Hf_{0.8}Zr_{0.2}O₂," *Appl. Phys. Lett.*, vol. 111, no. 2, pp. 022907-1–022907-4, Jun. 2017, doi: [10.1063/1.4993739](https://doi.org/10.1063/1.4993739).
- [12] Y.-C. Lin, F. McGuire, and A. D. Franklin, "Realizing ferroelectric Hf_{0.5}Zr_{0.5}O₂ with elemental capping layers," *J. Vac. Sci. Technol. A, Vac. Surf. Films*, vol. 36, no. 1, p. 011204, 2018, doi: [10.1116/1.5002558](https://doi.org/10.1116/1.5002558).
- [13] S. J. Kim, D. Narayan, J.-G. Lee, J. Mohan, J. S. Lee, J. Lee, H. S. Kim, Y.-C. Byun, A. T. Lucero, C. D. Young, S. R. Summerfelt, T. San, L. Colombo, and J. Kim, "Large ferroelectric polarization of TiN/Hf_{0.5}Zr_{0.5}O₂/TiN capacitors due to stress-induced crystallization at low thermal budget," *Appl. Phys. Lett.*, vol. 111, no. 24, p. 242901, 2017, doi: [10.1063/1.4995619](https://doi.org/10.1063/1.4995619).
- [14] M. H. Park, H. J. Kim, Y. J. Kim, W. Lee, T. Moon, and C. S. Hwang, "Evolution of phases and ferroelectric properties of thin Hf_{0.5}Zr_{0.5}O₂ films according to the thickness and annealing temperature," *Appl. Phys. Lett.*, vol. 102, no. 24, p. 242905, 2013, doi: [10.1063/1.4811483](https://doi.org/10.1063/1.4811483).
- [15] K. Chatterjee, A. J. Rosner, and S. Salahuddin, "Intrinsic speed limit of negative capacitance transistors," *IEEE Electron Device Lett.*, vol. 38, no. 9, pp. 1328–1330, Sep. 2017, doi: [10.1109/LED.2017.2731343](https://doi.org/10.1109/LED.2017.2731343).
- [16] J. A. Kittl, B. Obradovic, D. Reddy, T. Rakshit, R. M. Hatcher, and M. S. Rodder, "On the validity and applicability of models of negative capacitance and implications for MOS applications," *Appl. Phys. Lett.*, vol. 113, no. 4, p. 042904, 2018, doi: [10.1063/1.5036984](https://doi.org/10.1063/1.5036984).
- [17] A. K. Tagantsev, I. Stolichnov, N. Setter, J. S. Cross, and M. Tsukada, "Non-Kolmogorov-Avrami switching kinetics in ferroelectric thin films," *Phys. Rev. B, Condens. Matter*, vol. 66, p. 214109, Dec. 2002, doi: [10.1103/PhysRevB.66.214109](https://doi.org/10.1103/PhysRevB.66.214109).
- [18] J. Y. Jo, H. S. Han, J.-G. Yoon, T. K. Song, S.-H. Kim, and T. W. Noh, "Domain switching kinetics in disordered ferroelectric thin films," *Phys. Rev. Lett.*, vol. 99, no. 26, pp. 267602-1–267602-4, 2007, doi: [10.1103/PhysRevLett.99.267602](https://doi.org/10.1103/PhysRevLett.99.267602).
- [19] S. Zhukov, Y. A. Genenko, O. Hirsch, J. Glaum, T. Granzow, and H. von Seggern, "Dynamics of polarization reversal in virgin and fatigued ferroelectric ceramics by inhomogeneous field mechanism," *Phys. Rev. B, Condens. Matter*, vol. 82, no. 1, pp. 014109-1–014109-8, 2010, doi: [10.1103/PhysRevB.82.014109](https://doi.org/10.1103/PhysRevB.82.014109).
- [20] S. Mueller, S. R. Summerfelt, J. Müller, U. Schroeder, and T. Mikolajick, "Ten-nanometer ferroelectric Si:HfO₂ films for next-generation FRAM capacitors," *IEEE Electron Device Lett.*, vol. 33, no. 9, pp. 1300–1302, Sep. 2012, doi: [10.1109/LED.2012.2204856](https://doi.org/10.1109/LED.2012.2204856).
- [21] J. Müller, T. S. Böscke, S. Müller, E. Yurchuk, P. Polakowski, J. Paul, D. Martin, T. Schenk, K. Khullar, A. Kersch, W. Weinreich, S. Riedel, K. Seidel, A. Kumar, T. M. Arruda, S. V. Kalinin, T. Schlösser, R. Boschke, R. van Bentum, U. Schröder, and T. Mikolajick, "Ferroelectric hafnium oxide: A CMOS-compatible and highly scalable approach to future ferroelectric memories," in *IEDM Tech. Dig.*, Dec. 2013, pp. 10.8.1–10.8.4., doi: [10.1109/IEDM.2013.6724605](https://doi.org/10.1109/IEDM.2013.6724605).
- [22] H. Mulaosmanovic, J. Ocker, S. Müller, U. Schroeder, J. Müller, P. Polakowski, S. Flachowsky, R. van Bentum, T. Mikolajick, and S. Slesazek, "Switching kinetics in nanoscale hafnium oxide based ferroelectric field-effect transistors," *ACS Appl. Mater. Interfaces*, vol. 9, no. 4, pp. 3792–3798, 2017, doi: [10.1021/acami.6b13866](https://doi.org/10.1021/acami.6b13866).
- [23] N. Gong, X. Sun, H. Jiang, K. S. Chang-Liao, Q. Xia, and T. P. Ma, "Nucleation limited switching (NLS) model for HfO₂-based metal-ferroelectric-metal (MFM) capacitors: Switching kinetics and retention characteristics," *Appl. Phys. Lett.*, vol. 112, no. 26, p. 262903, 2018, doi: [10.1063/1.5010207](https://doi.org/10.1063/1.5010207).
- [24] J. F. Scott, L. Kammerdiner, M. Parris, S. Traynor, V. Ottenbacher, A. Shawabkeh, and W. F. Oliver, "Switching kinetics of lead zirconate titanate submicron thin-film memories," *J. Appl. Phys.*, vol. 64, no. 2, pp. 787–792, 1988, doi: [10.1063/1.341925](https://doi.org/10.1063/1.341925).

APPENDIX C

EXPERIMENTALLY VALIDATED, PREDICTIVE MONTE CARLO
MODELING OF FERROELECTRIC DYNAMICS AND VARIABILITY

Experimentally Validated, Predictive Monte Carlo Modeling of Ferroelectric Dynamics and Variability

C. Alessandri*, P. Pandey*, and A. C. Seabaugh

Department of Electrical Engineering, University of Notre Dame, Notre Dame, IN 46556, USA

Emails: calessan@nd.edu, ppandey@nd.edu, *Equal Contribution

Abstract—A physics-based, circuit-compatible Monte Carlo simulation framework, capable of predicting the dynamic response of a ferroelectric (FE) under any arbitrary input waveform, is developed by extending the nucleation-limited switching model. Measured polarization reversal data from fabricated FE W/Hf_{0.5}Zr_{0.5}O₂ (HZO)/W capacitors is used to extract the statistical distribution of FE grains, which show negligible variation with film thickness. After parameter extraction, the model is able to predict the dynamics of HZO and bilayer HZO/HfO₂ (FE-DE) thin films without further calibration. Unlike prior models, the proposed model is able to predict device-to-device variability, and quantify the resultant reduction in the memory window for highly scaled devices, revealing a significant reduction for FE capacitors having < 20 grains (~40×40 nm²). The memory window is further reduced in FE-DE stacks for the same programming voltage and pulse duration due to the dielectric depolarizing field.

I. INTRODUCTION

Interest in ferroelectric (FE) devices has increased significantly after the discovery of ferroelectricity in the CMOS-compatible HfO₂ material system [1], having a variety of applications including memory, steep slope transistors, and neuromorphic computing [2]. Describing the switching behavior of thin-film polycrystalline FEs is complicated by the fact that they are composed of a multitude of grains having different switching thresholds, the distribution of which is highly dependent on the growth conditions. Prior models based on the static Preisach model [3,4] approximate the multi-domain polarization-voltage (P-V) hysteresis loops by a hyperbolic tangent function, while the dynamic component is included by using equivalent circuits having either fixed or bias dependent time constants. Due to these approximations, such models do not keep track of the distributions of switching thresholds, and require interpolation and scaling of parameters to replicate the history dependence of partially polarized FEs. While such models generate fits that match experimental data, they are unable to accurately predict the FE response under arbitrary input waveforms and the effects of grain variations in small-area devices.

Here, we implement a Monte Carlo based simulation framework for describing the dynamic, history dependent switching behavior of a multi-domain FE. After a parameter extraction procedure, the model is able to accurately predict the dynamical behavior of FE HZO under various applied waveforms, both with and without the presence of an additional dielectric (DE) HfO₂ layer.

II. MODEL DESCRIPTION

The model presented in this approach is based on the nucleation limited switching (NLS) polarization reversal model [5,6], which considers the FE as being composed of an ensemble of grains experiencing variations in the local fields when a uniform external field is applied, due to grain boundaries, surface roughness, defects, trapped charges, etc. This is mathematically equivalent to the grains having different activation fields, which is computationally convenient. The cumulative probability of switching for any grain is governed by a stretched exponential law with a field dependent time constant (Fig. 4). The net polarization of the entire ensemble at any time is obtained by calculating the expectation value of the cumulative probability over the distribution function of activation fields. However, the NLS model is limited as it is a polarization reversal model, and can only describe the field dependent switching dynamics of an FE from one fully polarized state to another, under the application of a constant field.

In this Monte Carlo based simulation framework, a set of FE grains is instantiated with fixed activation fields drawn from a distribution obtained using measured polarization reversal characteristics. These grains can have one of two possible orientations, and the probability of transition from one orientation to the other is governed by a Weibull process [7], thereby extending the NLS model. The applied voltage waveform is then divided into discrete time intervals, and the conditional probability of transition for each unswitched grain at any time is calculated based on its accumulated time constants (Fig. 4). These time constants are in turn dependent on the activation field of each individual grain, and the applied field (Fig. 4). Therefore, the model is able to fully capture the hysteretic time and field dependent behavior of an FE.

III. PARAMETER EXTRACTION AND TRENDS

FE W/HZO/W capacitors were fabricated with HZO thickness being 8.3, 10.6, and 15 nm. The growth rate and thicknesses were characterized using both *in situ* ellipsometry and transmission electron microscopy (TEM), while a Hf:Zr ratio of 1:1 was verified with energy dispersive X-ray line scans. To validate the model for device and circuit simulations, ferroelectric-dielectric (FE-DE) W/HZO/HfO₂/W bilayer capacitors were also fabricated on the 10.6 nm HZO film with 6 nm and 8 nm HfO₂ (Fig. 1).

Polarization reversal measurements were carried out by applying pulses with varying amplitudes, and widths ranging from 300 ns to 10 ms (Fig. 5(a)), to the FE capacitors. The

switching parameters were then extracted by fitting the NLS model (Fig. 5(c-d)) to the polarization reversal measurements, and these parameters did not significantly vary if the distribution of activation fields was also left as a fitting parameter. The accuracy of the fits, and the weak dependence of the extracted parameters on the method of fitting underscores the physicality of the model.

As previously shown [8], the remnant polarization (P_R) decreases with increasing film thickness without significant change in the extracted activation field distributions. The extracted minimum switching time τ_0 (i.e. the time constant when an infinite field is applied) is of the order of ~ 100 ns, imposing a hard limit on the switching speed of these FEs. Furthermore, decreasing the FE thickness results in a higher P_R and a higher field for the same applied voltage, but τ_0 increases (Fig. 5(d)), leading to a speed trade-off.

IV. MODEL VALIDATION

The response of the FE to an applied external waveform was simulated using the extracted parameters, and the model closely replicates the measured behavior (Fig. 6(a-b)). Differences between the measured and simulated characteristics occur in part due to the assumption of a constant FE capacitance, whereas the measured capacitance exhibits the well-known butterfly shape (Fig. 3). The capability of the proposed model to accurately predict the behavior of the FE as it enters and exits the minor loops, as well as the drifting of the minor loops with field cycling, further highlights its advantage over the dynamic Preisach models [3,4], which scale the major loops to generate the minor loops.

Furthermore, due to the domain switching being a Weibull process with $n > 1$, the FE switching is faster upon application of a single long pulse, as compared to a pulse train having the same amplitude and the same cumulative duration (Fig. 6(c)). The model is able to accurately predict this difference since the switching probability of a grain is dependent on both its present and previous time constants, which Preisach models are unable to fully capture.

In the fabricated FE-DE bilayers, TEM showed that HfO₂ crystallized on the grain structure of the HZO film (Fig. 2), indicating a strain transfer from the latter to the former, leading to a thicker region of ferroelectricity with a lower percentage of FE grains having a thin DE layer in series. With the model parameters adjusted to account for these physical differences (increased FE thickness and reduced P_R), the model again shows close agreement with measurements (Fig. 6(d-e)). The fact that the sample with a thinner HfO₂ layer experienced a lower reduction in P_R and required a smaller increase of the FE thickness for accurate fits validates these changes. The capability of the model to predict these unexpected results further highlights its utility.

V. MODEL PREDICTIONS

A. Low Power Memory and Negative Capacitance FETs

FE-DE stacks form integral components of many proposed FE devices, in both memory and logic [2]. The widely used

Landau-Khalatnikov (L-K) based models predict a decrease in the switching voltage upon placing a DE in series with an FE, albeit with a reduced P_R (Fig. 7(a)), suggesting the possibility of low power memory devices and hysteresis free Negative Capacitance FETs. However, measurements performed on fabricated FE-DE bilayers do not show this trend, and the measured behavior is explained well using our model (Fig. 7(a)). The depolarizing field of the DE aids switching only when the magnitude of FE polarization is decreasing (i.e. from $\pm P_R$ to 0), but opposes the switching when its magnitude is increasing (i.e. from 0 to $\pm P_R$). Thus, irrespective of the pulse duration, the FE-DE starts switching earlier than the FE, but takes a longer time to fully switch, and the maximum switched charge is also reduced (Fig. 7(b)). These results also support the hypothesis that the enhancement in hysteresis-free FE FETs is due to the higher dielectric constant of HZO relative to HfO₂, rather than FE switching.

B. Variability

The Monte Carlo modeling approach allows the investigation of the effects of device-to-device variability due to the grains having a distribution of activation fields. This variability in FE switching characteristics increases with a reduction both in lateral dimensions and programming voltage (Fig. 8(a)), so much so that a device consisting of 20 grains (~ 40 nm x 40 nm) exhibits a 50% reduction in memory window when programmed with 1.5 V pulses, and no memory window if programmed by 1.25 V pulses of 10 μ s duration. A series DE reduces this variability in absolute terms, but there is no increase in the memory window due to the reduced maximum polarization, which is quite significant even for a very thin DE (Fig. 8(b)).

VI. CONCLUSIONS

An experimentally validated, circuit-compatible, physics based Monte Carlo model of FE behavior is used to make predictions regarding the variability, scaling, and memory application space of FE HZO and FE-DE bilayers by accurately simulating their response to arbitrary waveforms. The model highlights the need to develop processes yielding smaller, faster switching FE grains having activation field distributions with small standard deviations, and provides the tools to quantify the necessary improvements.

ACKNOWLEDGMENT

We gratefully acknowledge the contributions of T. Orlova and S. Rouvimov in the Notre Dame Integrated Imaging Facility for the TEM sample preparation and analysis.

REFERENCES

- [1] T. S. Böscke *et al.*, IEDM, 547, 2011. [2] A. Aziz *et al.*, DATE 1289, 2018.
- [3] K. Ni *et al.*, VLSI Tech. Symp., pp. 131-132, 2018. [4] B. Obradovic *et al.*, VLSI Tech. Symp., pp. 51-52, 2018. [5] A. K. Tagantsev *et al.*, Phys. Rev. B, vol. 66, 214109, 2002. [6] S. Zhukov *et al.*, J. Appl. Phys., vol. 108, 014106, 2010. [7] W. Lee *et al.*, Adv. Funct. Mater., 1801162, 2018. [8] M. H. Park *et al.*, Appl. Phys. Lett., vol. 102, 242905, 2013.

FE HZO Samples	FE-DE HZO/HfO ₂ Samples
DC Sputtering 200 nm W Bottom Electrode	
ALD HZO, 300 C, TEMA, TEMAZ, O ₂ Plasma	
DC Sputtering 40 nm top W	
RTA in N ₂ at 500 C for 30 s	
Selective wet etch of top W layer	
	ALD HfO ₂ , 300 C, TEMA, H ₂ O
Photolithography and liftoff 200 nm sputtered W top electrode	

Figure 1: Process flow for ferroelectric HZO (left) and bilayer HZO/HfO₂ (right) capacitors.

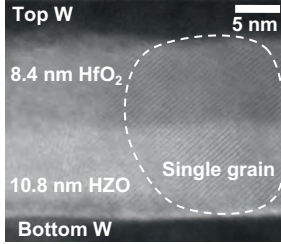


Figure 2: TEM of bilayer capacitor showing crystalline grain across HZO/HfO₂ interface.

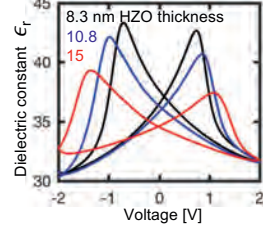


Figure 3: Measured dielectric constant from capacitance-voltage data (0.2 V/s sweep rate and 25 mV, 100 kHz AC)

Nucleation limited switching (NLS) model [5, 6]

Time constant τ is a function of applied field E and activation field E_a

$$\tau(E, E_a) = \tau_0 \exp \left\{ \left(\frac{E_a}{E} \right)^\alpha \right\}$$

Cumulative probability of domain switching for constant applied field E

$$P_{sw}(t, E, E_a) = 1 - \exp \left\{ - \left(\frac{t}{\tau(E, E_a)} \right)^n \right\}$$

For a distribution of activation fields $f(E_a)$, the mean polarization is

$$P(t, E) = P_R - 2P_R \int_0^\infty P_{sw}(t, E, E_a) f(E_a) dE_a$$

P_R : remanent polarization. Fitting parameters: n, α, τ_0

Monte Carlo simulation framework

1. Extract distribution of activation field $f(E_a)$ and parameters P_R, n, α, τ_0 from polarization reversal data.
2. Instantiate a set of N grains with activation field E_a drawn from probability distribution $f(E_a)$.
3. For each time interval and grain $i = 1..N$, compute switching probability according to Weibull process

$$p_{sw}^{(i)}(t_s < t + \Delta t | t_s > t) = 1 - \exp \{ -\tilde{h}_i(t + \Delta t)^n + \tilde{h}_i(t)^n \}$$
with accumulated time constant: $\tilde{h}_i(t) = \int_{t_0}^t \frac{dt}{\tau(E(t), E_{ai})}$
4. Update accumulated time constants $h(t) \rightarrow h(t) + \Delta t/\tau$. If grain switches, update polarization state ($p_i = \pm 1$) and reset $h(t)$.

$$Q_{FE}(t) = \frac{P_R}{N} \sum_{i=1}^N p_i(t) + \epsilon_{FE} E(t)$$

Figure 4: The NLS model (left) describes the FE as an ensemble of regions (grains) switching independently with a field dependent time constant. The FE statistics are captured by a distribution of activation field. Upon parameter extraction from the NLS model, the FE polarization dynamics can be predicted for arbitrary input waveforms using a Monte Carlo approach (right). A constant permittivity ϵ_{FE} was assumed to compute the total charge per unit area.

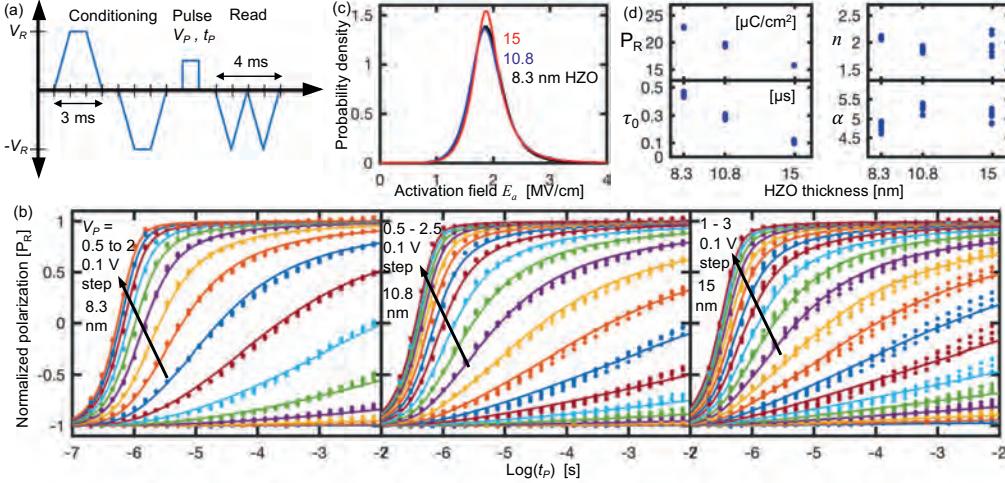


Figure 5: (a) Measurement protocol for parameter extraction. Pulse width (t_p) was stepped from 200 ns to 10 ms in increments of 1.5X, then amplitude (V_p) was stepped in increments of 100 mV. Reset and read amplitude (V_R) of 2.5, 3 and 3.5 V were used for 8.3, 10.8 and 15 nm capacitors, respectively. The procedure was repeated 3 times for each sample. (b) Partial polarization data for 3 runs (dots) show close agreement with fitted NLS model (solid line) over 5 decades. (c) Extracted distributions of activation field reflect minor variations in the statistical properties with film thickness. (d) Extracted parameters: P_R and τ_0 decrease by 0.6X and 0.25X respectively for thickness from 8.3 to 15 nm, whereas n and α show variations below 10% for different samples and thickness.

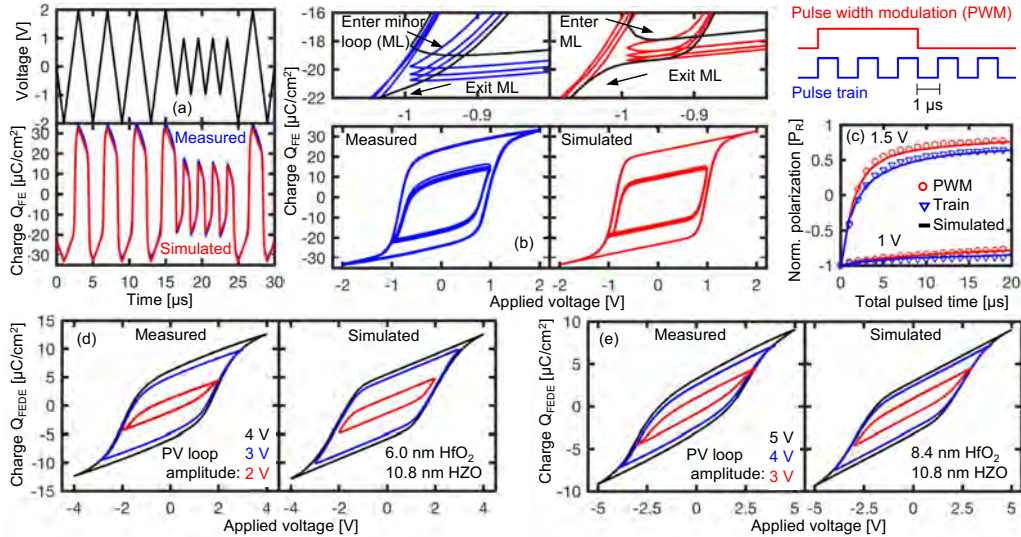


Figure 6: Experimental validation of Monte Carlo simulation framework. (a) Measured and simulated polarization vs. time for an 8.3 nm HZO capacitor with a triangular input waveform of varying amplitude (top). (b) Measured and simulated minor loops obtained from (a), with detail of the transition between minor loops and the saturated loop (top). (c) Experimental and simulated polarization obtained by pulse width modulation and a train of pulses with equivalent “on” time. Close agreement of measured and simulated PV loops for FE-DE structures with (d) 6/10.8 nm HfO₂/HZO and (e) 8.4/10.8 nm HfO₂/HZO.

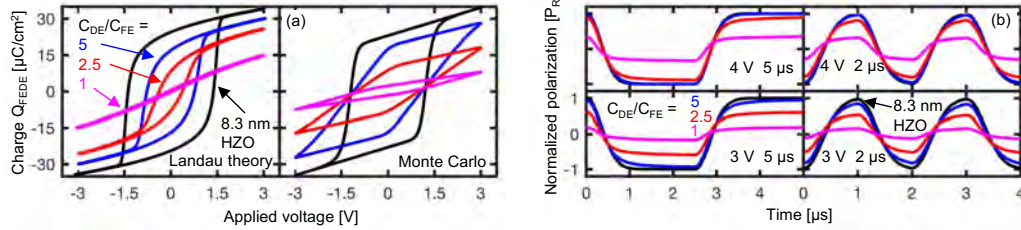


Figure 7: (a) Simulation of ferroelectric-dielectric P-V loops: Landau-Khalatnikov model shows a reduction in switching threshold with increasing dielectric thickness (decreasing capacitance). Monte Carlo simulation exhibits the behavior observed in experiments. (b) Simulated polarization vs. time of a FE capacitor and FE-DE structures with different dielectric capacitance, programmed with square waveforms of amplitudes 3 and 4 V with 2 μ s and 5 μ s period.

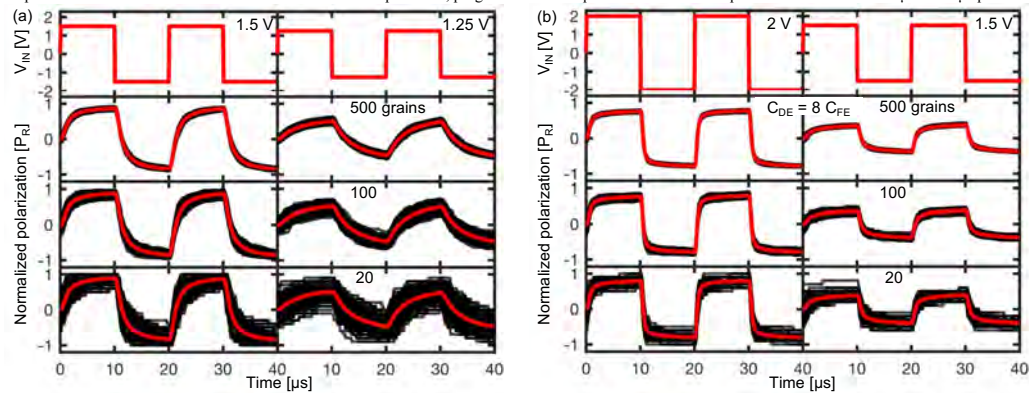


Figure 8: Simulated device-to-device variations of 200 devices (black) with 500, 100 and 20 grains for (a) 8 nm-thick FE and (b) FE-DE capacitor with $C_{DE} = 8 C_{FE}$. With 20 grains, the memory window of the FE is reduced by 50% with respect to the mean value (red) for a 1.5 V programming voltage, and is completely lost with 1.25 V. With the same number of grains, the FEDE requires a programming voltage above 1.5 V to obtain a memory window.

APPENDIX D

MONTE CARLO SIMULATION OF SWITCHING DYNAMICS IN POLYCRYSTALLINE FERROELECTRIC CAPACITORS

Monte Carlo Simulation of Switching Dynamics in Polycrystalline Ferroelectric Capacitors

Cristobal Alessandri¹, Student Member, IEEE, Pratyush Pandey, Student Member, IEEE, Angel Abusleme², Member, IEEE, and Alan Seabaugh, Fellow, IEEE

Abstract—Ferroelectric (FE) materials are being studied for a variety of applications in memory, logic, and neuromorphic computing, for which predictive models of FE polarization are essential. In this paper, we present a Monte Carlo simulation framework capable of predicting the dynamic, history-dependent response of an FE under arbitrary input waveforms. The simulation is developed by generalizing the physics-based nucleation-limited switching model for polarization reversal in a polycrystalline FE. Measured polarization reversal data from fabricated FE $\text{Hf}_{0.5}\text{Zr}_{0.5}\text{O}_2$ capacitors are used to extract the statistical distribution of FE grains. After parameter extraction, the model is able to predict the dynamics of the FE capacitor without further calibration. Finally, the model is applied to characterize the dynamic response of FE–dielectric bilayer structures and quantify the reduction in memory window due to device variability.

Index Terms—Ferroelectric (FE), hafnium zirconate (HZO), Monte Carlo, nucleation-limited switching (NLS).

I. INTRODUCTION

THE discovery of ferroelectricity in the CMOS-compatible HfO_2 material system [1] has led to a variety of applications, including memory [2], [3], steep-slope transistors [4], [5], and neuromorphic computing [6], [7]. To design devices for these applications and further explore the use of ferroelectrics (FEs) in circuit design, reliable and predictive models of the FE polarization dynamics are needed. However, describing the switching behavior of thin-film polycrystalline FEs is complicated by the fact that they are composed of a multitude of grains having different switching thresholds, the distribution of which is highly dependent on the growth

conditions. Therefore, to predict the time evolution of an FE film, it is necessary to keep track of the configuration of switched grains. Moreover, it was recently shown that deep submicrometer FE FETs exhibit abrupt FE switching dependent on the history of accumulated pulses [8]. In this paper, we show a Monte Carlo simulation approach that accounts for the history-dependent switching observed in FE films.

Prior dynamic models based on the static Preisach model [9]–[11] approximate the multidomain polarization–voltage (P – V) hysteresis loops by a hyperbolic tangent function, while the dynamic component is included by using equivalent circuits having either fixed or bias-dependent time constants [11]. Due to these approximations, such models do not keep track of the distributions of switching thresholds and resort to interpolation and scaling of parameters to replicate the history dependence of partially polarized FEs [9], [10].

On the other hand, nucleation-limited switching (NLS) models [12]–[14] provide an accurate description of the polarization reversal dynamics of FE thin films. The field-dependent NLS model characterizes the FE film as an ensemble of elementary regions that switch independently with a distribution of field-dependent time constants, effectively coupling the distribution of switching thresholds and the switching dynamics. These models have been experimentally validated in FE HfO_2 [15], [16], lead zirconate titanate [12]–[14], [17], and other material systems [17]. However, NLS models are limited as they are polarization reversal models and can only describe the switching dynamics of an FE starting from a fully polarized state and under the application of a constant field.

The Monte Carlo simulation framework describes the dynamic, history-dependent switching of a multidomain FE. In this framework, the field-dependent NLS model is generalized for use with arbitrary input waveforms. After a parameter extraction from polarization reversal measurements, the model is able to accurately predict the dynamical behavior of FE hafnium zirconate (HZO) under various applied waveforms without further parameter tuning, showing the predictive capability of the model. This model was outlined in [18]. This expanded treatment provides a detailed derivation of the model with further discussion of its physical interpretation. This paper is organized as follows. In Section II, the field-dependent NLS model for polarization reversal is described. In Section III, the Monte Carlo simulation framework is introduced for FE polarization reversal and then generalized to arbitrary input waveforms. Model predictions

Manuscript received March 29, 2019; revised May 3, 2019; accepted May 24, 2019. Date of publication June 27, 2019; date of current version July 23, 2019. This work was supported in part by the Center for Low Energy Systems Technology (LEAST), one of six centers of STARnet, through the Semiconductor Research Corporation Program sponsored by MARCO and DARPA, and in part by the National Science Foundation under Grant ECCS/GOALI-1408425. The review of this paper was arranged by Editor S.-M. Hong. (Cristobal Alessandri and Pratyush Pandey contributed equally to this work.) (Corresponding author: Cristobal Alessandri.)

C. Alessandri is with the Department of Electrical Engineering, University of Notre Dame, Notre Dame, IN 46556 USA, and also with the Department of Electrical Engineering, Pontificia Universidad Catolica de Chile, Santiago 7820436, Chile (e-mail: calessan@nd.edu).

P. Pandey and A. Seabaugh are with the Department of Electrical Engineering, University of Notre Dame, Notre Dame, IN 46556 USA (e-mail: seabaugh.1@nd.edu).

A. Abusleme is with the Department of Electrical Engineering, Pontificia Universidad Catolica de Chile, Santiago 7820436, Chile.

Color versions of one or more of the figures in this paper are available online at <http://ieeexplore.ieee.org>.

Digital Object Identifier 10.1109/TED.2019.2922268

0018-9383 © 2019 IEEE. Personal use is permitted, but republication/redistribution requires IEEE permission. See http://www.ieee.org/publications_standards/publications/rights/index.html for more information.

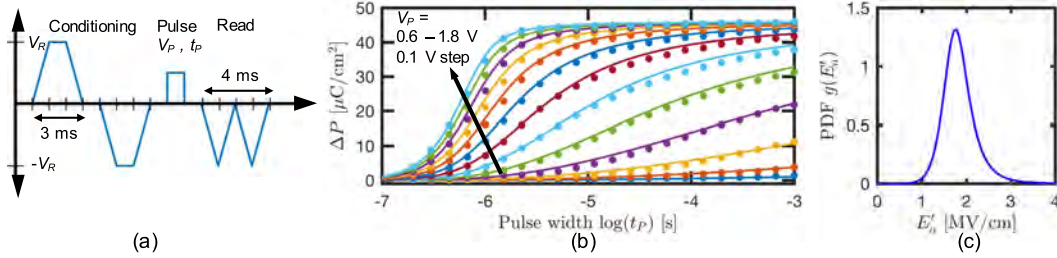


Fig. 1. (a) Measurement protocol for parameter extraction [15]. The pulsewidth (t_p) was swept from 200 ns to 1 ms in increments of $1.5\times$, and then, the amplitude (V_p) was stepped in increments of 100 mV. The conditioning and read amplitude V_R was set to 2.5 V. (b) Partial polarization data (dots) and fit NLS model (solid line). (c) Extracted distribution of effective activation field $g(E_a)$.

for FE–dielectric (FE–DE) stacks and device variability are analyzed in Section IV.

II. FIELD-DEPENDENT NLS MODEL FOR POLARIZATION REVERSAL

In the NLS model, the FE film is characterized as an ensemble of elementary regions that switch independently with a distribution of time constants [12]. These regions correspond to the grains in a polycrystalline FE film, considering that domain wall motion stops at the grain boundary and does not propagate to an adjacent grain. It is assumed that the switching of a grain occurs once a domain of reversed polarization is nucleated, and the wait time for the first nucleation event is much larger than the time needed for a nucleated domain wall to expand and occupy the entire grain. The NLS theory presented in [12] originally assumed that nucleation events occur spontaneously at a constant rate $1/\tau$, so the switching of a grain was modeled as a Poisson process, where the cumulative distribution function (cdf) of the switching time t_S is

$$P(t_S < t|\tau) = 1 - \exp\left(-\frac{t}{\tau}\right). \quad (1)$$

However, according to the classical nucleation theory, the nucleation rate is not constant [19]. Domain nucleation occurs in a series of stages, starting with an incubation period where small clusters with reversed FE polarization continuously form and decompose, the distribution of which evolves over time until a quasi-steady-state distribution is reached. During this period, the nucleation rate increases monotonically until it becomes almost constant [19]. The assumption of constant nucleation rate was originally introduced as a special case to model the polarization reversal in an infinite crystal [20], where multiple nucleation events occur until the FE volume has reversed its polarization. In this regime, the incubation period could be safely ignored, but it can be the dominant factor in a polycrystalline FE where the switching time is determined by the first nucleation event.

Based on experimental results, 1 was generalized to a stretched exponential with parameter β [13], [14], which can be interpreted as a Weibull process [21] where the cdf for the

switching time is given by

$$P(t_S < t|\tau, \beta) = 1 - \exp\left[-\left(\frac{t}{\tau}\right)^\beta\right]. \quad (2)$$

This results in a time-dependent switching rate

$$r(t) = \frac{\beta}{\tau} \left(\frac{t}{\tau}\right)^{\beta-1} \quad (3)$$

as opposed to a constant nucleation rate. Note that for $\beta = 1$, this reduces to a Poisson process with constant rate $1/\tau$. With $\beta > 1$, a monotonically increasing nucleation rate is obtained, which provides an approximation for the FE nucleation during the incubation period.

The distribution of time constants in 2 can be associated with variations in the local electric field in the FE film [13], [14]. Under this assumption, the time constant τ is a function of the local field E and an activation field E_a , which can be expressed by the empirical relation [14], [22]

$$\tau(E_a, E) = \tau_\infty \exp\left[\left(\frac{E_a}{E}\right)^\alpha\right] \quad (4)$$

where τ_∞ is the time constant obtained for an infinite applied field and α is an empirical parameter. Assuming an inhomogeneous and field-independent dielectric permittivity, the local electric field is expressed as $E = \eta E_{FE}$, where E_{FE} is an applied constant field across the FE and η is a random variable with probability density function (pdf) $f(\eta)$ and unity mean, defined in the interval $[0, \infty)$ [14]. The polarization reversal from $-P_S$ to $+P_S$ is computed as the expectation of (2) over the distribution of local field variations $f(\eta)$

$$P(E_{FE}, t) = -P_S + 2P_S \int_0^\infty P(t_S < t|\tau(E_a, \eta E_{FE}), \beta) f(\eta) d\eta. \quad (5)$$

With this mathematical formulation, the FE film is characterized by the parameters P_S , E_a , β , α , τ_∞ , and the pdf $f(\eta)$. As shown in [15], $f(\eta)$ is well described by a generalized beta distribution of type 2, whose pdf is

$$GB2(\eta|a, b, p, q) = \frac{(|a|/b)(\eta/b)^{ap-1}}{B(p, q)[1 + (\eta/b)^a]^{p+q}} \quad (6)$$

where $B(p, q)$ is the beta function. Fig. 1 shows the measurements of polarization reversal and the fit field-dependent

TABLE I
FE PARAMETERS EXTRACTED FROM POLARIZATION
REVERSAL MEASUREMENTS

Parameter	$f(\eta)$	$g(E'_a)$
E_a	1.77 MV/cm	-
a	12.1	12.1
b	0.99	1.79 MV/cm
p	0.633	0.691
q	0.691	0.633
P_R	22.9 $\mu\text{C}/\text{cm}^2$	
τ_∞	387 ns	
α	4.11	
β	2.07	

NLS model for an HZO film with thickness $T_{\text{FE}} = 8.3$ nm (fabrication details available in [18]). The time constant of the measurement setup was estimated to be below 10 ns, as described in [15]. Therefore, programming pulses above 200 ns were applied to ensure that the measurements are not limited by RC delays. The extracted parameters are shown in Table I. The extracted minimum time constant is over $30\times$ larger than the time constant of the experimental setup, which indicates that the speed limitation is intrinsic to this particular ferroelectric (FE) film.

Note that due to the form of (4), a distribution of local fields is mathematically equivalent to a distribution of effective activation fields $E'_a = E_a/\eta$ with probability density

$$g(E'_a) = \frac{\eta^2}{E_a} f(\eta). \quad (7)$$

The resulting pdf is shown in Fig. 1(c), which is also a generalized beta distribution of type 2. The parameters obtained with this formulation are shown in Table I under $g(E'_a)$ and are used in the subsequent simulations. An offset voltage of $V_{\text{OS}} = 80$ mV was measured from P - V loops, such that $V_{\text{FE}} = V_A + V_{\text{OS}}$, where V_A is the applied voltage and V_{FE} is the actual voltage across the FE. This offset was considered during parameter extraction and applied to all simulations. The field at the FE is computed as $E_{\text{FE}} = V_{\text{FE}}/T_{\text{FE}}$.

III. MONTE CARLO SIMULATION FRAMEWORK

For the Monte Carlo simulation, a set of N grains $g^{(i)}$, $i \in (1, N)$ is initialized by sampling values of activation fields $E_a^{(i)}$ from the distribution $g(E'_a)$. The parameters, P_S , β , α , and τ_∞ , are common to all the FE grains. Each FE grain can have one of two possible orientations, corresponding to a positive or negative polarization state ($s^{(i)} = \pm 1$), and the time evolution of each grain is governed by (2) and (4). The simulation is first introduced for the simple case of polarization reversal and then generalized to arbitrary input waveforms.

A. Polarization Reversal Simulation

For a polarization reversal simulation from $-P_S$ to P_S , all grains are initialized to the state $s^{(i)} = -1$. Under a constant applied field, a grain $g^{(i)}$ has a fixed time constant $\tau^{(i)}$ given by (4). The simulation is performed by dividing the time into discrete-time intervals and computing the probability of transition for each unswitched grain according to (2). This is

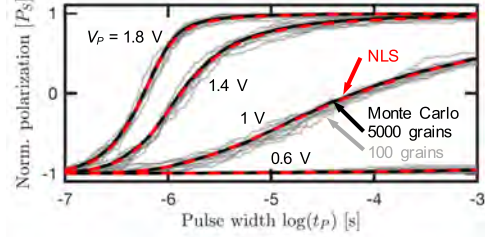


Fig. 2. Polarization reversal simulation with the NLS model (red dashed lines) and Monte Carlo simulation with 5000 grains (black lines) are indistinguishable. Monte Carlo simulations with 100 grains (gray lines) show variation around the mean value (10 repetitions).

expressed as the probability that the switching time t_S is in the time interval $[t, t + \Delta t]$, given that the grain has not switched until t

$$P^{(i)}(t_S < t + \Delta t | t_S > t) = 1 - \exp\left[\left(\frac{t}{\tau^{(i)}}\right)^\beta - \left(\frac{t + \Delta t}{\tau^{(i)}}\right)^\beta\right]. \quad (8)$$

For each grain, the switching probability is evaluated as a Bernoulli trial with probability $P^{(i)}$, and the state $s^{(i)}$ is updated to $+1$ in case of success. The total polarization due to the orientation of the FE grains is computed as

$$P_{\text{FE}}(t) = \frac{P_S}{N} \sum_{i=1}^N s^{(i)}(t). \quad (9)$$

For simplicity, it is assumed that the FE grains have the same area, but this can be generalized to account for different areas [12]. The Monte Carlo simulation for polarization reversal is summarized in Algorithm 1.

Algorithm 1 Monte Carlo Polarization Reversal

Instantiate FE:

Define parameters $\{P_S, \beta, \alpha, \tau_\infty\}$
Sample N activation fields $E_a^{(i)}$ from $g(E'_a)$

Initialization: for grains $g^{(i)}$, $i \in (1, N)$

$s^{(i)} \leftarrow -1$
 $\tau^{(i)} \leftarrow \tau_\infty \exp\left[\left(E_a^{(i)}/E_{\text{FE}}\right)^\alpha\right]$

Simulation: for timestep $[t, t + \Delta t]$ and grains $g^{(i)}$, $i \in (1, N)$

if $s^{(i)} = -1$
 $P^{(i)} \leftarrow 1 - \exp\left[\left(t/\tau^{(i)}\right)^\beta - \left((t + \Delta t)/\tau^{(i)}\right)^\beta\right]$
 if Bernoulli($P^{(i)}$) = 1
 $s^{(i)} \leftarrow 1$
 end if
end if

Fig. 2 shows the Monte Carlo simulations of polarization reversal and the analytic polarization reversal computed with the NLS model with the same parameters (see Table I). A Monte Carlo simulation with 5000 grains is indistinguishable from the NLS model, whereas 10 runs with 100 grains show variability around the mean value.

Note that, as shown in 8, the switching probability has an accumulation effect over time, even for a constant

applied field. Therefore, the state of a grain is not only determined by its polarization $s^{(i)} = \pm 1$ but also depends on the accumulated stimuli t/τ .

B. Generalization to Arbitrary Input Waveforms

For an arbitrary field at the FE $E_{FE}(t)$, the time constant $\tau^{(i)}$ is a function of time, so the accumulated stimuli t/τ is replaced by an auxiliary history parameter $h^{(i)}(t)$ that is defined as

$$h^{(i)}(t) = \int_{t_0}^t \frac{dt'}{\tau(E_{FE}(t'), E_a^{(i)})} \quad (10)$$

where t_0 indicates the time at which the stimuli to switch the grain started. The switching rate is expressed as

$$r^{(i)}(t) = \frac{\beta}{\tau^{(i)}(t)} (h^{(i)}(t))^{\beta-1} \quad (11)$$

which results in a switching probability

$$P^{(i)}(t_S < t + \Delta t | t_S > t) = 1 - \exp[(h^{(i)}(t))^{\beta} - (h^{(i)}(t + \Delta t))^{\beta}]. \quad (12)$$

The Monte Carlo simulation is performed, as shown in Algorithm 2. After instantiating an FE with N grains, the state of each grain is initialized by defining its polarization $s^{(i)} = \pm 1$ and setting the history parameter to 0. Note that only a scalar value $h^{(i)}$ is stored for each grain and updated during the simulation. Given that the FE switching can occur in both directions (i.e., from 1 to -1 or from -1 to 1), it is first verified that a grain is not already aligned with the external field. For the grains that are not aligned with the external field, the history parameter is updated to compute the switching probability, which is evaluated as a Bernoulli trial and the state of the grain is updated in case of success. Finally, the history parameter is updated when a grain switches according to a given relaxation rule, which needs to be determined. For a first approximation, two possible cases are evaluated: reset $h^{(i)}$ to 0 after a grain has switched or keep its current value.

The experimental protocol in Fig. 3(a) was applied to validate the Monte Carlo simulation and evaluate the relaxation condition for $h^{(i)}$. Starting with the FE fully polarized to the $+P_S$ state that has been resting for a minute, a double triangular waveform is applied. The first pulse completely polarizes the FE to the $-P_S$ state, whereas the second pulse is used to measure and subtract the current due to the dielectric response and leakage. After a hold time T_H , a double triangular waveform of the opposite polarity is applied to polarize the FE to the $+P_S$ state. After another hold time T_H , the procedure is repeated. The measured polarization response is plotted over the applied voltage in Fig. 3(b) with a 10-s hold time between pulses, which shows that transitions 1 and 3 (from $+P_S$ to $-P_S$) follow the same trajectories. Likewise, transitions 2 and 4 (from $-P_S$ to $+P_S$) also overlap. When the history parameter is reset after a grain switches (i.e., $h^{(i)} = 0$), the Monte Carlo simulation closely matches the experiment, shown with red lines in Fig. 3(b). When the hold time is reduced to 10 ms, a different behavior is observed. The first transition from $-P_S$ to P_S follows the same path as the

Algorithm 2 General Monte Carlo Simulation

Instantiate FE:

Define parameters $\{P_S, \beta, \alpha, \tau_{\infty}\}$

Sample N activation fields $E_a^{(i)}$ from $g(E'_a)$

Initialization: for grains $g^{(i)}, i \in (1, N)$

$s^{(i)} \leftarrow 1$ or $s^{(i)} \leftarrow -1$

$h^{(i)} \leftarrow 0$

Simulation: for timestep $[t, t + \Delta t]$ and grains $g^{(i)}, i \in (1, N)$

if $s^{(i)} E(t) < 0$

$\tau^{(i)} \leftarrow \tau_{\infty} \exp\left[\left(\frac{E_a^{(i)}}{|E(t)|}\right)^{\alpha}\right]$

$h_{new}^{(i)} \leftarrow h^{(i)} + \Delta t / \tau^{(i)}$

$P^{(i)} \leftarrow 1 - \exp\left[-(h^{(i)})^{\beta} - (h_{new}^{(i)})^{\beta}\right]$

$h^{(i)} \leftarrow h_{new}^{(i)}$

if Bernoulli($P^{(i)}$) = 1

Update $s^{(i)}$

$h^{(i)}$ relaxation

end if

end if

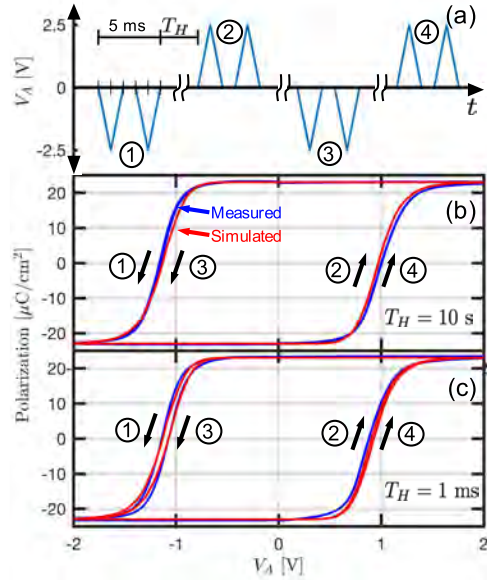


Fig. 3. (a) Experimental protocol to measure P - V loops. A double triangular waveform V_A is applied. The first triangle produces a current due to the linear capacitance and the polarization reversal. The displacement current due to the linear capacitance alone is measured by the second triangle, where there is no polarization current. A hold time T_H is applied between polarization pulses. Measured and simulated P - V loops with (b) 10-s hold time and (c) 1-ms hold time.

case with a 10-s hold time, given that the initial condition is the same. However, the subsequent transitions occur at a lower voltage (earlier in time), as shown in Fig. 3(c). This apparent speedup has been observed in similar experiments and could be related to the distribution of clusters after a

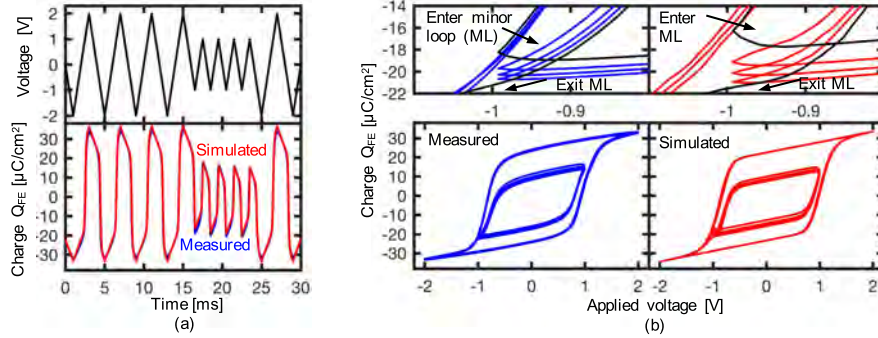


Fig. 4. Experimental validation of Monte Carlo simulation framework. (a) Measured and simulated polarization versus time for an 8.3-nm HZO capacitor with a triangular input waveform of varying amplitude. (b) Measured and simulated major and minor loops obtained from (a) with detail of the transition between minor loops and major loops.

grain switches [23]. A simulation performed for the extreme case, where $h^{(i)}(t)$ is not reset between transitions, produces a similar behavior [red lines in Fig. 3(b)].

Having verified that the Monte Carlo model closely matches the measurements of saturated P - V loops, the model predictions were evaluated for minor loops. Fig 4(a) and (b) shows the experimental and simulated data taken with a triangular waveform of varying amplitude. Under these conditions, the dielectric response is not canceled, as shown in Fig. 3, so the total FE charge is modeled as

$$Q_{FE}(t) = P_{FE}(t) + \epsilon_{FE}E(t) \quad (13)$$

where ϵ_{FE} is the permittivity of the FE film. For this simulation, $h^{(i)}(t)$ was not reset between transitions, as shown in Fig. 3(c). The Monte Carlo simulation accurately predicts the behavior of the FE as it enters and exits the minor loops, as well as the drifting of the minor loops with field cycling. Small differences between the measured and simulated characteristics occur in part due to the assumption of a constant FE capacitance, whereas the measured capacitance exhibits the well-known butterfly shape [15].

C. Further Study of Accumulation and Relaxation of the History-Dependent Switching Rate

Based on the experimental results, it has been observed that resetting the history parameter when a grain switches works well when a long resting period is applied between the pulses. For shorter resting periods or for periodic stimuli, not resetting $h(t)$ produces a close match with experimental measurements, although this extreme case results in a continuously increasing rate that will slowly depart from experiments. Therefore, a more general reset condition would be to set $h^{(i)}$ to a certain reset value h_S , which may be a function of the history parameter before switching and the grain parameters. In addition, a relaxation rule for the history parameter could be incorporated when there is no applied field or when the grain is already aligned with the external field. Such effects could be incorporated into the simulation as shown in Algorithm 3, although its functional form remains to be determined.

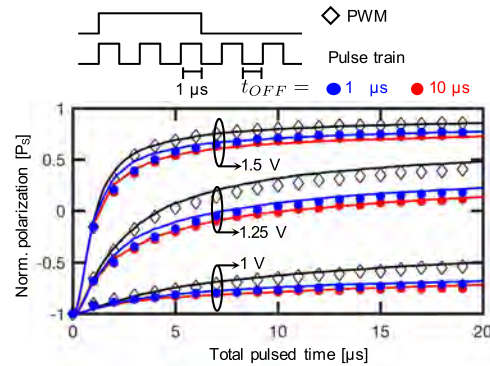


Fig. 5. Measured (markers) and simulated (solid lines) polarization obtained by pulsewidth modulation (diamonds) and a train of pulses (dots) with equivalent accumulated time.

The measurement protocol in Fig. 5 was applied to better understand the timescale of the relaxation behavior (the conditioning and readout protocols are the same, as shown in Fig. 1). Starting with an FE fully polarized in the $-P_S$ state, either a single pulse of varying width or a train of pulses with equivalent accumulated pulsed time are applied. The width-modulated pulse ranges from 1 to 20 μs . The train of pulses has a constant pulsewidth of 1 μs , with off time between the pulses t_{OFF} of either 1 or 10 μs . Amplitudes of 1, 1.25, and 1.5 V are applied for both the width-modulated pulse and the train of pulses.

The Monte Carlo simulation was implemented according to Algorithm 3, by applying a simple relaxation rule during the off time between the pulses, which is defined as

$$h^{(i)} \leftarrow h^{(i)} \times \gamma(t_{OFF}). \quad (14)$$

By setting $\gamma = 0.55$ for a 1- μs off time between the pulses and $\gamma = 0.3$ for 10- μs off time, the simulation closely matches the experiment for the pulses of 1-, 1.25-, and 1.5-V amplitude.

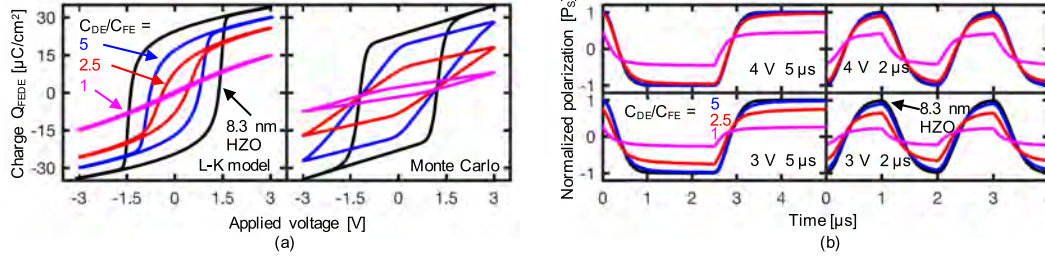


Fig. 6. (a) Simulation of FE–DE P – V loops with L–K model for single-grain FE and Monte Carlo simulation of polycrystalline FE. (b) Monte Carlo simulation of polarization versus time of an FE capacitor and FE–DE structures with different dielectric capacitances, programmed with square waveforms of amplitudes 3 and 4 V with 2- and 5- μ s period.

Algorithm 3 Monte Carlo Simulation With the Proposed Relaxation

Instantiate FE:

Define parameters $\{P_S, \beta, \alpha, \tau_\infty\}$
 Sample N activation fields $E_a^{(i)}$ from $g(E_a)$

Initialization: for grains $g^{(i)}, i \in (1, N)$

$s^{(i)} \leftarrow 1$ or $s^{(i)} \leftarrow -1$
 $h^{(i)} \leftarrow 0$

Simulation: for timestep $[t, t + \Delta t]$ and grains $g^{(i)}, i \in (1, N)$

if $s^{(i)}E(t) < 0$
 $\tau^{(i)} \leftarrow \tau_\infty \exp\left[\left(\frac{E_a^{(i)}}{|E(t)|}\right)^\alpha\right]$
 $h_{new}^{(i)} \leftarrow h^{(i)} + \Delta t/\tau^{(i)}$
 $P^{(i)} \leftarrow 1 - \exp\left[-(h^{(i)})^\beta - (h_{new}^{(i)})^\beta\right]$
 $h^{(i)} \leftarrow h_{new}^{(i)}$
if Bernoulli($P^{(i)}) = 1$
 Update $s^{(i)}$
 $h^{(i)} \leftarrow h_S$
end if

else

Relax $h^{(i)}$ // when $s^{(i)}E(t) \geq 0$

end if

It is proposed that further investigation of the dynamics of formation and decomposition of clusters in the incubation period will lead to a direct relation between the switching rate and the underlying distribution of clusters in order to define improved accumulation and relaxation equations.

IV. MODEL PREDICTIONS

FE–DE stacks are integral to many proposed FE devices in both memory and logic [5]. The Monte Carlo simulation framework was applied to model these structures and understand the key differences between polycrystalline FE films and a single-grain FE. The single-grain FE is simulated by the single-domain Landau–Khalatnikov (L–K) model [11]. Although this is a simplified model for illustrative purposes, it produces a close resemblance to the behavior obtained with a multidomain analysis [24]. Fig. 6(a) shows the simulated P – V loops for an 8.3-nm HZO capacitor and an FE–DE stack

of an 8.3-nm HZO film and a series dielectric with different capacitance ratios C_{DE}/C_{FE} . The P – V loops are simulated with a triangular waveform of 4-ms period and 3-V amplitude. According to the L–K model, adding a series capacitor results in a decreased switching voltage with an abrupt transition, suggesting that the programming voltage of an FE–DE stack can be lower than that of an FE capacitor. However, this behavior is not observed with a polycrystalline FE [18]. As shown in the Monte Carlo simulation in Fig. 6(a), the switching starts at a lower voltage due to the depolarizing field of the DE, but the transition is not abrupt. The depolarizing field of the DE aids switching only when the magnitude of FE polarization is decreasing (i.e., from $\pm P_S$ to 0) but opposes the switching when its magnitude is increasing (i.e., from 0 to $\pm P_S$). Therefore, as the DE capacitance decreases (DE thickness increases), fewer FE grains switch under the same programming conditions. Fig. 6(b) shows the Monte Carlo simulations of the polarization versus time for the same FE and FE–DE capacitors when a square programming waveform is applied, with 2- and 5- μ s period and amplitudes of 3 and 4 V. Irrespective of the pulse duration, the FE–DE starts switching earlier than the FE but takes a longer time to settle. As the DE capacitance decreases, the switched polarization is reduced due to the effect of the depolarizing field. Multidomain simulations of FE switching have also shown a reduction or inhibition of the voltage amplification predicted by the L–K model [25]–[28]. However, these simulations do not consider grain boundaries, which may be the dominant effect in a polycrystalline FE.

The Monte Carlo modeling approach also allows for the investigation of the effects of device-to-device variability due to the grains having a distribution of activation fields. Fig. 7(a) shows the simulated device-to-device variations of an 8.3-nm FE capacitor initialized with 500, 100, and 20 grains, programmed with a square waveform with 20- μ s period. For each case, the simulation is repeated 200 times and plotted with black lines, whereas the red line shows the mean value of all simulations. With a 1.5-V programming amplitude, a $2P_S$ memory window is obtained for 500 grains, which is reduced by approximately 50% for 20 grains. For a 1.25-V programming voltage, the memory window collapses with 20 grains. Fig. 7(b) shows the device-to-device variations of

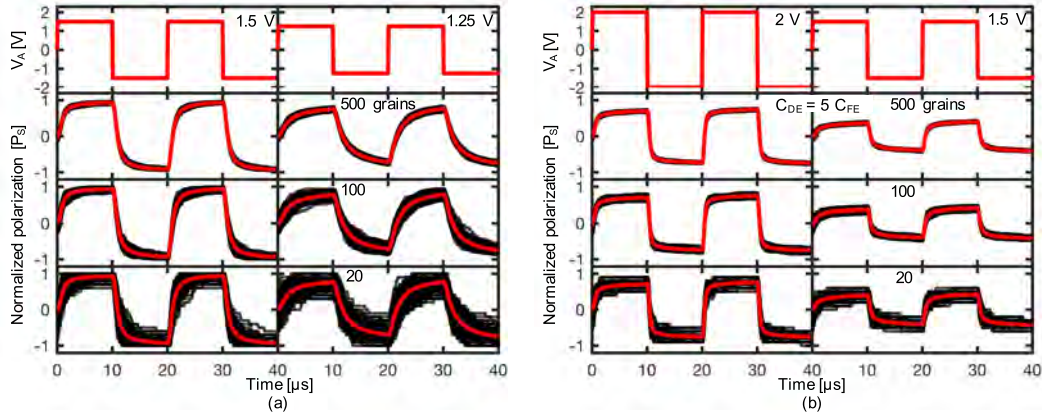


Fig. 7. Simulated device-to-device variations of 200 devices (black line) with 500, 100, and 20 grains for (a) 8-nm-thick FE and (b) FE-DE capacitor with $C_{DE} = 5C_{FE}$. With 20 grains, the memory window of the FE is reduced by 50% with respect to the mean value (red line) for a 1.5-V programming voltage and is completely lost with 1.25 V. With the same number of grains, the FE-DE requires a programming voltage above 1.5 V to obtain a memory window.

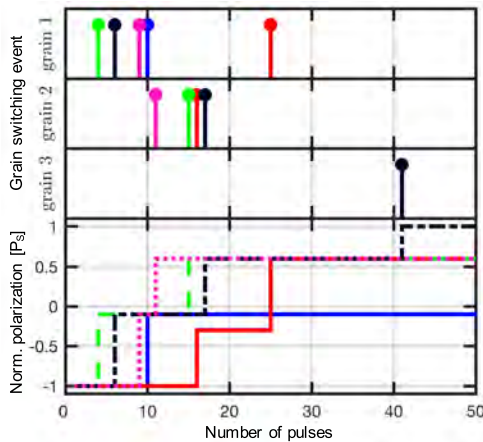


Fig. 8. Switching simulations of a three-grain FE capacitor with the activation fields of 1, 1.8, and 2.6 MV/cm under a train of pulses with 2-V amplitude and 100-ns width. The simulation is repeated five times, represented by different colors. The switching events for each grain are plotted as a function of the number of pulses, showing the inherent variability of the FE response. The normalized polarization is computed, assuming that the grains contribute a 0.45, 0.35, and 0.2 fraction of the total area.

an FE-DE stack with $C_{DE} = 5C_{FE}$ under the same conditions. In this case, a 1.5-V programming voltage produces a memory window close to P_S for 500 grains and close to 0 for 20 grains. The programming voltage needs to be increased to 2 V to obtain similar memory windows than an FE with 1.5-V programming voltage.

Finally, the model is applied to analyze the stochastic switching behavior and accumulation effect in an FE capacitor with only 3 grains, as shown in Fig. 8. The grains are

initialized with the activation fields of 1, 1.8, and 2.6 MV/cm, and it is assumed that the grains have the same polarization P_S , but different areas. The switching instants for five repetitions of a train of pulses show that grains with a higher activation field switch after a larger number of pulses, and the stochastic switching time is captured by the simulation. The resulting polarization shows a stair-like behavior, similar to what has been previously observed [29].

It is important to emphasize that this is a model for polycrystalline FE in a nucleation-limited regime. A fundamental assumption of nucleation-limited models is that the nucleation time dominates the polarization dynamics, whereas the transient of domain growth within a grain is negligible. This assumption does not necessarily hold for highly scaled FE, especially when there is a large series capacitance that stabilizes the domain wall expansion regime [24].

V. CONCLUSION

A Monte Carlo simulation framework, which is capable of predicting the dynamic, history-dependent response of an FE under arbitrary input waveforms, is presented. After a parameter extraction procedure from polarization reversal measurements, the proposed model can predict the polarization response of an HZO FE capacitor under different experimental conditions with the same set of parameters. The model was applied to characterize the dynamic response of FE-DE bilayer structures, showing that the response of polycrystalline FE is significantly different than that of single-grain FE. With the proposed model, the reduction in memory window due to device variability can also be quantified, both for FE capacitors and FE-DE stacks. Finally, an accumulation effect that leads to grain switching was studied and modeled for the first time by a history parameter. This effect is in agreement with a classical nucleation theory, and further theoretical and experimental study is proposed as future work to establish a direct relation

between the history-dependent switching probability and the underlying distribution of clusters during the incubation period of domain nucleation.

REFERENCES

- [1] T. S. Böscke, J. Müller, D. Bräuhäus, U. Schröder, and U. Böttger, "Ferroelectricity in hafnium oxide: CMOS compatible ferroelectric field effect transistors," in *IEDM Tech. Dig.*, Dec. 2011, pp. 24.5.1–24.5.4. doi: [10.1109/IEDM.2011.6131606](https://doi.org/10.1109/IEDM.2011.6131606).
- [2] X. Li *et al.*, "Advancing nonvolatile computing with nonvolatile NCFET latches and flip-flops," *IEEE Trans. Circuits Syst. I, Reg. Papers*, vol. 64, no. 11, pp. 2907–2919, Nov. 2017. doi: [10.1109/TCSI.2017.2702741](https://doi.org/10.1109/TCSI.2017.2702741).
- [3] A. Sharma and K. Roy, "1T non-volatile memory design using sub-10nm ferroelectric FETs," *IEEE Electron Device Lett.*, vol. 39, no. 3, pp. 359–362, May 2018. doi: [10.1109/LED.2018.2797887](https://doi.org/10.1109/LED.2018.2797887).
- [4] D. Kwon *et al.*, "Improved subthreshold swing and short channel effect in FDSOI n-channel negative capacitance field effect transistors," *IEEE Electron Device Lett.*, vol. 39, no. 2, pp. 300–303, Feb. 2018. doi: [10.1109/LED.2017.2787063](https://doi.org/10.1109/LED.2017.2787063).
- [5] A. Aziz *et al.*, "Computing with ferroelectric FETs: Devices, models, systems, and applications," in *Proc. Design, Automat. Test Eur. Conf. Exhib.*, Mar. 2018, pp. 1289–1298. doi: [10.23919/DATF.2018.8342213](https://doi.org/10.23919/DATF.2018.8342213).
- [6] E. W. Kinder, C. Alessandri, P. Pandey, G. Karbasian, S. Salahuddin, and A. Seabaugh, "Partial switching of ferroelectrics for synaptic weight storage," in *Proc. 75th Annu. Device Res. Conf. (DRC)*, Jun. 2017, pp. 1–2. doi: [10.1109/DRC.2017.7999427](https://doi.org/10.1109/DRC.2017.7999427).
- [7] S. Oh *et al.*, "HfZrO_x-based ferroelectric synapse device with 32 levels of conductance states for neuromorphic applications," *IEEE Electron Device Lett.*, vol. 38, no. 6, pp. 732–735, Jun. 2017. doi: [10.1109/LED.2017.2698083](https://doi.org/10.1109/LED.2017.2698083).
- [8] H. Mulaosmanovic, T. Mikolajick, and S. Slesazek, "Accumulative polarization reversal in nanoscale ferroelectric transistors," *ACS Appl. Mater. Interfaces*, vol. 10, no. 28, pp. 23997–24002, Jun. 2018. doi: [10.1021/acsami.8b08967](https://doi.org/10.1021/acsami.8b08967).
- [9] K. Ni, M. Jerry, J. A. Smith, and S. Datta, "A circuit compatible accurate compact model for ferroelectric-FETs," in *Proc. IEEE Symp. VLSI Technol.*, Jun. 2018, pp. 131–132. doi: [10.1109/VLSIT.2018.8510622](https://doi.org/10.1109/VLSIT.2018.8510622).
- [10] B. Obradovic, T. Rakshit, R. Hatcher, J. A. Kittl, and M. S. Rodder, "Ferroelectric switching delay as cause of negative capacitance and the implications to NCFETs," in *Proc. IEEE Symp. VLSI Technol.*, Jun. 2018, pp. 51–52. doi: [10.1109/VLSIT.2018.8510628](https://doi.org/10.1109/VLSIT.2018.8510628).
- [11] A. K. Saha, S. Datta, and S. K. Gupta, "'Negative capacitance' in resistor-ferroelectric and ferroelectric-dielectric networks: Apparent or intrinsic?" *J. Appl. Phys.*, vol. 123, no. 10, Feb. 2018, Art. no. 105102. doi: [10.1063/1.5016152](https://doi.org/10.1063/1.5016152).
- [12] A. K. Tagantsev, I. Stolichnov, N. Setter, J. S. Cross, and M. Tsukada, "Non-Kolmogorov–Avrami switching kinetics in ferroelectric thin films," *Phys. Rev. B, Condens. Matter*, vol. 66, no. 21, Dec. 2002, Art. no. 214109. doi: [10.1103/PhysRevB.66.214109](https://doi.org/10.1103/PhysRevB.66.214109).
- [13] J. Y. Jo, H. S. Han, J.-G. Yoon, T. K. Song, S.-H. Kim, and T. W. Noh, "Domain switching kinetics in disordered ferroelectric thin films," *Phys. Rev. Lett.*, vol. 99, no. 26, Dec. 2007, Art. no. 267602. doi: [10.1103/PhysRevLett.99.267602](https://doi.org/10.1103/PhysRevLett.99.267602).
- [14] S. Zhukov, Y. A. Genenko, O. Hirsch, J. Glaum, T. Granzow, and H. von Seggern, "Dynamics of polarization reversal in virgin and fatigued ferroelectric ceramics by inhomogeneous field mechanism," *Phys. Rev. B, Condens. Matter*, vol. 82, no. 1, Jul. 2010, Art. no. 014109. doi: [10.1103/PhysRevB.82.014109](https://doi.org/10.1103/PhysRevB.82.014109).
- [15] C. Alessandri, P. Pandey, A. Abusleme, and A. Seabaugh, "Switching dynamics of ferroelectric Zr-Doped HfO₂," *IEEE Electron Device Lett.*, vol. 39, no. 11, pp. 1780–1783, Nov. 2018. doi: [10.1109/LED.2018.2872124](https://doi.org/10.1109/LED.2018.2872124).
- [16] N. Gong, X. Sun, H. Jiang, K. S. Chang-Liao, Q. Xia, and T. P. Ma, "Nucleation limited switching (NLS) model for HfO₂-based metal-ferroelectric-metal (MFM) capacitors: Switching kinetics and retention characteristics," *Appl. Phys. Lett.*, vol. 112, no. 26, Jun. 2018, Art. no. 262903. doi: [10.1063/1.5010207](https://doi.org/10.1063/1.5010207).
- [17] Y. A. Genenko *et al.*, "Universal polarization switching behavior of disordered ferroelectrics," *Adv. Funct. Mater.*, vol. 22, no. 10, pp. 2058–2066, 2012. doi: [10.1002/adfm.201102841](https://doi.org/10.1002/adfm.201102841).
- [18] C. Alessandri, P. Pandey, and A. Seabaugh, "Experimentally validated, predictive monte carlo modeling of ferroelectric dynamics and variability," in *IEDM Tech. Dig.*, Dec. 2018, pp. 16.2.1–16.2.4. doi: [10.1109/IEDM.2018.8614607](https://doi.org/10.1109/IEDM.2018.8614607).
- [19] R. W. Balluffi, S. Allen, and W. C. Carter, *Kinetics of Materials*, 1st ed. Hoboken, NJ, USA: Wiley, 2005.
- [20] Y. Ishibashi and Y. Takagi, "Note on ferroelectric domain switching," *J. Phys. Soc. Jpn.*, vol. 31, no. 2, pp. 506–510, 1971. doi: [10.1143/JPSJ.31.506](https://doi.org/10.1143/JPSJ.31.506).
- [21] W. Lee *et al.*, "Investigation of time-dependent resistive switching behaviors of unipolar nonvolatile organic memory devices," *Adv. Funct. Mater.*, vol. 28, no. 35, Aug. 2018, Art. no. 1801162. doi: [10.1002/adfm.201801162](https://doi.org/10.1002/adfm.201801162).
- [22] J. F. Scott *et al.*, "Switching kinetics of lead zirconate titanate submicron thin-film memories," *J. Appl. Phys.*, vol. 64, no. 2, pp. 787–792, 1988. doi: [10.1063/1.341925](https://doi.org/10.1063/1.341925).
- [23] Y. Arayashiki, T. Nakajima, Y. Takahashi, and T. Furukawa, "Accelerated and decelerated polarization reversal in thin vinylidene fluoride/trifluoroethylene copolymer films," *IEEE Trans. Dielectr. Electr. Insul.*, vol. 17, no. 4, pp. 1066–1073, Aug. 2010. doi: [10.1109/TDEI.2010.5539676](https://doi.org/10.1109/TDEI.2010.5539676).
- [24] A. K. Yadav *et al.*, "Spatially resolved steady-state negative capacitance," *Nature*, vol. 565, no. 7740, pp. 468–471, 2019. doi: [10.1038/s41586-018-0855-y](https://doi.org/10.1038/s41586-018-0855-y).
- [25] A. Cano and D. Jiménez, "Multidomain ferroelectricity as a limiting factor for voltage amplification in ferroelectric field-effect transistors," *Appl. Phys. Lett.*, vol. 97, no. 13, Sep. 2010, Art. no. 133509. doi: [10.1063/1.3494533](https://doi.org/10.1063/1.3494533).
- [26] S. Smith, K. Chatterjee, and S. Salahuddin, "Multidomain phase-field modeling of negative capacitance switching transients," *IEEE Trans. Electron Devices*, vol. 65, no. 1, pp. 295–298, Jan. 2018. doi: [10.1109/TED.2017.2772780](https://doi.org/10.1109/TED.2017.2772780).
- [27] M. Hoffmann *et al.*, "Ferroelectric negative capacitance domain dynamics," *J. Appl. Phys.*, vol. 123, no. 18, Apr. 2018, Art. no. 184101. doi: [10.1063/1.5030072](https://doi.org/10.1063/1.5030072).
- [28] M. Hoffmann, M. Pešić, S. Slesazek, U. Schroeder, and T. Mikolajick, "On the stabilization of ferroelectric negative capacitance in nanoscale devices," *Nanoscale*, vol. 10, no. 23, pp. 10891–10899, 2018. doi: [10.1039/C8NR02752H](https://doi.org/10.1039/C8NR02752H).
- [29] H. Mulaosmanovic *et al.*, "Switching kinetics in nanoscale hafnium oxide based ferroelectric field-effect transistors," *ACS Appl. Mater. Interfaces*, vol. 9, no. 4, pp. 3792–3798, 2017. doi: [10.1021/acsami.6b13866](https://doi.org/10.1021/acsami.6b13866).

APPENDIX E

PROCESS DEPENDENT SWITCHING DYNAMICS OF FERROELECTRIC
HAFNIUM ZIRCONATE

Process Dependent Switching Dynamics of Ferroelectric Hafnium Zirconate

Pratyush Pandey, Cristobal Alessandri, and Alan C. Seabaugh

University of Notre Dame, Notre Dame, Indiana 46556, USA

Email: ppandey@nd.edu, seabaugh.1@nd.edu; Phone: (574)-631-4473

Introduction: The CMOS-compatible ferroelectrics (FE) based on HfO_2 are being widely explored for emerging memory, logic, and neuromorphic devices [1]. While the applications hinge on the dynamic switching of the FE, process optimization often relies on information obtained from measurement of the quasi-static polarization-field (P-E) hysteresis loops [2]. We have recently been refining methods for characterizing the polarization reversal dynamics of polycrystalline FEs, such as Hafnium Zirconate (HZO). Because of the close agreement between the nucleation limited switching (NLS) model and measurements, detailed physical information such as minimum switching time and activation field distributions can be extracted from polarization reversal measurements vs. pulse amplitude and duration [3]. This characterization has been successfully applied to the prediction of FE switching dynamics under arbitrary voltage waveforms [4]. Here, we utilize this method to study the dependence of the switching dynamics of FE HZO formed by atomic layer deposition (ALD) vs. electrode metal and post deposition anneal temperature.

Fabrication and Characterization: Symmetrical metal/HZO/metal capacitors having 25 μm radius were fabricated by optical lithography, with sputtered 100 nm TiN and W top/bottom electrodes, 10 nm Plasma Enhanced ALD HZO at 300 $^\circ\text{C}$ with TDMAH and TDMAZ precursors, having post deposition anneal temperatures of 400, 500, and 600 $^\circ\text{C}$ for 30 sec in N_2 . Polarization reversal curves were obtained by applying voltage pulses to these capacitors, with pulse widths ranging from 200 ns to 1 ms, and pulse amplitudes from 0.1 V to 2.5 V, and the nonvolatile switched FE charge was measured using a unipolar double triangular waveform. The obtained curves were then fitted using the NLS model [3], which considers the FE HZO film to be comprised of many independently switching FE grains with different activation fields belonging to a distribution function. The switching time constant of each grain depends on the applied field, the activation field, and the minimum switching time constant.

Results: The polarization reversal curves of the W/HZO/W capacitors saturated for 2.5 V, 1 ms pulses, while the TiN/HZO/TiN capacitors do not saturate. The non-saturating behavior of the latter can be understood by observing their responses to a single triangular voltage pulse, which show the FE starting to depolarize when the applied bias is reduced. This depolarization stems from the internal field generated by the movement of Ti/N species into the HZO film [5], and the depolarizing field increases for higher voltage pulse widths and amplitudes. Characterizing the degree of saturation by the slope $d(\log(P))/d(\log(t))$ (with zero meaning fully saturated) for the pulses with highest amplitudes and widths, it is observed that the saturation improves for higher anneal temperatures, but is insufficient for accurate NLS fitting. In contrast, the W/HZO/W capacitors saturate, allowing data extraction. The remnant polarization P_R was found to increase by $2.5\times$ upon increasing anneal temperature from 400 to 600 $^\circ\text{C}$ due to increased phase transformation of the amorphous PE-ALD HZO into the FE phase at higher anneal temperatures, in accordance with previously observed results [2]. An increase in the minimum switching time constant was also observed with increasing anneal temperature, leading to a trade-off between higher P_R and faster switching. The extracted distributions of activation fields show a reduced mean activation field upon increasing the anneal temperature, with no significant reduction in the standard deviation. The fact that the 400 $^\circ\text{C}$ sample has a smaller minimum time constant, but a larger activation field, is indicative of another trade-off, highlighted by plotting the mean switching time at different applied bias for the three samples - the 400 $^\circ\text{C}$ sample is slower to switch at voltages below 1.75 V, but is faster at higher biases. The 400 $^\circ\text{C}$ condition is, therefore, favored when speed is the motivating factor, while the 500 and 600 $^\circ\text{C}$ yield lower activation fields as desired in low power applications. Finally, despite the fact that the top and bottom electrodes are the same, the mean switching time is dependent on the direction of polarization reversal, indicating structural differences in the top and bottom W/HZO interfaces.

Conclusion: Systematic measurements of polarization reversal dynamics in FE HZO have been used to provide the first quantitative characterization of switching speed, remnant polarization, and activation field distributions vs. process condition. The trade-offs between electrode metal (W and TiN) and anneal reveal optimization directions.

[1] A. Aziz et al., 2018 Design, Automation & Test Europe (DATE) 1289-1298.

[2] S.J. Kim et al., J. Min. Met. & at. Soc. (JOM), vol. 71, 246-255 (2019).

[3] C. Alessandri et al., IEEE Electron Dev. Lett., vol. 39, 1780-1783 (2018).

[4] C. Alessandri et al., 2018 Int. Electron Dev. Meeting (IEDM), 16.2.1-4.

[4] G. Karbasian et al., Appl. Phys. Lett., vol 111, 022907 (2017).

Measurement Protocol and NLS Model

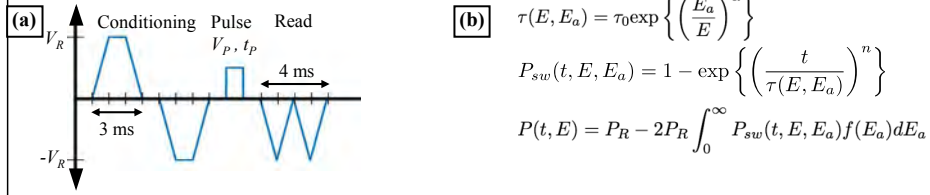


Fig. 1. (a) Measurement protocol for parameter extraction. (b) NLS Model for polarization reversal of polycrystalline FE. Time constant τ depends on applied field E and activation field E_a , which is distributed according to $f(E_a)$. Fitting parameters P_R , n , α , τ_0 , and distribution function $f(E_a)$ extracted from measurements.

TiN/HZO/TiN Capacitors –Non Saturation and Depolarization

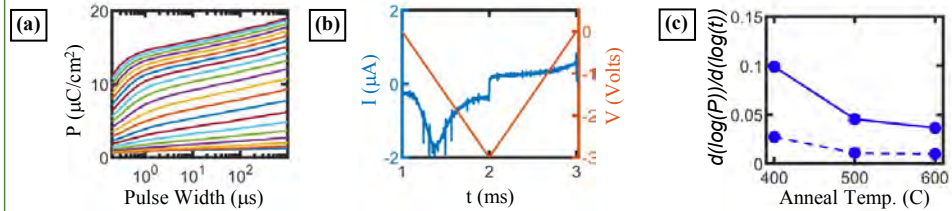


Fig. 2. (a) Polarization reversal characteristics of TiN/HZO/TiN capacitor annealed at 500 C do not saturate due to depolarization and movement of Ti/N. (b) Response to triangular waveform shows depolarization current at low bias. (c) Degree of saturation, measured by $d(\log(P))/d(\log(t))$, increases for higher anneal temperatures.

W/HZO/W Capacitors – Anneal Temperature Dependence

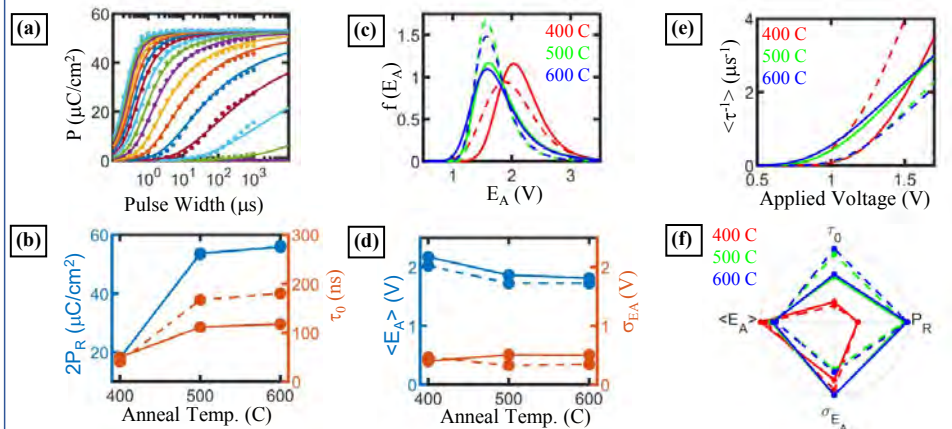


Fig. 3. (a) Measured (dots) and fitted (solid lines) polarization reversal characteristics of W/HZO/W capacitor annealed at 500 C. (b) Extracted remnant polarization ($2P_R$) and minimum time constant (τ_0) for positive (solid lines) and negative (dashed lines) applied voltage pulses. (c) Extracted activation field distributions $f(E_a)$ for different anneal temperatures, and positive (solid lines) and negative (dashed lines) applied voltage pulses. (d) Mean and standard deviation of activation field distributions. (e) Mean switching time for various applied voltages. (f) Optimization plot of extracted switching parameters for different anneal temperatures.

APPENDIX F

PROGRAMMING-PULSE DEPENDENCE OF FERROELECTRIC PARTIAL POLARIZATION: INSIGHTS FROM A COMPARATIVE STUDY OF PZT AND HZO CAPACITORS



Programming-Pulse Dependence of Ferroelectric Partial Polarization: Insights From a Comparative Study of PZT and HZO Capacitors

Pratyush Pandey¹, Student Member, IEEE, Wan Sik Hwang², Member, IEEE, K. R. Udayakumar, Ted S. Moise³, Fellow, IEEE, and Alan C. Seabaugh, Fellow, IEEE

Abstract—The programming of partial polarization in ferroelectric (FE) hafnium zirconate (HZO) capacitors is shown to depend on the delay between FE reset and the polarization write pulse (delay-before-write), revealing a subtle history dependence. Programming is substantially independent of delays inserted after the write and before the read (delay-before-read), with no decay in partial polarization observed from 1 μ s up to 260 ms. We further show that nonsaturation in FE polarization can be introduced if the pulse protocol is not strictly symmetric, where strictly symmetric means that the integral of the voltage waveform over a single measurement cycle is zero. The delay-before-write dependence in HZO is compared with lead-zirconium-titanate (PZT) capacitors used in FE random access memory (FRAM) which shows much weaker dependence. The delay dependence is attributed to the dynamics of subcritical nuclei formation in nucleation limited switching. For the first time, the decay of subcritical nuclei in HZO is shown to be observable up to 1 s, and an upper bound on their volume is estimated to be ~ 10 nm³, corresponding to $\sim 4 \times 4 \times 4$ unit cells.

Index Terms—Ferroelectric (FE), FE random access memory (FRAM), hafnium zirconate (HZO), lead zirconium titanate (PZT).

I. INTRODUCTION

THE partial switching of polycrystalline ferroelectrics (FEs) is being widely explored for analog weight storage to accelerate deep neural network training [1]–[4]. Partial switching also plays a role in write disturb in memory arrays [5]. While the history dependence of FE switching has received attention [6]–[8], for technology

Manuscript received June 1, 2020; revised July 27, 2020; accepted August 3, 2020. Date of publication August 21, 2020; date of current version September 22, 2020. The review of this article was arranged by Editor G. L. Snider. (Corresponding author: Pratyush Pandey.)

Pratyush Pandey and Alan C. Seabaugh are with the Department of Electrical Engineering, University of Notre Dame, Notre Dame, IN 46556 USA (e-mail: ppandey@nd.edu; seabaugh.1@nd.edu).

Wan Sik Hwang is with the Department of Materials Engineering, Korean Aerospace University, Goyang 10540, South Korea.

K. R. Udayakumar and Ted S. Moise are with Texas Instruments Incorporated, Dallas, TX 75243 USA.

Color versions of one or more of the figures in this article are available online at <http://ieeexplore.ieee.org>.

Digital Object Identifier 10.1109/TED.2020.3015794

applications, it is important to understand the factors that control writing the partially polarized state. This is especially relevant for use in neural network training acceleration schemes [4] that utilize stochastic pulsing to set the partial polarization. In such protocols, it is essential that the set partial polarization depends only upon the number of write pulses and is independent of the delays between the write pulses.

To characterize partial polarization, we show that it is important to adopt a strictly balanced pulse waveform to minimize history dependence related to ionic movement and charge trapping. We then show that the partially polarized state depends significantly on the delay between FE reset and the partial-polarization write pulse (delay-before-write). This dependence is consistent with a physical picture in which subcritical nuclei generated in the reset alter the charge set in the write pulse. The understanding gained from this study has application in the development of read/write protocols for analog weight storage using FEs.

II. DEVICE DESCRIPTION AND MEASUREMENTS

Atomic layer deposition (ALD) of 10-nm hafnium zirconate (HZO) was followed by a postdeposition anneal of 600 °C for 30 s on sputtered W and TiN symmetric capacitors (HZO1 and HZO2) having a 25 μ m radius. The process-dependent switching of these capacitors was first reported in [9]. Lead-zirconium-titanate (PZT) capacitors with thicknesses 65, 59, and 52 nm (PZT1, PZT2, and PZT3) were deposited by metal organic chemical vapor deposition (MOCVD) in Texas Instrument's production, five-level Cu metallization 130-nm FE random access memory (FRAM) process [10] with Ir/IrOx electrode thicknesses of 60 nm. The total capacitor area is 400 μ m² consisting of four 10 \times 10 μ m² capacitors in parallel using Cu metallization in a standard production test structure. In this process, switched polarization density has been shown to be independent of capacitor area in the range from 0.1 to 100 μ m² [11]. Electrical measurements were performed using a Keithley 4200 parameter analyzer with a 4225-PMU (pulse measurement unit) and two 4225-RPM remote preamplifiers [12]. Measurements were initiated after

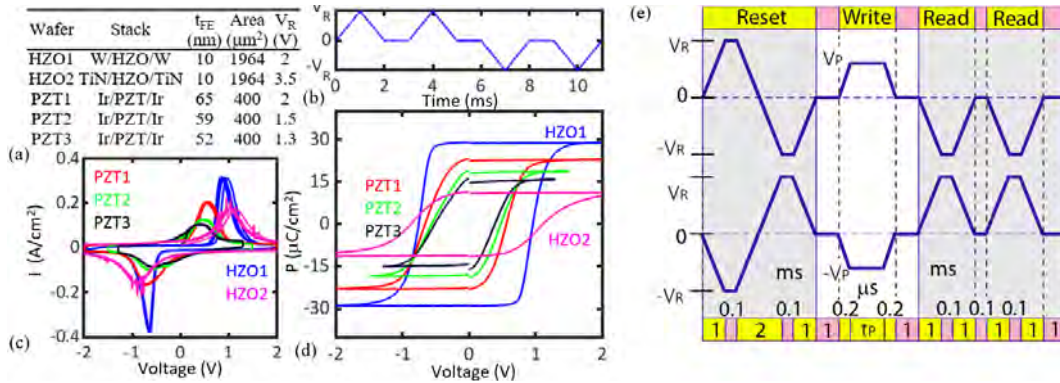


Fig. 1. (a) FE capacitor descriptions: FE layer thickness t_{FE} and reset voltage V_R . (b) Voltage waveform used to extract polarization–voltage (P – V) loops, compensating for leakage and displacement current. (c) Measured current response to the triangular waveform (20 cycles). (d) Extracted P – V loops. (e) Symmetric pulse protocol (1-cycle) used to measure FE partial polarization switched by a (V_P , t_P) pulse. Each positive pulse waveform (upper) is followed by its negative waveform (lower), so that the integral of pulse train is zero in every cycle.

a wake-up of 3000 cycles of 250 Hz triangular waves with amplitude set to exceed the coercive field and substantially switch the FE. The capacitor physical parameters and wake-up amplitudes are summarized in Fig. 1(a).

Fig. 1(b) shows the voltage waveform applied to extract the polarization–voltage (P – V) loops. The current response to the first and third triangular pulses are a combination of FE switching, capacitive displacement current, and leakage, while the response to the second and fourth pulses involves only the displacement current and leakage. Subtracting the current in the second (fourth) voltage pulse from the first (third) pulse gives the FE switching current, which is plotted with respect to applied bias in Fig. 1(c). Generally, it can be seen that HZO capacitors switch at a higher voltage than PZT. However, the FE switching in HZO occurs over a narrower range of voltages as compared to PZT, leading to a sharper thresholding behavior. Additionally, the current responses in Fig. 1(c) are not symmetric about 0 V, despite the use of symmetric electrode metals. Asymmetries in this case can still arise from differences between top and bottom electrode interfaces with the FE as well as from edge differences. The current waveforms in Fig. 1(c) are integrated to yield the P – V loops in Fig. 1(d), which show that the W/HZO (HZO1) and TiN/HZO (HZO2) capacitors have a remanent polarization (P_R) of 29 and 12 $\mu\text{C}/\text{cm}^2$, while Ir/PZT has a P_R which decreases with thickness, 24, 19, and 16 $\mu\text{C}/\text{cm}^2$, consistent with previous results for PZT [13].

III. MEASUREMENT RESULTS

We first show the importance of adopting a strictly symmetric programming pulse sequence to avoid the introduction of history dependence in setting the partial polarization state. By strictly symmetric, we mean that the integral of the voltage waveform in every measurement cycle is zero. The programming pulse sequence applied to measure the partial polarization switching, along with the fixed timing parameters, are shown in Fig. 1(e). The measurement cycle shown in Fig. 1(e) starts with the upper waveform followed immediately

by the lower waveform. In this measurement, the FE is initially set to a fully polarized state, and after a 1 ms delay-before-write, a write pulse of particular amplitude and duration is applied. After a 1 ms delay-before-read, a double read pulse is applied. This is a strictly symmetric measurement protocol with complementary positive and negative waveforms applied in every cycle so that no preference is given to one polarization direction over another. The instantaneous current due to the second read pulse is subtracted from that in the first read pulse, and this difference is integrated for the duration of the pulse to obtain the switched polarization charge for that particular pulse amplitude and duration. The pulse duration t_P is then stepped logarithmically from 200 ns to 2.5 ms, after which the pulse amplitude V_P is stepped from 0.2 V for HZO1 and PZT1, and 0.1 V for HZO2, PZT2, and PZT3, to the reset voltage V_R in 0.2 V increments.

It is certainly feasible to measure polarization reversal characteristics using an asymmetric measurement protocol as we have utilized in the past [9], [12]. In the asymmetric measurement protocol, the measurements corresponding to the upper waveform in Fig. 1(e), i.e., with positive pulse amplitudes, are performed in sequence to obtain all of the positive V_P , t_P characteristics. Following this, the negative V_P , t_P polarity pulses (lower waveform) are applied in sequence. If the reset is effective in always returning the FE to the same state, then the results of the symmetric and asymmetric protocols should be the same. However, polarization reversal measurements on HZO2 shown in Fig. 2(a) and (b) shows significant differences in the polarization reversal characteristics. Both measurements use a reset voltage of ± 3.5 V and write pulse amplitudes are stepped from 0.1 to ± 3.5 V with a step of 0.2 V. Under the asymmetric pulse protocol, Fig. 2(a), the polarization does not saturate for positive write voltages, but does saturate for negative write voltages, while using the symmetric pulsing protocol, Fig. 2(b), improved saturation is exhibited for both write polarities. It should be noted that these results are not related to fatigue or wake-up in the FE, since the three repeats exhibit similar behaviors.

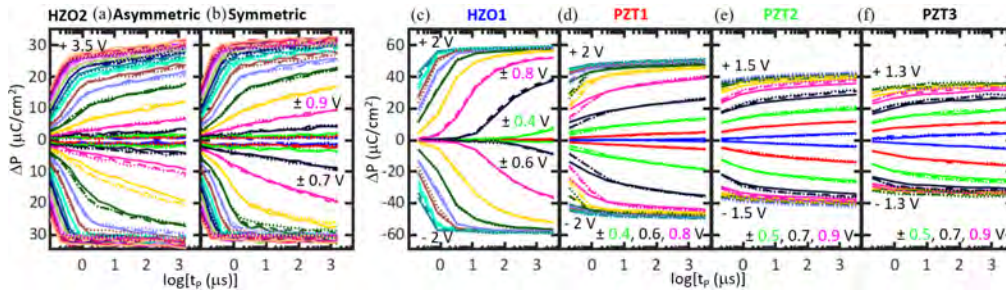


Fig. 2. Measured polarization reversal ΔP versus pulsewidth t_p and pulse amplitude V_p in HZO and PZT capacitors, with each measurement repeated thrice; the first, second, and third runs are plotted with solid, dashed, and dotted lines, respectively. (a) TiN/HZO capacitor HZO2 tested using an asymmetric pulse protocol and (b) using the symmetric pulse protocol. In the asymmetric pulse measurement, the $V_p > 0$ pulses are applied first, followed by the $V_p < 0$ pulses. (c) Measured ΔP - V_p , t_p characteristics of W/HZO capacitor HZO1 and (d)–(f) PZT capacitors, measured using the symmetric protocol.

The presence of ionic or trap charges at the metal–HZO interfaces can account for the observed nonsaturation under asymmetric pulsing and its reduction under symmetric pulsing. When programming with the asymmetric protocol, a bias over time is introduced. As the positive write voltages are incremented in sequence, the FE capacitor experiences negative voltages for a longer duration than positive voltages (due to the double pulse read). This causes charge, ionic or electronic, to accumulate at the electrodes. This charge is of opposite sign to the FE polarization charge switched by the write pulse. This can have two effects. First, this interfacial charge modifies the internal field of the HZO, thereby affecting the polarization reversal. Second, the accumulated charge has its own time dependence and does not return to the same initial condition during the reset. This accumulated charge introduces a history dependence in the polarization switching, causing more charge to be switched by the write pulse in the asymmetric protocol, leading to nonsaturating polarization reversal characteristics. The asymmetry in the polarization saturation shown in Fig. 2(a) suggests differences in the accumulated charge density at the two electrodes due to differences in the structural properties of these two interfaces.

In the measurement of partial polarization, it is not a general property of HZO to exhibit a dependence on asymmetric versus symmetric programming. The W/HZO capacitor (HZO1) was tested using the asymmetric pulse protocol, and no significant differences were observed between the two test methods. This is likely explained by the lower density of ionic/trap charges in W/HZO as compared to TiN/HZO (HZO2) capacitors [9]. The observed electrode dependence is consistent with Karbasian *et al.* [14], who reported a higher concentration of charged oxygen vacancies in the TiN/HZO system compared to W/HZO, attributed to the diffusion of N atoms into the HZO.

The polarization reversal characteristics of HZO and PZT are compared in Fig. 2 using the strictly symmetric measurement protocol with Fig. 2(c) showing HZO1, and Fig. 2(d)–(f) showing PZT with thicknesses 65, 59, and 52 nm, respectively. It can be seen that the minimum HZO switching time constant, which is the time taken for a majority of the FE grains to

switch polarity, is approximately 200 ns, consistent with prior studies [9], [12]. FE HZO has been shown to exhibit sub-5 ns partial switching by 4.5 V write pulses [15], corresponding to switching of the fastest FE grains. When PZT and HZO are compared at the same pulse amplitudes, PZT is clearly faster than HZO. PZT-based FRAM have been demonstrated having access/cycle times of 30–35 ns, with PZT switching in less than 5 ns [16]. This difference in the switching speeds of HZO and PZT is not related to RC delay, since the capacitance of the PZT is only $\sim 3\times$ lower than HZO, whereas the PZT switches $> 50\times$ faster than the HZO when switched at the same voltage. The difference in speed is reasonably associated with the lower coercive field in PZT as compared to HZO. In an application, power, speed, endurance, process integration, and other factors will ultimately drive the preferences of one FE over another.

The net charge switched is greater in HZO1 than in PZT1 which is not out of the ordinary: for HZO1 $P_R = 29 \mu\text{C}/\text{cm}^2$ and for PZT1 with a thickness of 65 nm, $24 \mu\text{C}/\text{cm}^2$. The HZO1 film shows significantly more switched-polarization asymmetry at subsaturation voltages, Fig. 2(c), than PZT, Fig. 2(d)–(f). In HZO, this is again likely due to structural asymmetry in the metal-FE electrodes arising from differences in FE-on-metal and metal-on-FE deposition during the capacitor fabrication [9]. The better symmetry of the PZT capacitor may be related to the maturity of the process and not any intrinsic difference in PZT versus HZO.

The dependence of polarization on the delay-before-read, t_{D2} , with a fixed delay-before-write, $t_{D1} = 1 \mu\text{s}$, was measured using the symmetric protocol shown in Fig. 3(a) and plotted for HZO and PZT in Fig. 3(b) and (c), respectively. In these figures, the delay-before-read was stepped in $4\times$ increments from $1 \mu\text{s}$ to 262.144 ms for write pulse durations of $1 \mu\text{s}$ (HZO) and $10 \mu\text{s}$ (PZT). As can be seen in Fig. 3(b) and (c), the FE polarization is independent of delay-before-read for all write amplitudes, highlighting that, once set, the partially polarized states in both HZO and PZT are stable in that they do not show significant decay up to 260 ms.

Polarization reversal measurements are shown in Fig. 3(d)–(g) as a function of delay-before-write t_{D1} ,

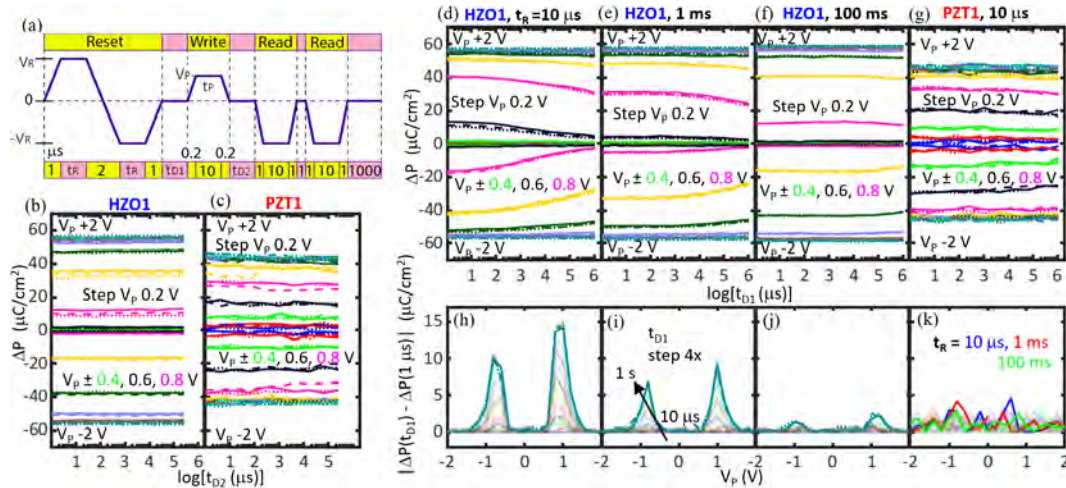


Fig. 3. Measured dependence of polarization reversal on delay-before-read t_{D2} , delay-before-write t_{D1} , and with reset pulsewidth t_R as a parameter. Each measurement is repeated thrice, and the first, second, and third runs are plotted with solid, dashed, and dotted lines, respectively. (a) Symmetric pulse protocol (positive branch) which is immediately followed by its negative. (b) Measured polarization reversal in HZO1 versus delay-before-read at $t_P = 1 \mu\text{s}$, $t_R = 10 \mu\text{s}$, and $t_{D1} = 1 \mu\text{s}$. (c) Measured polarization reversal in PZT1 versus delay-before-read at $t_P = 10 \mu\text{s}$, $t_R = 10 \mu\text{s}$, and $t_{D1} = 1 \mu\text{s}$. Measured polarization reversal versus delay-before-write at $t_{D2} = 1 \mu\text{s}$ and $t_P = 10 \mu\text{s}$. In HZO, the measured partial polarization depends also on the reset time t_R , (d) $10 \mu\text{s}$, (e) 1 ms , (f) 100 ms , while in (g) PZT, $10 \mu\text{s}$, there is no clear dependence on reset time. $|\Delta P(t_{D1}) - \Delta P(1 \mu\text{s})|$ plotted versus V_P in (h)–(k) corresponding to the measurements in (d)–(g). (k) For PZT, the results for all three t_{RS} are summarized.

again using the timing parameters in Fig. 3(a), with the delay-before-read t_{D2} fixed at $1 \mu\text{s}$. The switched polarization in the vicinity of the coercive voltage decreases as the delay-before-write is increased from $1 \mu\text{s}$ to 1.048576 s in $4\times$ increments, whereas the polarization is relatively constant for the FE in either of the two ($\pm P_R$) fully polarized states. The partial polarization change is indicative of a phenomenon inhibitory to FE switching that increases with time spent at zero bias, for write amplitudes V_P in the vicinity of the coercive voltage. This is more pronounced for HZO than PZT.

The PZT polarization reversal measurements shows an apparently greater fluctuation in the polarization density with delay-before-write, Fig. 3(g) compared to the HZO in Fig. 3(d)–(f). This is a consequence of the fact that the capacitor areas tested for PZT are $5\times$ smaller than the HZO capacitor so that fluctuations are amplified by $5\times$ when the polarization charge is divided by the area.

HZO ΔP versus t_{D1} is also found to depend on reset time as t_R is stepped from $10 \mu\text{s}$ to 1 to 100 ms , Fig. 3(d)–(f), respectively. In these figures, it is apparent that the switched polarization ΔP for the same write amplitude and delay-before-write decreases as the reset time is increased, again in the vicinity of the coercive voltage. As the duration of this reset pulse is increased, less FE polarization is switched. Therefore, the inhibitory mechanism that increases with time spent at zero bias (i.e., during t_{D1}) also increases with time spent at a bias of opposite polarity (i.e., during the t_R just preceding the write pulse). The repeatability of the measurements highlights that if the reset time, write delay, pulse amplitude, and pulse duration are fixed, the FE partial polarization can be set with precision. For application in neural network training,

especially using stochastic write pulses [4], the FE is not reset prior to setting the partially polarized state, and the delays between consecutive write pulses is not fixed. In these cases the delay dependencies will need evaluation for the cycle times of the proposed system.

To accentuate the delay-before-write dependence of the partial polarization on write pulse amplitude, we plot the difference in $|\Delta P(t_{D1}) - \Delta P(1 \mu\text{s})|$ versus V_P and as t_{D1} is incremented in $4\times$ steps from $1 \mu\text{s}$ to 1.048576 s , in Fig. 3(h)–(k). These plots show clearly that the strongest delay-before-write dependence occurs in the vicinity of the coercive voltage, or when the FE is partially polarized. Furthermore, as the reset pulsewidth is increased from $10 \mu\text{s}$ in Fig. 3(h) to 100 ms in (j), the amplitude of the partial polarization difference decreases. For PZT all of the measurements can be summarized in a single plot, Fig. 3(k). While the largest variations are near the coercive voltages, there is no clear dependence on reset pulsewidth.

IV. EXPLANATION

The observed delay dependencies in partial polarization can be understood from the nucleation-limited-switching model [17], [18], which considers a thin film polycrystalline FE comprised of independently switching FE grains. Any given FE grain is oriented with either $+P$ or $-P$ polarity. In a fully polarized FE ($\pm P_R$), all the grains are oriented with the same polarity, whereas partial polarization occurs when a fraction of the grains are oriented with opposite polarity. The process of a particular FE grain switching orientation is nucleation-limited, i.e., once a nucleus of the opposite orientation reaches a critical volume, it expands to switch

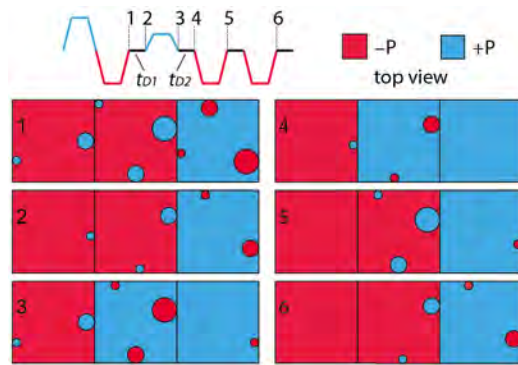


Fig. 4. Partial-polarization measurement waveform and time evolution of the subcritical nuclei within the FE grains. Three grains are shown at each time point to schematically illustrate how the nuclei grow and decay with time. The left and middle grains represent the majority of the polycrystalline film after the negative reset pulse, while the right grain accounts for the fact that for a given reset pulse some small number of grains may remain unswitched. These minority grains still develop subcritical nuclei during the pulse sequence and evolve with an opposing polarity over time.

the entire grain in a time short with respect to the nucleation time. A nucleus of subcritical size expands or contracts under the influence of an electric field, depending on the relative orientation of the field with respect to the nucleus. If the field is removed, a subcritical nucleus decays due to strain at its boundary, and these decaying nuclei can influence subsequent switching [6], [7]. When the FE is pulsed, an FE grain having larger subcritical nuclei will switch with a higher probability than a grain with smaller subcritical nuclei. The expansion of a subcritical nucleus occurs slowly for a low electric field, while it occurs quickly for a high electric field. Therefore, it is for intermediate values of electric field, close to the mean FE activation field, that the influence of subcritical nuclei on partial polarization is most prominent.

A simple picture is provided in Fig. 4 to explain the dependence of delay-before-write and delay-before-read on partial polarization switching. This picture is a simple extension of the nucleation-limited switching dynamics discussed by Mulaosmanovic [6], [7]. Following the completion of a negative reset pulse at time 1 the polarization is substantially set to the $-P$ state (red), but there may exist a few unflipped $+P$ grains (blue). In each of the grains some number of subcritical nuclei are shown. These nuclei grow or decay with time depending on the electric field magnitude and polarity. When no voltage is applied, as between times 1 and 2 (delay-before-write) and times 3 and 4 (delay-before-read), the subcritical nuclei decrease in volume over time independent of their polarity. On the other hand, when a positive voltage is applied, as during the write pulse, the $+P$ (blue) nuclei expand and $-P$ (red) nuclei contract, and during the negative read pulses the opposite occurs.

The decrease in switched polarization with increasing delay-before-write can be understood by considering the time interval between 1 and 2 in Fig. 4. Each of the grains contain

subcritical nuclei with opposing polarity; these nuclei reduce in size with increasing time spent at zero bias, i.e., during the delay-before-write t_{D1} . As a result, the switched polarization caused by longer delay-before-write in the range of the coercive voltage is reduced because there are fewer near-critical nuclei to enable the switching process.

For a fixed delay-before-write and write pulse amplitude, a lower FE polarization is switched as the reset time t_R is increased. This can be explained by the reduction in volume of the subcritical nuclei as the reset pulse time is increased. Therefore, a longer reset time leads to smaller subcritical nuclei at time 1 itself, leading to smaller subcritical nuclei at time 2 before the write pulse, causing less grains to be switched. These effects are most prominent for write pulses with amplitudes close to the mean activation field.

As our measurements show, Fig. 3(d)–(f), subcritical nuclei remain active for a remarkably long time, extending up to 1 s. Their effect on the switched FE grains (i.e., $\Delta P(t_{D1})$) decreases approximately as the logarithm of the delay-before-write time. This suggests the presence of processes opposing the decay of subcritical nuclei in the absence of any field; such processes may be due to interactions of the nuclei with interfaces or defect complexes, as well as thermal excitations. Comparing HZO and PZT, the latter does not show a significant delay-before-write dependence. This may simply be due to the PZT switching faster than the HZO, and therefore, the delay-before-write in PZT being significant only for t_{D1} smaller than 1 μ s. More delay-before-write dependence might be expected in PZT if testing were to be conducted with shorter reset times; however, to fully saturate PZT, a reset time greater than 1 μ s is needed, Fig. 2(d), for the conditions evaluated in this study. The larger grain size and lower activation field (as opposed to activation voltage) in PZT may play a role in the quick decay of subcritical nuclei. In case the long decay time in HZO is primarily related to defects, this may indicate a lower defect density in PZT, since it is FE as-deposited via MOCVD, whereas the HZO requires a postdeposition recrystallisation anneal, which can then introduce defects.

The independence of switched polarization on delay-before-read can also be understood using Fig. 4. Since in this measurement the delay-before-write time is fixed, the condition at time interval 2 is fixed. As the delay-before-read is increased between interval 3 and 4, the sizes of the subcritical nuclei decrease. The negative read pulse has an amplitude $-V_R$, which resets the grains switched during the write pulse, shown by the switching of the middle grain at time 5. This switching is independent of the size of the remaining nuclei which is consistent with the experimental observation. While our proposed explanation qualitatively explains the experiment, we recognize that a quantitative model that is able to account for the delay-before-write dependence is an important avenue of future research.

The dependence of switched polarization on delay-before-write indicates that subcritical nuclei are generated, and that these nuclei enhance the charge switched in a subsequent write pulse. For short (10 μ s), low voltage (0.1 V) write pulses, the subcritical nucleus volume is large, and yet no polarization change is detected in the delay-before-read measurements,

Fig. 3(b). This fact can be used to infer a maximum size of the subcritical nuclei, whose volume must represent a charge which should be measurable unless it is below the system measurement limits. Based on the specifications for the Keithley 4225-PMU, the current resolution is 0.5%, which means the charge resolution is approximately 1%. From this, we can infer that the subcritical volume is less than 1% of the grain volume. For a cubic HZO grain with sides commensurate with the thickness of the film, the volume is 1000 nm^3 . This suggests a subcritical grain volume of approximately 10 nm^3 , or a $4 \times 4 \times 4$ array of HZO unit cells. This volume represents approximately $0.29 \mu\text{C}/\text{cm}^2$ of polarization charge when summed over all the FE grains in the $50\text{-}\mu\text{m}$ diameter capacitor. Remarkably, this small subcritical charge gives rise to measured polarization enhancement as large as $\sim 15 \mu\text{C}/\text{cm}^2$, Fig. 3(h), and representing a polarization gain of ~ 50 .

V. CONCLUSION

Using a strictly symmetric pulse measurement protocol to minimize the effects of electron trapping and ion motion, we have shown that subcritical nuclei in HZO, generated during FE reset, persist for a time up to 1 s. These subcritical nuclei then have a substantial influence on the switching of the partially polarized state, by as much as $15 \mu\text{C}/\text{cm}^2$ in HZO capacitors that are written within $10 \mu\text{s}$ of reset. For HZO, these findings are relevant to the development of pulse update protocols for FE capacitors, tunnel junctions, and field-effect transistors, used for weight storage in neural network training. For PZT, no effects of delay-before-read and delay-before-write are discernable in the investigated range of applied field and switching times, however, these may well be revealed in higher speed pulse measurements. The apparent higher speed switching response in PZT versus HZO when measured at the same pulse amplitudes likely arises from PZT's lower activation field and larger grain size. Differences in the nature of defects must also exist due to differences in electrodes and growth processes.

ACKNOWLEDGMENT

The authors would like to thank Scott Summerfelt for useful discussions of FE testing, pulse protocol and spurious charging due to mobile ions and traps.

REFERENCES

- [1] E. W. Kinder, C. Alessandri, P. Pandey, G. Karbasian, S. Salahuddin, and A. Seabaugh, "Partial switching of ferroelectrics for synaptic weight storage," in *Proc. 75th Annu. Device Res. Conf. (DRC)*, Jun. 2017, pp. 1–2, doi: [10.1109/DRC.2017.7999427](https://doi.org/10.1109/DRC.2017.7999427).
- [2] M. Jerry *et al.*, "Ferroelectric FET analog synapse for acceleration of deep neural network training," in *IEDM Tech. Dig.*, Dec. 2017, pp. 6.2.1–6.2.4, doi: [10.1109/IEDM.2017.8268338](https://doi.org/10.1109/IEDM.2017.8268338).
- [3] K. Chatterjee *et al.*, "Challenges to partial switching of $\text{Hf}_{0.8}\text{Zr}_{0.2}\text{O}_2$ gated ferroelectric FET for multilevel/analog or low-voltage memory operation," *IEEE Electron Device Lett.*, vol. 40, no. 9, pp. 1423–1426, Sep. 2019, doi: [10.1109/LED.2019.2931430](https://doi.org/10.1109/LED.2019.2931430).
- [4] T. Gokmen and Y. Vlasov, "Acceleration of deep neural network training with resistive cross-point devices: Design considerations," *Frontiers Neurosci.*, vol. 10, p. 333, Jul. 2016, doi: [10.3389/fnins.2016.00333](https://doi.org/10.3389/fnins.2016.00333).
- [5] K. Ni, X. Li, J. A. Smith, M. Jerry, and S. Datta, "Write disturb in ferroelectric FETs and its implication for 1T-FeFET AND memory arrays," *IEEE Electron Device Lett.*, vol. 39, no. 11, pp. 1656–1659, Nov. 2018, doi: [10.1109/LED.2018.2872347](https://doi.org/10.1109/LED.2018.2872347).
- [6] H. Mulaosmanovic *et al.*, "Switching kinetics in nanoscale hafnium oxide based ferroelectric field-effect transistors," *ACS Appl. Mater. Interfaces*, vol. 9, no. 4, pp. 3792–3798, Jan. 2017, doi: [10.1021/acsami.6b13866](https://doi.org/10.1021/acsami.6b13866).
- [7] H. Mulaosmanovic, T. Mikolajick, and S. Slesazek, "Accumulative polarization reversal in nanoscale ferroelectric transistors," *ACS Appl. Mater. Interfaces*, vol. 10, no. 28, pp. 23997–24002, Jul. 2018, doi: [10.1021/acsami.8b08967](https://doi.org/10.1021/acsami.8b08967).
- [8] A. K. Saha, K. Ni, S. Dutta, S. Datta, and S. Gupta, "Phase field modeling of domain dynamics and polarization accumulation in ferroelectric HZO," *Appl. Phys. Lett.*, vol. 114, no. 20, May 2019, Art. no. 202903, doi: [10.1063/1.5092707](https://doi.org/10.1063/1.5092707).
- [9] P. Pandey, C. Alessandri, and A. C. Seabaugh, "Process dependent switching dynamics of ferroelectric hafnium zirconate," in *Proc. Device Res. Conf. (DRC)*, Jun. 2019, pp. 49–50, doi: [10.1109/DRC46940.2019.9046408](https://doi.org/10.1109/DRC46940.2019.9046408).
- [10] T. S. Moise *et al.*, "Demonstration of a 4 Mb, high density ferroelectric memory embedded within a 130 nm, 5 LM Cu/FSG logic process," in *IEDM Tech. Dig.*, Dec. 2002, pp. 535–538, doi: [10.1109/IEDM.2002.1175897](https://doi.org/10.1109/IEDM.2002.1175897).
- [11] T. S. Moise *et al.*, "Electrical properties of submicron ($\geq 0.13 \mu\text{m}^2$) Ir/PZT/Ir capacitors formed on W plugs," in *IEDM Tech. Dig.*, Dec. 1999, pp. 940–942, doi: [10.1109/IEDM.1999.824305](https://doi.org/10.1109/IEDM.1999.824305).
- [12] C. Alessandri, P. Pandey, A. Abusleme, and A. Seabaugh, "Switching dynamics of ferroelectric Zr-doped HfO_2 ," *IEEE Electron Device Lett.*, vol. 39, no. 11, pp. 1780–1783, Nov. 2018, doi: [10.1109/LED.2018.2872124](https://doi.org/10.1109/LED.2018.2872124).
- [13] S. R. Gilbert *et al.*, "Preparation of $\text{Pb}(\text{Zr}, \text{Ti})\text{O}_3$ thin films by metalorganic chemical vapor deposition for low voltage ferroelectric memory," *J. Appl. Phys.*, vol. 93, no. 3, pp. 1713–1717, Feb. 2003, doi: [10.1063/1.1534380](https://doi.org/10.1063/1.1534380).
- [14] G. Karbasian, R. D. Reis, A. K. Yadav, A. J. Tan, C. Hu, and S. Salahuddin, "Stabilization of ferroelectric phase in tungsten capped $\text{Hf}_{0.8}\text{Zr}_{0.2}\text{O}_2$," *Appl. Phys. Lett.*, vol. 111, no. 2, Jul. 2017, Art. no. 022907, doi: [10.1063/1.4993739](https://doi.org/10.1063/1.4993739).
- [15] X. Lyu, M. Si, P. R. Shrestha, K. P. Cheung, and P. D. Ye, "First direct measurement of sub-nanosecond polarization switching in ferroelectric hafnium zirconium oxide," in *IEDM Tech. Dig.*, Dec. 2019, pp. 15.2.1–15.2.4, doi: [10.1109/IEDM19573.2019.8993509](https://doi.org/10.1109/IEDM19573.2019.8993509).
- [16] H. P. McAdams *et al.*, "A 64-Mb embedded FRAM utilizing a 130-nm 5LM Cu/FSG logic process," *IEEE J. Solid-State Circuits*, vol. 39, no. 4, pp. 667–677, Apr. 2004, doi: [10.1109/JSSC.2004.825241](https://doi.org/10.1109/JSSC.2004.825241).
- [17] A. K. Tagantsev, I. Stolichnov, N. Setter, J. S. Cross, and M. Tsukada, "Non-Kolmogorov-Avrami switching kinetics in ferroelectric thin films," *Phys. Rev. B, Condens. Matter*, vol. 66, no. 21, Dec. 2002, Art. no. 214109, doi: [10.1103/PhysRevB.66.214109](https://doi.org/10.1103/PhysRevB.66.214109).
- [18] C. Alessandri, P. Pandey, A. Abusleme, and A. Seabaugh, "Monte Carlo simulation of switching dynamics in polycrystalline ferroelectric capacitors," *IEEE Trans. Electron Devices*, vol. 66, no. 8, pp. 3527–3534, Aug. 2019, doi: [10.1109/TED.2019.2922268](https://doi.org/10.1109/TED.2019.2922268).

APPENDIX G

TRAVELER WITH FABRICATION DETAILS OF W/HZO/W AND
TIN/HZO/TIN CAPACITORS

Process Summary

1. Clean fresh Si wafer (Solvent, MOS Clean)
2. Remove native SiO₂
3. Cleave wafer in 2
4. Sputter bottom electrode
 - a. 100 nm W on PR58_1
 - b. 100 nm TiN on PR58_2
5. ALD 10 nm HZO
6. Photolithography for Top Electrode (Mask JS2)
7. Sputter top electrode
 - a. 100 nm W on PR58_1
 - b. 100 nm TiN on PR58_2
8. Liftoff
9. Cleave each half-wafer into 3, resulting in a total of 6 pieces
10. Anneal wafers, X °C, 30 s, 5 SLM N₂
 - a. PR58_1_1 annealed at 400 °C
 - b. PR58_1_2 annealed at 500 °C
 - c. PR58_1_3 annealed at 600 °C
 - d. PR58_2_1 annealed at 400 °C
 - e. PR58_2_2 annealed at 500 °C
 - f. PR58_2_3 annealed at 600 °C

General Guidelines

- Use plastic tweezers or Teflon coated tweezers for all processing except high temperature steps, in which case use metal tweezers to avoid melting of tweezers.
- Make sure tweezers are clean before using.
 - Rinse with ACE, IPA, DI if necessary.
- Triple rinse glassware with DI before and after any use.
- Use designated glassware for each solution whenever possible.
- In general, be aware of cleanliness, what you and your tweezers touch, and where the wafer is placed.
- Generally, do not stop processing for the day/night if:
 - A critical semiconductor or other surface is exposed such as a contact layer or FET channel or gate oxide.
 - Photoresist, etc. remains on the wafer
- Observe wafer in microscope after every step (Generally, there may be exceptions)

Solvent Clean

Tool: Solvent Bench, Class 100 Area

1. Soak in hot acetone (boiling point 56.5 °C) hot plate 60 °C, 5 min
2. Soak in hot IPA (boiling point 65.0 °C) hot plate 60 °C, 5 min
3. Rinse in deionized water (DI) 30 s
4. Blow dry with N₂

MOS Clean

Tool: MOS Clean Bench, Class 100 Area

1. Prepare fresh RCA1, RCA2 baths on MOS Clean Bench, Class 100 Area
 - a. RCA1 – 10:1:1 NH₄OH:H₂O₂:DI H₂O
 - b. RCA2 – 10:1:1 HCl:H₂O₂:DI H₂O
2. Heat RCA1, RCA2 baths to 70 °C
3. 10 min dip in RCA1
 - a. Use dedicated tweezers and wafer carrier in the MOS Bench
 - b. Recorded Temp: 68.2 °C
 - c. QDR2, 2 cycles
4. 10 min dip in RCA2
 - a. Use dedicated tweezers and wafer carrier in the MOS Bench
 - b. Recorded Temp: 69.1 °C
 - c. QDR3, 2 cycles
5. 15 s dip in 50:1 HF
 - a. Use wafer carrier in the MOS Bench
 - b. Do not put tweezers in HF
 - c. QDR4, 2 cycles
6. Blow dry with N₂ gun
7. Cleave wafer in MOS Clean bench
 - a. Use dedicated MOS Clean tweezers
 - b. Cleave on wipe; ensure no Si debris remains on bench
 - c. Keep quarter pieces on MOS Clean bench
 - d. Ensure scribe does not touch the bench; only the wafer and the wipe
 - e. Label backs of pieces – 1, 2

Sputter Bottom Electrode

Tool: Oerlikon SCSS, Class 1000 Area

1. Clamp sample #1 on wafer handler
2. Load into loadlock
3. Initiate pumpdown to 10^{-4} mbar
4. Transfer to chamber at 10^{-6} mbar
5. Sputter 100 nm W
 - a. Power: Expected 300 W, Actual 300 W
 - b. DC Bias 475 V
 - c. Power ramp time 45 s
 - d. Deposition rate 12.3 nm/min
 - e. Sputter time 8 min 15 s
 - f. Expected thickness 101 nm
 - g. Pressure 10^{-3} mbar
 - h. Gas flows: 25 sccm Ar
6. Transfer to loadlock at 10^{-4} mbar
7. Remove sample
8. Clamp sample #2 on wafer handler
9. Load into loadlock
10. Initiate pumpdown to 10^{-4} mbar
11. Transfer to chamber at 10^{-6} mbar
12. Sputter 100 nm TiN
 - a. Power: Expected 300 W, Actual 300 W
 - b. DC Bias 476 V
 - c. Power ramp time 45 s
 - d. Deposition rate 6 nm/min
 - e. Sputter time 16 min 40 s
 - f. Expected thickness 100 nm
 - g. Pressure 2×10^{-3} mbar
 - h. Gas flows: 25 sccm Ar, 5 sccm N_2
13. Transfer to loadlock at 10^{-4} mbar
14. Remove sample

Atomic Layer Deposition

Tool: Oxford FlexAL ALD, Class 10,000 Area

HZO Recipe – “Table PP HZO TD 300C”:

1. Pumpdown – 1 min
 - a. APC controller setpoint as 0 mTorr.
 - b. Table temperature set 300 °C.
2. Preheat – 3 min
 - a. Chamber pressure 200 mTorr.
 - b. 100 sccm Ar flow.
3. TDMAH Dose – 250 ms
 - a. Chamber pressure 15 mTorr.
4. TDMAH Purge – 5 s
 - a. APC controller setpoint as 0 mTorr.
5. Gas stabilization – 500 ms

- a. Chamber pressure 15 mTorr.
 - b. 60 sccm O₂.
6. O₂ Plasma – 6 s
 - a. Chamber pressure 15 mTorr.
 - b. 60 sccm O₂.
 - c. RF generator forward power 300 W.
7. Plasma purge – 10 s
 - a. Chamber pressure 15 mTorr.
 - b. 100 sccm Ar through purge line.
8. Repeat steps 3-7.
9. TDMAZ Dose – 300 ms
 - a. Chamber pressure 15 mTorr.
10. TDMAZ Purge – 5 s
 - a. APC controller setpoint as 0 mTorr.
11. Gas stabilization – 500 ms
 - a. Chamber pressure 15 mTorr.
 - b. 60 sccm O₂.
12. O₂ Plasma – 6 s
 - a. Chamber pressure 15 mTorr.
 - b. 60 sccm O₂.
 - c. RF generator forward power 300 W.
13. Plasma purge – 10 s
 - a. Chamber pressure 15 mTorr.
 - b. 100 sccm Ar through purge line.
14. Repeat steps 9-13.
15. Repeat 3-14 for required number of supercycles.
16. Pump chamber – 1 min
 - a. APC controller setpoint as 0 mTorr.
17. Argon purge – 10 s
 - a. Chamber pressure 60 mTorr.
 - b. Total 200 sccm Ar flow, 100 sccm through Ar line, 100 sccm through Ar purge line.

Fabrication procedure followed:

1. Season chamber with 100 supercycles HZO
2. ALD 10 nm HZO
 - a. 17 supercycles
 - b. Expected thickness – 9 nm
 - c. Observed thickness (Gaertner Ellipsometer) – 9.6 nm

Contact Pad Layer - Lithography

Tool: AS200, Class 100 Area

1. Spin SPR700-1.2
 - a. Recipe: ICFAB 4000 rpm, 30 s, 1.2 μm expected thickness
2. Soft bake 90 °C, 1 min
3. Expose IPEL2L3/L3 with AS200 0.30 s
4. Develop in AZ917-MIF, 35 s
5. Rinse with DI gun
6. Blow dry with N₂
7. Microscope inspect to confirm lithography
 - a. Olympus MX61
 - b. Check fiducials to confirm development
 - c. Use both bright and dark field imaging

Contact Pad Layer – Sputtering and Liftoff

Tool: Oerlikon SCSS, Class 1000 Area

1. Clamp sample #1 on wafer handler
2. Load into loadlock
3. Initiate pumpdown to 10⁻⁴ mbar
4. Transfer to chamber at 10⁻⁶ mbar
5. Sputter 100 nm W
 - a. Power: Expected 300 W, Actual 300 W
 - b. DC Bias 476 V
 - c. Power ramp time 45 s
 - d. Deposition rate 12.3 nm/min
 - e. Sputter time 8 min 15 s
 - f. Expected thickness 101 nm
 - g. Pressure 10⁻³ mbar
 - h. Gas flows: 25 sccm Ar
6. Transfer to loadlock at 10⁻⁴ mbar
7. Remove sample
8. Clamp sample #2 on wafer handler
9. Load into loadlock
10. Initiate pumpdown to 10⁻⁴ mbar
11. Transfer to chamber at 10⁻⁶ mbar
12. Sputter 100 nm TiN
 - a. Power: Expected 300 W, Actual 300 W
 - b. DC Bias 475 V
 - c. Power ramp time 45 s
 - d. Deposition rate 6 nm/min
 - e. Sputter time 16 min 40 s
 - f. Expected thickness 100 nm
 - g. Pressure 2x10⁻³ mbar
 - h. Gas flows: 25 sccm Ar, 5 sccm N₂
13. Transfer to loadlock at 10⁻⁴ mbar
14. Remove sample
15. Place PG remover in glass beaker on a hot plate at 90 °C

- a. Liftoff for 20 mins
16. Soak in IPA at room temperature
 - a. IPA in glass beaker
 - b. Removes PG Remover residue
17. Cleave samples #1, #2 into 3 pieces each
 - a. Scribe backs of wafer #1 pieces with 11, 12, 13
 - b. Scribe backs of wafer #2 pieces with 21, 22, 23

Anneal

Tool: AllWin RTA, Class 1000 Area

1. Run recipe PPHZO600.RCP with only carrier wafer
2. Place sample #11 on carrier wafer
 - a. Run PPHZO400.RCP
 - b. Ramp up time – 10 s
 - c. Anneal time – 30 s
 - d. Ramp down time – 10 s
 - e. Flow Rate – 5 SLPM N₂
3. Place sample #12 on carrier wafer
 - a. Run PPHZO500.RCP
 - b. Ramp up time – 10 s
 - c. Anneal time – 30 s
 - d. Ramp down time – 10 s
 - e. Flow Rate – 5 SLPM N₂
4. Place sample #13 on carrier wafer
 - a. Run PPHZO600.RCP
 - b. Ramp up time – 10 s
 - c. Anneal time – 30 s
 - d. Ramp down time – 10 s
 - e. Flow Rate – 5 SLPM N₂
5. Place sample #21 on carrier wafer
 - a. Run PPHZO400.RCP
 - b. Ramp up time – 10 s
 - c. Anneal time – 30 s
 - d. Ramp down time – 10 s
 - e. Flow Rate – 5 SLPM N₂
6. Place sample #22 on carrier wafer
 - a. Run PPHZO500.RCP
 - b. Ramp up time – 10 s
 - c. Anneal time – 30 s
 - d. Ramp down time – 10 s
 - e. Flow Rate – 5 SLPM N₂
7. Place sample #23 on carrier wafer
 - a. Run PPHZO600.RCP
 - b. Ramp up time – 10 s
 - c. Anneal time – 30 s
 - d. Ramp down time – 10 s
 - e. Flow Rate – 5 SLPM N₂

APPENDIX H

SPECIFICATIONS OF COMPONENTS IN INTERNAL PHOTOEMISSION SETUP

Source (EQ-77-EC)

Overview

- CW spectral output from 170nm - 2100nm
- Large collectable view angle – Numerical Aperture (NA): up to 0.50
- Typical bulb life >9,000 hrs.
- Electronic output control for light attenuation

Physical Specifications

EQ-77	System Dimensions (H x W x D)	Weight
• Lamp House	128mm x 175mm x 102mm	2.2 kg (4.9 lb)
• Laser Drive Module	152mm x 250mm x 132mm	2.9 kg (6.5 lb)

Utility Requirements

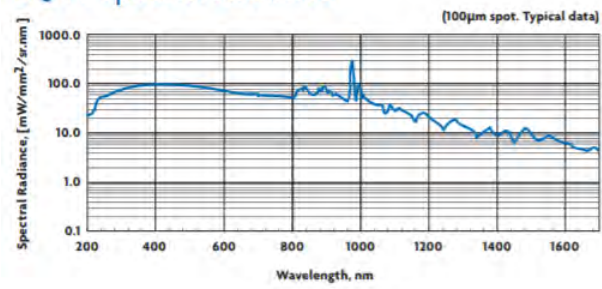
- | | |
|------------------|----------------------------------------|
| • Electrical | 100-240 VAC, 350W max. |
| • Cooling Water | 1.0 liter/min (.27 gal/min) |
| • Purge Nitrogen | 190 sccm @ 20psig; Grade 6 recommended |
| • Compliance | CE Mark |

Model EQ-77 LDLS™ Laser-Driven Light Source Operation Manual, Revision 3, Energetiq, Woburn, Massachusetts, USA, April 2016

Figure H.1. IPE light source specifications, Part 1

Source (EQ-77)

EQ-77 Spectral Radiance



OAP Mirror (EQ-77-OAP004)

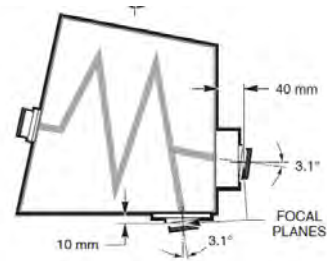
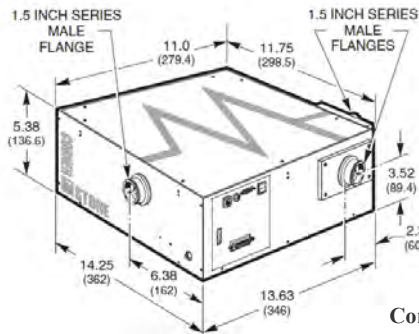
Effective Focal Length (EFL)	Diameter	Magnification	Numeric Aperture	f/#
4.0"(101.6mm)	1.5"	2x	0.188	2.67

Sam Gunnell, Personal Communication, April 4 2017

Figure H.2. IPE light source specifications, Part 2

Monochromator (Newport 74100)

Focal Length	260 mm
F/number	F/3.9
Usable Wavelength Range	180 nm to 24 μm , with interchangeable gratings
Wavelength Accuracy	0.35 nm
Resolution (triple grating instrument)*	0.15 nm
Resolution (double grating instrument)*	0.10 nm**
Wavelength Precision	0.08 nm
Maximum Slew Rate	205 nm/s***
Weight	(9,5 kg)



Cornerstone™ 260 1/4 m Monochromators,
[Online]

https://www.newport.com/medias/sys_master/images/h61/h4f/9134874624030/DS-121401-Cornerstone-260.pdf

Figure H.3. Monochromator specifications

Grating (Newport 74063/74069/74080)

	74063	74069	74080
Primary Wavelength Region	200 to 1400 nm	875 to 2200 nm	2500 to 12000 nm
Wavelength of Maximum Efficiency	360 nm	1325 nm	4000 nm
Coating Type	AlMgF2 broadband reflective	AlMgF2 broadband reflective	AlMgF2 broadband reflective
Grooves per mm	1200	600	150
Type	Ruled	Ruled	Ruled
Peak Efficiency	0.8	0.85	0.88
Reciprocal Dispersion	3.2 nm/mm	6.2 nm/mm	25.8 nm/mm
Blaze Wavelength	360 nm	1325 nm	4000 nm
Resolution	0.25 nm	0.47 nm	1.97 nm
Multichannel Array Bandpass			655 nm

Diffraction gratings for Oriel® CS260 monochromators and MS260i imaging spectrographs
 [Online]
<https://www.newport.com/f/diffraction-gratings-for-cs260-monochromators-and-ms260i-spectrographs>

Figure H.4. Monochromator grating specifications

Filter Wheel (Newport USFW-100)

Filter Wheel Size: 6.75 x 6.38 x 2.13 inches
Input/output ports: 1.5 inch Series male and female flanges
Mounting: Flange mount (male and female)
Rod mount (#1/4-20 mounting thread)
Number of positions: 6
Filter diameter: 1 inch (25.4 mm)
Filter thickness: 0.6 inch (10.2 mm) max
Clear aperture: 0.875 inch (23 mm)
Speed: <2 s per position

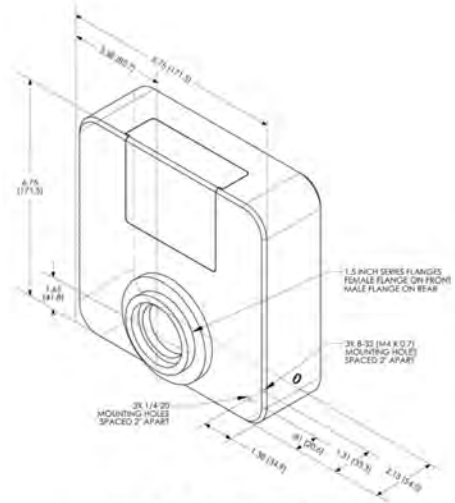


Figure 1: Dimensional Diagram

USFW-100 Oriel Universal Filter Wheel User's Manual, Revision B, Newport, Irvine, California, USA, 2015

Figure H.5. Monochromator filter wheel specifications

Filters (Newport)

Filter 1 – No filter

Filter 2 – 51250

Filter 3 – 51310

Filter 4 – 51352

Cut-on Wavelength (nm)	Refractive Index (n*) @587.6 nm	Reflection Correction Factor*	Temperature Coefficient Factor	Schott Model No.	Transmittance Graph		1 inch (25.4 mm) Diameter		2 inch (50.8 mm) Diameter	
					Page No.	Fig. No.	Model No.	Price	Model No.	Price
Long Pass Filters										
235	1.47	0.93	0.02	WG 225	10-8	6	51215		59418	
285	1.49	0.93	0.02	WG 280	10-8	6	51220		59423	
299	1.52	0.92	0.03	WG 295	10-9	7	51225		59425	
309	1.52	0.92	0.03	WG 305	10-8	6	51250		59450	
324	1.58	0.90	0.05	WG 320	10-9	7	51255		59458	
385	1.58	0.91	0.07	GG 385	10-9	8	51270		59470	
395	1.62	0.90	0.08	GG 395	10-9	7	51271		59471	
400	1.54	0.91	0.07	GG 400	10-9	8	51272		59472	
420	1.54	0.91	0.07	GG 420	10-9	8	51280		59480	
435	1.54	0.91	0.07	GG 435	10-10	9	51282		59482	
455	1.54	0.91	0.08	GG 455	10-10	9	51284		59484	
475	1.54	0.91	0.09	GG 475	10-10	10	51290		59490	
495	1.54	0.91	0.10	GG 495	10-10	9	51292		59492	
515	1.54	0.91	0.11	OG 515	10-11	11	51294		59494	
530	1.54	0.91	0.12	OG 530	10-11	12	51300		59500	
550	1.54	0.91	0.13	OG 550	10-11	12	51302		59502	
570	1.54	0.91	0.14	OG 570	10-10	10	51310		59510	
590	1.54	0.91	0.15	OG 590	10-11	11	51311		59511	
610	1.54	0.91	0.16	RG 610	10-12	13	51312		59512	
630	1.54	0.91	0.17	RG 630	10-12	14	51320		59520	
645	1.54	0.91	0.17	RG 645	10-13	15	51325		59523	
665	1.54	0.91	0.17	RG 665	10-12	14	51330		59530	
695	1.54	0.91	0.18	RG 695	10-13	16	51340		59540	
715	1.54	0.91	0.18	RG 715	10-13	16	51345		59545	
725	1.54	0.91	0.07	RG 9	10-12	14	51315		59509	
780	1.54	0.91	0.22	RG 780	10-13	16	51350		59550	
830	1.56	0.91	0.23	RG 830	10-12	13	51352		59552	
850	1.56	0.91	0.24	RG 850	10-13	15	51360		59560	
1000	1.55	0.91	0.38	RG 1000	10-12	13	51362		59562	
Heat Absorbing Filters										
	1.52	0.92		KG 4	10-14	17	51942		59042	
	1.52	0.92		KG 2	10-14	17	51944		59044	
	1.52	0.92		KG 1	10-14	17	51950		59050	
	1.52	0.92		KG 3	10-14	18	51960		59060	
	1.51	0.92		KG 5	10-14	18	51962		59062	
Visible Absorbing Filters										
	1.55	0.91		Hoya U-330	10-15	19	51122		59152	
	1.57	0.91		Hoya U-340	10-15	19	51124		59154	

* The curves shown on pages 10-6 to 10-15, for these filters, show internal transmittance; multiply by this factor to obtain external transmittance.

Lana Pryde, Personal Communication, Nov 19 2020

Figure H.6. Monochromator filter specifications

**Spectral Response - Filter 2
(#51250)**

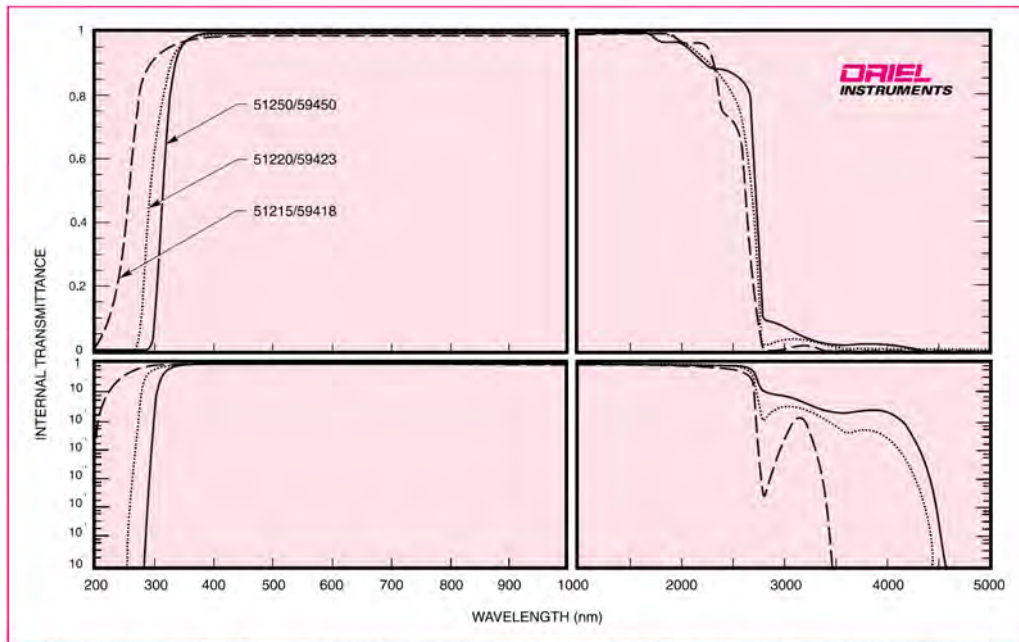


Fig. 6 Internal transmittance of various Colored Glass Filters; multiply by the Reflection Correction Factor (page 10-5) to obtain external transmittance.

Lana Pryde, Personal Communication, Nov 19 2020

Figure H.7. Monochromator filter 2 spectral response

Spectral Response - Filter 3 (#51310)

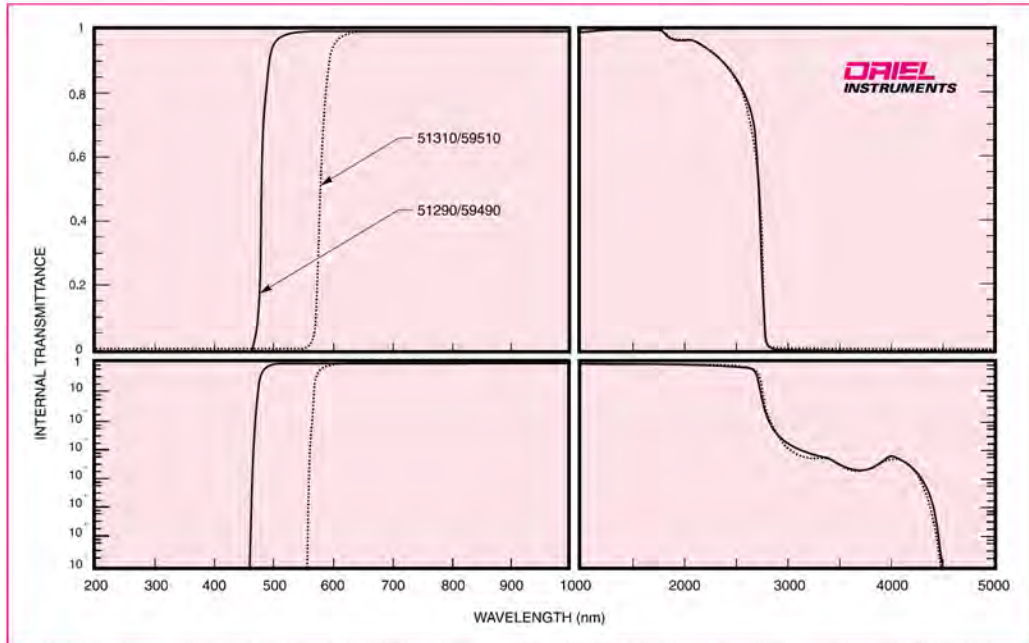


Fig. 10 Internal transmittance of various Colored Glass Filters; multiply by the Reflection Correction Factor (page 10-5) to obtain external transmittance.

Lana Pryde, Personal Communication, Nov 19 2020

Figure H.8. Monochromator filter 3 spectral response

**Spectral Response - Filter 4
(#51352)**

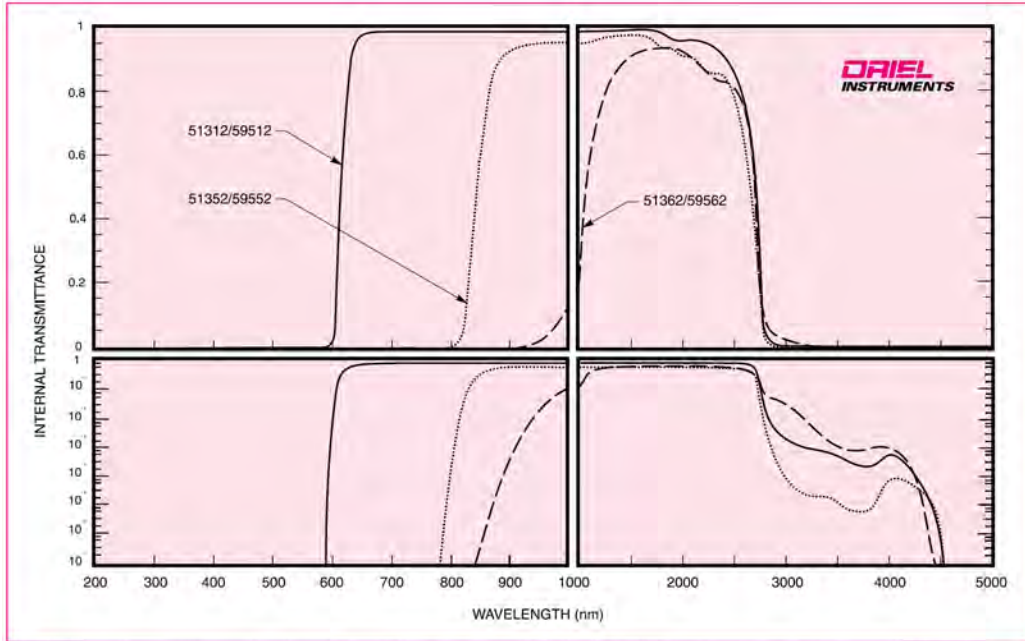


Fig. 13 Internal transmittance of various Colored Glass Filters; multiply by the Reflection Correction Factor (page 10-5) to obtain external transmittance.

Lana Pryde, Personal Communication, Nov 19 2020

Figure H.9. Monochromator filter 4 spectral response

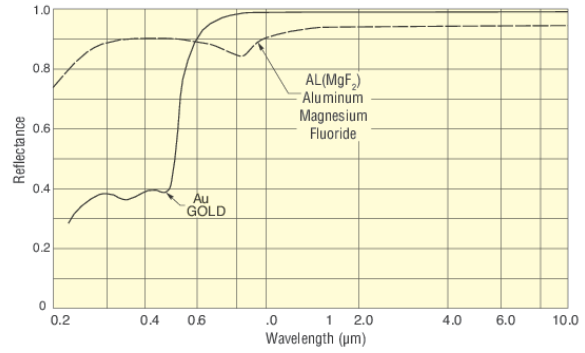
Collimator (Newport 50338AL)

Coating Type	Protected Aluminum	Coating Code	AL
Wavelength Range	190-2000 nm	Coating Adhesion	MIL-F-48616
Mirror Shape	Parabolic	Coating Hardness	MIL-F-48616 modified to 0.5lb
Diameter	38.1 mm	Humidity Resistance	MIL-F-48616
Height	41.15 mm	Surface Quality	60-40 scratch-dig
Effective Focal Length	4.0 in.	Surface Roughness, Typical	25 Å
Focal Length	2.000 in.	Wavefront Distortion	$\leq 2\lambda$ @ 633 nm (typical)
Focal Base Distance	0.800 in.	Clear Aperture	$\geq 90\%$ of diameter
Material	Aluminum	Operating Temperature Range	-80°F to 160°F
Wavelength Region	Broadband		

Parabolic mirror, off-axis-replicated, 1.5 in., 4.0in. EFL, Aluminum [Online]
<https://www.newport.com/p/50338AL>

Figure H.10. Newport collimator specifications, Part 1

Collimator (Newport 50338AL)



OAP-ADAPT

Optic Diameter	76.2 mm	Special Features	Parabolic Mirror Adapter
-----------------------	---------	-------------------------	--------------------------

71311

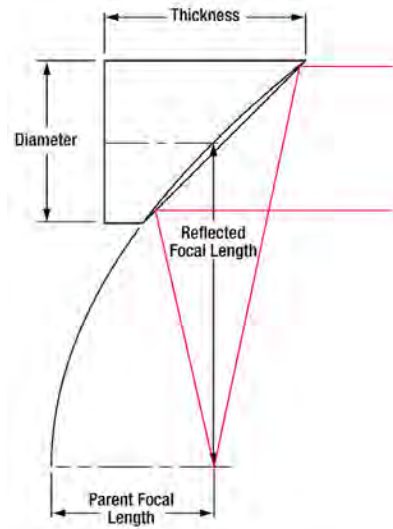
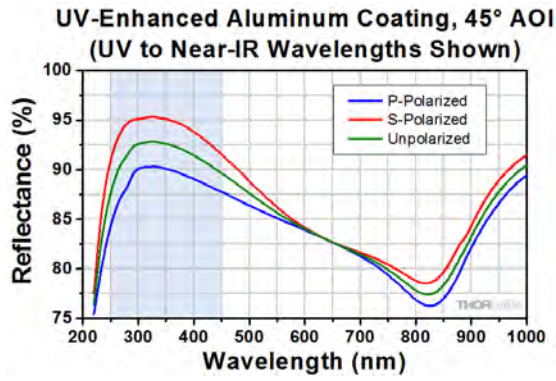
Type	Adjustable Light Shield	Flange Series Size	1.5 Inch
Length	54 to 81 mm		

Parabolic mirror adapter, 1.5 in. series flange [Online]
<https://www.newport.com/p/OAP-ADAPT>

Adjustable light shield, 2.1 to 3.2 in., 1.5 inch flange [Online]
<https://www.newport.com/p/71311>

Figure H.11. Newport collimator specifications, Part 2

Fiber Coupling (Thorlabs RC08FC-F01)



Reflective collimators, UV-enhanced aluminum coating [Online]
https://www.thorlabs.com/newgrouppage9.cfm?objectgroup_id=4953

Figure H.13. Thorlabs fiber coupler specifications, Part 1

Fiber Coupling (Thorlabs RC08FC-F01)

Common Specifications			
Coating	UV-Enhanced Aluminum	Fiber Connector	FC/PC
Wavelength Range	250 - 450 nm	Clear Aperture	Ø11 mm
Reflectance (Avg)	>90%	Beam Diameter	4 mm
Surface Quality	40-20 Scratch-Dig	Mirror NA	0.36
Surface Roughness	<100 Å RMS	RFL	15 mm
Reflected Wavefront Error	$\lambda/4$ at 633 nm	PFL	7.5 mm
Full Angle Beam Divergence	0.02°	Pointing Error (FC/PC- and FC/APC-Connectorized Models)	<10 mrad

Reflective collimators, UV-enhanced aluminum coating [Online]
https://www.thorlabs.com/newgrouppage9.cfm?objectgroup_id=4953

Figure H.14. Thorlabs fiber coupler specifications, Part 2

Optical Fiber (Thorlabs FT200EMT)

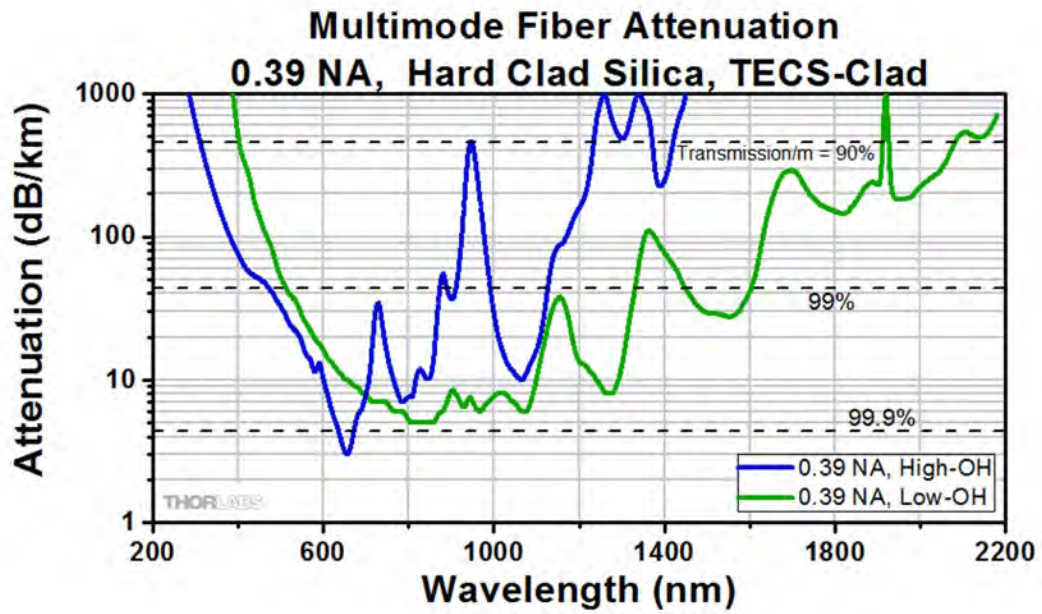
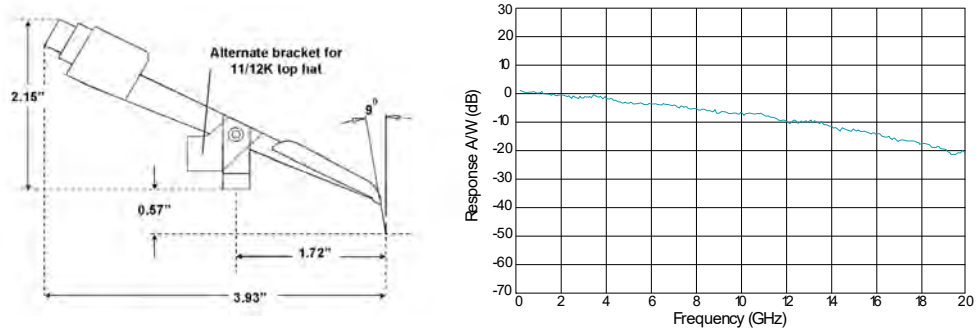


Figure 6. Thorlabs data for the output of both the UV (High-OH) and the Ordinary (Low-OH) fibers. ^[9]

0.39 NA TECS hard-clad step-index, multimode fiber, Revision G, Thorlabs, Newton, New Jersey, April 2019
[Online] https://www.thorlabs.com/newgrouppage9.cfm?objectgroup_id=6845&pn=FT200EMT#5652

Figure H.15. Thorlabs optic fiber spectral attenuation

Fiber Optic Probe (Cascade LWP-LEN-MM)



Fiber Type	Minimum Illumination Diameter	Wavelength	Numeric Aperture	Insertion Loss
Lensed multi-mode (LEN-MM)	50 μm	850 nm – 1550 nm	NA	0.5 dB

Cascade LWP multi-configurable optical probe for photonic device characterization, Formfactor, Livermore, California, 2018
 [Online] <https://www.formfactor.com/download/twp-datasheet/>

Figure H.16. Cascade fiber optic probe specifications

Probe Positioner (Cascade DPP210-M-L)

Feature resolution	2 μm (DPP210)
Travel range (X / Y / Z)	12.5 mm / 12.5 mm / 12.5 mm
Screw resolution* (X / Y / Z)	500 μm / 500 μm / 500 μm (DPP205) 250 μm / 250 μm / 250 μm (DPP210) 125 μm / 125 μm / 125 μm (DPP220)
Mounting	Magnetic
Footprint (W x D)	90 mm x 60 mm
Station compatibility	Tesla, Elite™ 300, PA300 MicroAlign™, Summit12000
Application	IV/CV probing Failure analysis

Cascade probe positioners, Formfactor, Livermore, California, 2018
[Online] <https://www.formfactor.com/download/probe-positioners-brochure/?wpdmdl=20350&refresh=5fbb2b4f9ea7e1606101839>

Figure H.17. Cascade probe positioner specifications

Power Meter (Thorlabs S120VC)

Specifications

Detector Type	Silicon Photodiode (UV extended)
Wavelength Range	200 - 1100 nm
Optical Power Working Range	50 nW - 50 mW
Max Average Power Density	20 W/cm ²
Max Pulse Energy	20 μJ
Linearity	± 0.5%
Resolution ¹⁾	1nW
Measurement Uncertainty ²⁾	±3% 440 - 980 nm ±5% 280 - 439 nm, ±7% 200 - 279 nm, 981 - 1100 nm
Typical Application	Low Power Lasers
Laser Types	Diode, Diode Arrays, He-Ne, Dye, Ion Lasers (Ar+, Kr+)
Coating /Diffuser ³⁾	Reflective ND (OD1.5)
Cooling	Convection
Head Temperature Measurement	NTC Thermistor 4.7kΩ
Console Compatibility	PM100D, PM100A, PM100USB, PM200, PM320E
Response Time	< 1 μs
Sensor Dimensions	Ø30.5 mm x 12.7 mm
Active Detector Area	9.7 mm x 9.7 mm
Input Aperture	Ø9.5 mm
Cable Length	1.5 m
Connector	Sub-D 9p male
Weight	0.07 kg
Post ³⁾	#8-32 & M4 thread
Aperture Thread	SM1, outer thread
Fiber Adapters (optional)	FC, SC, LC, SMA, ST

¹⁾ Measured with PM100D console in bandwidth low setting.

²⁾ Beam diameter > 1mm

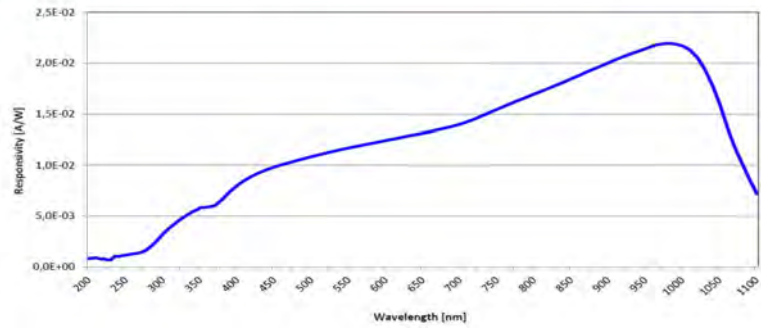
³⁾ This specification is valid for S120VC devices from serial number 1203xxx. For older versions, please contact technical support.

Compact photodiode power head with silicon detector, Revision C, Thorlabs, Newton, New Jersey, February 2016
 [Online] <https://www.thorlabs.com/drawings/f8d2474577e021a5-A6365D95-CA7D-672F-A453F9BBDED83461/S120VC-SpecSheet.pdf>

Figure H.18. Thorlabs power meter specifications

Power Meter (Thorlabs S120VC)

Typical Response Graph



Compact photodiode power head with silicon detector, Rev C, February
2016, Thorlabs, Newton, New Jersey
[Online] <https://www.thorlabs.com/drawings/f8d2474577e021a5-A6365D95-CA7D-672F-A453F9BBDED83461/S120VC-SpecSheet.pdf>

Figure H.19. Thorlabs power meter response

USB Power Meter Interface

(Thorlabs PM100USB)

Interface	
Type	USB2.0
Connector	Mini USB, left side
Power Supply	
External power supply	5V DC via USB
Accessories	
USB cable A to Mini-B, 2 m	
USB Stick with <ul style="list-style-type: none">- Application Software- Instrument Drivers- Thorlabs Instrument Communicator- Thorlabs DFU (Device Firmware Upgrade) Wizard	
General	
Operating Temperature Range ¹⁾	0 to + 40 °C
Storage Temperature Range	-40 to +70 °C
Dimensions (W x H x D)	93.1 mm x 60.4 mm x 28.7 mm (3.67" x 2.38" x 1.13")
Weight	approx. 0.15 kg
Relative Humidity	max. 80 % up to 31° C, decreasing to 50 % at 40° C
Operation Altitude	< 3000 m

*PM100USB Operation Manual, Version 1.5, Thorlabs, Newton, New Jersey,
USA, March 2020*

Figure H.21. Thorlabs USB power meter interface specifications

SourceMeter (Keithley 2636A)

IEEE-488: IEEE-488.1 compliant. Supports IEEE-488.2 common commands and status model topology.

RS-232: Baud rates from 300bps to 115200bps. Programmable number of data bits, parity type, and flow control (RTS/CTS hardware or none). When not programmed as the active host interface, the SourceMeter instrument can use the RS-232 interface to control other instrumentation.

ETHERNET: RJ-45 connector, LXI Class C, 10/100BT, no auto MDIX.

EXPANSION INTERFACE: The TSP-Link expansion interface allows TSP enabled instruments to trigger and communicate with each other.

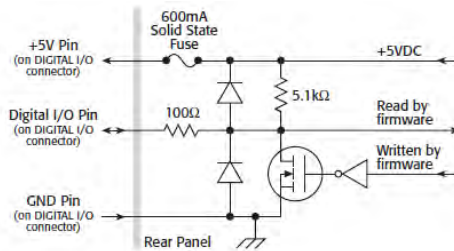
Cable Type: Category 5e or higher LAN crossover cable.

Length: 3 meters maximum between each TSP enabled instrument.

LXI COMPLIANCE: LXI Class C 1.2.

LXI TIMING: Total Output Trigger Response Time: 245 μ s min., 280 μ s typ., (not specified) max. **Receive LAN[0-7] Event Delay:** Unknown. **Generate LAN[0-7] Event Delay:** Unknown.

DIGITAL I/O INTERFACE:



Series 2600A System SourceMeter® Reference Manual, Revision E, Keithley, Cleveland, Ohio, USA, August 2011

Figure H.22. Keithley sourcemeter specifications, Part 1

Sourcimeter (Keithley 2636A)

Connector: 25-pin female D.

Input/Output Pins: 14 open drain I/O bits.

Absolute Maximum Input Voltage: 5.25V.

Absolute Minimum Input Voltage: -0.25V.

Maximum Logic Low Input Voltage: 0.7V, +850 μ A max.

Minimum Logic High Input Voltage: 2.1V, +570 μ A.

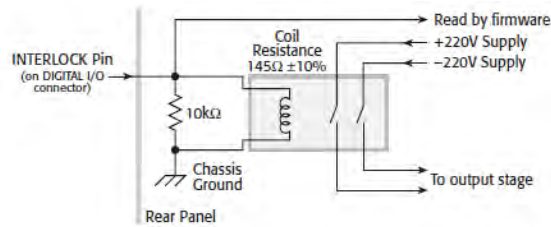
Maximum Source Current (flowing out of Digital I/O bit): +960 μ A.

Maximum Sink Current @ Maximum Logic Low Voltage (0.7V): -5.0mA.

Absolute Maximum Sink Current (flowing into Digital I/O pin): -11mA.

5V Power Supply Pin: Limited to 600mA, solid state fuse protected.

Safety Interlock Pin: Active high input. >3.4V @ 24mA (absolute maximum of 6V) must be externally applied to this pin to ensure 200V operation. This signal is pulled down to chassis ground with a 10k Ω resistor. 200V operation will be blocked when the INTERLOCK signal is <0.4V (absolute minimum -0.4V). See figure below:



Series 2600A System SourceMeter® Reference Manual, Revision E, Keithley, Cleveland, Ohio, USA, August 2011

Figure H.23. Keithley sourcimeter specifications, Part 2

Sourcemeater (Keithley 2636A)

USB: USB 1.0 Host Controller (Memory Stick I/O).

POWER SUPPLY: 100V to 250VAC, 50–60Hz (auto sensing), 240VA max.

COOLING: Forced air. Side intake and rear exhaust. One side must be unobstructed when rack mounted.

EMC: Conforms to European Union Directive 2004/108/EEC, EN 61326-1.

SAFETY: Conforms to European Union Directive 73/23/EEC, EN 61010-1, and UL 61010-1.

DIMENSIONS: 89mm high × 213mm wide × 460mm deep (3½ in × 83/8 in × 17½ in). Bench Configuration (with handle and feet): 104mm high × 238mm wide × 460mm deep (41/8 in × 93/8 in × 17½ in).

WEIGHT: **2635A:** 4.75kg (10.4 lbs). **2636A:** 5.50kg (12.0 lbs).

ENVIRONMENT: For indoor use only. **Altitude:** Maximum 2000 meters above sea level.

Operating: 0°–50°C, 70% R.H. up to 35°C. Derate 3% R.H./°C, 35°–50°C.

Storage: –25°C to 65°C.

Series 2600A System SourceMeter® Reference Manual, Revision E, Keithley, Cleveland, Ohio, USA, August 2011

Figure H.24. Keithley sourcemeater specifications, Part 3

GPIB to Ethernet
(GPIB-ENET/1000 781630-05)

Performance

GPIB	
3-wire.....	up to 1480 kbytes/s
HS488.....	up to 5600 kbytes/s

Power Requirements

+9–30 VDC.....	250 mA @ +12 V, Typical
	500 mA @ +12 V, Maximum

Physical Characteristics

Dimensions.....	21.0 cm × 12.7 cm × 3.7 cm (8.3 in. × 5.0 in. × 1.4 in.)
Weight.....	394 g (13.9 oz)
Connector	
GPIB.....	IEEE 488 standard 24 pin
Ethernet.....	RJ-45 with integrated LEDs

Environment

Operating ambient temperature.....	0 °C to 55 °C
	(Tested in accordance with IEC 60068-2-1 and IEC 60068-2-2.)
Operating relative humidity.....	10% to 90%, noncondensing
	(Tested in accordance with IEC 60068-2-56.)

*Installation guide and specifications GPIB Hardware, National Instruments, Austin, Texas,
USA, July 2018*
[Online] <https://www.ni.com/pdf/manuals/370426t.pdf>

Figure H.25. GPIB to Ethernet connector specifications, Part 1

GPIB to Ethernet

(GPIB-ENET/1000 781630-05)

Storage ambient temperature	-40 °C to 70 °C (Tested in accordance with IEC 60068-2-1 and IEC 60068-2-2.)
Storage relative humidity.....	5% to 95%, noncondensing (Tested in accordance with IEC 60068-2-56.)

Shock and Vibration

Operating shock.....	30 g peak, half-sine, 11 ms pulse (Tested in accordance with IEC 60068-2-27; test profile developed in accordance with MIL-PRF-28800F.)
Random vibration	
Operating.....	5 Hz to 500 Hz, 0.3 grms
Nonoperating.....	5 Hz to 500 Hz, 2.4 grms (Tested in accordance with IEC 60068-2-64. Nonoperating test profile exceeds the requirements of MIL-PRF-28800F, Class 3.)

*Installation guide and specifications GPIB Hardware, National Instruments, Austin, Texas,
USA, July 2018*
[Online] <https://www.ni.com/pdf/manuals/370426t.pdf>

Figure H.26. TGPIB to Ethernet connector specifications, Part 2

APPENDIX I

TRAVELER WITH FABRICATION DETAILS OF PD/HZO/P⁺ SI
CAPACITORS

Process Summary

1. Clean fresh Si wafer (Solvent, MOS Clean)
2. Remove native SiO₂
3. Cleave wafer in 4
 - a. Sputter 100nm W on 2 pieces for W/HfO₂/W (#1) and W/HZO/W (#2)
 - b. Other 2 pieces for Si/HfO₂/W (#3) and Si/HZO/W (#4)
4. ALD 7 nm HfO₂ on wafers #1 and #3
5. ALD 7 nm HZO on wafers #2 and #4
6. Sputter 100 nm W on all wafers
7. Wet etch W with H₂O₂
8. Photolithography for Contact Pads (Mask IPEL3)
9. Deposit 150 nm Pd
10. Liftoff
11. Photolithography for Transparent Electrode (Mask IPEL2)
12. Deposit 10 nm Pd
13. Liftoff

General Guidelines

- Use plastic tweezers or Teflon coated tweezers for all processing except high temperature steps, in which case use metal tweezers to avoid melting of tweezers.
- Make sure tweezers are clean before using.
 - Rinse with ACE, IPA, DI if necessary.
- Triple rinse glassware with DI before and after any use.
- Use designated glassware for each solution whenever possible.
- In general, be aware of cleanliness, what you and your tweezers touch, and where the wafer is placed.
- Generally, do not stop processing for the day/night if:
 - A critical semiconductor or other surface is exposed such as a contact layer or FET channel or gate oxide.
 - Photoresist, etc. remains on the wafer
- Observe wafer in microscope after every step (Generally, there may be exceptions)

Solvent Clean

Tool: Solvent Bench, Class 100 Area

1. Soak in hot acetone (boiling point 56.5 °C) hot plate 60 °C, 5 min
2. Soak in hot IPA (boiling point 65.0 °C) hot plate 60 °C, 5 min
3. Rinse in deionized water (DI) 30 s
4. Blow dry with N₂

MOS Clean

Tool: MOS Clean Bench, Class 100 Area

1. Prepare fresh RCA1, RCA2 baths on MOS Clean Bench, Class 100 Area
 - a. RCA1 – 10:1:1 NH₄OH:H₂O₂:DI H₂O
 - b. RCA2 – 10:1:1 HCl:H₂O₂:DI H₂O
2. Heat RCA1, RCA2 baths to 70 °C
3. 10 min dip in RCA1
 - a. Use dedicated tweezers and wafer carrier in the MOS Bench
 - b. Recorded Temp: 67.5 °C
 - c. QDR2, 2 cycles
4. 10 min dip in RCA2
 - a. Use dedicated tweezers and wafer carrier in the MOS Bench
 - b. Recorded Temp: 68.3 °C
 - c. QDR3, 2 cycles
5. 15 s dip in 50:1 HF
 - a. Use wafer carrier in the MOS Bench
 - b. Do not put tweezers in HF
 - c. QDR4, 2 cycles
6. Blow dry with N₂ gun
7. Cleave wafer in MOS Clean bench
 - a. Use dedicated MOS Clean tweezers
 - b. Cleave on wipe; ensure no Si debris remains on bench
 - c. Keep quarter pieces on MOS Clean bench
 - d. Ensure scribe does not touch the bench; only the wafer and the wipe
 - e. Label backs of pieces – 1, 2, 3, 4
 - f. Keep #3, #4 on MOS Clean bench

Sputter 100 nm Bottom W

Tool: Oerlikon SCSS, Class 1000 Area

1. Clamp sample #1, #2 on wafer handler
2. Load into loadlock
3. Initiate pumpdown to 10^{-4} mbar
4. Transfer to chamber at 10^{-6} mbar
5. Sputter 100 nm W
 - a. Power: Expected 300 W, Actual 300 W
 - b. DC Bias 544 V
 - c. Power ramp time 30 s (Longer ramp up may cause arcing)
 - d. Deposition rate 9.9 nm/min
 - e. Sputter time 10 min
 - f. Expected thickness 99 nm
 - g. Pressure 10^{-3} mbar
 - h. Gas flows: 25 sccm Ar
6. Transfer to loadlock at 10^{-4} mbar
7. Remove samples

Atomic Layer Deposition

Tool: Oxford FlexAL ALD, Class 10,000 Area

HZO Recipe – “Table PP HZO TD 300C”:

1. Pumpdown – 1 min
 - a. APC controller setpoint as 0 mTorr.
 - b. Table temperature set 300 °C.
2. Preheat – 3 min
 - a. Chamber pressure 200 mTorr.
 - b. 100 sccm Ar flow.
3. TDMAH Dose – 250 ms
 - a. Chamber pressure 15 mTorr.
4. TDMAH Purge – 5 s
 - a. APC controller setpoint as 0 mTorr.
5. Gas stabilization – 500 ms
 - a. Chamber pressure 15 mTorr.
 - b. 60 sccm O₂.
6. O₂ Plasma – 6 s
 - a. Chamber pressure 15 mTorr.
 - b. 60 sccm O₂.
 - c. RF generator forward power 300 W.
7. Plasma purge – 10 s
 - a. Chamber pressure 15 mTorr.
 - b. 100 sccm Ar through purge line.
8. Repeat steps 3-7.
9. TDMAZ Dose – 300 ms
 - a. Chamber pressure 15 mTorr.
10. TDMAZ Purge – 5 s

- a. APC controller setpoint as 0 mTorr.
11. Gas stabilization – 500 ms
 - a. Chamber pressure 15 mTorr.
 - b. 60 sccm O₂.
12. O₂ Plasma – 6 s
 - a. Chamber pressure 15 mTorr.
 - b. 60 sccm O₂.
 - c. RF generator forward power 300 W.
13. Plasma purge – 10 s
 - a. Chamber pressure 15 mTorr.
 - b. 100 sccm Ar through purge line.
14. Repeat steps 9-13.
15. Repeat 3-14 for required number of supercycles.
16. Pump chamber – 1 min
 - a. APC controller setpoint as 0 mTorr.
17. Argon purge – 10 s
 - a. Chamber pressure 60 mTorr.
 - b. Total 200 sccm Ar flow, 100 sccm through Ar line, 100 sccm through Ar purge line.

Fabrication procedure followed:

1. Season chamber with 100 supercycles HZO
2. ALD 7 nm HZO on sample #1
 - a. 13 supercycles
 - b. Measured thickness (Gaertner Ellipsometer) – 6.9 nm
3. ALD 5 nm HZO on sample #4
 - a. 10 supercycles
 - b. Measured thickness (Gaertner Ellipsometer) – 5.6 nm
4. ALD 4 nm HfO₂ on sample #2
 - a. 8 supercycles
 - b. Measured thickness (Gaertner Ellipsometer) – 4.28 nm
5. ALD 3 nm HfO₂ on sample #2
 - a. 6 supercycles
 - b. Measured thickness (Gaertner Ellipsometer) – 3.8 nm

Sputter 100 nm Top W

Tool: Oerlikon SCSS, Class 1000 Area

1. Clamp samples on wafer handler
2. Load into loadlock
3. Initiate pumpdown to 10⁻⁴ mbar
4. Transfer to chamber at 10⁻⁶ mbar
5. Sputter 100 nm W
 - a. Power: Expected 300 W, Actual 300 W
 - b. DC Bias 543 V
 - c. Power ramp time 30 s
 - d. Deposition rate 9.9 nm/min
 - e. Sputter time 10 min
 - f. Expected thickness 99 nm

- g. Pressure 10^{-3} mbar
- h. Gas flows: 25 sccm Ar
6. Transfer to loadlock at 10^{-4} mbar
7. Remove samples

Anneal

Tool: AllWin RTA, Class 1000 Area

1. Run recipe PPHZO550.RCP with only carrier wafer
2. Place sample on carrier wafer
 - a. Run PPHZO550.RCP
 - b. Ramp up time – 10 s
 - c. Anneal time – 30 s
 - d. Ramp down time – 10 s
 - e. Flow Rate – 5 SLPM N_2
 - f. Place only one sample at a time, else samples get displaced by gas flow

Wet Etch Top W

Tool: Acid Bench, Class 1000 Area

1. Pour H_2O_2 solution in glass beaker
2. Etch target 100 nm
 - a. Etch rate: 45 nm / min
 - b. Etch time: 180 s
 - c. Overetch: 50%
3. Rinse in DI H_2O
4. Blow dry N_2 gun

Contact Pad Layer - Lithography

Tool: AS200, Class 100 Area

1. Spin SPR700-1.2
 - a. Recipe: ICFAB 4000 rpm, 30 s, 1.2 μm expected thickness
2. Soft bake 90 °C, 1 min
3. Expose IPEL2L3/L3 with AS200 0.30 s
4. Develop in AZ917-MIF, 37 s
5. Rinse with DI gun
6. Blow dry with N_2
7. Microscope inspect to confirm lithography
 - a. Olympus MX61
 - b. Check fiducials to confirm development
 - c. Use both bright and dark field imaging

Contact Pad Layer – Deposition and Liftoff

Tool: FC1800#1, Class 1000 Area

1. Use U-bar to load samples
2. Deposition 150 nm Pd
 - a. Pressure 0.7E-6 torr
 - b. Deposition rate 1.86 A/s
 - c. Deposited thickness 152 nm
3. Remove samples
4. Place PG remover in glass beaker on a hot plate at 90 °C
 - a. Liftoff for 20 mins
5. Soak in IPA at room temperature
 - a. IPA in glass beaker
 - b. Removes PG Remover residue
6. Rinse with DI H₂O
7. Blow dry with N₂ Gun

Semitransparent Electrode – Lithography

Tool: AS200, Class 100 Area

1. Spin SPR700-1.2
 - d. Recipe: ICFAB 4000 rpm, 30 s, 1.2 μm expected thickness
2. Soft bake 90 °C, 1 min
3. Expose IPEL2L3/L2 with AS200 0.30 s
4. Align to L3:
 - a. Align right mark in x and y.
 - b. Pressing the “d” letter changes the operation of the arrow keys from moving the stage incrementally to moving the stage by entire dies. Pressing the “e” letter returns to the normal mode.
 - c. Use the “d” and “e” letters to toggle between dies, aligning the right mark in x and y and checking the theta with the other dies.
5. Develop in AZ917-MIF, 37 s
6. Rinse with DI gun
7. Blow dry with N₂
8. Microscope inspect to confirm lithography
 - a. Olympus MX61
 - b. Check fiducials to confirm development
 - c. Use both bright and dark field imaging

Semitransparent Electrode – Deposition and Liftoff

Tool: FC1800#1, Class 1000 Area

1. Use U-bar to load samples
2. Deposition 10 nm Pd
 - a. Starting pressure 0.8E-6 Torr
 - b. Deposition Rate 1.2 A/s
 - c. Deposited Thickness 11 nm
3. Remove samples
4. Place PG remover in glass beaker on a hot plate at 90 °C
 - a. Liftoff for 20 mins
5. Soak in IPA at room temperature
 - a. IPA in glass beaker
 - b. Removes PG Remover residue
6. Rinse with DI H₂O
7. Blow dry with N₂ Gun

Back Electrode – Deposition and Liftoff

Tool: FC1800#1, Class 1000 Area

1. Use U-bar to load samples
2. Scratch back of samples with diamond scribe
3. Load samples with electrodes facing U-bar and wafer backside facing source
4. Deposition 225 nm Au
 - a. Starting pressure 1.2E-6 Torr
 - b. Deposition Rate 2.1 A/s
 - c. Deposited Thickness 218 nm
5. Remove samples

APPENDIX J

CODES DEVELOPED TO CONTROL INSTRUMENTS IN INTERNAL PHOTOEMISSION SETUP

J.1 Monochromator

J.1.1 setmono4

The input format is `setmono4(grating, wavelength)`. The code sets the grating and wavelength of the monochromator with input shutter closed. After this is done, the code queries the set grating and wavelength, and outputs the received values of set grating and wavelength as an array `[Result, Wavelength, Grating]`. Once complete, the Result is returned as 'DONE'.

Set monochromator grating and wavelength

Table of Contents

Initialize function	1
Connecting to the monochromator	1
Setting the grating	1
Setting the wavelength	2
Disconnect from instrument Object, Mono	2

Initialize function

```
function [res,wavv,graa] = setmono4(gra,wav)
```

Connecting to the monochromator

```
%Find the instrument
Mono = instrfind('Type', 'visa-
gpib', 'RsrcName', 'GPIB0::4::INSTR', 'Tag', '');

% Create the VISA-GPIB Object if it does not exist
% otherwise use the Object that was found.
if isempty(Mono)
    Mono = visa('NI', 'GPIB0::4::INSTR');
else
    fclose(Mono);
    Mono = Mono(1);
end

% Connect to instrument Object, Mono.
fopen(Mono);

% Configure instrument Object, Mono.
set(Mono, 'EOSMode', 'read&write');
set(Mono, 'EOSCharCode', 10);
set(Mono, 'Timeout', 30);
fprintf(Mono, 'SHUTTER C');
fclose(Mono);
```

Setting the grating.

```
fopen(Mono);
flushinput(Mono);
flushoutput(Mono);
```

```
%clrdevice(Mono)
temp = query(Mono, 'GRAT?');
%fprintf(temp);

%Query what is the current grating
grat_now = str2double(temp(1));

%Set the grating if it is not the same as the current grating
if grat_now ~= gra
    clrdevice(Mono);
    fprintf(Mono, strcat('GRAT ', 32, num2str(gra)));
    pause(10);
    mon_erro(Mono);
end
flushinput(Mono);
flushoutput(Mono);
fclose(Mono);
```

Setting the wavelength.

```
fopen(Mono);
%clrdevice(Mono)
fprintf(Mono, strcat('GOWAVE ', 32, num2str(wav)));
pause(1);
mon_erro(Mono);

flushinput(Mono);
flushoutput(Mono);
res = 'DONE.';
wavv = query(Mono, 'WAVE?');
graa = query(Mono, 'GRAT?');
clrdevice(Mono);
```

Disconnect from instrument Object, Mono.

```
disp('Close VISA Mono.');
```

```
fclose(Mono);

% Clean up all Objects.
delete(Mono);
clear Mono;
% disp('Mono closed successfully.');
```

```
% disp(' ');

end
```

Published with MATLAB® R2019b

J.1.2 monoshutteron

The input format is `monoshutteron(grating, wavelength)`. The code sets the grating and wavelength of the monochromator with input shutter open. After this is done, the code queries the set grating and wavelength, and outputs the received values of set grating and wavelength as an array `[Result, Wavelength, Grating]`. Once complete, the Result is returned as 'DONE'.

Mono Shutter On

Table of Contents

Intitiate the function	1
Connecting to the monochromator	1
Setting the grating	1
Setting the wavelength	2
Disconnect from instrument Object, Mono	2

Intitiate the function

```
function [res,wavv,graa] = monoshutteron(gra,wav)
```

Connecting to the monochromator

```
%Find the instrument
Mono = instrfind('Type', 'visa-
gpib', 'RsrcName', 'GPIB0::4::INSTR', 'Tag', '');

% Create the VISA-GPIB Object if it does not exist
% otherwise use the Object that was found.
if isempty(Mono)
    Mono = visa('NI', 'GPIB0::4::INSTR');
else
    fclose(Mono);
    Mono = Mono(1);
end

% Connect to instrument Object, Mono.
fopen(Mono);

% Configure instrument Object, Mono.
set(Mono, 'EOSMode', 'read&write');
set(Mono, 'EOSCharCode', 10);
set(Mono, 'Timeout', 30);
fprintf(Mono, 'SHUTTER O');
fclose(Mono);
```

Setting the grating.

```
fopen(Mono);
flushinput(Mono);
flushoutput(Mono);

%clrdevice(Mono)
temp = query(Mono, 'GRAT?');
fprintf(temp);
```

```
grat_now = str2double(temp(1));
if grat_now ~= gra
    clrdevice(Mono);
    fprintf(Mono, strcat('GRAT ', 32, num2str(gra)));
    pause(10);
    mon_erro(Mono);
end
flushinput(Mono);
flushoutput(Mono);
fclose(Mono);
```

Setting the wavelength.

```
fopen(Mono);
%clrdevice(Mono)
fprintf(Mono, strcat('GOWAVE ', 32, num2str(wav)));
pause(1);
mon_erro(Mono);

flushinput(Mono);
flushoutput(Mono);
res = 'DONE.';
wavv = query(Mono, 'WAVE?');
graa = query(Mono, 'GRAT?');
clrdevice(Mono);
```

Disconnect from instrument Object, Mono.

```
disp('Close VISA Mono.');
```

```
fclose(Mono);

% Clean up all Objects.
delete(Mono);
clear Mono;
% disp('Mono closed successfully.');
```

```
% disp(' ');

end
```

Published with MATLAB® R2019b

J.1.3 monoshutteroff

The input format is `monoshutteroff(grating, wavelength)`. This code is interchangeably used with `setmono4`.

Mono Shutter Off

Table of Contents

Initiate function	1
Connecting to the monochromator	1
Setting the grating	1
Setting the wavelength	2
Disconnect from instrument Object, Mono	2

Initiate function

```
function [res, wavv, graa] = monoshutteroff(gra, wav)
```

Connecting to the monochromator

```
%Find the instrument
Mono = instrfind('Type', 'visa-gpib', 'RsrcName',
    'GPIB0::4::INSTR', 'Tag', '');

% Create the VISA-GPIB Object if it does not exist
% otherwise use the Object that was found.
if isempty(Mono)
    Mono = visa('NI', 'GPIB0::4::INSTR');
else
    fclose(Mono);
    Mono = Mono(1);
end

% Connect to instrument Object, Mono.
fopen(Mono);

% Configure instrument Object, Mono.
set(Mono, 'EOSMode', 'read&write');
set(Mono, 'EOSCharCode', 10);
set(Mono, 'Timeout', 30);
fprintf(Mono, 'SHUTTER C');
fclose(Mono);
```

Setting the grating.

```
fopen(Mono);
flushinput(Mono);
flushoutput(Mono);

%clrdevice(Mono)
temp = query(Mono, 'GRAT?');
fprintf(temp);
```

```
grat_now = str2double(temp(1));  
if grat_now ~= gra  
    clrdevice(Mono);  
    fprintf(Mono, strcat('GRAT ', 32, num2str(gra)));  
    pause(10);  
    mon_erro(Mono);  
end  
flushinput(Mono);  
flushoutput(Mono);  
fclose(Mono);
```

Setting the wavelength.

```
fopen(Mono);  
%clrdevice(Mono)  
fprintf(Mono, strcat('GOWAVE ', 32, num2str(wav)));  
pause(1);  
mon_erro(Mono);  
  
flushinput(Mono);  
flushoutput(Mono);  
res = 'DONE.';  
wavv = query(Mono, 'WAVE?');  
graa = query(Mono, 'GRAT?');  
clrdevice(Mono);
```

Disconnect from instrument Object, Mono.

```
disp('Close VISA Mono.');
```

```
fclose(Mono);  
  
% Clean up all Objects.  
delete(Mono);  
clear Mono;  
% disp('Mono closed successfully.');
```

```
% disp(' ');  
  
end
```

Published with MATLAB® R2019b

J.2 Filter wheel

J.2.1 setfilterV4

The input format is `setfilterV4(wavelength)`. The wavelength switchpoints at which the filter wheel changes filters are defined in this code. The output is an array [Result, Initial Filter, Final Set Filter].

Set filter wheel

Table of Contents

Initiate function	1
Initialize the filter wheel	1
Setting the filter	1
Disconnect and Clean Up	2

Set the filter based on wavelength

Initiate function

```
function [res, filtin, filtout] = setfilterV4(wav)
```

Initialize the filter wheel.

```
%Find the VISA object corresponding to the filter wheel
FilWh = instrfind('Type', 'visa-generic', 'RsrcName',
    'USB0::0x104D::0x1011::6C03020C210D2774::0::RAW', 'Tag', '');

% Create the VISA-GENERIC FilWhect if it does not exist
% otherwise use the FilWhect that was found.
if isempty(FilWh)
    FilWh = visa('NI',
        'USB0::0x104D::0x1011::6C03020C210D2774::0::RAW');
else
    fclose(FilWh);
    FilWh = FilWh(1);
end

fopen(FilWh);
%set (FilWh, 'Timeout', 30);

flushinput(FilWh)
flushoutput(FilWh)

tem = query(FilWh, 'FILT?');
filt_now = str2double(tem(1));
```

Setting the filter

```
if wav < 311
    if filt_now ~= 1
        clrdevice(FilWh)
        fprintf(FilWh, strcat('FILT ', num2str(1)));
        pause(5);
    end
elseif wav < 600
```

```
        if filt_now ~= 2
            clrdevice(FilWh)
            fprintf(FilWh, strcat('FILT ', num2str(2)));
            pause(5);
        end
    elseif wav < 1100
        if filt_now ~= 3
            clrdevice(FilWh)
            fprintf(FilWh, strcat('FILT ', num2str(3)));
            pause(5);
        end
    else
        if filt_now ~= 4
            clrdevice(FilWh)
            fprintf(FilWh, strcat('FILT ', num2str(4)));
            pause(5);
        end
    end

flushinput(FilWh)
flushoutput(FilWh)

res = 'DONE.';
filtin = tem;
filtout = query(FilWh, 'FILT?');
fclose(FilWh);
```

Disconnect and Clean Up

```
%disp(' ');
% disp ('Close VISA Filter.');
```

```
fclose(FilWh);
delete(FilWh);
clear FilWh;% Find a GPIB FilWhect.
% disp ('Filter closed successfully.');
```

```
% disp(' ');

end
```

Published with MATLAB® R2019b

J.3 Power meter

J.3.1 `setpower_v2`

The input format is `setpower_v2(wavelength)`. The incident wavelength must be specified. The output array is of the form `[Result, Power]`.

Get optical power reading from power meter

Table of Contents

Initialize function	1
Specify resource name and vendor of driver Power	1
Open VISA connection and set parameters	1
Read Power	1
Close VISA connection	2

Initialize function

```
function [res,pow] = setpower_v2(wav)
```

Specify resource name and vendor of driver Power

```
power_addr = 'USB0::0x1313::0x8072::P2010480::INSTR';  
power_vendor = 'NI';
```

Open VISA connection and set parameters

```
powerm = visa (power_vendor, power_addr);  
fopen (powerm);  
  
%set (power, 'Timeout', 30);  
set (powerm, 'EOSMode', 'read');  
% Set averaging value for power measurements  
fprintf (powerm, [':AVER ', 10]);
```

Read Power

```
flushinput(powerm)  
flushoutput(powerm)  
  
% Reading the Power.  
fprintf(powerm,sprintf('CORR:WAV %s',num2str(wav)));  
fprintf (powerm, 'CONF:POW');  
fprintf (powerm, ':INIT');  
res = 'DONE.';  
pow = str2double (query (powerm, ':FETCH?'));  
  
flushinput(powerm)  
flushoutput(powerm)
```

Close VISA connection

```
disp ('Close Power connection.');
```

```
fclose (powerm);  
delete (powerm);  
clear power;  
% disp ('Power closed successfully.');
```

```
end
```

Published with MATLAB® R2019b

J.4 Keithley Sourcemeeter

J.4.1 openKeithley_Eth

The function is called without any arguments, as `openKeithley_Eth()`. The code creates a GPIB object corresponding to the Keithley in the Matlab environment. The handle for the GPIB object is output as 'Keith', and is used to communicate with the Keithley.

Establish connection with Keithley Sourcemeter

Table of Contents

Initiate the function	1
Instrument Connection	1

Initiate the function

```
function [Keith] = openKeithley_Eth()
```

Instrument Connection

Find a GPIB object.

```
Keith = instrfind('Type', 'visa-tcpip', 'RsrcName', 'TCPIP0::least-  
sourcemeter.ee.nd.edu::inst0::INSTR', 'Tag', '');  
  
% Create the GPIB object if it does not exist  
% otherwise use the object that was found.  
if isempty(Keith)  
    Keith = visa('NI', 'TCPIP0::least-  
sourcemeter.ee.nd.edu::inst0::INSTR');  
else  
    fclose(Keith);  
    Keith = Keith(1);  
end  
  
% Connect to instrument object, obj1.  
  
%Set the input buffer size  
Keith.InputBufferSize = 2048;  
  
%Set the timeout (in sec)  
fopen(Keith);  
Keith.timeout = 180;  
% Keith.EOSMode = 'read';  
% Keith.EOSCharCode = 13;  
  
fclose(Keith);  
  
end
```

Published with MATLAB® R2019b

J.4.2 VoltageListSweep

The input format is VoltageListSweep(Keith, vlist, stime, points, ilimit, sense). In the inputs, Keith corresponds to the GPIB object handle for the Keithley sourceme-
ter, vlist is a list of voltages for the sweep, stime is the user defined settling time for
each voltage list point, points is the number of voltages in the list sweep, sense is
set as 2 or 4 to perform a 2 wire or a 4 wire measurement, respectively, and ilimit
is the current limit for the entire measurement. Note that the user defined settling
time is in addition to the current range dependent settling time introduced by the
sourceme-ter itself.

Perform I-V sweep with a specified voltage list

Initialize function

```
function [voltage, current] = VoltageListSweep(Keith, vlist, stime,
    points, ilimit, sense)
fopen(Keith);

flushinput(Keith);
flushoutput(Keith);

fprintf(Keith, '%s\n', 'dataqueue.clear()');
fprintf(Keith, '%s\n', 'reset()');

fprintf(Keith, '%s\n', 'smua.reset()');

fprintf(Keith, '%s\n', 'smua.nvbuffer1.clear()');
fprintf(Keith, '%s\n', 'smua.nvbuffer1.appendmode = 0');
fprintf(Keith, '%s\n', 'smua.nvbuffer1.collectsourcevalues = 1');
fprintf(Keith, '%s\n', 'smua.nvbuffer1.collecttimestamps = 0');
fprintf(Keith, '%s\n', 'smua.measure.filter.count = 1');
fprintf(Keith, '%s\n', 'smua.measure.autorange1 = 1');
fprintf(Keith, '%s\n', sprintf('smua.source.limit1=%s',
    num2str(ilimit)));

if sense==2
    fprintf(Keith, '%s\n', 'smua.sense=smua.SENSE_LOCAL');
elseif sense==4
    fprintf(Keith, '%s\n', 'smua.sense=smua.SENSE_REMOTE');
end

fprintf(Keith, '%s\n', sprintf('vlist = {%s}', vlist));

fprintf(Keith, '%s\n', sprintf('SweepVListMeasureI(smua, vlist, %s,
    %s)', num2str(stime), num2str(points)));
fprintf(Keith, '%s\n', 'waitcomplete()');

current=query(Keith, sprintf('printbuffer(1, %s,
    smua.nvbuffer1.readings)', num2str(points)), '%s\n', '%s\n');
voltage=query(Keith, sprintf('printbuffer(1, %s,
    smua.nvbuffer1.sourcevalues)', num2str(points)), '%s\n', '%s\n');

current = str2double(split(current, ','));
voltage = str2double(split(voltage, ','));

flushinput(Keith);
flushoutput(Keith);
```

Perform I-V sweep with
a specified voltage list

```
clrdevice(Keith);  
fclose(Keith);  
  
end
```

Published with MATLAB® R2019b

J.4.3 VoltagePulseSweepCycle

The input format is `VoltagePulseSweepCycle(Keith, vapp, stime, cycles)`. The code applies bipolar pulses to the DUT, and is used to wake-up the FE. In the inputs, `Keith` corresponds to the GPIB object handle for the Keithley sourcemeter, `vapp` is the amplitude of the bipolar pulses, `stime` is pulse duration, and `cycles` defines the number of pulses to be applied. No measurements are made in this code, and no output is returned.

Perform pulsed I-V sweep

Initialize function

```
function done = VoltagePulseSweepCycle(Keith, vapp, stime, cycles)
fopen(Keith);

flushinput(Keith);
flushoutput(Keith);

fprintf(Keith, '%s\n', 'reset()');

fprintf(Keith, '%s\n', 'smua.reset()');

fprintf(Keith, '%s\n', 'smua.nvbuffer1.clear()');
fprintf(Keith, '%s\n', 'smua.nvbuffer1.appendmode = 0');
fprintf(Keith, '%s\n', 'smua.nvbuffer1.collectsourcevalues = 0');
fprintf(Keith, '%s\n', 'smua.nvbuffer1.collecttimestamps = 0');
%fprintf(Keith, 'smua.measure.nplc = 1');

fprintf(Keith, '%s\n', sprintf('PulseVMeasureI(smua, -%s, %s,
    %s, %s, %s)', num2str(vapp), num2str(vapp), num2str(stime),
    num2str(stime), num2str(cycles)));

fprintf(Keith, '%s\n', 'smua.nvbuffer1.clear()');

fprintf(Keith, '%s\n', 'smua.reset()');
fprintf(Keith, '%s\n', 'status.reset()');

fprintf(Keith, '%s\n', 'waitcomplete()');

done=query(Keith, 'print(1)', '%s\n', '%s\n');

flushinput(Keith);
flushoutput(Keith);
clrdevice(Keith);

fclose(Keith);

end
```

Published with MATLAB® R2019b

J.5 Combined codes

These codes combine the individual codes listed above in different orders for specific measurements.

J.5.1 Calibration

The optical power is measured for a specified sweep of photon energies output by the monochromator. The energy sweep is defined by a starting energy, stopping energy, and steps. The energy sweep is then converted to a wavelength sweep. The code then performs the wavelength sweep, and measures the optical power for every wavelength. The data is saved as a Matlab .mat file.

Calibration

Table of Contents

Define sweep	1
Initialize	1
Perform Sweep	2

Obtain optical power vs wavelength

Define sweep

```
% Set min, max, and energy steps
MinVal=1.25;
MaxVal=4.0;
Inc=0.05;

%Create energy array
EnergApp = MinVal:Inc:MaxVal;

%Translate into wavelength array, taking integer wavelengths
wave=floor(1240./EnergApp);
```

Initialize

```
%Set initial grating for sweep, and switchpoint between gratings
Grat = 1;
GratSwitchPoint = 1000;

repeats = 1;

Filename = '20p0903_Cal_Long_Fine';

tic

%Make sure that the Mono is working and Reading
setmono4(Grat, wave(1));

%Create array to store calibration data
wavsize = length(wave);
```

```
caldata = zeros(wavsize, 2, 2, repeats);
```

Perform Sweep

```
for count0 = 1 : repeats
    disp(count0);

    % Forward Sweep
    for count1 = 1:1:wavsize
        %1: Set mono
        if(wave(count1)>=GratSwitchPoint)
            Grat=2;
        else
            Grat=1;
        end

        [buff1, wavdata, buff2]=setmono4(Grat, wave(count1));
        wavdata=str2double(wavdata);

        %Open mono shutter
        monoshutteron(Grat, wave(count1));

        %2: Set filter wheel based on wavelength
        [buff1, buff2, buff3]=setfilterV4(wavdata);

        %3: Record power
        [buff1, powdata]=setpower_v2(wavdata);
        %4: Save
        caldata(count1, :, 1, count0) = [wavdata, powdata];
        %5: Display
        disp(['Measurement ', num2str(wave(count1)), ' ', 'Wavelength
(nm) = ', num2str(wavdata), ' | Power (W) =', num2str(powdata)]);
        disp(' ');
    end

    %Reverse Sweep
    for count1 = wavsize:-1:1
        %1: Mono
        if(wave(count1)>=GratSwitchPoint)
            Grat=2;
        else
            Grat=1;
        end

        [buff1, wavdata, buff2]=setmono4(Grat, wave(count1));
        wavdata=str2double(wavdata);
        monoshutteron(Grat, wave(count1));

        %2: FilterWheel
        [buff1, buff2, buff3]=setfilterV4(wavdata);
```

```
    %3: PowerMeter
    [buff1, powdata]=setpower_v2(wavdata);
    %4: Save
    caldata(count1, :, 2, count0) = [wavdata, powdata]; %Saves
Data
    %5: Display
    disp(['Measurement ', num2str(wave(count1)), ': ',
    'Wavelength (nm) = ', num2str(wavdata), ' | Power (W) = ',
    num2str(powdata)]);
    disp(' ');
end
end

%Set mono wavelength to 300 nm, and close shutter
monoshutteroff(1, 300);

%Save
save(Filename, 'caldata');

toc
```

Published with MATLAB® R2019b

J.5.2 TER_Meas

Transient polarization dependant I-V measurements are performed on the DUT. User inputs are taken via a prompt, and the output is saved as a Matlab .mat file.

Perform polarization dependant I-V sweeps

Table of Contents

Define sweep parameters from user input	1
Initialize instruments	2
Perform DC I-V sweep	2
Perform Pol-Dep IV	3
Save data	4

Full current transients are measured

Define sweep parameters from user input

```
close all
clear all

prompt = {'Min Voltage (abs, V)', 'Max Voltage (abs, V)', 'Voltage
Step (V)', 'Repeats', 'Reset Voltage (V)', 'Hold Time (s)', 'Set
Points', 'Settle Points', 'Current Compl. Limit (A)', 'Wakeup
Cycles', 'Filename', '2/4 Wire Sense', 'NetID'};
dlgtitle = 'IPE FE Sweep Parameters';
dims = [1 35];
defaultinputs = {'0.1', '1.5', '0.1', '2', '2.8', '0.001', '3',
'20', '1e-6', '1', '20p0615_PR62_2_D11_TER_1', '2', 'ppandey'};
Inputs = inputdlg(prompt, dlgtitle, dims, defaultinputs);

MinVal = str2double(Inputs{1});
MaxVal = str2double(Inputs{2});
Inc = str2double(Inputs{3});
runs = str2double(Inputs{4});

Vset = str2double(Inputs{5});
HTime = str2double(Inputs{6});
Spoints = str2double(Inputs{7});
Npoints = str2double(Inputs{8});
ILim = str2double(Inputs{9});
Wak_cyc = str2double(Inputs{10});

Filename = Inputs{11};
sense = str2double(Inputs{12});
NetID = Inputs{13};

meas = struct;
meas.Inputs = Inputs;
meas.prompt = prompt;
```

```
avgpoints=3;
```

```
tic
```

Initialize instruments

```
%Open Communications with Keithley
Keith = openKeithley_Eth();

%Wake-up the device
VoltagePulseSweepCycle(Keith, Vset, HTime, Wak_cyc)

time=toc;
fprintf('%s wakeup cycles completed, time %s\n', num2str(Wak_cyc),
num2str(time));
```

Perform DC I-V sweep

```
Vsweep = [0:0.1:1, 0.9:-0.1:-0.9, -1:0.1:0];
Vsweepsize = length(Vsweep);
Vsweep = regexprep(num2str(Vsweep), '\s+', ', ');

Keith = openKeithley_Eth();

[vol, curr] = VoltageListSweep(Keith, Vsweep, 0.001, Vsweepsize,
1e-9, sense);

figure(3)
semilogy(vol, abs(curr))

meas.DC_IV = [vol, curr];

Vapp = [-MaxVal:Inc:-MinVal, MinVal:Inc:MaxVal, MaxVal:-Inc:MinVal,
-MinVal:-Inc:-MaxVal];
Vsize=length(Vapp);
meas.Vapp = Vapp;
colors = distinguishable_colors(Vsize);

IVdata=zeros(3, Vsize, runs);
figure(1)
hold on

figure(2)
hold on
```

Perform Pol-Dep IV

```
for count0=1:1:runs

    for count1=1:1:Vsize

        %Define sweep, first applying set voltage,
        then IPE
        %voltage. Negative set voltage applied here.
        Vsweep=[-Vset*ones(1, Spoints),
        Vapp(count1)*ones(1, Npoints)];
        Vsweepsize = length(Vsweep);
        Vsweep = regexprep(num2str(Vsweep), '\s+', '');

        [vol, curr1] = VoltageListSweep(Keith, Vsweep,
        HTime, Vsweepsize, ILim, sense);
        %Take mean using avgpoints
        Ineg = mean(curr1(end-avgpoints:end));

        %Store the entire current waveform
        meas.IV{count0, count1, 1}=[vol, curr1];

        time=toc;
        fprintf('%s V, Ineg %s A, time %s\n',
        num2str(Vapp(count1)), num2str(Ineg), num2str(time));

        figure(1)
        plot(curr1(Spoints+3:end), 'Color',
        colors(count1, :), 'LineStyle', '-');
        drawnow;

        %Positive voltage set
        Vsweep=[Vset*ones(1, Spoints),
        Vapp(count1)*ones(1, Npoints)];
        Vsweepsize = length(Vsweep);
        Vsweep = regexprep(num2str(Vsweep), '\s+', '');

        [vol, curr2] = VoltageListSweep(Keith, Vsweep,
        HTime, Vsweepsize, ILim, sense);
        Ipos = mean(curr2(end-avgpoints:end));

        figure(1)
        plot(curr2(Spoints+3:end), 'Color',
        colors(count1, :), 'LineStyle', '-', 'Marker', '.');
        drawnow;

        %Store the entire current waveform
        meas.IV{count0, count1, 2}=[vol, curr2];
```

Perform polarization de-
pendant I-V sweeps

```
        time=toc;
        fprintf('%s V,  Ipos %s A,  time %s\n',
num2str(Vapp(count1)), num2str(Ipos), num2str(time));

        %4: Save Data
        IVdata(:, count1, count0) =
[Ineg;Ipos;Vapp(count1)];

        meas.IVdata=IVdata;

        save(Filename, 'meas');

        %5: Display
        figure(2)
        plot(IVdata(3, 1:count1, count0), IVdata(1,
1:count1, count0), 'k', 'LineStyle', '-');
        drawnow;
        figure(2)
        plot(IVdata(3, 1:count1, count0), IVdata(2,
1:count1, count0), 'k', 'LineStyle', '-', 'Marker', '.');
        drawnow;

        xlim([-MaxVal MaxVal]);
        ylabel('Current (A)');
        xlabel('Voltage (V)');

        end

        time = toc;
        fprintf('TER run %s complete,  time %s\n', num2str(count0),
num2str(time));

end

delete(Keith);
clear Keith;
```

Save data

```
%Save Data and Input Parameters as mat file,  and also the I vs
wavelength
%plot as a png file
save(Filename, 'meas');
figure(1)
print(sprintf( '%s_IPE_currs.png',  Filename), '-dpng', '-r1000');
close(1)
```

Perform polarization de-
pendant I-V sweeps

```
figure(2)
print(sprintf( '%s_IV.png', Filename), '-dpng', '-r1000');
close(2)

% Clean up all objects.

% %% Send Email
% mail = 'ipesetup@gmail.com'; %Mono email address, I set it up
% solely for this.
% password = 'IPEsetup1'; %Email password
% setpref('Internet', 'E_mail', mail);
% setpref('Internet', 'SMTP_Server', 'smtp.gmail.com');
% setpref('Internet', 'SMTP_Username', mail);
% setpref('Internet', 'SMTP_Password', password);
% props = java.lang.System.getProperties;
% props.setProperty('mail.smtp.auth', 'true');
% props.setProperty('mail.smtp.socketFactory.class', ...
% 'javax.net.ssl.SSLSocketFactory');
% props.setProperty('mail.smtp.socketFactory.port', '465');
% sendmail(sprintf('%s@nd.edu', NetID), 'IPE is finished!'); %insert
% your own email to get a notification when sweep is finished
toc
```

Published with MATLAB® R2019b

J.5.3 IPE_Pol

Polarization dependant IPE is performed. User inputs are taken via a prompt, and the output is saved as a Matlab .mat file. This is a wrapper function, taking user input and saving data, which calls another function (IPE_Pol_fun_debugfull_chop) to perform the measurement.

Polarization Dependant IPE - Wrapper

Table of Contents

Define sweep parameters from user input	1
Initialize instruments	2
Wake-up the device	2
Perform DC I-V sweep	2
Perform Pol-Dep IPE	3
Save data	3
Send Email	3

Takes user inputs and runs polarization dependant IPE function

Define sweep parameters from user input

```
close all
clear all

prompt = {'Start Energy (eV)', 'End Energy (eV)', 'Energy Step (eV)',
          'IPE Voltages (V, Comma Separated)', 'IPE Repeats', 'Reset
          Voltage (V)', 'Hold Time (s)', 'Settle Points', 'Current Compl.
          Limit (A)', 'Wakeup Cycles', 'Wakeup Time (s)', 'Filename', '2/4 Wire
          Sense', 'NetID'};
dlgtitle = 'IPE FE Sweep Parameters';
dims = [1 35];
defaultinputs = {'1.25', '3.9', '0.05', '1', 1.1,
                 1.2, '1', '3.5', '0.001', '20', ...
                 '1e-4', '100', '0.001', '20p0613_PR62_1_D2_FE_1', '2', 'ppandey'};
Inputs = inputdlg(prompt, dlgtitle, dims, defaultinputs);

MinVal = str2double(Inputs{1});
MaxVal = str2double(Inputs{2});
Inc = str2double(Inputs{3});
Vlist = Inputs{4};
Vapp = str2double(split(Vlist, ','));
Vsize = max(size(Vapp));
runs = str2double(Inputs{5});

Vset = str2double(Inputs{6});
HTime = str2double(Inputs{7});
NPoints = str2double(Inputs{8});
ILim = str2double(Inputs{9});
Wak_cyc = str2double(Inputs{10});
HTime_wak = str2double(Inputs{11});

Filename = Inputs{12};
```

```
sense = str2double(Inputs{13});
NetID = Inputs{14};

meas = struct;
meas.Inputs = Inputs;
meas.prompt = prompt;
```

Initialize instruments

```
%Define Initial Grating
Grat = 1;

%Define Grating Switch Point
GratSwitchPoint = 900;

tic

%Make sure that the Mono is working and Reading
[buff1, buff2, buff3]=setmono4(Grat, MinVal);

%Open Communications with Keithley
Keith = openKeithley_Eth();
```

Wake-up the device

```
VoltagePulseSweepCycle(Keith, Vset, HTime_wak, Wak_cyc)

time=toc;
fprintf('%s wakeup cycles completed, time %s\n', num2str(Wak_cyc),
num2str(time));
```

Perform DC I-V sweep

```
Vsweep = [0:0.1:1, 0.9:-0.1:-0.9, -1:0.1:0];
Vsweepsize = length(Vsweep);
Vsweep = regexprep(num2str(Vsweep), '\s+', ', ');

Keith = openKeithley_Eth();

[vol, curr] = VoltageListSweep(Keith, Vsweep, 0.001, Vsweepsize, 1e-8,
sense);

figure(1)
```

```
semilogy(vol, abs(curr))  
hold on  
  
meas.IV = [vol, curr];  
  
eta=1.5;
```

Perform Pol-Dep IPE

```
[IPEdata, currson, currsoff]= IPE_Pol_fun_debugfull_chop(MinVal,  
MaxVal, Inc, Vlist, Vset, HTime, NPoints, ILim, runs, sense, Keith);  
meas.IPEdata=IPEdata;  
  
time = toc;  
fprintf('IPE cycle complete, time %s\n', num2str(time));  
  
delete(Keith);  
clear Keith;
```

Save data

```
%Save Data and Input Parameters as mat file, and also the I vs  
wavelength  
%plot as a png file  
save(Filename, 'meas', 'currson', 'currsoff');  
figure(1)  
print(sprintf('s_IPE_IV.png', Filename), '-dpng', '-r1000');  
close(1)  
  
figure(3)  
print(sprintf('s_IPE.png', Filename), '-dpng', '-r1000');  
close(3)  
  
% Clean up all objects.
```

Send Email

```
mail = 'ipesetup@gmail.com'; %Mono email address, I set it up solely for this. password = 'IPE-  
setup!'; %Email password setpref('Internet', 'E_mail', mail); setpref('Internet', 'SMTP_Server', 'smt-  
p.gmail.com'); setpref('Internet', 'SMTP_Username', mail); setpref('Internet', 'SMTP_Password', pass-  
word); props = java.lang.System.getProperties(); props.setProperty('mail.smtp.auth', 'true'); props.setProp-  
erty('mail.smtp.socketFactory.class', ... 'javax.net.ssl.SSLSocketFactory'); props.setProperty('mail.smt-  
p.socketFactory.port', '465'); sendmail(sprintf('%s@nd.edu', NetID), 'IPE is finished!'); %insert your own  
email to get a notification when sweep is finished
```

```
toc
```

Published with MATLAB® R2019b

J.5.4 IPE_Pol_fun_debugfull_chop

This function performs the polarization dependant IPE measurement and passes the saved data to the wrapper function.

Polarization Dependant IPE - Function

Table of Contents

Get inputs from wrapper	1
Initialize and define variables	1
Sweep	1

Run by wrapper to measure polarization dependant IPE

Get inputs from wrapper

```
function [IPEdata, currson, currsoff] =  
    IPE_Pol_fun_debugfull_chop(MinVal, MaxVal, Inc, Vlist, Vset, HTime,  
    points, ILim, runs, sense, Keith)
```

Initialize and define variables

```
Vapp = str2double(split(Vlist, ','));  
Vsize = max(size(Vapp));  
  
% No. of points to avg for a current reading  
avgpoints=5;  
%No. of points to leave at set voltage  
setpoints=3;  
  
%Define Initial Grating  
Grat = 1;  
  
%Define Grating Switch Point  
GratSwitchPoint = 1000;  
  
%Create structure to store all current waveforms  
currson = struct;  
currsoff = struct;
```

Sweep

```
%Create energy array  
EnergApp = MinVal:Inc:MaxVal;  
  
%Translate into wavelength array, taking integer wavelengths  
waveApp=floor(1240./EnergApp);  
  
wavsize = length(waveApp);  
IPEdata = zeros(wavsize, 4, Vsize, 2, runs);  
  
colors = distinguishable_colors(Vsize);  
figure(3)  
hold on
```

```

count_curron=1;
count_curroff=1;

for RepeatNumber = 1:1:runs

    %Backward Sweep First (i.e. low energy photons first)
    for wavcount = 1:1:wavsize

        %1: Mono

        %Choose grating
        if(waveApp(wavcount)>=GratSwitchPoint)
            Grat=2;
        else
            Grat=1;
        end

        %Set mono
        [buff1, dataWF1, buff2]=setmono4(Grat,
waveApp(wavcount));
        dataWF=str2double(dataWF1);

        %2: Set FilterWheel
        [buff1, buff2, buff3]=setfilterV4(dataWF);

        %Close Mono Shutter
        [buff1, buff2, buff3] = monoshutteroff(Grat,
waveApp(wavcount));

        %Perform Keithley Sweep
        for vcount=1:1:Vsize

            %Open Mono Shutter
            [buff1, buff2, buff3] = monoshutteron(Grat,
waveApp(wavcount));

            %Define sweep, first applying set voltage, then
            IPE
            %voltage.
            Vsweep=[-Vset*ones(1, setpoints), -
Vapp(vcount)*ones(1, points)];
            Vsweepsize = length(Vsweep);
            Vsweep = regexprep(num2str(Vsweep), '\s+', ', ');

            %Perform sweep
            [vol, curr1on] = VoltageListSweep(Keith, Vsweep,
HTime, Vsweepsize, ILim, sense);

```

Polarization Dependant IPE - Function

```
        %Store the entire current waveform for mono ON
        currson.IV{count_currson}=[vol, curr1on];
        currson.info{count_currson}=[-1, Vapp(vcount),
dataWF, RepeatNumber];
        count_currson=count_currson+1;

        %Close Mono Shutter
        [buff1, buff2, buff3] = monoshutteroff(Grat,
waveApp(wavcount));

        %Perform sweep for mono OFF (i.e dark current)
        [vol, currloff] = VoltageListSweep(Keith, Vsweep,
HTime, Vsweepsize, ILim, sense);

        %Store the entire current waveform
        currsoff.IV{count_curroff}=[vol, currloff];
        currsoff.info{count_curroff}=[-1, Vapp(vcount),
dataWF, RepeatNumber];
        count_curroff=count_curroff+1;

        %Take mean using avgpoints and subtracting dark
current
        Ineg = mean(curr1on(end-avgpoints:end)) -
mean(currloff(end-avgpoints:end));

        time=toc;
        fprintf('%s V, Ineg %s A, Wavelength %s time %s
\n', num2str(Vapp(vcount)), num2str(Ineg), num2str(waveApp(wavcount)),
num2str(time));

        %Now repeating for positive set

        %Open Mono Shutter
        [buff1, buff2, buff3] = monoshutteron(Grat,
waveApp(wavcount));

        %Positive voltage set
        Vsweep=[Vset*ones(1, setpoints),
Vapp(vcount)*ones(1, points)];
        Vsweepsize = length(Vsweep);
        Vsweep = regexprep(num2str(Vsweep), '\s+', ', ');

        [vol, curr2on] = VoltageListSweep(Keith, Vsweep,
HTime, Vsweepsize, ILim, sense);

        currson.IV{count_currson}=[vol, curr2on];
        currson.info{count_currson}=[1, Vapp(vcount),
dataWF, RepeatNumber];
        count_currson=count_currson+1;
```

Polarization Dependant IPE - Function

```
        %Close Mono Shutter
        [buff1, buff2, buff3] = monoshutteroff(Grat,
waveApp(wavcount));

        %Perform sweep for mono OFF (i.e dark current)
        [vol, curr2off] = VoltageListSweep(Keith, Vsweep,
HTime, Vsweepsize, ILim, sense);

        %Store the entire current waveform
        currsoff.IV{count_curroff}=[vol, curr2off];
        currsoff.info{count_curroff}=[1, Vapp(vcount),
dataWF, RepeatNumber];
        count_curroff=count_curroff+1;

        %Take mean using avgpoints and subtracting dark
current
        Ipos = mean(curr2on(end-avgpoints:end)) -
mean(curr2off(end-avgpoints:end));

        time=toc;
        fprintf('%s V, Ipos %s A, Wavelength %s time %s
\n', num2str(Vapp(vcount)), num2str(Ipos), num2str(waveApp(wavcount)),
num2str(time));

        %4: Save Data
        IPEdata(wavcount, :, vcount, 1, RepeatNumber) =
[dataWF;Ineg;Ipos;Vapp(vcount)];

save('buffersave', 'IPEdata', 'currson', 'currsoff');

        %5: Display
        figure(3)
        plot(IPEdata(1:wavcount, 1, vcount,
1, RepeatNumber), IPEdata(1:wavcount, 2, vcount, 1,
RepeatNumber), 'Color', colors(vcount, :), 'LineStyle', '-');
        drawnow;
        plot(IPEdata(1:wavcount, 1,
vcount, 1, RepeatNumber), IPEdata(1:wavcount,
3, vcount, 1, RepeatNumber), 'Color',
colors(vcount, :), 'LineStyle', '-', 'Marker', 'o');
        drawnow;

        xlim([1240./MaxVal 1240./MinVal]);
        ylabel('Current (A)');
        xlabel('Wavelength (nm)');
```

```

end

end

%Forward Sweep
for wavcount = wavsize:-1:1

    %1: Mono
    if(waveApp(wavcount)>=GratSwitchPoint)
        Grat=2;
    else
        Grat=1;
    end

    [buff1, dataWF1, buff2]=setmono4(Grat,
waveApp(wavcount));
    dataWF=str2double(dataWF1);

    %2: FilterWheel
    [buff1, buff2, buff3]=setfilterV4(dataWF);

    %Close Mono Shutter
    [buff1, buff2, buff3] = monoshutteroff(Grat,
waveApp(wavcount));

    %Perform Keithley Sweep
    for vcount=1:1:Vsize
        %Open Mono Shutter
        [buff1, buff2, buff3] = monoshutteron(Grat,
waveApp(wavcount));

        %Define sweep, first applying set voltage, then
IPE
        %voltage.
        Vsweep=[-Vset*ones(1, setpoints), -
Vapp(vcount)*ones(1, points)];
        Vsweepsize = length(Vsweep);
        Vsweep = regexprep(num2str(Vsweep), '\s+', ', ');

        %Perform sweep
        [vol, currlon] = VoltageListSweep(Keith, Vsweep,
HTime, Vsweepsize, ILim, sense);

        %Store the entire current waveform for mono ON
        currson.IV{count_curron}=[vol, currlon];
        currson.info{count_curron}=[-1, Vapp(vcount),
dataWF, RepeatNumber];
        count_curron=count_curron+1;

```

Polarization Dependant IPE - Function

```
        %Close Mono Shutter
        [buff1, buff2, buff3] = monoshutteroff(Grat,
waveApp(wavcount));

        %Perform sweep for mono OFF (i.e dark current)
        [vol, currloff] = VoltageListSweep(Keith, Vsweep,
HTime, Vsweepsize, ILim, sense);

        %Store the entire current waveform
        currsoff.IV{count_curroff}=[vol, currloff];
        currsoff.info{count_curroff}=[-1, Vapp(vcount),
dataWF, RepeatNumber];
        count_curroff=count_curroff+1;

        %Take mean using avgpoints and subtracting dark
current
        Ineg = mean(curr1on(end-avgpoints:end)) -
mean(currloff(end-avgpoints:end));

        time=toc;
        fprintf('%s V, Ineg %s A, Wavelength %s time %s
\n', num2str(Vapp(vcount)), num2str(Ineg), num2str(waveApp(wavcount)),
num2str(time));

        %Now repeating for positive set

        %Open Mono Shutter
        [buff1, buff2, buff3] = monoshutteron(Grat,
waveApp(wavcount));

        %Positive voltage set
        Vsweep=[Vset*ones(1, setpoints),
Vapp(vcount)*ones(1, points)];
        Vsweepsize = length(Vsweep);
        Vsweep = regexprep(num2str(Vsweep), '\s+', ', ');

        [vol, curr2on] = VoltageListSweep(Keith, Vsweep,
HTime, Vsweepsize, ILim, sense);

        currson.IV{count_currson}=[vol, curr2on];
        currson.info{count_currson}=[1, Vapp(vcount),
dataWF, RepeatNumber];
        count_currson=count_currson+1;

        %Close Mono Shutter
        [buff1, buff2, buff3] = monoshutteroff(Grat,
waveApp(wavcount));
```

Polarization Dependant IPE - Function

```
        %Perform sweep for mono OFF (i.e dark current)
        [vol, curr2off] = VoltageListSweep(Keith, Vsweep,
HTime, Vsweepsize, ILim, sense);

        %Store the entire current waveform
        currsoff.IV{count_curroff}=[vol, curr2off];
        currsoff.info{count_curroff}=[1, Vapp(vcount),
dataWF, RepeatNumber];
        count_curroff=count_curroff+1;

        %Take mean using avgpoints and subtracting dark
current
        Ipos = mean(curr2on(end-avgpoints:end)) -
mean(curr2off(end-avgpoints:end));

        time=toc;
        fprintf('%s V, Ipos %s A, Wavelength %s time %s
\n', num2str(Vapp(vcount)), num2str(Ipos), num2str(waveApp(wavcount)),
num2str(time));

        %4: Save Data
        IPEdata(wavcount, :, vcount, 2, RepeatNumber) =
[dataWF;Ineg;Ipos;Vapp(vcount)];

save('buffersave', 'IPEdata', 'currson', 'currsoff');

        %5: Display
        figure(3)
        plot(IPEdata(wavcount:end, 1, vcount,
2, RepeatNumber), IPEdata(wavcount:end, 2, vcount, 2,
RepeatNumber), 'Color', colors(vcount, :), 'LineStyle', '-');
        drawnow;
        plot(IPEdata(wavcount:end, 1,
vcount, 2, RepeatNumber), IPEdata(wavcount:end,
3, vcount, 2, RepeatNumber), 'Color',
colors(vcount, :), 'LineStyle', '-', 'Marker', 'o');
        drawnow;

        xlim([1240./MaxVal 1240./MinVal]);
        ylabel('Current (A)');
        xlabel('Wavelength (nm)');
end

        %Close Mono Shutter
        [buff1, buff2, buff3] = monoshutteroff(Grat,
waveApp(wavcount));
```

```
end  
end
```

Published with MATLAB® R2019b

REFERENCES

1. J. Backus, “Can programming be liberated from the von Neumann style? A functional style and its algebra of programs,” *Communications of the ACM*, vol. 21, no. 8, p. 613–641, Aug. 1978. <https://doi.org/10.1145/359576.359579>
2. Y. Xi, B. Gao, J. Tang, A. Chen, M. Chang, X. S. Hu, J. Van Der Spiegel, H. Qian, and H. Wu, “In-memory learning with analog resistive switching memory: A review and perspective,” *Proceedings of the IEEE*, pp. 1–29, 2020.
3. M. A. Zidan, J. P. Strachan, and W. D. Lu, “The future of electronics based on memristive systems,” *Nature Electronics*, vol. 1, pp. 22–29, 2018. <https://doi.org/10.1038/s41928-017-0006-8>
4. V. Sze, Y.-H. Chen, T.-J. Yang, and J. Emer, “Efficient processing of deep neural networks: A tutorial and survey,” *Proceedings of the IEEE*, vol. 105, pp. 2295 – 2329, March 2017.
5. G. W. Burr, R. M. Shelby, A. Sebastian, S. Kim, S. Kim, S. Sidler, K. Virwani, M. Ishii, P. Narayanan, A. Fumarola, L. L. Sanches, I. Boybat, M. L. Gallo, K. Moon, J. Woo, H. Hwang, and Y. Leblebici, “Neuromorphic computing using non-volatile memory,” *Advances in Physics: X*, vol. 2, no. 1, pp. 89–124, 2017. <https://doi.org/10.1080/23746149.2016.1259585>
6. W. Haensch, T. Gokmen, and R. Puri, “The next generation of deep learning hardware: Analog computing,” *Proceedings of the IEEE*, vol. 107, no. 1, pp. 108–122, Jan 2019.
7. G. Cristiano, M. Giordano, S. Ambrogio, L. P. Romero, C. Cheng, P. Narayanan, H. Tsai, R. M. Shelby, and G. W. Burr, “Perspective on training fully connected networks with resistive memories: Device requirements for multiple conductances of varying significance,” *Journal of Applied Physics*, vol. 124, no. 15, p. 151901, 2018. <https://doi.org/10.1063/1.5042462>
8. S. Slesazeck and T. Mikolajick, “Nanoscale resistive switching memory devices: a review,” *Nanotechnology*, vol. 30, no. 35, p. 352003, Jun 2019.
9. T. P. Xiao, C. H. Bennett, B. Feinberg, S. Agarwal, and M. J. Marinella, “Analog architectures for neural network acceleration based on non-volatile memory,” *Applied Physics Reviews*, vol. 7, no. 3, p. 031301, 2020. <https://doi.org/10.1063/1.5143815>

10. S. V. Kalinin, A. N. Morozovska, L. Q. Chen, and B. J. Rodriguez, "Local polarization dynamics in ferroelectric materials," *Reports on Progress in Physics*, vol. 73, no. 5, p. 056502, Apr 2010. <https://doi.org/10.1088%2F0034-4885%2F73%2F5%2F056502>
11. H. Ishiwara, "Proposal of adaptive-learning neuron circuits with ferroelectric analog-memory weights," *Japanese Journal of Applied Physics*, vol. 32, no. Part 1, No. 1B, pp. 442–446, Jan 1993. <https://doi.org/10.1143%2Fjjap.32.442>
12. D. Lee, S. M. Yang, T. H. Kim, B. C. Jeon, Y. S. Kim, J.-G. Yoon, H. N. Lee, S. H. Baek, C. B. Eom, and T. W. Noh, "Multilevel data storage memory using deterministic polarization control," *Advanced Materials*, vol. 24, no. 3, pp. 402–406, 2012. <https://onlinelibrary.wiley.com/doi/abs/10.1002/adma.201103679>
13. A. Chanthbouala, V. Garcia, R. O. Cherifi, K. Bouzehouane, S. Fusil, X. Moya, S. Xavier, H. Yamada, C. Deranlot, N. D. Mathur, M. Bibes, A. Barthélémy, and J. Grollier, "A ferroelectric memristor," *Nature Materials*, vol. 11, p. 860, Sep 2012. <https://doi.org/10.1038/nmat3415>
14. S. Boyn, J. Grollier, G. Lecerf, B. Xu, N. Locatelli, S. Fusil, S. Girod, C. Carrétéro, K. Garcia, S. Xavier, J. Tomas, L. Bellaiche, M. Bibes, A. Barthélémy, S. Saïghi, and V. Garcia, "Learning through ferroelectric domain dynamics in solid-state synapses," *Nature Communications*, vol. 8, p. 14736, Apr 2017. <https://doi.org/10.1038/ncomms14736>
15. M. H. Park, Y. H. Lee, T. Mikolajick, U. Schroeder, and C. S. Hwang, "Review and perspective on ferroelectric HfO₂-based thin films for memory applications," *MRS Communications*, vol. 8, no. 3, p. 795–808, 2018.
16. S. J. Kim, J. Mohan, S. R. Summerfelt, and J. Kim, "Ferroelectric Hf_{0.5}Zr_{0.5}O₂ thin films: A review of recent advances," *JOM*, vol. 71, no. 1, pp. 246–255, Jan 2019. <https://doi.org/10.1007/s11837-018-3140-5>
17. T. S. Böske, J. Müller, D. Bräuhaus, U. Schröder, and U. Böttger, "Ferroelectricity in hafnium oxide: CMOS compatible ferroelectric field effect transistors," in *2011 International Electron Devices Meeting*, Dec 2011, pp. 24.5.1–24.5.4.
18. M. Jerry, P. Chen, J. Zhang, P. Sharma, K. Ni, S. Yu, and S. Datta, "Ferroelectric FET analog synapse for acceleration of deep neural network training," in *2017 IEEE International Electron Devices Meeting (IEDM)*, Dec 2017, pp. 6.2.1–6.2.4.
19. E. W. Kinder, C. Alessandri, P. Pandey, G. Karbasian, S. Salahuddin, and A. Seabaugh, "Partial switching of ferroelectrics for synaptic weight storage," in *2017 75th Annual Device Research Conference (DRC)*, June 2017, pp. 1–2.
20. S. Oh, T. Kim, M. Kwak, J. Song, J. Woo, S. Jeon, I. K. Yoo, and H. Hwang, "HfZrO_x-based ferroelectric synapse device with 32 levels of conductance states for neuromorphic applications," *IEEE Electron Device Letters*, vol. 38, no. 6, pp. 732–735, June 2017.

21. X. Sun, P. Wang, K. Ni, S. Datta, and S. Yu, "Exploiting hybrid precision for training and inference: A 2T-1FeFET based analog synaptic weight cell," in 2018 IEEE International Electron Devices Meeting (IEDM), Dec 2018, pp. 3.1.1–3.1.4.
22. R. Berdan, T. Marukame, K. Ota, M. Yamaguchi, M. Saitoh, S. Fujii, J. Deguchi, and Y. Nishi, "Low-power linear computation using nonlinear ferroelectric tunnel junction memristors," *Nature Electronics*, vol. 3, no. 5, pp. 259–266, May 2020. <https://doi.org/10.1038/s41928-020-0405-0>
23. S. Dünkel, M. Trentzsch, R. Richter, P. Moll, C. Fuchs, O. Gehring, M. Majer, S. Wittek, B. Müller, T. Melde, H. Mulaosmanovic, S. Slesazek, S. Müller, J. Ocker, M. Noack, D. . Löhr, P. Polakowski, J. Müller, T. Mikolajick, J. Höntschel, B. Rice, J. Pellerin, and S. Beyer, "A FeFET based super-low-power ultra-fast embedded NVM technology for 22nm FDSOI and beyond," in 2017 IEEE International Electron Devices Meeting (IEDM), Dec 2017, pp. 19.7.1–19.7.4.
24. C. Alessandri, P. Pandey, A. Abusleme, and A. Seabaugh, "Switching Dynamics of Ferroelectric Zr-Doped HfO₂," *IEEE Electron Device Letters*, vol. 39, no. 11, pp. 1780–1783, Nov 2018.
25. T. Mikolajick, U. Schroeder, and S. Slesazek, "The past, the present, and the future of ferroelectric memories," *IEEE Transactions on Electron Devices*, vol. 67, no. 4, pp. 1434–1443, 2020.
26. K. R. Udayakumar, T. S. Moise, S. R. Summerfelt, K. Boku, K. Remack, J. Rodriguez, M. Arendt, G. Shinn, J. Eliason, R. Bailey, and P. Staubs, "Manufacturable high-density 8 Mbit one transistor–one capacitor embedded ferroelectric random access memory," *Japanese Journal of Applied Physics*, vol. 47, no. 4, pp. 2710–2713, Apr 2008. <https://doi.org/10.1143%2Fjjap.47.2710>
27. T. S. Moise, S. R. Summerfelt, H. McAdams, S. Aggarwal, K. R. Udayakumar, F. G. Celii, J. S. Martin, G. Xing, L. Hall, K. J. Taylor, T. Hurd, J. Rodriguez, K. Remack, M. D. Khan, K. Boku, G. Stacey, M. Yao, M. G. Albrecht, E. Zielinski, M. Thakre, S. Kuchimanchi, A. Thomas, B. McKee, J. Rickes, A. Wang, J. Grace, J. Fong, D. Lee, C. Pietrzyk, R. Lanham, S. R. Gilbert, D. Taylor, J. Amano, R. Bailey, F. Chu, G. Fox, S. Sun, and T. Davenport, "Demonstration of a 4 Mb, high density ferroelectric memory embedded within a 130nm, 5LM Cu/FSG logic process," in IEEE International Electron Devices Meeting, Dec. 2002, pp. 535–538. <https://doi.org/10.1109/IEDM.2002.1175897>
28. J. Rodriguez, K. Remack, J. Gertas, K. Boku, K. R. Udayakumar, S. Summerfelt, G. Shinn, S. Madan, H. Mcadams, T. Moise, J. Eliason, R. Bailey, M. Depner, D. Kim, and P. Staubs, "Reliability demonstration of a ferroelectric random access memory embedded within a 130nm cmos process," in 2007 Non-Volatile Memory Technology Symposium, 2007, pp. 64–66.

29. T. S. Moise, S. R. Summerfelt, G. Xing, L. Colombo, T. Sakoda, S. R. Gilbert, A. Loke, S. Ma, R. Kavari, L. A. Wills, T. Hsu, J. Amano, S. T. Johnston, D. J. Vestyck, M. W. Russell, and S. M. Bilodeau, “Electrical properties of submicron ($\geq 0.13 \mu\text{m}^2$) Ir/PZT/Ir capacitors formed on W plugs,” in 1999 International Electron Devices Meeting, Dec. 1999, pp. 940–942. <https://doi.org/10.1109/IEDM.1999.824305>
30. S. R. Gilbert, S. Hunter, D. Ritchey, C. Chi, D. V. Taylor, J. Amano, S. Aggarwal, T. S. Moise, T. Sakoda, S. R. Summerfelt, K. K. Singh, C. Kazemi, D. Carl, and B. Bierman, “Preparation of $\text{Pb}(\text{Zr},\text{Ti})\text{O}_3$ thin films by metalorganic chemical vapor deposition for low voltage ferroelectric memory,” *Journal of Applied Physics*, vol. 93, no. 3, pp. 1713–1717, Feb. 2003. <https://doi.org/10.1063/1.1534380>
31. M. Jerry, S. Dutta, A. Kazemi, K. Ni, J. Zhang, P.-Y. Chen, P. Sharma, S. Yu, X. S. Hu, M. Niemier, and S. Datta, “A ferroelectric field effect transistor based synaptic weight cell,” *Journal of Physics D: Applied Physics*, vol. 51, no. 43, p. 434001, Aug 2018. <https://doi.org/10.1088%2F1361-6463%2Faad6f8>
32. R. Laibowitz, L. Esaki, and P. Stiles, “Electron transport in Nb-Nb oxide-Bi tunnel junctions,” *Physics Letters A*, vol. 36, no. 5, pp. 429 – 430, 1971. <http://www.sciencedirect.com/science/article/pii/0375960171902933>
33. M. Hoffmann, S. Slesazek, U. Schroeder, and T. Mikolajick, “What’s next for negative capacitance electronics?” *Nature Electronics*, vol. 3, no. 9, pp. 504–506, Sep 2020. <https://doi.org/10.1038/s41928-020-00474-9>
34. K. Ni, X. Li, J. A. Smith, M. Jerry, and S. Datta, “Write disturb in ferroelectric FETs and its implication for 1T-FeFET and memory arrays,” *IEEE Electron Device Letters*, vol. 39, no. 11, pp. 1656–1659, Nov. 2018. <https://doi.org/10.1109/LED.2018.2872347>
35. T. Gokmen and Y. Vlasov, “Acceleration of deep neural network training with resistive cross-point devices: Design considerations,” *Frontiers in Neuroscience*, vol. 10, p. 333, 2016. <https://www.frontiersin.org/article/10.3389/fnins.2016.00333>
36. M. Kobayashi, Y. Tagawa, F. Mo, T. Saraya, and T. Hiramoto, “Ferroelectric HfO_2 tunnel junction memory with high TER and multi-level operation featuring metal replacement process,” *IEEE Journal of the Electron Devices Society*, vol. 7, pp. 134–139, 2019.
37. J. G. Simmons, “Generalized formula for the electric tunnel effect between similar electrodes separated by a thin insulating film,” *Journal of Applied Physics*, vol. 34, no. 6, pp. 1793–1803, 1963. <https://doi.org/10.1063/1.1702682>
38. Y. LeCun, Y. Bengio, and G. Hinton, “Deep learning,” *Nature*, vol. 521, p. 436, May 2015. <https://doi.org/10.1038/nature14539>

39. C. Alessandri, P. Pandey, A. Abusleme, and A. Seabaugh, "Monte Carlo simulation of switching dynamics in polycrystalline ferroelectric capacitors," *IEEE Transactions on Electron Devices*, vol. 66, no. 8, pp. 3527–3534, Jun. 2019. <https://doi.org/10.1109/TED.2019.2922268>
40. P. Pandey, W. S. Hwang, K. R. Udayakumar, T. S. Moise, and A. C. Seabaugh, "Programming-pulse dependence of ferroelectric partial polarization: Insights from a comparative study of PZT and HZO capacitors," *IEEE Transactions on Electron Devices*, pp. 1–6, 2020.
41. C. Alessandri, P. Pandey, and A. C. Seabaugh, "Experimentally validated, predictive Monte Carlo modeling of ferroelectric dynamics and variability," in 2018 IEEE International Electron Devices Meeting (IEDM), Dec 2018, pp. 16.2.1–16.2.4.
42. P. Pandey, C. Alessandri, and A. C. Seabaugh, "Process dependent switching dynamics of ferroelectric hafnium zirconate," in 2019 Device Research Conference (DRC), Jun. 2019, pp. 49–50. <https://doi.org/10.1109/DRC46940.2019.9046408>
43. Y. Ishibashi and Y. Takagi, "Note on ferroelectric domain switching," *Journal of the Physical Society of Japan*, vol. 31, no. 2, pp. 506–510, 1971. <https://doi.org/10.1143/JPSJ.31.506>
44. A. K. Tagantsev, I. Stolichnov, N. Setter, J. S. Cross, and M. Tsukada, "Non-Kolmogorov-Avrami switching kinetics in ferroelectric thin films," *Phys. Rev. B*, vol. 66, p. 214109, Dec 2002. <https://link.aps.org/doi/10.1103/PhysRevB.66.214109>
45. T. P. Ma and Jin-Ping Han, "Why is nonvolatile ferroelectric memory field-effect transistor still elusive?" *IEEE Electron Device Letters*, vol. 23, no. 7, pp. 386–388, 2002.
46. J. Y. Jo, H. S. Han, J.-G. Yoon, T. K. Song, S.-H. Kim, and T. W. Noh, "Domain switching kinetics in disordered ferroelectric thin films," *Phys. Rev. Lett.*, vol. 99, p. 267602, Dec 2007. <https://link.aps.org/doi/10.1103/PhysRevLett.99.267602>
47. J. F. Scott, L. Kammerdiner, M. Parris, S. Traynor, V. Ottenbacher, A. Shawabkeh, and W. F. Oliver, "Switching kinetics of lead zirconate titanate submicron thin-film memories," *Journal of Applied Physics*, vol. 64, no. 2, pp. 787–792, 1988. <https://doi.org/10.1063/1.341925>
48. S. Zhukov, Y. A. Genenko, O. Hirsch, J. Glaum, T. Granzow, and H. von Seggern, "Dynamics of polarization reversal in virgin and fatigued ferroelectric ceramics by inhomogeneous field mechanism," *Phys. Rev. B*, vol. 82, p. 014109, Jul 2010. <https://link.aps.org/doi/10.1103/PhysRevB.82.014109>
49. I. Tan, G. L. Snider, L. D. Chang, and E. L. Hu, "A self-consistent solution of Schrödinger–Poisson equations using a nonuniform mesh," *Journal of Applied Physics*, vol. 68, no. 8, pp. 4071–4076, 1990. <https://doi.org/10.1063/1.346245>

50. V. V. Afanas'ev, A. Stesmans, F. Chen, X. Shi, and S. A. Campbell, "Internal photoemission of electrons and holes from (100)Si into HfO₂," *Applied Physics Letters*, vol. 81, no. 6, pp. 1053–1055, 2002. <https://doi.org/10.1063/1.1495088>
51. T. Schenk, E. Yurchuk, S. Mueller, U. Schroeder, S. Starschich, U. Böttger, and T. Mikolajick, "About the deformation of ferroelectric hystereses," *Applied Physics Reviews*, vol. 1, no. 4, p. 041103, 2014. <https://doi.org/10.1063/1.4902396>
52. C. Alessandri, "Ferroelectric memory and architecture for deep neural network training in resistive crossbar arrays," Ph.D. dissertation, University of Notre Dame, Notre Dame, Indiana, 4 2019.
53. M. Pešić, F. P. G. Fengler, L. Larcher, A. Padovani, T. Schenk, E. D. Grimley, X. Sang, J. M. LeBeau, S. Slesazek, U. Schroeder, and T. Mikolajick, "Physical mechanisms behind the field-cycling behavior of hfo2-based ferroelectric capacitors," *Advanced Functional Materials*, vol. 26, no. 25, pp. 4601–4612, 2016. <https://onlinelibrary.wiley.com/doi/abs/10.1002/adfm.201600590>
54. S. Starschich, S. Menzel, and U. Böttger, "Evidence for oxygen vacancies movement during wake-up in ferroelectric hafnium oxide," *Applied Physics Letters*, vol. 108, no. 3, p. 032903, 2016. <https://doi.org/10.1063/1.4940370>
55. E. D. Grimley, T. Schenk, X. Sang, M. Pešić, U. Schroeder, T. Mikolajick, and J. M. LeBeau, "Structural changes underlying field-cycling phenomena in ferroelectric hfo2 thin films," *Advanced Electronic Materials*, vol. 2, no. 9, p. 1600173, 2016. <https://onlinelibrary.wiley.com/doi/abs/10.1002/aelm.201600173>
56. F. Mehmood, T. Mikolajick, and U. Schroeder, "Wake-up mechanisms in ferroelectric lanthanum-doped Hf_{0.5}Zr_{0.5}O₂ thin films," *physica status solidi (a)*, vol. n/a, no. n/a, p. 2000281. <https://onlinelibrary.wiley.com/doi/abs/10.1002/pssa.202000281>
57. S. S. Fields, S. W. Smith, P. J. Ryan, S. T. Jaszewski, I. A. Brummel, A. Salanova, G. Esteves, S. L. Wolfley, M. D. Henry, P. S. Davids, and J. F. Ihlefeld, "Phase-exchange-driven wake-up and fatigue in ferroelectric hafnium zirconium oxide films," *ACS Applied Materials & Interfaces*, vol. 12, no. 23, pp. 26 577–26 585, 2020, pMID: 32410447. <https://doi.org/10.1021/acsami.0c03570>
58. R. Batra, T. D. Huan, J. L. Jones, G. Rossetti, and R. Ramprasad, "Factors favoring ferroelectricity in hafnia: A first-principles computational study," *The Journal of Physical Chemistry C*, vol. 121, no. 8, pp. 4139–4145, 2017. <https://doi.org/10.1021/acs.jpcc.6b11972>
59. G. Karbasian, R. dos Reis, A. K. Yadav, A. J. Tan, C. Hu, and S. Salahuddin, "Stabilization of ferroelectric phase in tungsten capped Hf_{0.8}Zr_{0.2}O₂," *Applied Physics Letters*, vol. 111, no. 2, p. 022907, 2017. <https://doi.org/10.1063/1.4993739>

60. H. P. McAdams, R. Acklin, T. Blake, Xiao-Hong Du, J. Eliason, J. Fong, W. F. Kraus, D. Liu, S. Madan, T. Moise, S. Natarajan, N. Qian, Y. Qiu, K. A. Remack, J. Rodriguez, J. Roscher, A. Seshadri, and S. R. Summerfelt, "A 64Mbit embedded FeRAM utilizing a 130-nm 5LM Cu/FSG logic process," *IEEE Journal of Solid-State Circuits*, vol. 39, no. 4, pp. 667–677, Mar. 2004. <https://doi.org/10.1109/JSSC.2004.825241>
61. M. Si, X. Lyu, P. R. Shrestha, X. Sun, H. Wang, K. P. Cheung, and P. D. Ye, "Ultrafast measurements of polarization switching dynamics on ferroelectric and anti-ferroelectric hafnium zirconium oxide," *Applied Physics Letters*, vol. 115, no. 7, p. 072107, 2019. <https://doi.org/10.1063/1.5098786>
62. H. Mulaosmanovic, J. Ocker, S. Muller, U. Schroeder, J. Muller, P. Polakowski, S. Flachowsky, R. van Bentum, T. Mikolajick, and S. Slesazeck, "Switching kinetics in nanoscale hafnium oxide based ferroelectric field-effect transistors," *ACS Applied Materials & Interfaces*, vol. 9, no. 4, pp. 3792–3798, Jan. 2017. <https://doi.org/10.1021/acsami.6b13866>
63. H. Mulaosmanovic, T. Mikolajick, and S. Slesazeck, "Accumulative polarization reversal in nanoscale ferroelectric transistors," *ACS Applied Materials & Interfaces*, vol. 10, no. 28, pp. 23997–24002, 2018. <https://doi.org/10.1021/acsami.8b08967>
64. V. V. Afanas'ev and A. Stesmans, "Internal photoemission at interfaces of high-k insulators with semiconductors and metals," *Journal of Applied Physics*, vol. 102, no. 8, p. 081301, 2007. <https://doi.org/10.1063/1.2799091>
65. V. V. Afanas'ev, D. Chiappe, A. Leonhardt, M. Houssa, C. Huyghebaert, I. Radu, and A. Stesmans, "(Invited) Internal photoemission of electrons from 2-dimensional semiconductors," *Meeting Abstracts*, vol. MA2017-02, no. 14, p. 836, 2017. <http://ma.ecsdl.org/content/MA2017-02/14/836.abstract>
66. V. Afanas'ev, *Internal Photoemission Spectroscopy*, 2nd ed. Elsevier, 2014.
67. R. J. Powell, "Interface barrier energy determination from voltage dependence of photoinjected currents," *Journal of Applied Physics*, vol. 41, no. 6, pp. 2424–2432, 1970. <https://doi.org/10.1063/1.1659238>
68. M. Born, E. Wolf, A. B. Bhatia, P. C. Clemmow, D. Gabor, A. R. Stokes, A. M. Taylor, P. A. Wayman, and W. L. Wilcock, *Principles of Optics: Electromagnetic Theory of Propagation, Interference and Diffraction of Light*, 7th ed. Cambridge University Press, 1999.
69. Light collection and systems throughput. <https://www.newport.com/t/light-collection-and-systems-throughput>
70. MATLAB, *version 9.4.0 (R2018a)*. Natick, Massachusetts: The MathWorks Inc., 2018.

71. Q. Zhang, Personal communication via email, March 2020.
72. L. Chen, T.-Y. Wang, Y.-W. Dai, M.-Y. Cha, H. Zhu, Q.-Q. Sun, S.-J. Ding, P. Zhou, L. Chua, and D. W. Zhang, “Ultra-low power $\text{Hf}_{0.5}\text{Zr}_{0.5}\text{O}_2$ based ferroelectric tunnel junction synapses for hardware neural network applications,” *Nanoscale*, vol. 10, pp. 15 826–15 833, 2018. <http://dx.doi.org/10.1039/C8NR04734K>
73. X. Tian and A. Toriumi, “New opportunity of ferroelectric tunnel junction memory with ultrathin HfO_2 -based oxides,” in 2017 IEEE Electron Devices Technology and Manufacturing Conference (EDTM), Feb 2017, pp. 36–64.
74. S. M. Sze and K. K. Ng, *Physics of Semiconductor Devices*, 3rd ed. John Wiley and Sons, 2006, pp. 201–202.
75. H. B. Michaelson, “Work functions of the elements,” *Journal of Applied Physics*, vol. 21, no. 6, pp. 536–540, 1950. <https://doi.org/10.1063/1.1699702>
76. V. Afanas’ev, *Internal Photoemission Spectroscopy*, 2nd ed. Elsevier, 2014, pp. 44–47.
77. —, *Internal Photoemission Spectroscopy*, 2nd ed. Elsevier, 2014, pp. 84–92.
78. V. Afanas’ev, M. Houssa, A. Stesmans, G. Adriaenssens, and M. Heyns, “Energy barriers between (100)Si and Al_2O_3 and ZrO_2 -based dielectric stacks: internal electron photoemission measurements,” *Microelectronic Engineering*, vol. 59, no. 1, pp. 335 – 339, 2001, 12th Biannual Conference on Insulating Films on Semiconductors. <http://www.sciencedirect.com/science/article/pii/S0167931701006542>
79. V. Afanas’ev, *Internal Photoemission Spectroscopy*, 2nd ed. Elsevier, 2014, p. 102.
80. T. Gokmen and Y. Vlasov, “Acceleration of deep neural network training with resistive cross-point devices: Design considerations,” *Frontiers in Neuroscience*, vol. 10, p. 333, 2016. <https://www.frontiersin.org/article/10.3389/fnins.2016.00333>